A Multi-Wavelength Census of Star Formation at Redshifts $z \sim 2$

Thesis by
Naveen A. Reddy

In Partial Fulfillment of the Requirements
for the Degree of
Doctor of Philosophy

California Institute of Technology
Pasadena, California

2006

(Defended May 15, 2006)

Acknowledgements

This thesis work, and the valuable experience I have gained as a graduate student at Caltech, were made possible by more people than I can name here. During my first year at Caltech the senior graduate students made us feel welcome and provided us with great insights into the department and the faculty. I would like to thank Nick Scoville for making Caltech a less intimidating place with his informal yet enthusiastic presence. Thanks to my former collaborators in the world of long wavelength astronomy, including Nick, Andrew Blain, Dave Frayer, and Lee Armus. I would especially like to acknowledge Lee for teaching me the correct way to handle Keck ToO requests. Thanks to Shardha for her patience while teaching me the ropes at OVRO.

I am grateful to the peers in my graduate class, especially Pranjal Trivedi, Alison Farmer, Dawn Erb, and George Becker, for going through classes with me and sharing in the trials and tribulations of graduate school. Thanks also to my regular lunch group, including Micol Christopher, George, Edo Berger, Dawn, Alison, Dave Kaplan, and Jackie Kessler, for providing a necessary respite during the middle of the day.

I am indebted to my former officemates, Dawn Erb, Alison Farmer, Jackie Kessler, Alicia Soderberg, and Joanna Brown, for providing just the right amount of distraction to keep me going throughout the day. A special acknowledgment goes out to Alison for keeping me company in the office when no one else seemed to be around, and for our endless discussions of Daleks and hemispherical bugs. And Jackie, for staying in the office late while working on her thesis and accompanying me on trips to Baskin Robins to get a Chocolate Vortex. And Alicia, both for keeping me company in the office and for keeping me apprised of who was making all that noise outside our office.

A special thanks to the Astronomy Department systems administrators, Patrick Shopbell, Cheryl Southard, and Anu Mahabal, for always being ready with a solution whenever my machine, nicmos, started acting up. They know more about computers than anyone else I know, and my thesis work would not have been possible without their support. I am grateful to the Caltech ITS technician, Kar Cheung, for tirelessly working for 6 straight months to get my Mac laptop working again.

All of the work in this thesis is based on a spectroscopic sample of galaxies obtained with Keck, and I am indebted to the staff there, including Marc Kassis and Paolo Amico,

for the best possible instrument support. Thanks to Jean Mueller and Karl Dunscombe for their lively company during the long nights at Palomar, and Dipali and Rose for their good cooking and hospitality at the Monastery.

I am lucky to have been a part of an excellent collaborative group, including Alice Shapley, Max Pettini, Kurt Adelberger, Dawn Erb, and Matt Hunt. I especially want to acknowledge Max for being a steadfast collaborator who always provided insightful comments and suggestions, and great humor during observing runs and conferences. Kurt was also an excellent resource of information and, while we did not overlap at Caltech, I am grateful that he accompanied us on a few observing trips to Keck. And of course Dawn Erb, who has been there since the beginning as a classmate, collaborator, and a good friend.

I would be amiss not to mention the support and encouragement of two very close friends, Micol Christopher and Alice Shapley, whom I've come to think of as siblings. Thanks, Micol, for being a loyal friend and a constant pillar of support for me through some tough times, and for sharing in the good times. Thanks also for letting me bug you everyday to make light conversation when I needed some distraction from work. And, of course, Alice, who has been an unwavering source of enthusiasm, support, and encouragement, and with whom I've had many conversations about galaxies, ramekins, and menudo, which kept me going throughout the day.

I am grateful to Min Yun whose mentoring and friendship while I was a summer student at NRAO prompted my decision to pursue astrophysics as a career. And, last but not least, none of this would have been possible without my advisor, Chuck Steidel. Despite his busy schedule, Chuck was always available to look at drafts of papers, send comments, suggest new avenues to pursue, and answer my questions with patience. He provided just the right amount of independence and encouragement. I also particularly enjoyed the scientific discussions I had with Chuck. Chuck is an easy person to work with; his approachability and modesty are only superseded by his incredible grasp of astronomy, and he is one of the smartest people I know. I am very grateful to have had the opportunity to be his graduate student. Finally, I could not have come this far without the support and encouragement of my parents. They believed in me and kept me going to make this all possible.

A Multi-Wavelength Census of Star Formation at Redshifts $z \sim 2$

by

Naveen A. Reddy

In Partial Fulfillment of the

Requirements for the Degree of

Doctor of Philosophy

Abstract

We examine the census of star-forming galaxies and their extinction properties at redshift $z \sim 2$, when a large fraction of the stellar mass in the universe formed. We find a good agreement between the X-ray, radio, and de-reddened UV estimates of the average star formation rate (SFR) for our sample of $z \sim 2$ galaxies of $\sim 50\ M_{\odot}\ \mathrm{yr}^{-1}$, indicating that the locally calibrated SFR relations appear to be statistically valid from redshifts $1.5 \lesssim z \lesssim 3.0$. *Spitzer* MIPS data are used to assess the extinction properties of individual star-forming galaxies, and we find that the rest-frame UV slope of most galaxies at $z \sim 2$ can be used to infer their attenuation factors, $L_{\mathrm{bol}}/L_{\mathrm{UV}}$. As in the local universe, the obscuration, $L_{\mathrm{FIR}}/L_{\mathrm{UV}}$, is strongly dependent on bolometric luminosity, and ranges in value from < 1 to ~ 1000 within the sample considered. However, the obscuration is ~ 10 times smaller at a given L_{bol} (or, equivalently, a similar level of obscuration occurs at luminosities ~ 10 times larger) at $z \sim 2$ than at $z \sim 0$. This trend is expected as galaxies age and their gas becomes more dust-enriched. Specific SFRs indicate wide range in the evolutionary state of galaxies at $z \sim 2$, from galaxies that have just begun to form stars to those that have already accumulated most of their stellar mass and are about to become, or already are, passively evolving. Finally, we examine two techniques for assessing the census of galaxies at $z \sim 2$. In the first, we select galaxies using optical, near-IR, and sub-mm criteria, and find a large overlap between optical and near-IR selected samples of galaxies at $z \sim 2$. The second technique involves reconstructing the luminosity function of $z \sim 2$ galaxies as determined from Monte Carlo simulations. We find that the SFR density increases between $z = 4$ to 2 by a factor of ~ 1.2. However, this increase is mild compared to the much steeper

increase from $z \sim 6$ to $z \sim 4$, suggesting that the processes responsible for the increase in SFR density at early epochs saturate around $z \sim 2$.

Contents

List of Figures

List of Tables

Chapter 1

Introduction

Understanding the star formation history and stellar mass evolution of galaxies is perhaps one of the most fundamental issues in cosmology. Observations of the stellar mass and star formation rate density, the number density of QSOs, and galaxy morphology at both low ($z \lesssim 1$) and high ($z \gtrsim 3$) redshifts indicate that most of the activity responsible for shaping the bulk properties of galaxies to their present form occured in the epochs between $1 \lesssim z \lesssim 3$ (e.g., Dickinson et al. 2003b; Rudnick et al. 2003; Chapman et al. 2005; Madau et al. 1996; Lilly et al. 1996, 1995; Steidel et al. 1999; Shaver et al. 1996; Fan et al. 2001; Di Matteo et al. 2003; Conselice et al. 2004; Papovich et al. 2003; Shapley et al. 2001; Giavalisco et al. 1996). Galaxy studies during this intermediate redshift range have suffered, however, because of our inability to identify large samples of galaxies during this critical epoch. The primary difficulty at these redshifts was due to the fact that the lines used for redshift identification are shifted into the near-UV where detector sensitivity has lagged, or to the near-IR where spectroscopy is more difficult due to higher backgrounds.

However, the advent of $8-10$ m class telescopes and improvements in detector technology have allowed us to make significant progress by making it possible to select large samples of galaxies during the critical epochs corresponding to redshifts $1.4 \lesssim z \lesssim 3.0$. There are essentially two ways in which to proceed in order to assess the census of galaxies at high redshift. The first is to observe galaxies over as wide a range in wavelengths as possible in order to select those that comprise the bulk of the total star formation rate density (SFRD). Along this line, several color criteria have been developed to target galaxies over the redshift range $1.4 \lesssim z \lesssim 3.0$. The first method, and the one upon which most of this thesis is based, is optical selection of galaxies through the $U_nG\mathcal{R}$ bands (Adelberger et al.

2004; Steidel et al. 2004). The second method is to select galaxies by their near-IR $z - K$ color, taking advantage of the fact that for redshifts $z \gtrsim 1.4$, the $z-$ and K-bands bracket the age-sensitive Balmer and 4000 Å break features in the spectra of most star-forming and "passively evolving" (or quiescent) galaxies (Daddi et al. 2004b). The third method selects either passively evolving or star-forming galaxies at redshifts $z \gtrsim 2$ based on the single color criteria $J - K_{\rm s} > 2.3$ (in Vega magnitudes), again taking advantage of the Balmer and 4000 Å breaks (Franx et al. 2003). The fourth method relies on the monochromatic flux at 850 μm to select dusty, high redshift galaxies (Blain et al. 1999). Each selection method presents its own advantages and disadvantages, but one critical issue that has previously been neglected is that one must take into account the substantial overlap between these samples when estimating the total SFRD (Reddy et al. 2005). Each of the selection criteria and their respective overlap and contributions to the SFRD are discussed in Chapter 3.

The second approach to assessing the total star formation rate density is to simulate many realizations of the intrinsic distribution of galaxy properties at high redshift, subject these realizations to the same photometric methods and selection criteria as applied to real data, and then adjust the simulated realizations until convergence is reached between the expected and observed distribution of galaxy properties. This Monte Carlo approach has the advantage, unlike the first method, of not requiring the observational effort necessary to conduct a panchromatic assessment of the total SFRD. The method works especially well when applied to joint spectroscopic and photometric samples of galaxies and therefore works best for optically-selected samples where spectroscopy is much more feasible than for near-IR selected samples. Perhaps the main disadvantage of this method is the inability to correct sample completeness for galaxies that are completely missed (i.e., not scattered into the color selection windows). Nevertheless, applying this method to spectroscopically confirmed samples of high redshift galaxies allows one to evaluate the systematic effects of photometric scatter and the intrinsic variation in colors due to line emission and absorption with great accuracy. We can further evaluate the signficance and magnitude of the dust extinction corrections necessary to translate UV luminosities to total bolometric luminosities (see below and Chapters 2, 3, 4, and 6). Our Monte Carlo approach to computing sample incompleteness can then be used to reconstruct the total SFRD. This method is discussed in detail in Chapter 6.

1.1 The Optical Selection of High Redshift Galaxies

1.1.1 Photometric Selection

Constructing a practical set of selection criteria to select all galaxies in any desired redshift range and reject all others is an intractable problem. One extreme is to select all objects down to a given magnitude limit, such as in flux-limited surveys of high redshift galaxies, but unfortunately such studies suffer from significant amounts of foreground contamination. Without additional color criteria, one may spend 99% of the time spectroscopically confirming low redshift contaminants before assembling a significant sample of galaxies at the desired redshift range. Color-selected samples have the distinct advantage of allowing one to specifically target a desired redshift range while minimizing the number of interlopers. Perhaps the most successful of the various color criteria that have been designed to select galaxies at different epochs is rest-frame UV color selection, pioneered by Steidel et al. (1995) to select galaxies at $z \sim 3$, and extended to higher redshifts (e.g., Bouwens et al. 2005, 2004; Bunker et al. 2004; Dickinson et al. 2004; Yan et al. 2003). The success of this technique is partly due to its simplicity in that only a few broadband filters are required to assemble such samples and, at lower redshifts ($1.4 \lesssim z \lesssim 3.5$), where the galaxies can be spectroscopically observed and precise redshifts can be obtained in a short amount of observing time. Combined, these surveys have given us an unprecedented view of galaxy evolution over almost the entire age of the universe.

For the past several years, the main focus of our group has been to assemble a large sample of galaxies at the peak epoch of galaxy formation and black hole growth, corresponding to redshifts $1.5 \lesssim z \lesssim 2.6$. The selection criteria aim to select actively star-forming galaxies at $z \sim 2$ with the same range in intrinsic UV color and extinction as Lyman break galaxies (LBGs) at $z \sim 3$ (Steidel et al. 2003). While galaxies at $z \sim 2$ do not have any of the strong spectral breaks across the $U_nG\mathcal{R}$ bands used to select higher redshift galaxies (Figure 1.1), they do occupy a particular area of $U_nG\mathcal{R}$ color space that can be singled out (Figure 1.2).

We have used the "BX" criteria of Adelberger et al. (2004) and Steidel et al. (2004) to select galaxies at redshifts $2.0 \lesssim z \lesssim 2.6$, placing the following requirements on the observed

colors:

$$\begin{aligned} G-\mathcal{R} &\geq -0.2 \\ U_n-G &\geq G-\mathcal{R}+0.2 \\ G-\mathcal{R} &\leq 0.2(U_n-G)+0.4 \\ U_n-G &\leq G-\mathcal{R}+1.0. \end{aligned} \tag{1.1}$$

Similarly we have selected "BM" galaxies at redshifts $1.5 \lesssim z \lesssim 2.0$ using the following criteria:

$$\begin{aligned} G-\mathcal{R} &\geq -0.2 \\ U_n-G &\geq G-\mathcal{R}-0.1 \\ G-\mathcal{R} &\geq 0.2(U_n-G)+0.4 \\ U_n-G &\leq G-\mathcal{R}+0.2. \end{aligned} \tag{1.2}$$

To ensure a sample of galaxies amenable to spectroscopic followup, we imposed a magnitude limit of $\mathcal{R} = 25.5$. This limit corresponds to an absolute magnitude 0.6 mag fainter at $z = 2.2 \pm 0.4$ (the mean and dispersion of the measured redshift distribution for BX candidates with $z > 1$) than at $z \sim 3$. We also excluded candidates with $\mathcal{R} < 19$ since almost all of these objects are stars. Given the constraints of the color criteria and the self-imposed magnitude limits, the combined BM, BX, and LBG samples constitute 25 to 30% of the total $\mathcal{R}$ and $K_{\rm s}$ band counts to $\mathcal{R} = 25.5$ and $K_{\rm s}(AB) = 24.4$, respectively.

1.1.2 Spectroscopic Followup

The spectroscopic followup to the optically selected sample is discussed in detail in the following chapters. Briefly, we took advantage of the multi-object capabilities of the Keck LRIS (Low Resolution Imaging Spectrograph; Oke et al. 1995) instrument to obtain spectroscopy. The unrivaled near-UV sensitivity of the blue arm of LRIS (LRIS-B; Steidel et al. 2004) is necessary for spectroscopically identifying galaxies in the so-called spectroscopic desert where BX and BM selected galaxies are expected to lie and where the stellar and interstellar absorption lines typically used for redshift identification are shifted into the

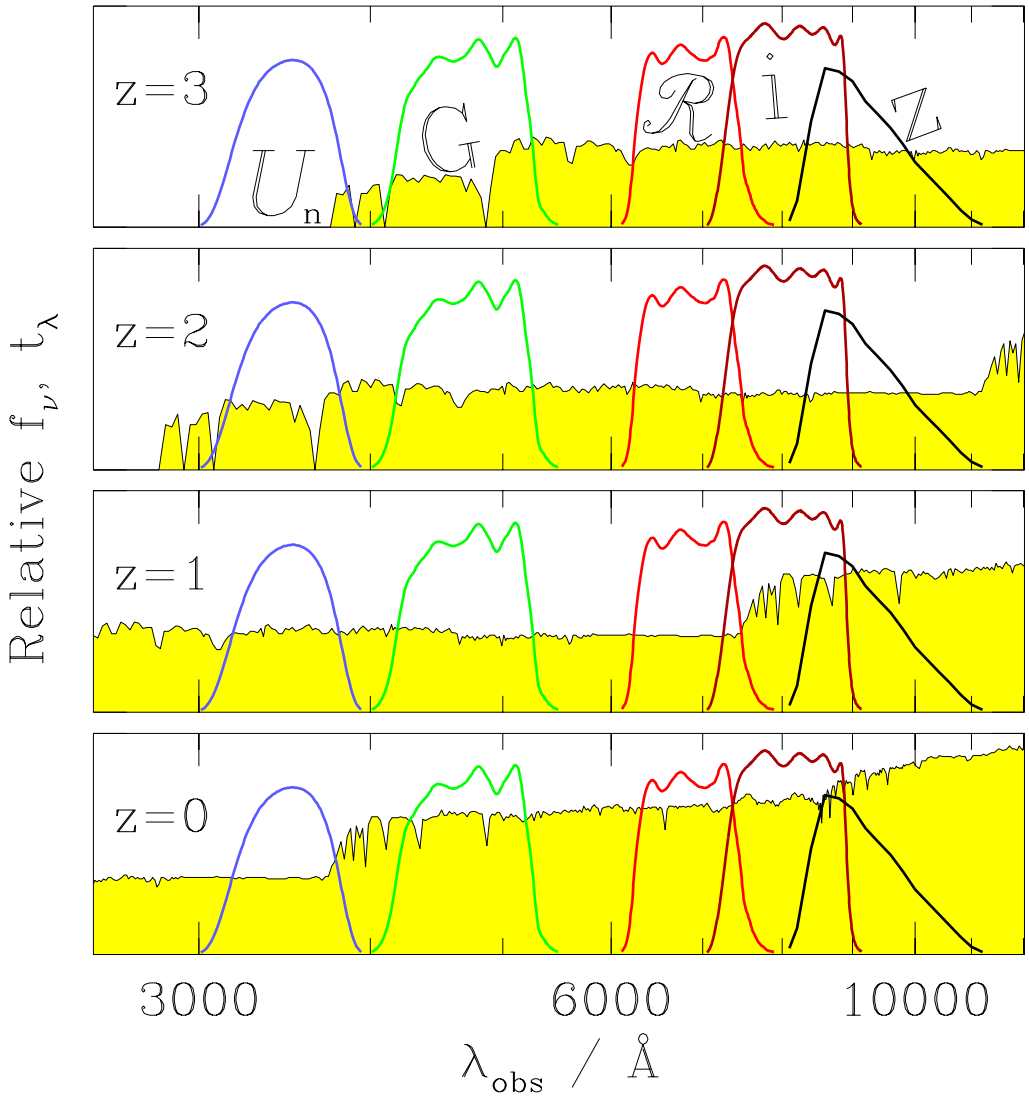

Figure 1.1 Relative placement of the $U_nG\mathcal{R}Iz$ bands with respect to a constant star forming galaxy at redshifts $z = 0 - 4$ (figure from Adelberger et al. 2004).

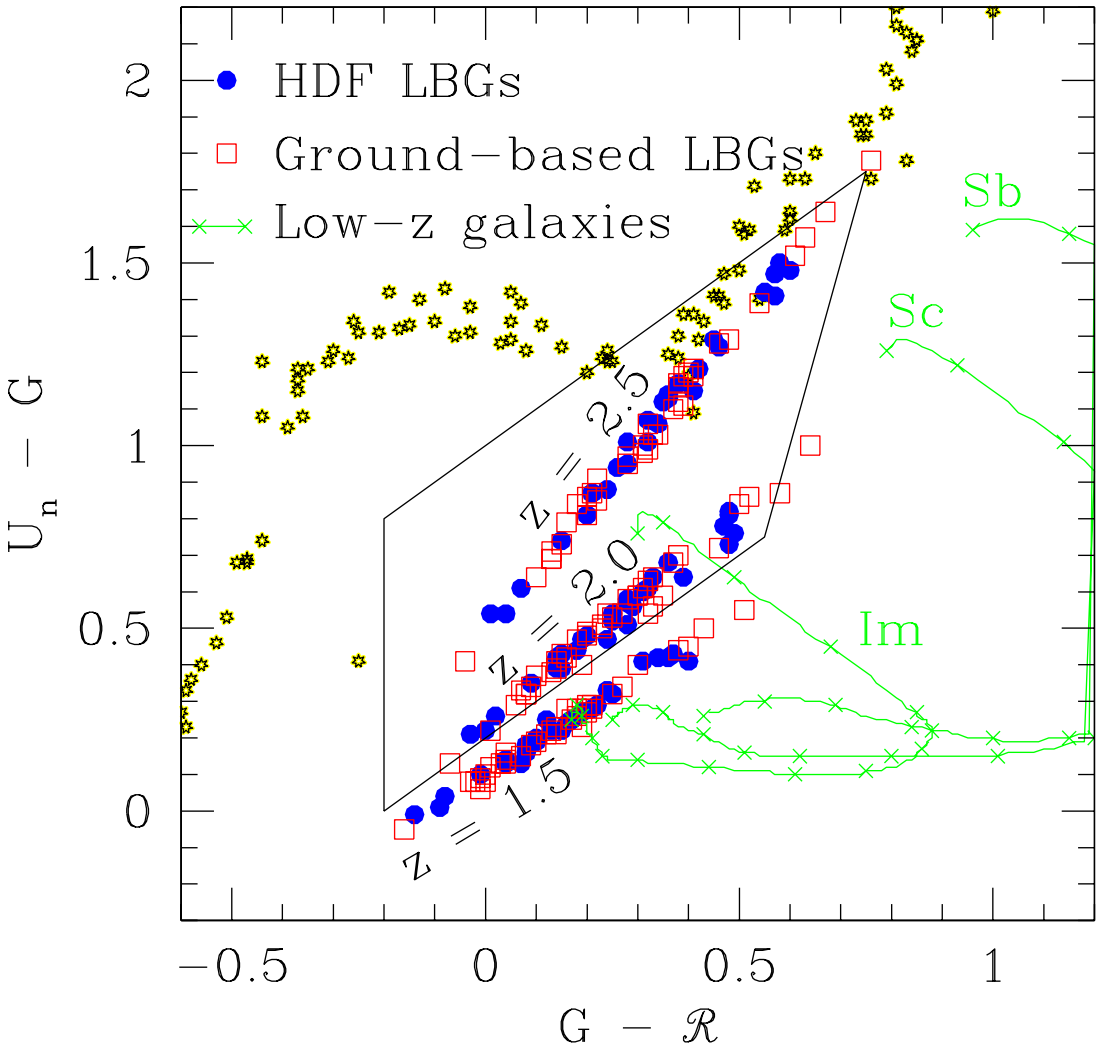

Figure 1.2 Expected $U_nG\mathcal{R}$ colors of stars (stars; from Gunn & Stryker 1983) and star-forming galaxies at redshifts $z = 1.5$, 2.0, and 2.5 (blue circles and red squares; data from Papovich et al. 2001 and Shapley et al. 2001). Green tracks indicate the colors of galaxies of different spectral types (Im, Sb, Sc), proceeding from $z = 0$ to $z = 1.5$, in intervals of $\delta z = 0.1$ as denoted by the crosses. The trapezoid denotes the BX selection window, as defined by Equation 1.1, which is designed to include as many galaxies at redshifts $2.0 \lesssim z \lesssim 2.6$ while excluding stars and low redshift $z < 1.5$ galaxies (figure from Adelberger et al. 2004).

near-UV. The spectroscopic sample presently consists of 104 BM, 1125 BX, and 1444 LBG galaxies (spread throughout multiple uncorrelated fields), with mean spectroscopic redshifts of $\langle z \rangle = 1.72 \pm 0.34$, $\langle z \rangle = 2.20 \pm 0.32$, and $\langle z \rangle = 2.96 \pm 0.26$, for the BM, BX, and LBG samples, respectively (Figure 1.3). It is the spectroscopic samples at $z \sim 2$ (BM and BX) that form the basis of the work presented in Chapters 2, 3, 4, and 5. In Chapter 6, we consider the joint photometric and spectroscopic samples to compute the luminosity function and the contribution of optically-selected galaxies to the total star formation rate density at $z \sim 2$.

1.2 Bolometric Measures of Star Formation Rates

Estimating the star formation rates of galaxies based on a single monochromatic flux (or even broadband SEDs) entails many assumptions, some of which have been tested and others which have not. For example, one must assume a particular form of the initial mass function (IMF) of stars in order to estimate a star formation rate, but directly measuring the IMF is very difficult for everything except local global clusters where stars can be individually resolved. Another assumption that was previously untested at high redshift is the relationship between the observed UV luminosities of star forming galaxies and their total bolometric luminosities. Prior to the advent of large-scale multi-wavelength surveys, it was common to make untested extinction corrections to galaxies in UV surveys based on relationships established locally. The situation has changed significantly with panchromatic surveys which have allowed us to examine the extinction free measures of star formation rates in high redshift galaxies and compare these estimates with the observed UV emission, as discussed in Chapters 2 and 4. Combining our census of the star-forming galaxy population at high redshift and our intimate knowledge of the extinction corrections required to estimate bolometric SFRs, we can now make assertions regarding the star formation history and buildup of stellar mass in the Universe with much more confidence than previously possible.

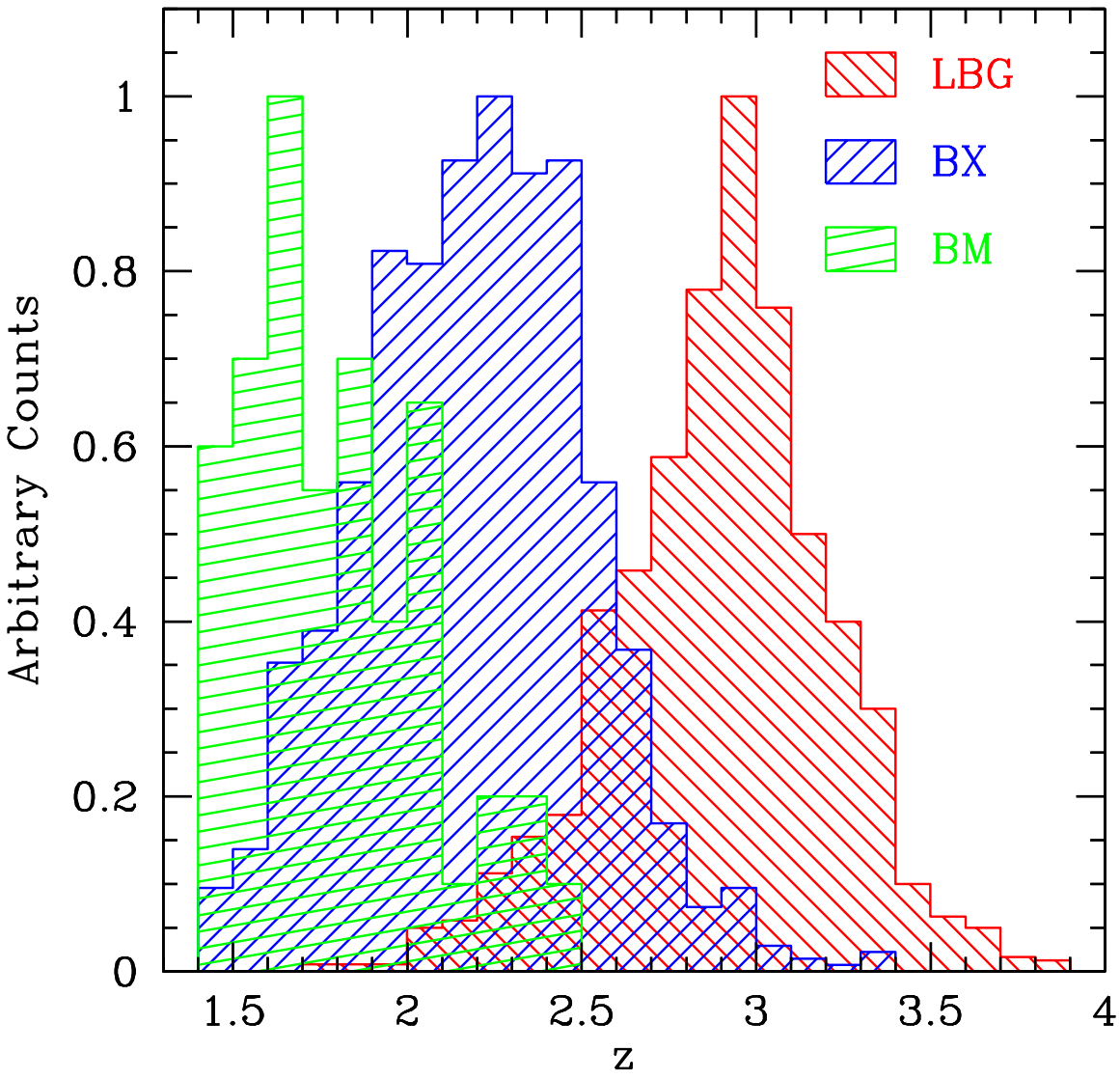

Figure 1.3 Arbitrarily normalized spectroscopic redshift distributions of galaxies with $z >$ 1.4 in the BM, BX, and LBG samples. The total number of galaxies represented here is 2673.

1.3 Outline of the Thesis

The outline of this thesis is as follows. In the next chapter, we use deep X-ray and radio emission as independent probes of the star formation rates and bolometric activity in galaxies at $z \sim 2$. While the X-ray and radio data are not sufficiently sensitive to detect most optically-selected galaxies at these redshifts, we can use stacking analyses to infer important information regarding the average star formation rates of well-selected subsamples of galaxies. In Chapter 3, we perform a detailed comparison of galaxies selecting using optical, near-IR, and sub-mm criteria. We quantify the overlap between these samples and, using stacked X-ray emission, demonstrate that this sample overlap must be taken into account when estimating the total star formation rate density. We extend the results of the census of star-forming galaxies presented in Chapter 3 by examining the rest-frame infrared emission from $z \sim 2$ galaxies selected in various ways. We also discuss how the average extinction factors for galaxies of a given luminosity change as a function of redshift, from $z \sim 2$ to $z = 0$. We go on to show how bolometric measures of the star formation rates of galaxies, combined with stellar mass estimates from population synthesis modelling, can be used to deduce the evolutionary state of galaxies in terms of their propensity for future star formation. In Chapter 5 we discuss in detail the spectroscopic sample of optically-selected galaxies in the GOODS-North field (Giavalisco et al. 2004b; Dickinson et al. 2003a), which is the basis for the work presented in Chapters 2, 3, and 4. Using multi-wavelength data in this field, we examine the properties of obscured AGN in optically-selected host galaxies. Finally, in Chapter 6, we use sophisticated Monte Carlo analysis of our joint photometric and spectroscopic samples of galaxies in the $z \sim 2$ survey (e.g., Adelberger et al. 2004; Steidel et al. 2004) to estimate the effects of photometric scattering, Lyman-alpha line perturbations, and other systematic effects introduced by the optical selection of star-forming galaxies at redshift $z \sim 2$. We use these results to construct the luminosity function at $z \sim 2$, and incorporating our knowledge of extinction, to estimate the total star formation rate density and the implications for the star formation history and buildup of stellar mass in the Universe. Finally, in the epilogue, we discuss several unresolved but important issues to consider for obtaining even more stringent constraints on the cosmic star formation history, as well as determining the evolutionary paths of individual galaxies.

Chapter 2

X-Ray and Radio Emission from UV-Selected Star Forming Galaxies at Redshifts $1.5 \lesssim Z \lesssim 3.0$ in the GOODS-North Field*†

Naveen A. Reddy & Charles C. Steidel

California Institute of Technology, MS 105–24, Pasadena, CA 91125; nar@astro.caltech.edu, ccs@astro.caltech.edu

Abstract

We have examined the stacked radio and X-ray emission from UV-selected galaxies spectroscopically confirmed to lie between redshifts $1.5 \lesssim z \lesssim 3.0$ in the GOODS-North field to determine their average extinction and star formation rates (SFRs). The X-ray and radio data are obtained from the Chandra 2 Msec survey and the Very Large Array, respectively. There is a good agreement between the X-ray, radio, and de-reddened UV estimates of the average SFR for our sample of $z \sim 2$ galaxies of ~ 50 $M_\odot$ yr^{-1}, indicating that the locally calibrated SFR relations appear to be statistically valid from redshifts $1.5 \lesssim z \lesssim 3.0$. We find that UV-estimated SFRs (uncorrected for extinction) underestimate the bolometric

*Based on data obtained at the W. M. Keck Observatory, which is operated as a scientific partnership among the California Institute of Technology, the University of California, and NASA, and was made possible by the generous financial support of the W. M. Keck Foundation.

†A version of this chapter was published in *The Astrophysical Journal*, vol. 603, 13–16.

SFRs as determined from the 2 to 10 keV X-ray luminosity by a factor of ~ 4.5 to 5.0 for galaxies over a large range in redshift from $1.0 \lesssim z \lesssim 3.5$.

2.1 Introduction

Estimating global star formation rates (SFRs) of galaxies typically requires using relations that can be quite uncertain as they incorporate a large number of assumptions in converting between specific and bolometric luminosities (e.g., assumed IMF, extinction, etc.; e.g., Adelberger & Steidel 2000). The varied efforts in the Great Observatories Origins Deep Survey (GOODS; Giavalisco et al. 2004b) allow us to examine the same galaxies over a broad range of wavelengths to mitigate some of these uncertainties. X-ray, radio, and UV emission are all thought to result directly from massive stars and are consequently used as tracers of current star formation (e.g., Ranalli et al. 2003; Condon 1992; Gallego et al. 1995). Here we use the X-ray, radio, and UV emission, each differently affected by extinction (or not at all), to determine SFRs of galaxies at $z \sim 2$.

Observations of the QSO and stellar mass density, and morphological diversification all point to the epoch around $z \sim 2$ as an important period in cosmic history (e.g., Di Matteo et al. 2003; Chapman et al. 2003). Until recently, this epoch has been largely unexplored as lines used for redshift identification are shifted to the near-UV, where detector sensitivity has been poor or to the near-IR, where spectroscopy is more difficult due to higher backgrounds. With the recent commissioning of the blue side of the Low Resolution Imaging Spectrograph (LRIS; Oke et al. 1995) on the Keck I telescope, we have for the first time been able to obtain spectra for large numbers of galaxies at these redshifts. Adding to the multi-wavelength efforts in the GOODS-North field, we have undertaken a program to identify photometric candidates in this field between $1.5 \lesssim z \lesssim 3.0$ and perform followup spectroscopy with LRIS-B (Steidel et al. 2004). This UV-selected sample of galaxies forms the basis for our subsequent multi-wavelength analysis.

Current sensitivity limits at X-ray and radio wavelengths preclude the direct detection of normal star forming galaxies at $z \gtrsim 1.5$. Nonetheless, we can use a "stacking" procedure to add the emission from a class of objects in order to determine their average emission properties (e.g., Nandra et al. 2002; Brandt et al. 2001; Seibert et al. 2002). In this paper, we present a stacking analysis of the radio and X-ray emission from UV-selected star forming

galaxies at redshifts $1.5 \lesssim z \lesssim 3.0$ to cross-check three different techniques of estimating SFRs at high redshifts. $H_o = 70$ km s^{-1} Mpc^{-1}, $\Omega_{\rm M} = 0.3$, and $\Omega_\Lambda = 0.7$ are assumed throughout.

2.2 Data

The techniques for selecting galaxies at $z \sim 2$ are designed to cover the same range of UV properties and extinction to those used to select Lyman-break galaxies (LBGs) at higher redshifts ($z \gtrsim 3.0$; Adelberger et al. 2004). Here, we simply mention that we have two spectroscopic samples at $1.5 \lesssim z \lesssim 2.5$: a "BX" sample of galaxies selected on the expected $U_{\rm n}G\mathcal{R}$ colors of LBGs de-redshifted to $2.0 \lesssim z \lesssim 2.5$; and a "BM" sample targeting $z \sim 1.5 - 2.0$. (see Adelberger et al. 2004; Steidel et al. 2004 for a complete description). We presently have 138 redshifts ($\langle z \rangle \sim 2.2 \pm 0.3$) and 48 redshifts ($\langle z \rangle \sim 1.7 \pm 0.3$) in the GOODS-North BX and BM samples, respectively.

The X-ray data are from the Chandra 2 Msec survey of the GOODS-North region (Alexander et al. 2003). We made use of their raw images and exposure maps in the Chandra soft X-ray band ($0.5 - 2.0$ keV). Dividing the raw image by the appropriate exposure map yields an image with the count rates corrected for vignetting, exposure time, and variations in instrumental sensitivity. The on-axis soft band sensitivity is $\sim 2.5 \times 10^{-17}$ ergs cm^{-2} s^{-1} ($3\ \sigma$).

The radio data are from the Richards (2000) Very Large Array (VLA) survey of the Hubble Deep Field North (HDF-N), reaching a $3\ \sigma$ sensitivity of $\sim 23\,\mu$Jy beam^{-1} at 1.4 GHz. The final naturally weighted image has a pixel size of $0\farcs4$ and resolution of $2\farcs0$, with astrometric accuracy of $< 0\farcs03$.

2.3 Stacking Procedure

We divided the spectroscopic data into subsets based on selection (BX and BM) and redshift, removed sources with matching X-ray or radio counterparts within $2\farcs5$ (or sources whose apertures are large enough to contain emission from a nearby extended X-ray or radio source), and stacked galaxies in these subsets. Four of the removed x-ray/radio sources are detected at 850 μm with the Submillimeter Common-User Bolometer Array (SCUBA).

The X-ray data were stacked using the following procedure. We added the flux within apertures randomly dithered by $0\farcs5$ at the positions of the galaxies (targets) in the X-ray images to produce a signal. Similarly sized apertures were randomly placed within $5''$ of the galaxy positions to sample the local background near each galaxy while avoiding known X-ray sources. This was repeated 1000 times to estimate the mean signal and background. The Chandra PSF widens for large angles from the average pointing (off-axis angle), and we fixed the aperture sizes to the 50% encircled energy (EE) radii (Feigelson et al. 2002) for off-axis angles $> 6'$. Background included at large off-axis angles becomes significant due to increasing aperture size and this can degrade the total stacked signal. Consequently, we only stacked galaxies within the off-axis angle that results in the highest S/N (this varies for each subsample, from 6 to $8'$). Including all sources in the stack reduces the S/N but does not affect the absolute flux value. For sources $< 6'$ from the pointing center, the 50% EE radius falls below $2\farcs5$, and we adopted a fixed $2\farcs5$ radius aperture to avoid the possibility of placing an aperture off a target as a result of dithering or astrometric errors—which are $\sim 0\farcs3$—for sources very close to the average pointing. Stacking was performed on both the raw and normalized images to calculate the S/N and total count rate, respectively. Aperture corrections were applied to the raw counts and count rate. The conversion between count rate and flux was determined by averaging the count rate to flux conversions for the 74 optically bright X-ray sources in Table 7 of Alexander et al. (2003) that are assumed to have a photon index of $\Gamma = 2.0$, typical of the X-ray emission from star forming regions (e.g., Kim et al. 1992; Nandra et al. 2002), and incorporate corrections for the QE degredation of the ACIS-I chips. In converting flux to rest-frame luminosity, we assume $\Gamma = 2.0$ and a Galactic absorption column density of $N_{\rm H} = 1.6 \times 10^{20}$ cm^{-2} (Stark et al. 1992). Uncertainties in flux and luminosity are dominated by Poisson noise and not the dispersion in measured values for each stacking repetition, so we assume the former.

To stack the radio data, we extracted subimages at the locations of the targets from the mosaicked radio data of Richards (2000). These were corrected for the primary beam attenuation of the VLA with a maximum gain correction of 15%, coadded using a $1/\sigma^2$ weighted average to produce a stacked signal with maximal $S/N \sim 4.5$, and smoothed by $1\farcs5$. The integrated flux density, $S_{1.4\,\rm GHz}$, and error were computed from the standard

AIPS[1] task JMFIT using an elliptical gaussian to model the stacked emission. We assume a synchrotron spectral index of $\gamma = -0.8$, typical of the non-thermal radio emission from star-forming galaxies (Condon 1992). Results of the X-ray and radio stacks for various subsamples are presented in Table 2.1. Four subsamples contain too few sources to yield a robust estimate of the stacked radio flux.

2.4 Results and Discussion

2.4.1 SFR Estimates

The relations established at $z = 0$ to convert luminosities to SFRs for our $z \sim 2$ sample are adopted from the following sources: Kennicutt (1998a,b) for conversion of the $1500-2800$ Å luminosity; Ranalli et al. (2003) for the $2-10$ keV luminosity; and Yun et al. (2001) for the 1.4 GHz luminosity. These relations must be used with caution when applied to individual galaxies given uncertainties in the SFR relations (e.g., burst age, IMF) as well as the factor of ~ 2 dispersion in the correlations between different specific luminosities. However, they should yield reasonable results when applied to an ensemble of galaxies, as we have done here.

Table 2.2 shows the SFR estimates based on the $2-10$ keV ("$\mathrm{SFR_X}$"), 1.4 GHz ("$\mathrm{SFR_{1.4\ GHz}}$"), and UV ("$\mathrm{SFR_{UV}}$") luminosities, with typical error of $\sim 20\%$. We approximate the UV luminosity by using the 1600 Å rest-frame flux for all samples except the highest redshift bin sample ($2.5 < z \lesssim 3.0$) where we use the 1800 Å rest-frame flux. UV-estimated SFRs were corrected for extinction using the observed $G - \mathcal{R}$ colors, a spectral template assuming constant star formation for $> 10^8$ yr (after which the UV colors are essentially constant), and applying the reddening law of Calzetti et al. (2000) and Meurer et al. (1999). We created four additional subsamples of galaxies according to de-reddened UV-estimated SFR, also shown in Table 2.2.

[1]AIPS is the Astronomical Image Processing System software package written and supported by the National Radio Astronomy Observatory.

2.4.2 Stacked Galaxy Distribution and AGN

Stacking only indicates the average emission properties of galaxies, not their actual distribution, and the observed signal may result from a few luminous sources lying just below the detection threshold. To investigate this, we plot the average distribution in counts for the sample of 147 stacked spectroscopic galaxies (Figure 2.1). Much of the high-end tail of the distribution results from random positive fluctuations. Only three sources consistently had > 7 counts. Removing those objects whose apertures have > 6 counts still results in a stacked signal with $S/N \sim 2.5$ and an average loss of 21 galaxies ($\sim 14\%$ of the sample). It is therefore likely that most of the stacked galaxies contribute to the signal, particularly given their wide range in optical, and likely X-ray, properties.

Contribution of low luminosity AGNs to the stacked signal is a concern. This is a problem with most X-ray stacking analyses, but we also possess the UV spectra for our sources. There are two objects undetected in X-rays for which the UV spectra show emission lines consistent with an AGN. Our ability to identify AGNs from their UV spectra regardless of their X-ray properties, and having identified only 2 such objects out of 149, suggests that subthreshold luminous AGNs do not contribute significantly to the stacked X-ray flux. Furthermore, UV selection biases against the dustiest sources so we do not expect to find many Compton-thick AGNs in our sample.

There are also two BM galaxies coincident with known radio sources that are not detected in X-rays and are not included in the stacked samples. Removing such objects ensures excluding radio-loud AGN that might have unassuming UV and X-ray properties. For comparison, the 3 σ radio sensitivity is sufficient to detect SFR$\gtrsim 170$ $M_\odot$ yr^{-1}, a factor of 4 higher than the median SFR of our sample based on the X-ray or de-reddened UV SFR estimates. The stacked X-ray emission indicates a SFR of ~ 42 $M_\odot$ yr^{-1}. The on-axis soft-band flux limit implies a sensitivity to SFR$\gtrsim 186$ $M_\odot$ yr^{-1} at $z \sim 2$, a factor of 4.5 higher than the average SFR for spectroscopic $z \sim 2$ galaxies. Stacking the radio flux for the full spectroscopic sample indicates average SFRs from $33 - 70$ $M_\odot$ yr^{-1} depending on which estimator is used: the Bell (2003), Condon (1992), and Yun et al. (2001) calibrations give low, high, and median (~ 56 $M_\odot$ yr^{-1}) values, assuming $\gamma = -0.8$. We adopted the Yun et al. (2001) calibration as it is most relevant to the radio luminosity range considered here.

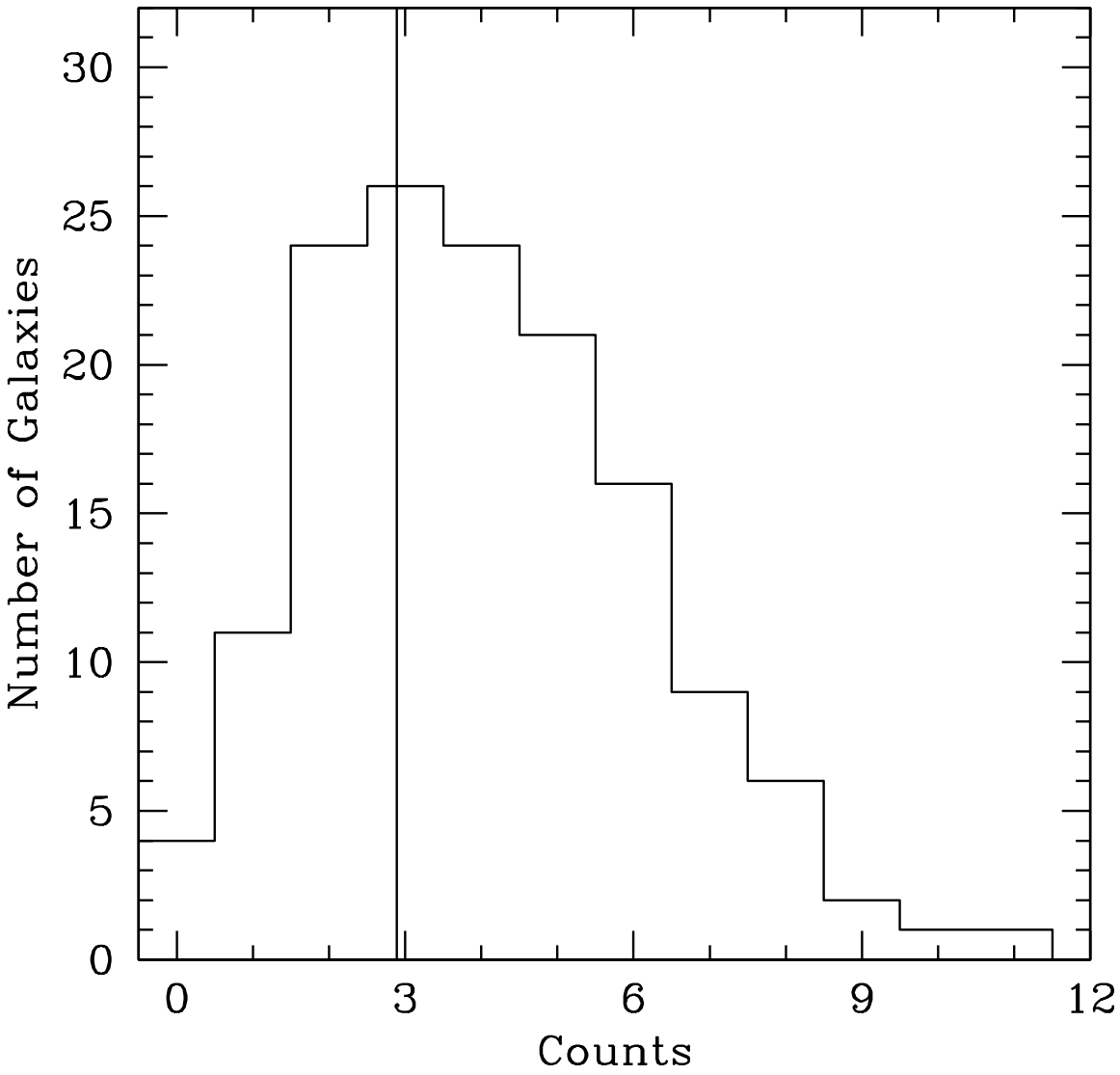

Figure 2.1 Average distribution of counts for the spectroscopic sample. The vertical line denotes the average background count per aperture. The number excess at high counts (> 7) results from random positive fluctuations.

2.4.3 Bolometric Properties of $z \sim 2$ Galaxies

The UV-implied reddening indicates $A_{\rm V} \sim 0.5$ mag and $N_{\rm H} \sim 7.5 \times 10^{20}$ cm^{-2} assuming the Galactic calibration (Diplas & Savage 1994). For this column density, absorption in the $2-10$ keV band is negligible, and we therefore assume that SFR$_{\rm X}$ is indicative of the bolometric SFR. In this case, we find a good agreement between the SFRs determined from the X-ray, radio, and de-reddened UV luminosities ($L_{\rm X}$, $L_{1.4\ {\rm GHz}}$, and $L_{\rm UV}$), suggesting that the locally calibrated relations between specific luminosity and SFR remain valid within the uncertainties at $z \sim 2$, under the caution that we cannot independently test for these relations as we have no direct measure of $L_{\rm bol}$.

The $\langle L_{\rm X} \rangle$ and $\langle L_{1.4\ {\rm GHz}} \rangle$ of spectroscopically identified $z \sim 2$ galaxies are comparable to those of local starbursts. The X-ray/FIR relation for local galaxies (Ranalli et al. 2003) implies $\langle L_{\rm FIR} \rangle \sim 2.6 \times 10^{11}$ L$_\odot$. The stacked $L_{1.4\ {\rm GHz}}$ implies $\langle L_{\rm FIR} \rangle = 1.1 \times 10^{11}$ L$_\odot$ (Yun et al. 2001). These estimates are similar to the FIR luminosity of luminous infrared galaxies (LIRGs), and are expected to have $S_{850\mu{\rm m}} \sim 0.3$ mJy (e.g., Webb et al. 2003) and would therefore be missing in confusion-limited SCUBA surveys to 2 mJy. *Spitzer* will have the same rest-frame 7 μm sensitivity to $z \sim 2$ galaxies as ISO has at $z \sim 1$ for $L_{\rm FIR} \gtrsim 5 \times 10^{10}$ L$_\odot$ galaxies (Weedman et al. 2004; Flores et al. 1999). Therefore, unlike the stacked averages presented here, the *Spitzer* data will be the first extinction-free tracer of the SFR distribution of the $z \sim 2$ sample as the stacked galaxies should be individually detected at 24 μm.

For a fair comparison between the three redshift bins for $1.5 < z \lesssim 3.0$, we have added back those direct X-ray detections in the stacks for the $1.5 < z \leq 2.0$ and $2.0 < z \leq 2.5$ samples that would not have been detected if they had $z > 2.5$. There were no such sources with $1.5 < z \leq 2.0$ and only one with $2.0 < z \leq 2.5$, increasing $\langle L_{2-10\ {\rm keV}} \rangle$ by 2% to 2.38×10^{41} ergs s^{-1}.

The distance independent ratio SFR$_{\rm X}$/SFR$_{\rm UV}^{uncor}$ (Table 2.2) is similar among the selection and redshift subsamples indicating that on average *UV-estimated SFRs (uncorrected for extinction) are a factor of* ~ 4.5 *times lower than the bolometric SFRs for galaxies between redshifts* $1.5 < z \leq 3.0$. For comparison, Nandra et al. (2002) find this factor to be ~ 5 for both the $z \sim 1$ BBG and $z \sim 3$ LBG populations, and the factor is comparable to that of local starburst galaxies (Seibert et al. 2002). The attenuation computed for the

BX/BM sample using the Calzetti et al. (2000) extinction law is similar to that computed from $\mathrm{SFR_X/SFR_{UV}^{\mathit{uncor}}}$. The de-reddened UV-estimated SFRs ($\mathrm{SFR_{UV}^{\mathit{cor}}}$) agree well with those predicted from the radio continuum for the two samples for which radio estimates could be obtained. Finally, we note the factor of ~ 5 UV attenuation is similar to that advocated by Steidel et al. (1999) for UV-selected samples at all redshifts.

The average attenuation factor increases as the SFR increases, as shown by the last four subsamples in Table 2.2, and is expected if galaxies with higher SFRs have greater dust content on average (Adelberger & Steidel 2000). $\mathrm{SFR_{UV}^{\mathit{cor}}}$ follows the bolometric SFR even for low luminosity systems, indicating that the observed correlations are not entirely driven by only the most luminous galaxies.

2.5 Conclusions

We have made significant progress in estimating and comparing SFRs determined from UV, X-ray, and radio emission from galaxies between redshifts $1.5 \lesssim z \lesssim 3.0$, postulated to be the most "active" epoch for galaxy evolution. The locally calibrated SFR relations, though uncertain in individual systems, appear to remain statistically valid at high redshift. Stacking the X-ray and radio emission from UV-selected galaxies at $z \sim 2$ indicates that these galaxies have an average SFR of ~ 50 $\mathrm{M_\odot\ yr^{-1}}$ and an average UV attenuation factor of ~ 4.5. The prospect of increased radio sensitivity with the E-VLA, as well as X-ray campaigns in different fields to similar depth as the 2 Msec survey in the GOODS-North field, will allow for a more direct probe of the radio and X-ray flux distribution for the stacked galaxies. *Spitzer* MIPS 24 μm data for the GOODS-N field will trace the dusty star formation in $z \sim 2$ galaxies and allow for the cross-checking of the results presented here.

We thank Alice Shapley, Dawn Erb, Matt Hunt, and Kurt Adelberger for help in obtaining the data presented here. CCS has been supported by grants AST 0070773 and 0307263 from the National Science Foundation (NSF) and by the David and Lucile Packard Foundation. NAR acknowledges support from an NSF Graduate Research Fellowship.

Table 2.1. Radio and X-ray Stacking Results

Sample	N_s[a]	$\langle z \rangle$[b]	S/N[c]	$F_{0.5-2.0\,\mathrm{keV}}$[d] ($\times 10^{-18}$ ergs cm^{-2} s^{-1})	$L_{2.0-10\,\mathrm{keV}}$[e] ($\times 10^{41}$ ergs s^{-1})	$S_{1.4\,\mathrm{GHz}}$[f] (μJy)	$L_{1.4\,\mathrm{GHz}}$[g] ($\times 10^{22}$ W Hz^{-1})	νL_ν[h] ($\times 10^{10}$ L$_\odot$)
BX+BM	147	2.09	8.9	5.65 ± 0.68	2.11 ± 0.25	2.30 ± 0.65	5.90 ± 1.66	3.50
BX	109	2.22	6.8	4.83 ± 0.79	2.09 ± 0.34	2.09 ± 0.75	6.17 ± 2.21	3.86
BM	38	1.71	6.0	8.04 ± 1.34	1.84 ± 0.31	...	...	2.46
$1.5 < z \leq 2.0$	54	1.82	5.6	6.89 ± 1.27	1.84 ± 0.33	...	...	2.81
$2.0 < z \leq 2.5$	73	2.24	6.0	5.24 ± 0.96	2.33 ± 0.43	...	...	4.05
$2.5 < z \leq 3.0$	43	2.87	3.3	4.21 ± 1.46	3.40 ± 1.18	...	...	4.61

[a]Number of galaxies stacked

[b]Mean redshift

[c]Signal-to-noise calculated in a manner analogous to that in Nandra et al. 2002

[d]Average soft-band X-ray flux per object

[e]Average rest-frame X-ray luminosity per object, assuming $\Gamma = 2.0$ and $N_\mathrm{H} = 1.6 \times 10^{20}$ cm^{-2}, for our adopted cosmology

[f]Average integrated radio flux density per object

[g]Average rest-frame 1.4 GHz luminosity per object, assuming synchrotron spectral index of $\gamma = -0.8$

[h]Average UV luminosity computed from G and $\mathcal{R}$ magnitudes approximating the 1600 and 1800 Å fluxes, respectively.

Table 2.2. Star Formation Rate Estimates

Sample	SFR_X ($M_\odot$ yr^{-1})	SFR_R ($M_\odot$ yr^{-1})	SFR_{UV}^{cor} ($M_\odot$ yr^{-1})	SFR_X/SFR_{UV}^{uncor}
BX+BM	42	56	50	4.5
BX	42	58	54	4.2
BM	37	...	38	4.8
$1.5 < z \leq 2.0$	37	...	49	4.3
$2.0 < z \leq 2.5$	47	...	57	4.4
$2.5 < z \leq 3.0$	68	...	70	4.7
$SFR_{UV}^{cor} \leq 20$ $M_\odot$ yr^{-1}	14	...	11	2.3
$20 < SFR_{UV}^{cor} \leq 40$ $M_\odot$ yr^{-1}	40	...	38	4.4
$40 < SFR_{UV}^{cor} \leq 60$ $M_\odot$ yr^{-1}	44	...	48	4.7
$SFR_{UV}^{cor} > 60$ $M_\odot$ yr^{-1}	72	...	73	5.1

Chapter 3

A Census of Optical and Near-Infrared Selected Star-Forming and Passively Evolving Galaxies at Redshift $z \sim 2$*†

Naveen A. Reddy,[a] Dawn K. Erb,[b] Charles C. Steidel,[a] Alice E. Shapley,[c] Kurt L. Adelberger,[d] & Max Pettini[e]

[a]California Institute of Technology, MS 105–24, Pasadena, CA 91125

[b]Harvard-Smithsonian Center for Astrophysics, 60 Garden Street, Cambridge, MA 02138

[c]Astronomy Department, University of California, Berkeley, 601 Campbell Hall, Berkeley, CA 94720

[d]McKinsey & Company, 1420 Fifth Avenue, Suite 3100, Seattle, WA 98101

[e]Institute of Astronomy, Madingley Road, Cambridge CB3 OHA, UK

Abstract

Using the extensive multi-wavelength data in the GOODS-North field, including our ground-based rest-frame UV spectroscopy and near-IR imaging, we construct and draw comparisons between samples of optical and near-IR selected star-forming and passively evolving galaxies

*Based, in part, on data obtained at the W. M. Keck Observatory, which is operated as a scientific partnership among the California Institute of Technology, the University of California, and NASA, and was made possible by the generous financial support of the W. M. Keck Foundation.

†A version of this chapter was published in *The Astrophysical Journal*, vol. 633, 748–767.

at redshifts $1.4 \lesssim z \lesssim 2.6$. We find overlap at the $70-80\%$ level in samples of $z \sim 2$ star-forming galaxies selected by their optical ($U_{\rm n}G\mathcal{R}$) and near-IR (BzK) colors when subjected to common K-band limits. Deep *Chandra* data indicate a $\sim 25\%$ AGN fraction among near-IR selected objects, much of which occurs among near-IR bright objects ($K_{\rm s} < 20$; Vega). Using X-rays as a proxy for bolometric star formation rate (SFR) and stacking the X-ray emission for the remaining (non-AGN) galaxies, we find the SFR distributions of $U_{\rm n}G\mathcal{R}$, BzK, and $J - K_{\rm s} > 2.3$ galaxies (i.e., Distant Red Galaxies; DRGs) are very similar as a function of $K_{\rm s}$, with $K_{\rm s} < 20$ galaxies having $\langle SFR \rangle \sim 120\ M_{\odot}\ {\rm yr}^{-1}$, a factor of 2 to 3 higher than those with $K_{\rm s} > 20.5$. The absence of X-ray emission from the reddest DRGs and BzK galaxies with $(z-K)_{\rm AB} \gtrsim 3$ indicates they must have declining star formation histories to explain their red colors and low SFRs. While the M/L ratio of passively-evolving galaxies may be larger on average, the *Spitzer*/IRAC data indicate that their inferred stellar masses do not exceed the range spanned by optically selected galaxies, suggesting that the disparity in current SFR may not indicate a fundamental difference between optical and near-IR selected massive galaxies ($M^{*} > 10^{11}\ {\rm M}_{\odot}$). We consider the contribution of optical, near-IR, and submillimeter-selected galaxies to the star formation rate density (SFRD) at $z \sim 2$, taking into account sample overlap. The SFRD in the interval $1.4 \lesssim z \lesssim 2.6$ of $U_{\rm n}G\mathcal{R}$ and BzK galaxies to $K_{\rm s} = 22$, and DRGs to $K_{\rm s} = 21$ is $\sim 0.10 \pm 0.02\ M_{\odot}\ {\rm yr}^{-1}\ {\rm Mpc}^{-3}$. Optically-selected galaxies to $\mathcal{R} = 25.5$ and $K_{\rm s} = 22.0$ account for $\sim 70\%$ of this total. Greater than 80% of radio-selected submillimeter galaxies to $S_{850\mu{\rm m}} \sim 4$ mJy with redshifts $1.4 < z < 2.6$ satisfy either one or more of the BX/BM, BzK, and DRG criteria.

3.1 Introduction

A number of surveys have been developed to select galaxies at $z \sim 2$, determine their bolometric star formation rates (SFRs), and compare with other multi-wavelength studies to form a census of the total star formation rate density (SFRD) at $z \sim 2$ (e.g., Steidel et al. 2004; Rubin et al. 2004; Daddi et al. 2004b). A parallel line of study has been to compare optical and near-IR selected galaxies that are the plausible progenitors of the local population of passively evolving massive galaxies. However, biases inherent in surveys that select galaxies based on their star formation activity (e.g., Steidel et al. 2004) and stellar mass (e.g., Cimatti et al. 2002b; Glazebrook et al. 2004) can complicate such comparisons. Only

with an accurate knowledge of the overlap between these samples can we begin to address the associations between galaxies selected in different ways, their mutual contribution to the SFRD at $z \sim 2$, and the prevalence and properties of passively evolving and massive galaxies at high redshift. Quantifying this overlap between optical and near-IR surveys is a primary goal of this paper.

In practice, optical surveys are designed to *efficiently* select galaxies with a specific range of properties. The imaging required for optical selection is generally a small fraction of the time required for near-IR imaging, and can cover much larger areas within that time. In contrast, near-IR surveys sample galaxies over a wider baseline in wavelength than optical surveys, and can include galaxies relevant to studying both the star formation rate and stellar mass densities at high redshift. However, in order to achieve a depth similar (and area comparable) to that of optical surveys, near-IR selection requires extremely deep imaging and can be quite expensive in terms of telescope time due to the relatively small size of IR arrays compared to CCDs. Furthermore, the "color" of the terrestrial background for imaging is $(B - K_{\rm s})_{\rm AB} \simeq 7$ magnitudes, much redder than all but the most extreme $z \sim 2$ galaxies. Once selected, of course, such extreme galaxies then require heroic efforts to obtain spectra, whereas optical selection, particularly at redshifts where key features fall shortward of the bright OH emission "forest," virtually guarantees that one can obtain a spectroscopic redshift with a modest investment of 8 - 10m telescope time and a spectrograph with reasonably high throughput. As we show below, optical and near-IR surveys complement each other in a way that is necessary for obtaining a reasonably complete census of galaxies at high redshift.

The SFRs of $z \sim 2$ galaxies are typically estimated by employing locally calibrated relations between emission at which the galaxies can be easily detected (e.g., UV, Hα) and their FIR emission. The X-ray luminosity of local non-active galaxies results primarily from high mass X-ray binaries, supernovae, and diffuse hot gas (e.g., Grimm et al. 2002; Strickland et al. 2004); all of these sources of X-ray emission are related to the star formation activity on timescales of $\lesssim 100$ Myr. Observations of galaxies in the local Universe show a tight correlation between X-ray and FIR luminosity, prompting the use of X-ray emission as an SFR indicator (Ranalli et al. 2003). This correlation between X-ray emission and SFR applies to galaxies with a very large range in SFRs, from $\sim 0.1 - 1000\ M_{\odot}\ {\rm yr}^{-1}$. Stacking

analyses at X-ray and radio wavelengths, and comparison with UV emission, indicate that the local SFR relations appear to give comparable estimates of the instantaneous SFRs of galaxies after assuming continuous star formation models and correcting for dust (e.g., Reddy & Steidel 2004; Nandra et al. 2002; Seibert et al. 2002).

Two surveys designed to select massive galaxies at redshifts $1.4 \lesssim z \lesssim 2.5$ and passively-evolving (PE) galaxies at redshifts $z \gtrsim 2$, respectively, are the K20 and FIRES surveys. The K20 and FIRES selection criteria were developed to take advantage of the sensitivity of rest-frame optical light and color to stellar mass and the strength of the Balmer break, respectively, for $z \sim 2$ galaxies (e.g., Cimatti et al. 2002a; Franx et al. 2003). The Gemini Deep Deep Survey (GDDS) extends this near-IR technique to target massive galaxies at slightly lower redshifts ($0.8 \lesssim z \lesssim 2.0$; Abraham et al. 2004).

X-ray stacking analyses of the brightest galaxies in the K20 and FIRES surveys indicate an average SFR a factor of 4 to 5 times larger than for optically-selected $z \sim 2$ galaxies (Daddi et al. 2004a; Rubin et al. 2004), inviting the conclusion that optical selection misses a large fraction of the star formation density at high redshift. While it is certainly true that optical surveys miss some fraction of the SFRD, the past quoted difference in the average SFRs of galaxies selected optically and in the near-IR disappears once the galaxies are subjected to a common near-IR magnitude limit, as we show below.

We have recently concluded a campaign to obtain deep near-IR imaging for fields in the $z \sim 2$ optical survey (Steidel et al. 2004), allowing for a direct comparison of optical and near-IR selected galaxies. One result of this comparison is that $K_{\rm s} < 20$ (Vega) optically-selected galaxies show similar space densities, stellar masses, and metallicities as $K_{\rm s}$-bright galaxies in near-IR samples (Shapley et al. 2004). More recently, Adelberger et al. (2005a) show that the correlation lengths for $K_{\rm s}$-bright galaxies among optical and near-IR samples are similar, suggesting an overlap between the two sets of galaxies, both of which plausibly host the progenitors of massive elliptical galaxies in the local Universe. These results suggest that near-IR bright galaxies have similar properties regardless of the method used to select them.

In this paper, we extend these results by examining the color distributions and X-ray properties of near-IR and optically selected galaxies at $z \sim 2$ in the GOODS-North field (Giavalisco et al. 2004b). The field is well-suited for this analysis given the wealth of

complementary data available, including *Chandra*/X-ray, ground-based optical and near-IR, and *Spitzer*/IRAC imaging. Multi-wavelength data in a single field are particularly useful in that we can use a common method for extracting photometry that is not subject to the biases that may exist when comparing galaxies in different fields whose fluxes are derived in different ways. The addition of our rest-frame UV spectroscopic data in the GOODS-N field provides for a more detailed analysis than otherwise possible of the properties of galaxies as a function of selection technique. Furthermore, the GOODS-N field coincides with the *Chandra* Deep Field North (CDF-N) region which have the deepest (2 Ms) X-ray data available (Alexander et al. 2003). The X-ray data allow for an independent estimate of bolometric SFRs and the available depth allows more leeway in stacking smaller numbers of sources to obtain a statistical detection, as well as identifying AGN to a lower luminosity threshold than possible in other fields that have shallower X-ray data.

The outline of the paper is as follows. In § 2, we describe the optical, near-IR, X-ray, and IRAC data and present the optical and near-IR selection criteria and X-ray stacking method. Color distributions, direct X-ray detections, and stacked results are examined in § 3. In § 4, we discuss the SFR distributions of optical and near-IR selected $z \sim 2$ galaxies and their relative contributions to the SFRD, and the presence of a passively evolving population of galaxies. A flat ΛCDM cosmology is assumed with $H_0 = 70$ km s^{-1} Mpc^{-1} and $\Omega_\Lambda = 0.7$.

3.2 Data and Sample Selection

3.2.1 Imaging

Optical $U_{\rm n}G\mathcal{R}$ images in the GOODS-North field were obtained in April 2002 and 2003 under photometric conditions using the KPNO and Keck I telescopes. The KPNO/MOSAIC U-band image was obtained from the GOODS team (PI: Giavalisco) and was transformed to reflect $U_{\rm n}$ magnitudes (e.g., Steidel et al. 2004). The Keck I G and $\mathcal{R}$ band images were taken by us with the Low Resolution Imaging Spectrograph (LRIS; Oke et al. 1995, Steidel et al. 2004), and were oriented to provide the maximum overlap with the GOODS ACS and *Spitzer* survey region. The images cover $11' \times 15'$ with FWHM $\sim 0\farcs7$ to a depth of $\mathcal{R} \sim 27.5$ ($3\ \sigma$). Image reduction and photometry were done following the procedures described in

Steidel et al. (2003). We obtained deep B-band images of the GOODS-N field from a public distribution of *Subaru* data (Capak et al. 2004). The deep z-band data are acquired from the public distribution of the *HST* Advanced Camera for Surveys (ACS) data (Giavalisco et al. 2004b). The B and z band data have 5 σ depths of 26.9 and 27.4 mag measured in 3 $''$ and $0\farcs2$ diameter apertures, respectively. The $K_{\rm s}$ and J imaging was accomplished with the Wide Field Infrared Camera (WIRC) on the Palomar Hale 5 m telescope (Wilson et al. 2003), providing $8\farcm7 \times 8\farcm7$ coverage in the central portion of the GOODS-N field. The near-IR images cover $\sim 43\%$ of the optical image. The images had FWHM $\sim 1\farcs0$ under photometric conditions and 3 σ sensitivity limits of ~ 22.6 and ~ 24.1 mag in the $K_{\rm s}$ and J bands, respectively. The near-IR data are described in detail by Erb et al. (2006c). The total area studied in the subsequent analysis is ~ 72.3 arcmin^2.

The procedures for source detection and photometry are described in Steidel et al. (2003). Briefly, $U_{\rm n}G\mathcal{R}$ magnitudes were calculated assuming isophotal apertures that were adjusted to the $\mathcal{R}$-band flux profiles. Source detection was done at $K_{\rm s}$-band. BzK and J magnitudes are computed assuming the isophotal apertures adjusted to the $K_{\rm s}$-band flux profiles, unless the $\mathcal{R}$-band isophotes gave a more significant $K_{\rm s}$ detection. In the analysis to follow, "$K_{\rm s}$" and J magnitudes are in Vega units. We use the conversion $K_{\rm AB} = K_{\rm s} + 1.82$. All other magnitudes are in AB units.

Fully reduced *Spitzer*/IRAC mosaics of the GOODS-North field were made public in the first data release of the GOODS Legacy project (PI: Dickinson). The IRAC data overlap completely with our $K_{\rm s}$-band image, but currently only two channels (either 3.6 μm and 5.8 μm, or 4.5 μm and 8.0 μm) are available over most of the image. A small area of overlap has coverage in all four channels. The images are deep enough that source confusion is an issue. We have mitigated the effects of confusion noise by employing the higher spatial resolution $K_{\rm s}$-band data to constrain source positions and de-blend confused IRAC sources. We performed PSF photometry using the procedure described in Shapley et al. (2005).

3.2.2 Selection Criteria

3.2.2.1 Optical Selection of Star-Forming Galaxies

We have optically-selected $z \sim 2$ galaxies in the GOODS-N field based on their observed $U_nG\mathcal{R}$ colors (Adelberger et al. 2004; Steidel et al. 2004) to a limiting magnitude of $\mathcal{R} =$

25.5. The selection criteria aim to select actively star-forming galaxies at $z \sim 2$ with the same range in UV properties and extinction as LBGs at $z \sim 3$ (Steidel et al. 2003). "BX" galaxies are selected to be at redshifts $2.0 \lesssim z \lesssim 2.6$ using the following criteria:

$$\begin{aligned} G - \mathcal{R} &\geq -0.2 \\ U_n - G &\geq G - \mathcal{R} + 0.2 \\ G - \mathcal{R} &\leq 0.2(U_n - G) + 0.4 \\ U_n - G &\leq G - \mathcal{R} + 1.0, \end{aligned} \tag{3.1}$$

and "BM" objects are selected to be at redshifts $1.5 \lesssim z \lesssim 2.0$ using the following criteria:

$$\begin{aligned} G - \mathcal{R} &\geq -0.2 \\ U_n - G &\geq G - \mathcal{R} - 0.1 \\ G - \mathcal{R} &\leq 0.2(U_n - G) + 0.4 \\ U_n - G &\leq G - \mathcal{R} + 0.2 \end{aligned} \tag{3.2}$$

(Adelberger et al. 2004; Steidel et al. 2004). For subsequent analysis, we will refer to BX and BM objects as those that are optically-, or "BX/BM"-, selected.

Optical color selection of $z \sim 2$ galaxies in the $11'$ by $15'$ area of the GOODS-North field yielded 1360 BX and BM candidates, of which 620 lie in the region where we have complementary $J-$ and K-band data (§ 3.2.1), and 199 have $K_{\rm s} < 21.0$. Followup spectroscopy with the blue channel of the Low Resolution Imaging Spectrograph (LRIS-B) yielded 147 redshifts for objects with $K_{\rm s}$-band data (248 redshifts over the entire optical field). Of these 147 objects with redshifts and $K_{\rm s}$-band data, 129 have $z > 1$, and 60 have $z > 1$ *and* $K_{\rm s} < 21$. The mean redshift of the 60 BX/BM objects is $\langle z \rangle = 1.99 \pm 0.36$. The spectroscopic interloper fractions in the BX/BM sample are summarized in Table 3.1. The BX and BM selection functions (shown as shaded distributions in Figure 3.1) have distributions with mean redshifts $\langle z \rangle = 2.2 \pm 0.3$ and $\langle z \rangle = 1.7 \pm 0.3$, respectively (Steidel et al. 2004), and the combination of these two samples comprise our BX/BM-selected $z \sim 2$ sample. In the analysis to follow, we designate an interloper as any object with $z < 1$.

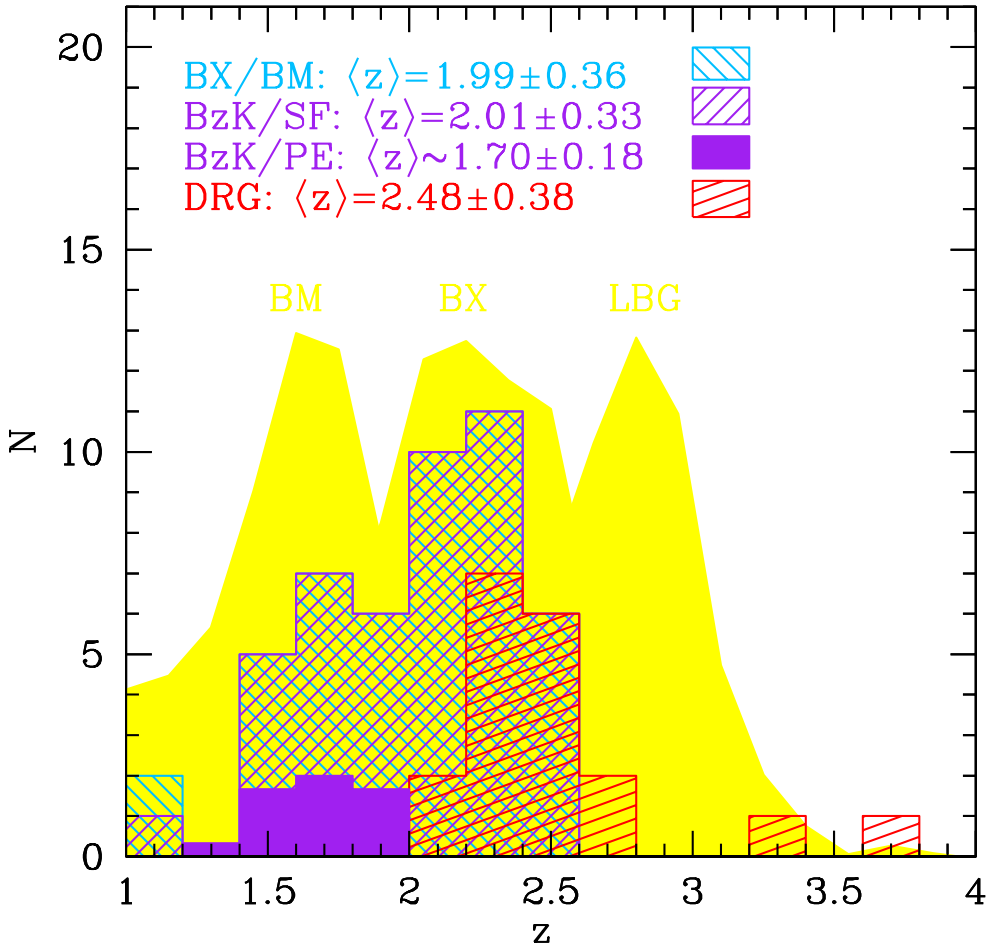

Figure 3.1 *Spectroscopic* redshift distributions to $K_s = 21$ for the various samples considered here. The BX/BM and BzK/SF distributions (hashed histograms) include sources from our sample in the GOODS-North field and overlap almost completely. The DRGs have a higher mean redshift of $\langle z \rangle = 2.48 \pm 0.38$ from our sample of $J - K_s > 2.3$ sources with $z > 1$ in all four fields of the optical survey (Steidel et al. 2004) where we have complementary $J-$ and K-band imaging. The redshift distribution of DRGs within our sample (all of which are selected with the BX/BM or $z \sim 3$ LBG criteria) is similar to that found by van Dokkum et al. (2004), van Dokkum et al. (2003), and Förster Schreiber et al. (2004b). The solid histogram shows the redshift distribution for BzK/PE galaxies from Daddi et al. (2004a) and Daddi et al. (2005b), scaled down by a factor of 3 for clarity. The background shaded regions show the arbitrarily normalized redshift distributions for optically-selected BX and BM galaxies, and LBGs.

3.2.2.2 Near-IR Selection of Star-Forming Galaxies

The near-IR properties of galaxies can be used both to target star forming galaxies and to identify those with extremely red colors that may indicate passive evolution. To address the former issue, we have employed the "BzK" selection criteria of Daddi et al. (2004a) to cull objects in the GOODS-N field and directly compare with those selected on the observed optical properties of $z \gtrsim 2$ galaxies. Daddi et al. (2004a) define the quantity "BzK":

$$BzK \equiv (z - K) - (B - z); \tag{3.3}$$

star-forming galaxies with $z > 1.4$ are targeted by the following criterion:

$$BzK \geq -0.2, \tag{3.4}$$

in AB magnitudes. Of the 1185 sources with $> 3\,\sigma$ B, z, and K detections and $K_{\rm s} < 21$, 221 satisfy Equation 3.4. The surface density of BzK galaxies with $K_{\rm s} < 21$ is ~ 3 arcmin^{-2}, similar to the surface density of BX/BM galaxies to a similar $K_{\rm s}$-band depth. These star-forming BzK galaxies will be referred to as "BzK/SF" galaxies, and their spectroscopic redshift distribution *from our spectroscopic sample* is shown in Figure 3.1. Our deep near-IR imaging allows us to determine the redshift distribution for BzK/SF galaxies with $K_{\rm s} > 20$ (and which also satisfy the BX/BM criteria), and the results are shown in Figure 3.2. The mean redshifts of the $K_{\rm s} \leq 20$ and $K_{\rm s} > 20$ distributions are $\langle z \rangle = 2.13 \pm 0.22$ and $\langle z \rangle = 2.03 \pm 0.41$, respectively, and agree within the uncertainty. We note, however, that the BzK/SF criteria select $K_{\rm s} > 20$ objects over a broader range in redshift ($1.0 \leq z \leq 3.2$) than $K_{\rm s} \leq 20$ objects. This reflects the larger range in BzK colors of $K_{\rm s} > 20$ BzK/SF galaxies compared with those having $K_{\rm s} \leq 20$. Additionally, the photometric scatter in colors is expected to increase for fainter objects, so a broadening of the redshift distribution for BzK/SF objects with fainter $K_{\rm s}$ magnitudes is not surprising.

We emphasize that we only know the redshifts for BzK/SF galaxies that also happen to fall in the BX/BM sample. In general, the true redshift distribution, $N_o^{BzK/SF}(z)$, of the BzK/SF sample will be broader than the distributions shown in Figure 3.1 and Figure 3.2, call them $N_c^{BzK/SF}(z)$), which are effectively convolved with the BX/BM selection function. For example, the rapid dropoff in $N_c^{BzK/SF}(z)$ for $z > 2.6$ (Figure 3.2) may simply reflect

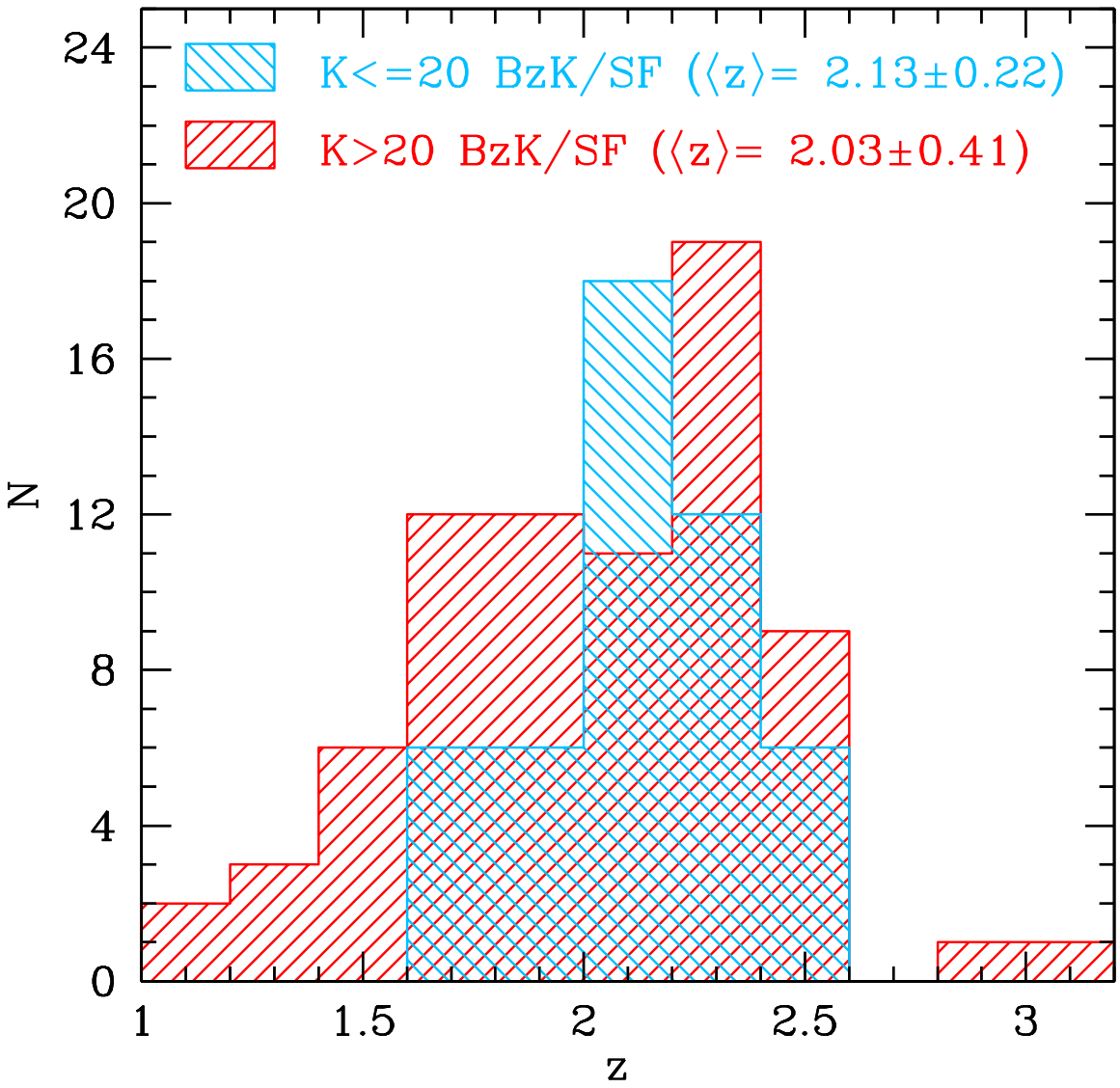

Figure 3.2 Arbitrarily normalized spectroscopic redshift distribution of BzK/SF galaxies in our spectroscopic sample to $K_s \sim 22.5$, with separate emphasis on $K_s \leq 20$ and $K_s > 20$ BzK/SF objects. The BzK/SF criteria select $K_s > 20$ objects over a broader range in redshift than $K_s \leq 20$ objects.

the dropoff in the BX selection function for $z > 2.6$. However, the $N_c^{BzK/SF}(z)$ we derive here is similar to that of the *photometric* redshift distribution of K20 galaxies from Daddi et al. (2004a), which is subject to its own systematic errors, suggesting that a reasonable approximation is to take $N_o^{BzK/SF}(z) \simeq N_c^{BzK/SF}(z)$.

3.2.2.3 Near-IR Selection of Passively Evolving Galaxies

In addition to the criteria above, several methods have been developed to select passively evolving high redshift galaxies by exploiting the presence of absorption or continuum breaks in the SEDs of galaxies with dominant old stellar populations. The BzK selection criteria

$$\begin{aligned} BzK &< -0.2 \\ z - K &> 2.5 \end{aligned} \tag{3.5}$$

are designed to select passively evolving galaxies at $z > 1.4$ (Cimatti et al. 2004; Daddi et al. 2004a). One galaxy that has a secure B-band detection, and an additional 16 with B-band limits, satisfy these criteria, implying a surface density of BzK/PE galaxies of 0.24 arcmin^{-2} to $K_s = 21$. Galaxies selected by their BzK colors to be passively-evolving are referred to as "BzK/PE" objects. The redshift distribution of BzK/PE galaxies, taken from the spectroscopic samples of Daddi et al. (2004a) and Daddi et al. (2005b), shows that they mostly lie between redshifts $1.4 \lesssim z \lesssim 2$ (Figure 3.1). We note that we may be incomplete for the BzK/PE objects despite the very deep B-band data considered here and these missing objects may be more easily selected using the $J - K_s > 2.3$ criteria discussed below (see also § 4.2.3).

The $J - K_s$ color probes the age-sensitive Balmer and 4000 Å breaks for galaxies with redshifts $2.0 \lesssim z \lesssim 4.5$ (Figure 3.3). The criterion

$$J - K_s > 2.3 \tag{3.6}$$

(Franx et al. 2003) can be used to select both passively evolving and heavily reddened star-forming galaxies with $E(B-V) > 0.3$. Galaxies satisfying this criterion are also referred to as Distant Red Galaxies (DRGs; Franx et al. 2003; van Dokkum et al. 2004). There are 62 galaxies with $J - K_s > 2.3$ that are detected in J, and an additional 11 have J-band limits.

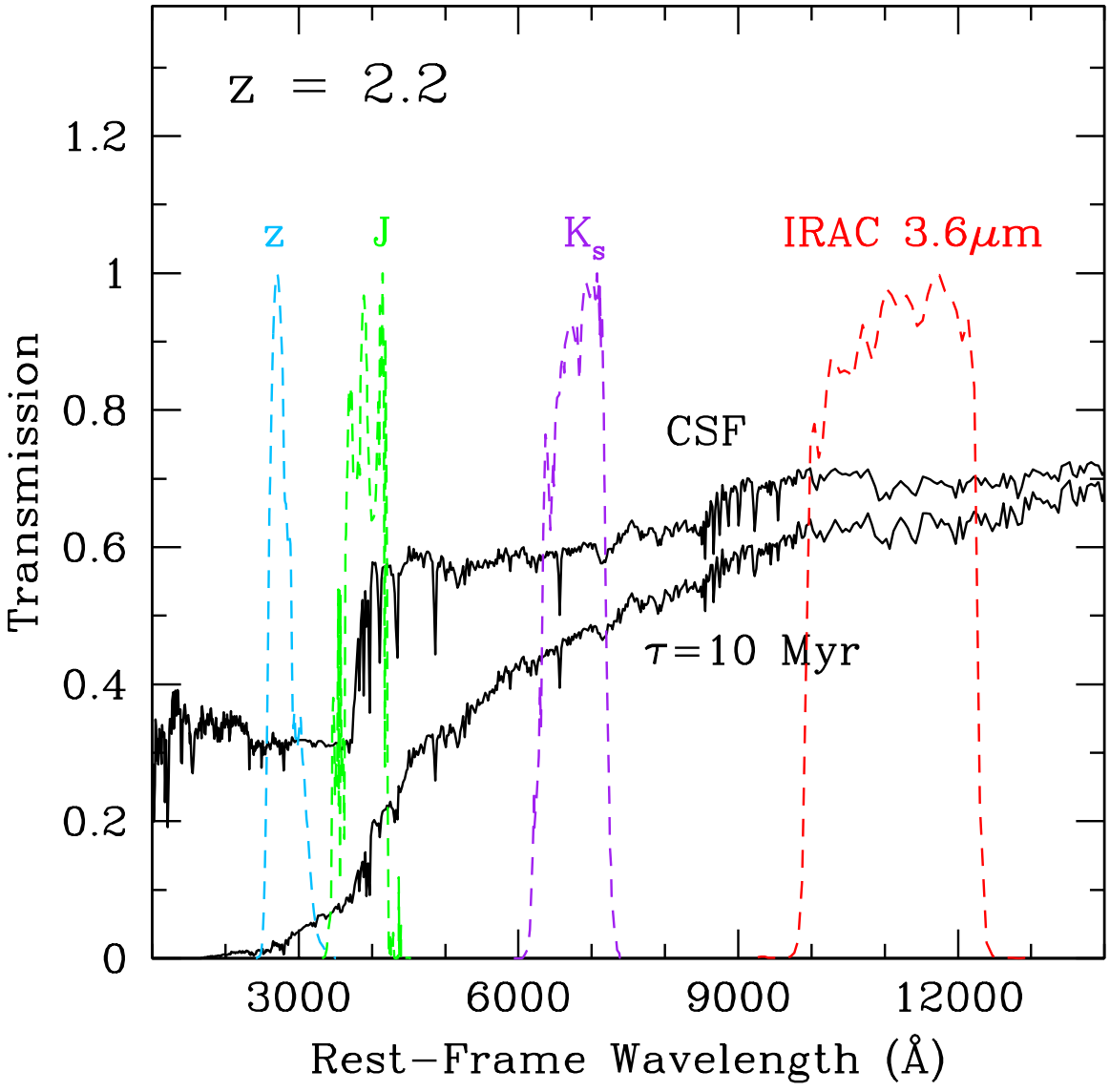

Figure 3.3 Relative transmission of the z, J, K_s, and IRAC 3.6 μm filters at rest-frame wavelengths for $z = 2.2$. Also shown are typical (unreddened) galaxy SEDs assuming constant star formation (CSF) and instantaneous star formation ($\tau = 10$ Myr) aged to 1 Gyr. For redshifts $z \sim 1.88 - 2.38$, the J-band brackets the prominent Balmer and 4000 Å breaks.

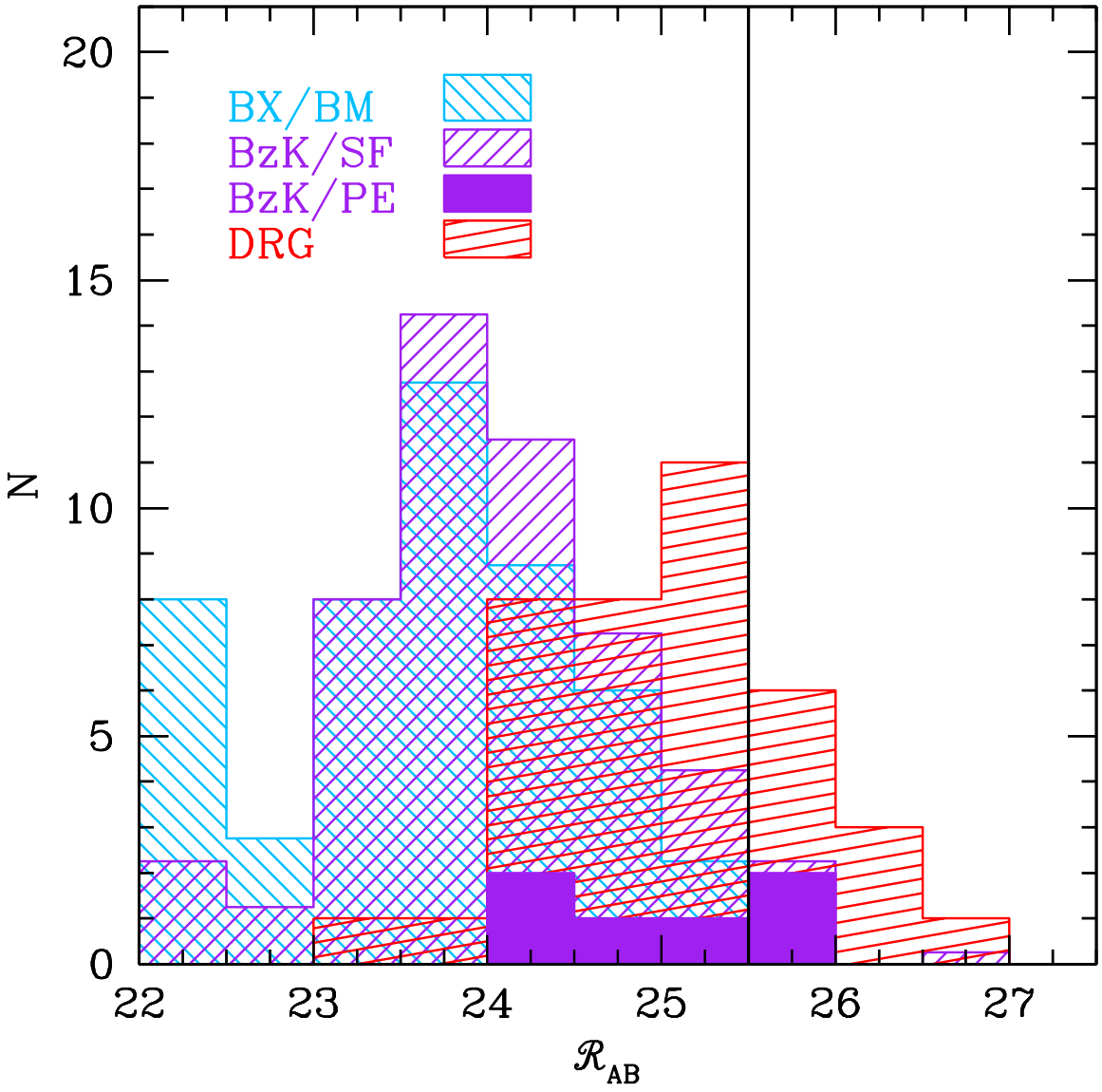

Figure 3.4 Optical magnitude distributions for photometrically selected $K_s < 21$ galaxies in the BX/BM, BzK, and DRG samples. The solid vertical line denotes the magnitude limit for galaxies in the optically-selected (BX/BM) sample. Approximately 47% of DRGs (34/73) have $\mathcal{R} > 27.0$ and are not shown in the figure. The distribution of BzK/PE galaxies has been arbitrarily normalized for clarity.

The observed surface density of DRGs is 1.01 ± 0.12 arcmin^{-2} to $K_{\rm s} = 21$, in very good agreement with the surface density found by van Dokkum et al. (2004) and Förster Schreiber et al. (2004b). The *spectroscopic* redshift distribution of DRGs from the four fields of the optical survey where we have deep J and $K_{\rm s}$-band imaging is shown in Figure 3.1, and is consistent with the redshift distributions found by van Dokkum et al. (2004), van Dokkum et al. (2003), and Förster Schreiber et al. (2004b). Star-forming and passively-evolving DRGs are referred to as "DRG/SF" and "DRG/PE", respectively. The depth of our J-band image implies that our sample of DRGs will be incomplete for those with $K_{\rm s} > 21$. Therefore, we have limited ourselves to galaxies with $K_{\rm s} < 21$ when comparing DRGs with BzK and/or BX/BM selected galaxies. We reconsider BX/BM and BzK galaxies with $K_{\rm s} > 21$ as noted below.

The optical magnitude distributions for galaxies with $K_{\rm s} < 21$ are shown in Figure 3.4. The catalog of BX/BM galaxies is restricted to $\mathcal{R} < 25.5$. However, our optical imaging is significantly deeper ($\mathcal{R} = 27.5$; 3 σ), allowing us to extract optical magnitudes for galaxies much fainter than those in the BX/BM catalog. Most of those galaxies with $\mathcal{R} > 25.5$ are DRGs. The nature of optically faint DRGs is discussed in § 3.4.2.

For most of the analysis that follows, we either use only the spectroscopically confirmed subsample of BX/BM galaxies, or we apply our knowledge of the contamination fraction of the photometric sample to deduce any inferred quantities. The small available spectroscopic samples using the near-IR criteria prevent us from applying similar corrections when deducing properties for the near-IR samples.

3.2.3 X-ray Data and Stacking Method

One focus of this paper is to draw comparisons between galaxies selected by the techniques described above by using their stacked X-ray emission as a proxy for their bolometric SFRs. X-ray stacking allows us to determine instantaneous bolometric SFRs in a manner that is independent of extinction and the degeneracies associated with stellar population modeling. For example, the average reddening of rest-frame UV selected galaxies of $E(B-V) \sim 0.15$ implies a column density of $N_{\rm H} \sim 7.5 \times 10^{20}$ cm^{-2}, assuming the Galactic calibration (Diplas & Savage 1994). Absorption in the rest-frame $2-10$ keV band is negligible for these column densities. The X-ray data are taken from the *Chandra* 2 Ms survey of the GOODS-N field

(Alexander et al. 2003). We made use primarily of the soft-band (SB; $0.5-2.0$ keV) data for our analysis, but we also include hard-band (HB; $2.0-8.0$ keV) data to examine the nature of directly detected X-ray sources. The data are corrected for vignetting, exposure time, and instrumental sensitivity in producing the final mosaicked image. The final product has an SB on-axis sensitivity of $\sim 2.5 \times 10^{-17}$ erg s^{-1} cm^{-2} (3 σ), sufficient to directly detect $L_{2-10\ \mathrm{keV}} > 9.3 \times 10^{41}$ ergs s^{-1} objects at $z \sim 2$, corresponding to an SFR of ~ 190 M$_\odot$ yr^{-1}.

The stacking procedure followed here is the same as that discussed in Reddy & Steidel (2004). Apertures used to extract X-ray fluxes had radii set to $2\farcs5$ for sources within $6'$ of the average *Chandra* pointing origin, and set to the 50% encircled energy radius for sources with off-axis angles greater than $6'$ (Feigelson et al. 2002). X-ray fluxes were computed by adding the counts within apertures randomly dithered by $0\farcs5$ at the galaxy positions. Background estimates were computed by randomly placing the same sized apertures within $5''$ of the galaxy positions, careful to prohibit the placing of a background aperture on a known X-ray detection. This procedure of placing random apertures was repeated 1000 times. The mean X-ray flux of a galaxy is taken to be the average of all the flux measurements from the $0\farcs5$ dithered apertures and the background noise is taken to be the dispersion in fluxes measured from the background apertures. We applied aperture corrections to the fluxes and assumed count rate to flux conversions based on the results compiled in Table 7 of Alexander et al. (2003), a photon index $\Gamma = 2.0$, and a Galactic absorption column density of $N_{\mathrm{H}} = 1.6 \times 10^{20}$ cm^{-2} (Stark et al. 1992). Poisson errors dominate the uncertainties in flux.

3.3 Results

3.3.1 Direct X-ray Detections

Of the 221 BzK/SF candidates with $K_{\mathrm{s}} < 21$, 32 (14%) have an X-ray counterpart within $1\farcs5$ (Alexander et al. 2003), with a $\sim 0.22\%$ probability for chance superposition. The X-ray detection fractions are 24%, 6%, and 26%, for the BzK/PE, BX/BM, and DRG samples, respectively, and are summarized in Table 3.2. Eleven of the 36 directly detected BzK sources (32 in the BzK/SF sample and 4 in the BzK/PE sample) would not have been detected with the sensitivity of the shallower 1 Msec data in the GOODS-South field

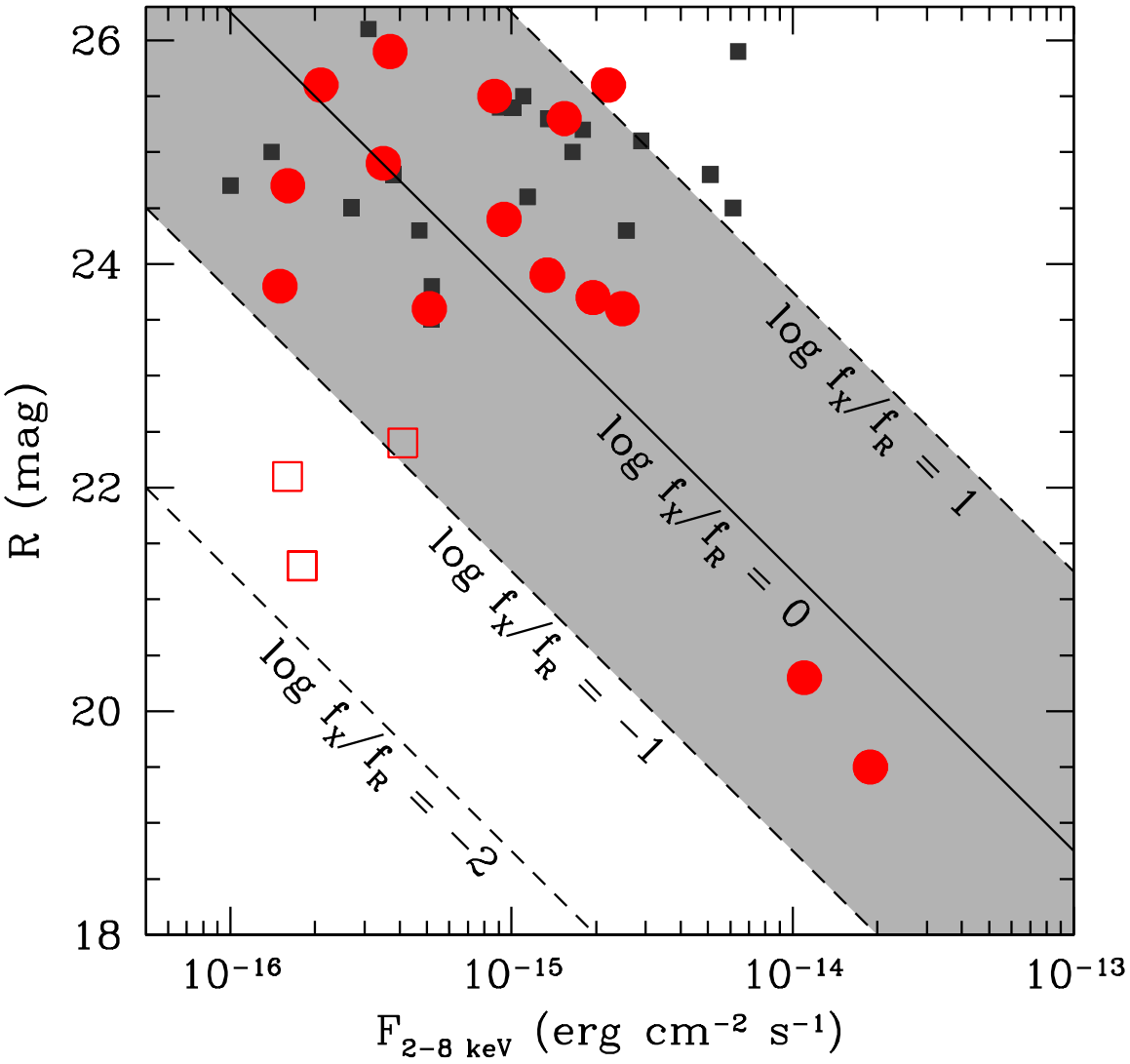

Figure 3.5 Optical/X-ray flux ratios, defined as $\log f_{\rm X}/f_{\rm R} = \log f_{\rm X} + 5.50 + R/2.5$ (Hornschemeier et al. 2001), for all directly detected hard-band X-ray sources in the BX/BM, BzK (SF/PE), and DRG samples. The abscissa is the observed hard-band flux, corresponding to rest-frame energies of $6-24$ keV, and the ordinate is the observed *Cousins* R magnitude from the compilation of Barger et al. (2003). Large circles denote sources with spectroscopic redshifts $z > 1$, and are likely AGNs given their direct hard-band detections. Sources with hard-band detections but no redshift identification are shown by the small squares. Almost all sources have optical/X-ray flux ratios between $-1 < \log f_{\rm X}/f_{\rm R} < 1$ (shaded region), values commonly found for AGNs. Those with $\log f_{\rm X}/f_{\rm R} < -1$ are confirmed interlopers, shown by the large open squares. Starburst galaxies generally have $\log f_{\rm X}/f_{\rm R} < -1$.

studied by Daddi et al. (2004a). After taking into account the sensitivity difference, we find a direct X-ray detection rate comparable to that of Daddi et al. (2004a) of $\sim 11\%$. Figure 3.5 shows the X-ray/optical flux ratios ($\log f_{\rm X}/f_{\rm R}$) for sources in all four samples (BX/BM, BzK/SF, BzK/PE, and DRG) directly detected in the *Chandra* hard-band ($2-8$ keV). Direct hard-band detections must be AGN if they are at $z \sim 2$, since starburst galaxies with no accretion activity are expected to have little flux at rest-frame energies of $6-20$ keV. Indeed, the X-ray/optical flux ratios for directly detected hard-band sources lie in the region typically populated by AGNs (shaded area of Figure 3.5). A smaller fraction of galaxies with direct hard-band detections (and the three sources with the smallest $\log f_{\rm X}/f_{\rm R}$) are spectroscopically confirmed interlopers at $z < 1$. From Table 3.2, it is easy to see that much of the AGN contamination in star-forming samples of galaxies (e.g, BX/BM, BzK/SF) occurs for magnitudes $K_{\rm s} < 20$.

Figure 3.5 only shows those X-ray sources with hard-band detections. Eleven additional sources had direct soft-band ($0.5-2.0$ keV) detections, but no hard-band detections. Of these 11, 5 sources have $R > 22.0$, $f_{0.5-2.0\ \rm keV} \lesssim 0.1 \times 10^{-15}$ erg cm^{-2} s^{-1}, and $\log f_{\rm X}/f_{\rm R} < -1$, indicating they may be starburst galaxies. These five sources and their properties are summarized in Table 3.3. Three of the five sources have spectra taken by us or by Barger et al. (2003) indicating no obvious AGN spectral features. These sources may be rapidly star-forming galaxies and for fairness we include them in the stacking analysis as indicated below and in Table 3.2.

It is interesting to also consider the rest-frame near-IR properties of the directly detected X-ray sources as indicated by their *Spitzer*/IRAC colors. Figure 3.6 shows the $3.6-5.8$ μm color as a function of 3.6 μm magnitude for all samples considered here. There is a clear segregation in the IRAC colors of X-ray detections where they show, on average, brighter IRAC magnitudes and redder IRAC colors when compared with the colors of star-forming galaxies in the BX/BM and BzK/SF samples. Such a trend might be expected if the rest-frame near-IR light from the X-ray sources is dominated by thermal continuum from circumnuclear dust heated by the AGN. The increase in flux density across the IRAC bands for AGN has been seen for ERO samples at redshifts $z \sim 1-3$ (Frayer et al. 2004), similar to what is observed here. Finally, the five objects listed in Table 3.3 have $m_{3.6\mu{\rm m}-5.8\mu{\rm m}} \sim -0.35$ to 0.35 and $m_{3.6\mu{\rm m}} = 20.2-22.0$, lying in the same region of IRAC color space as some of

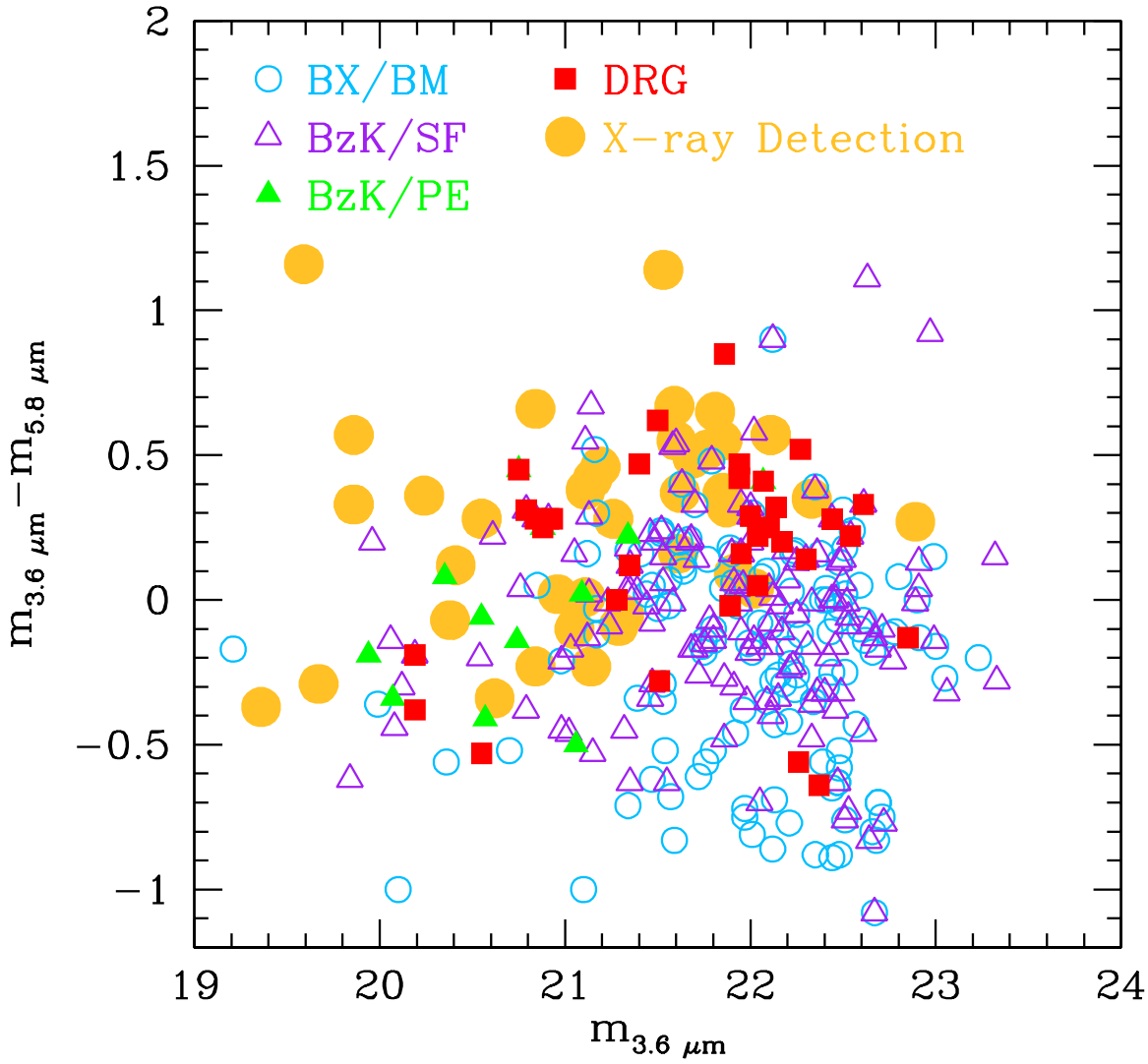

Figure 3.6 *Spitzer*/IRAC 3.6 − 5.8 μm color versus 3.6 μm magnitude (in AB units) for all samples considered here, with emphasis on directly detected X-ray sources (large circles). These direct detections generally have brighter IRAC magnitudes and redder colors than star forming BX/BM and BzK/SF galaxies, likely due to thermal continuum from circumnuclear dust proximate to the AGN.

the star-forming BX/BM and BzK/SF candidates.

At times in the following analysis, we also consider submillimeter galaxies and their relation to optical and near-IR selected objects. These heavily star-forming objects are generally associated with directly detected X-ray sources, and we reconsider the X-ray emission from these sources as pointed out below. Unless otherwise stated, however, we have excluded all directly detected hard-band X-ray sources from the analysis under the assumption that their X-ray emission is contaminated by AGN.

3.3.2 Overlap Between Samples

Galaxies selected solely by the presence of some unobscured star formation (BX/BM selection), and those selected by some combination of stellar mass and star formation (DRG and BzK selection) can be distinguished by their observed near-IR color distributions (Figure 3.7). The mean $(z-K)_{\rm AB}$ color for BX/BM galaxies is ~ 0.54 mag bluer than the BzK/SF sample, just within the 1 σ dispersion of both samples. This difference in average $(z-K)_{\rm AB}$ color between BX/BM and BzK/SF galaxies partly stems from the fact that the width of the BzK selection window below $(z-K)_{\rm AB}=1$ narrows to the point where photometric scatter becomes increasingly important in determining whether a galaxy with blue colors (i.e., $(z-K)_{\rm AB}<1$) is selectable with the BzK/SF criteria.[1] On the other hand, the BX/BM criteria are less efficient than BzK selection for galaxies with $(z-K)_{\rm AB}\gtrsim 1.6$. BX/BM galaxies with red near-IR colors are systematically fainter in the optical than those with blue near-IR colors (Figure 3.8), reflecting both the correlation between $\mathcal{R}$ and z as these filters lie close in wavelength, as well as the $K_{\rm s}<21$ limit adopted in Figure 3.8. Therefore, the optical catalog limit of $\mathcal{R}=25.5$ would appear to exclude from the BX/BM sample those galaxies with $(z-K)_{\rm AB}\gtrsim 3$ (Figure 3.8). As we show § 3.4, the exclusion of $(z-K)_{\rm AB}\gtrsim 3$ galaxies by optical selection is not a fault of the criteria themselves: the $\mathcal{R}=25.5$ limit is imposed so that spectroscopic followup is feasible on the candidate galaxies. Rather, the exclusion of $(z-K)_{\rm AB}\gtrsim 3$ galaxies from optical surveys simply reflects a fundamental change in the star formation properties of such red galaxies.

[1] None of the selection criteria considered here have boxcar selection functions in either color or redshift space due to various effects, including photometric errors. The effect of this is to suppress the efficiency for selecting objects whose intrinsic colors lie close to the edges of the selection window.

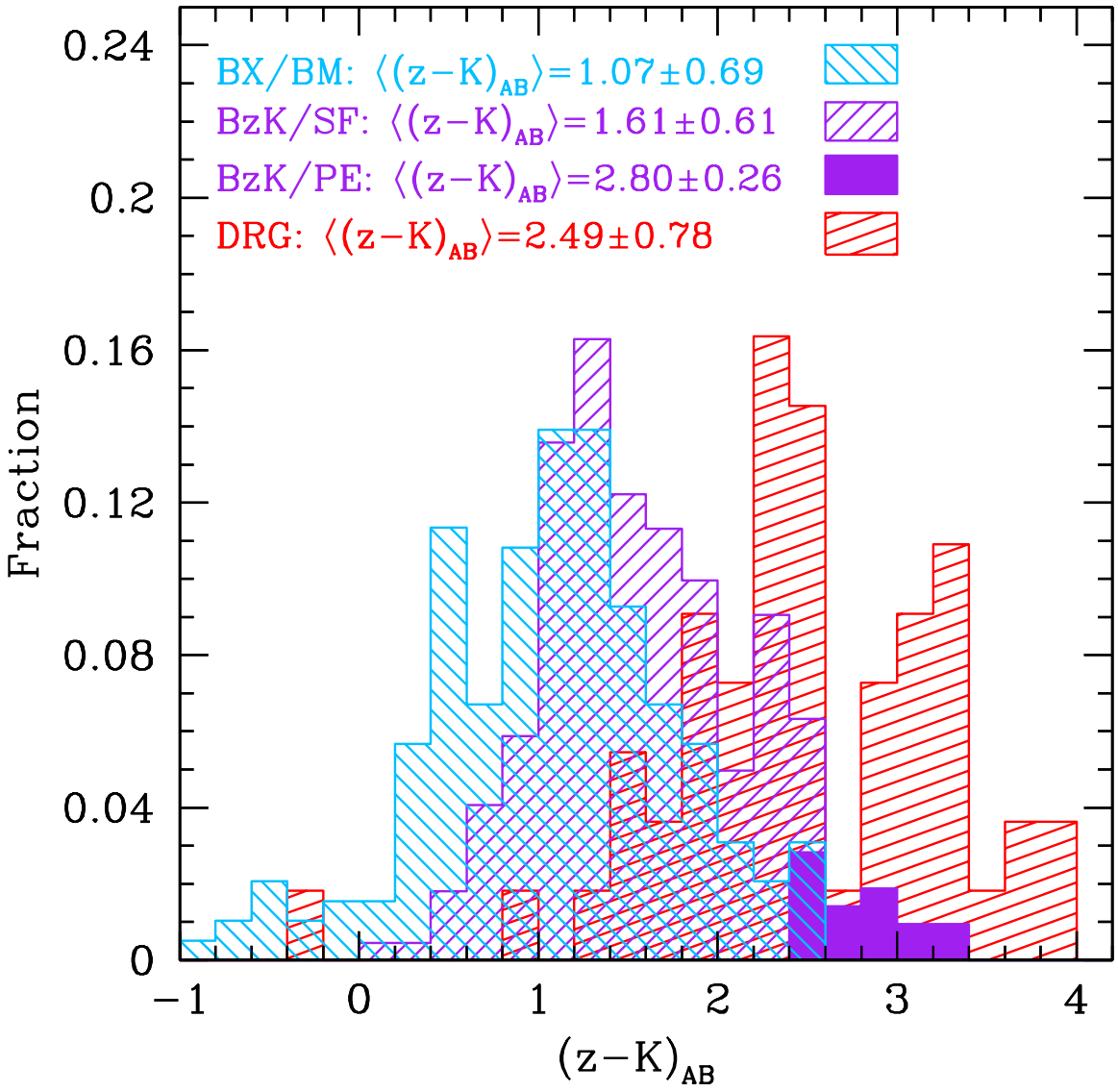

Figure 3.7 $z-K$ color distribution for BX/BM, star-forming BzK, and DRG galaxies to $K_{\rm s}=21$. The mean $z-K$ color of galaxies becomes redder for the BX/BM to BzK to DRG samples. BX/BM selection is more efficient in selecting objects with blue $(z-K)_{\rm AB}\lesssim 1$ and DRG selection is more efficient in selecting objects with very red $(z-K)_{\rm AB}\gtrsim 3$. The BzK criteria spans the middle range of $(z-K)_{\rm AB}$ color. The small solid histogram shows the arbitrarily normalized distribution in $(z-K)_{\rm AB}$ color for passively-evolving BzK galaxies.

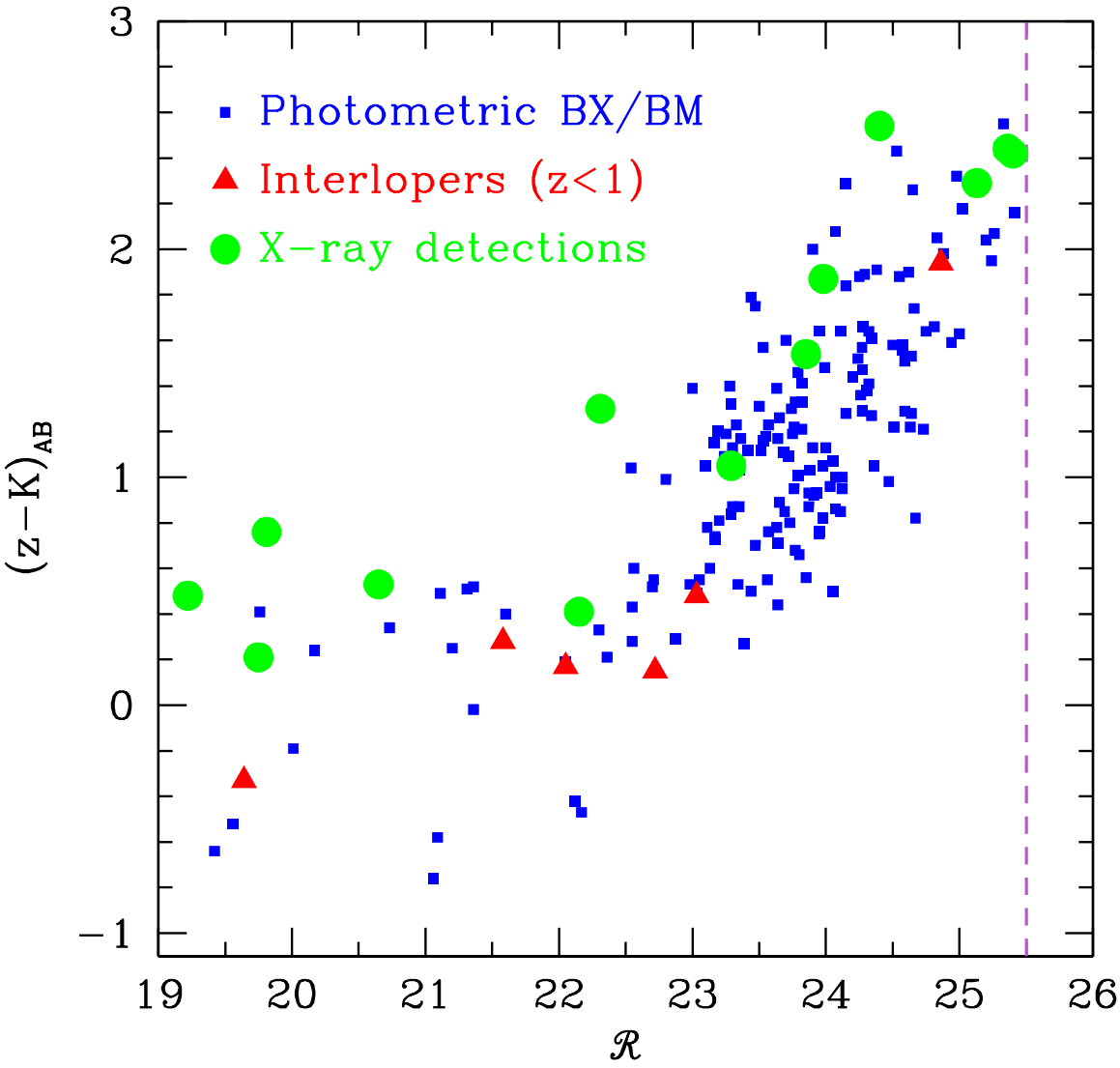

Figure 3.8 $(z-K)_{\rm AB}$ versus $\mathcal{R}$ for photometric BX/BM galaxies (squares) to $K_{\rm s}=21$, showing that optically selected galaxies with red near-IR colors are optically fainter on average than those with blue near-IR colors. This effect is due to the $K_{\rm s}=21$ limit as well as the correlation between $\mathcal{R}-$ and z-band magnitude as the two filters lie close in wavelength. Objects with $(z-K)_{\rm AB}\gtrsim 2.6$ are missed by BX/BM selection as they fall below the $\mathcal{R}=25.5$ BX/BM catalog limit (dashed vertical line). Also shown are BX/BM sources with direct X-ray detections (large circles) and spectroscopically confirmed interlopers (triangles).

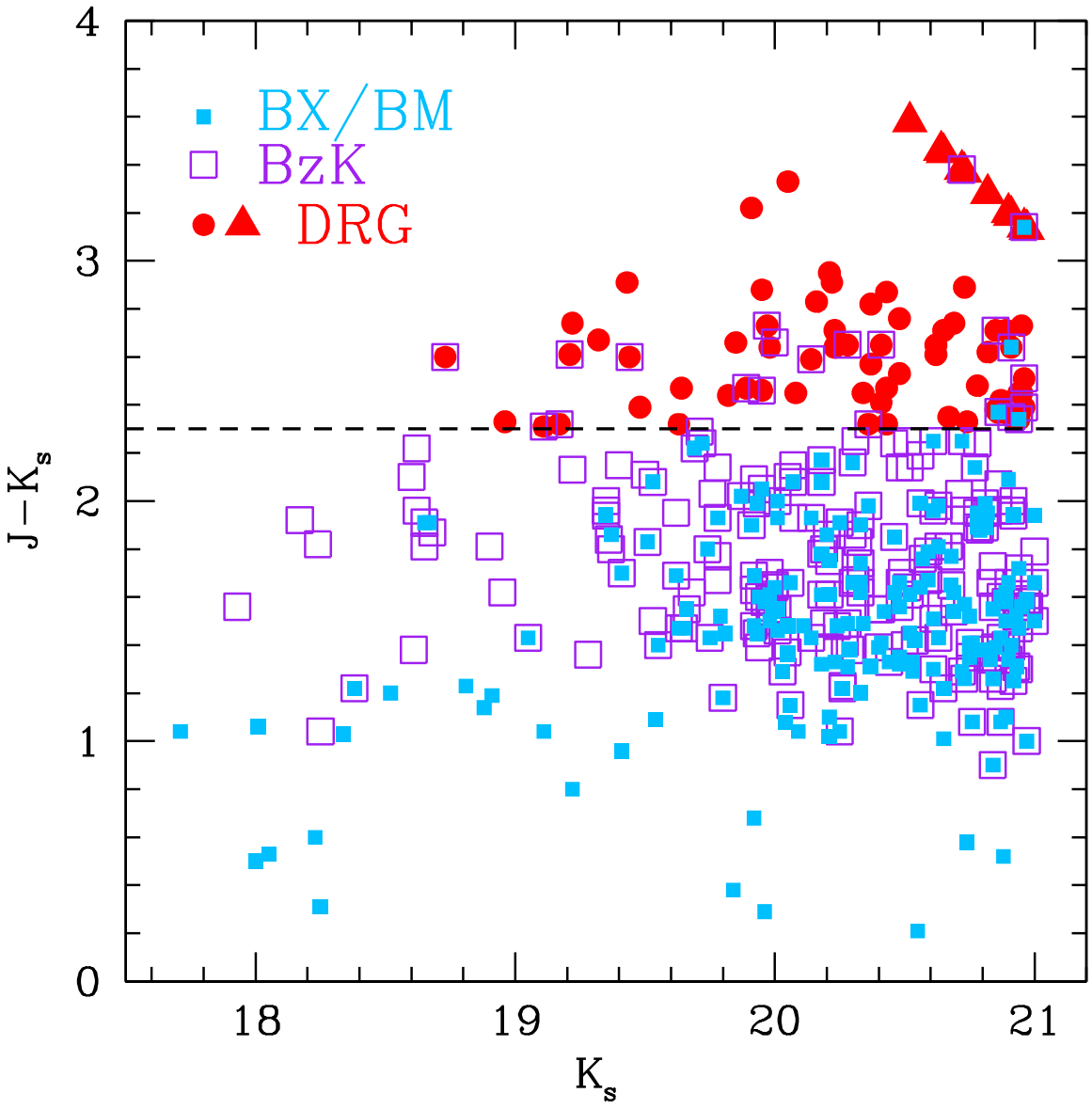

Figure 3.9 $J - K_s$ color versus K_s for BX/BM (filled squares), BzK (open squares), and DRG (circles) samples to $K_s = 21$. The hashed horizontal line denotes the $J - K_s = 2.3$ limit. DRGs with limits in J-band are indicated by the triangles. Approximately 5% of DRGs satisfy the BX/BM criteria, but the fraction rises to $\sim$ 12% if we include those selected by the $z \sim 3$ LBG criteria.

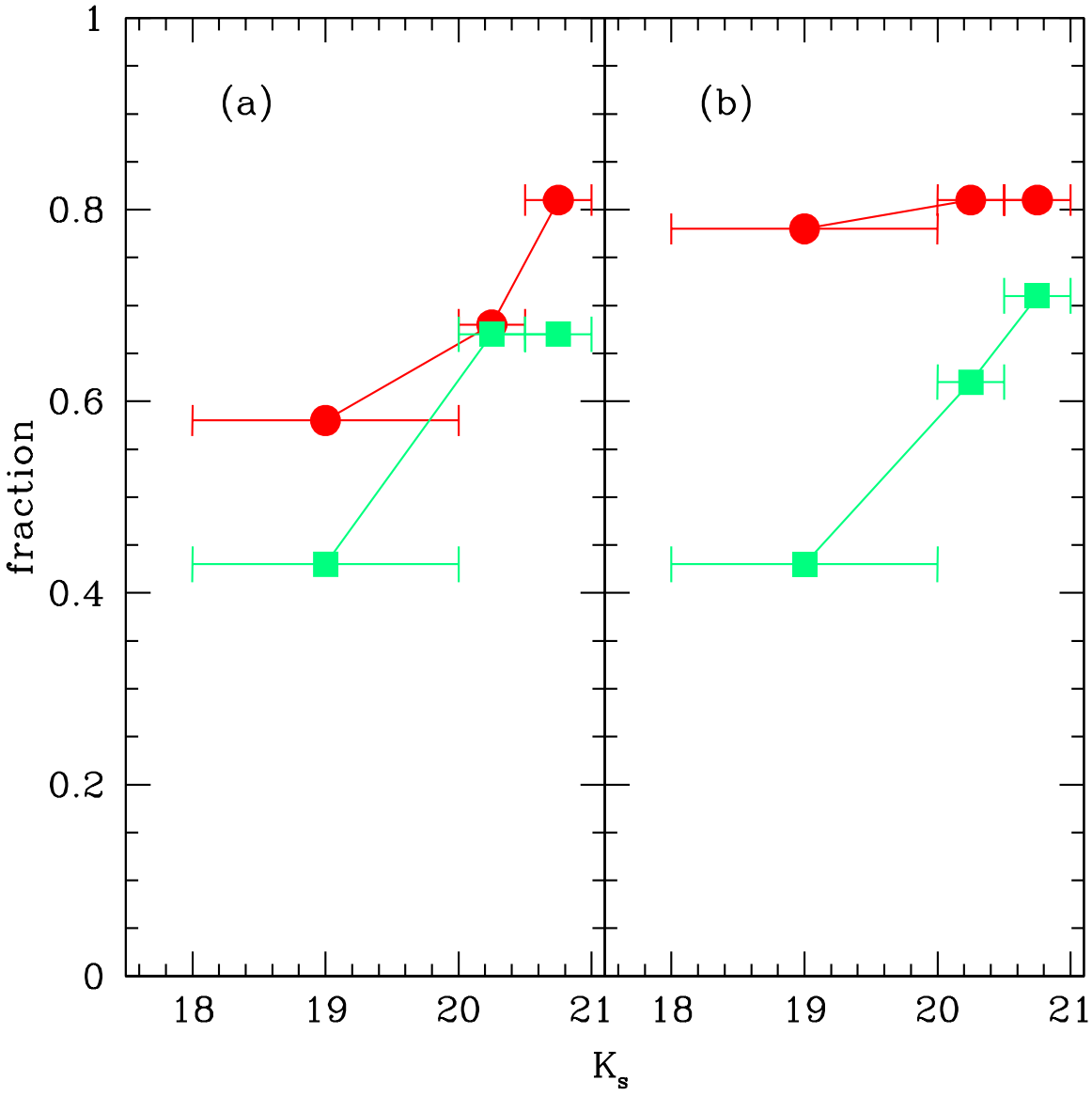

Figure 3.10 (a) Fraction of BzK/SF sources that are optically selected with the BX/BM criteria when including (squares) and excluding (circles) directly detected X-ray sources that are likely AGN (§ 3.3.1); (b) Fraction of photometric BXs and BMs that are BzK/SF selected (squares) and the fraction of BXs and BMs with confirmed redshifts $z > 1.4$ that are BzK/SF selected (circles).

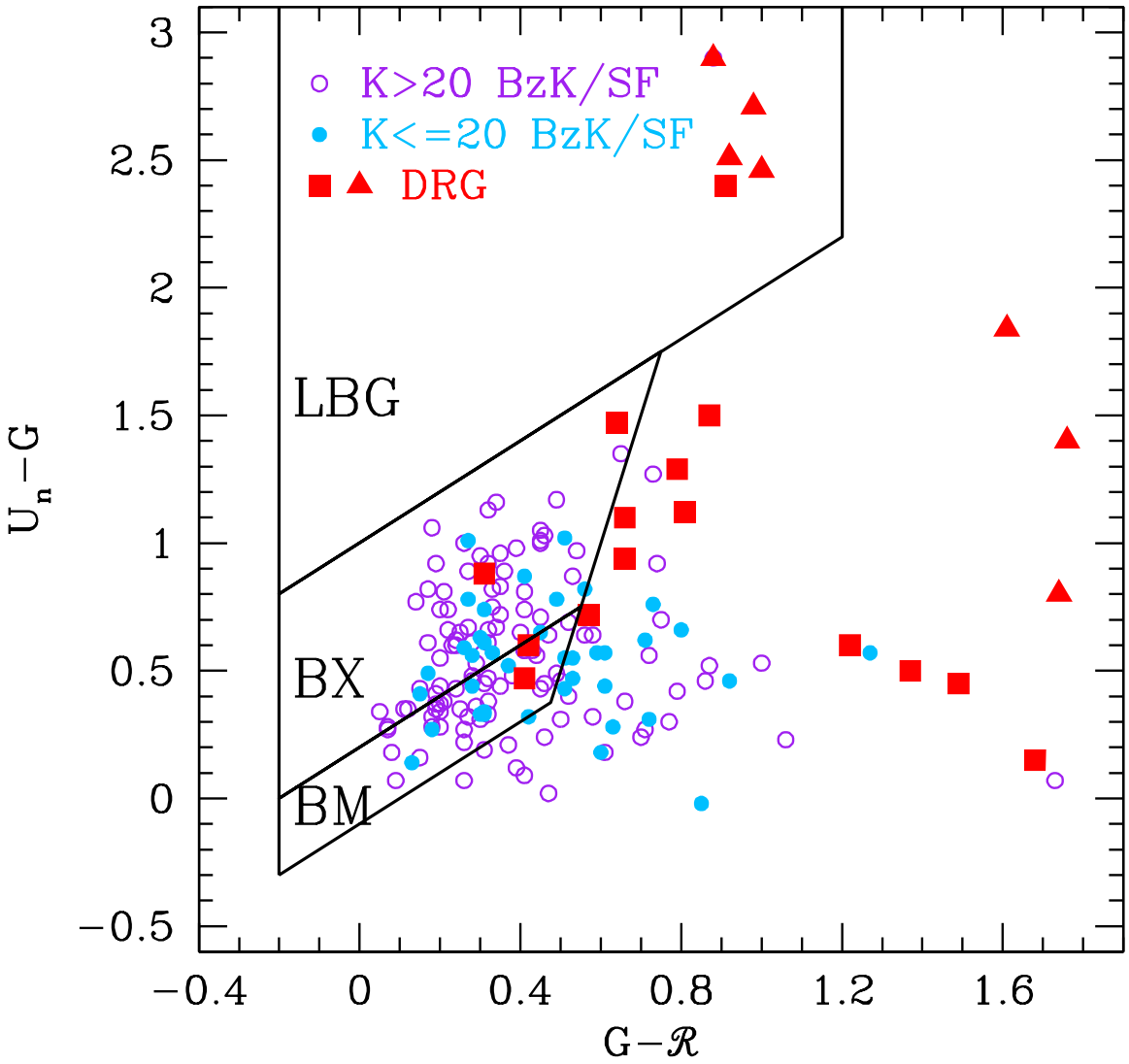

Figure 3.11 BX/BM colors of BzK/SF galaxies (circles) and DRGs with $\mathcal{R} < 25.5$, excluding direct X-ray detections. Squares denote DRGs with > 5 σ detections in $U_{\rm n}$, G, and $\mathcal{R}$; triangles denote DRGs with 5 σ limits in $U_{\rm n}$. All points are for galaxies with $K_{\rm s} < 21$. Also indicated are the BX/BM selection criteria for $z \sim 2$ BMs and BXs, as well as the $z \sim 3$ LBG criteria of Steidel et al. (2003). Approximately 40% of our DRG sample galaxies have $\mathcal{R} < 25.5$. Of all DRGs, including those not shown in the figure and that have $\mathcal{R} > 25.5$, $\sim 12\%$ can be selected using the BX, BM, or LBG criteria. Note the number of BzK and DRG galaxies that lie very close (e.g., within $\lesssim 0.2$ mag) of the BX/BM selection windows.

Separately, DRGs have a very red $\langle (z-K)_{\rm AB} \rangle = 2.49 \pm 0.78$. Approximately 10% of $z > 1.4$ BzK/SF galaxies also have $J - K_{\rm s} > 2.3$ (Figure 3.9), similar to that found by Daddi et al. (2004a). The fact that there is some, albeit small, overlap between the BzK/SF and DRG samples is not surprising since the two criteria can be used to target reddened galaxies and both have redshift distributions that overlap in the range $2.0 < z < 2.6$ (Figure 3.1). The DRG fraction among BzK selected galaxies does not change appreciably if we add in the BzK/PE sources—only 5 of 17 BzK/PE galaxies have $J - K_{\rm s} > 2.3$—as the BzK/PE galaxies are mostly at redshifts lower than the DRGs ($z \lesssim 2$). Finally, we note that DRGs include objects with much redder $(z-K)_{\rm AB}$ colors than found among BX/BM and BzK/SF/PE galaxies, i.e., those with $(z-K)_{\rm AB} > 3$. The absence of these galaxies from star-forming selected samples is discussed in § 3.4.2.

We can directly quantify the overlap between BzK/SF and BX/BM galaxies. Figure 3.10 shows the fraction of BzK/SF galaxies satisfying the BX/BM criteria (left panel) and the fraction of BX/BM galaxies satisfying the BzK/SF criteria (right panel). Most of the contamination of the BzK/SF sample (that we know of) is from X-ray detected AGN (§ 3.3.1), while most of the contamination of the BX/BM sample is from low redshift interlopers (Table 3.1). Both sources of contamination tend to occupy the bright end of the K-band apparent magnitude distribution. We also show the overlap fractions in Figure 3.10 excluding X-ray detected AGN and interlopers. The BX/BM criteria recover an increasing fraction of BzK/SF selected sources proceeding from $K_{\rm s} < 20$ galaxies ($\sim 60\%$ recovery fraction) to $K_{\rm s} \sim 21$ galaxies ($\sim 80\%$ recovery fraction) after excluding directly detected X-ray sources that are likely AGN (see § 3.3.1). Conversely, the BzK/SF criteria recover $\sim 80\%$ of spectroscopically confirmed BX/BM galaxies at $z > 1.4$, and are evidently effective at recognizing most of the BX/BM low redshift interlopers that tend to occupy the bright end of the K-band apparent magnitude distribution. This result stems from the fact that low redshift interlopers tend to have bluer colors than necessary to satisfy the BzK/SF criteria.

Figures 3.11 and 3.12 show that a significant portion of BzK/SF galaxies missed by BX/BM selection, and conversely, have colors that place them within $\lesssim 0.2$ mag of the selection windows, which is comparable to the photometric uncertainties. The BX/BM criteria likely miss some BzK/SF galaxies not because of some failure of the criteria, but

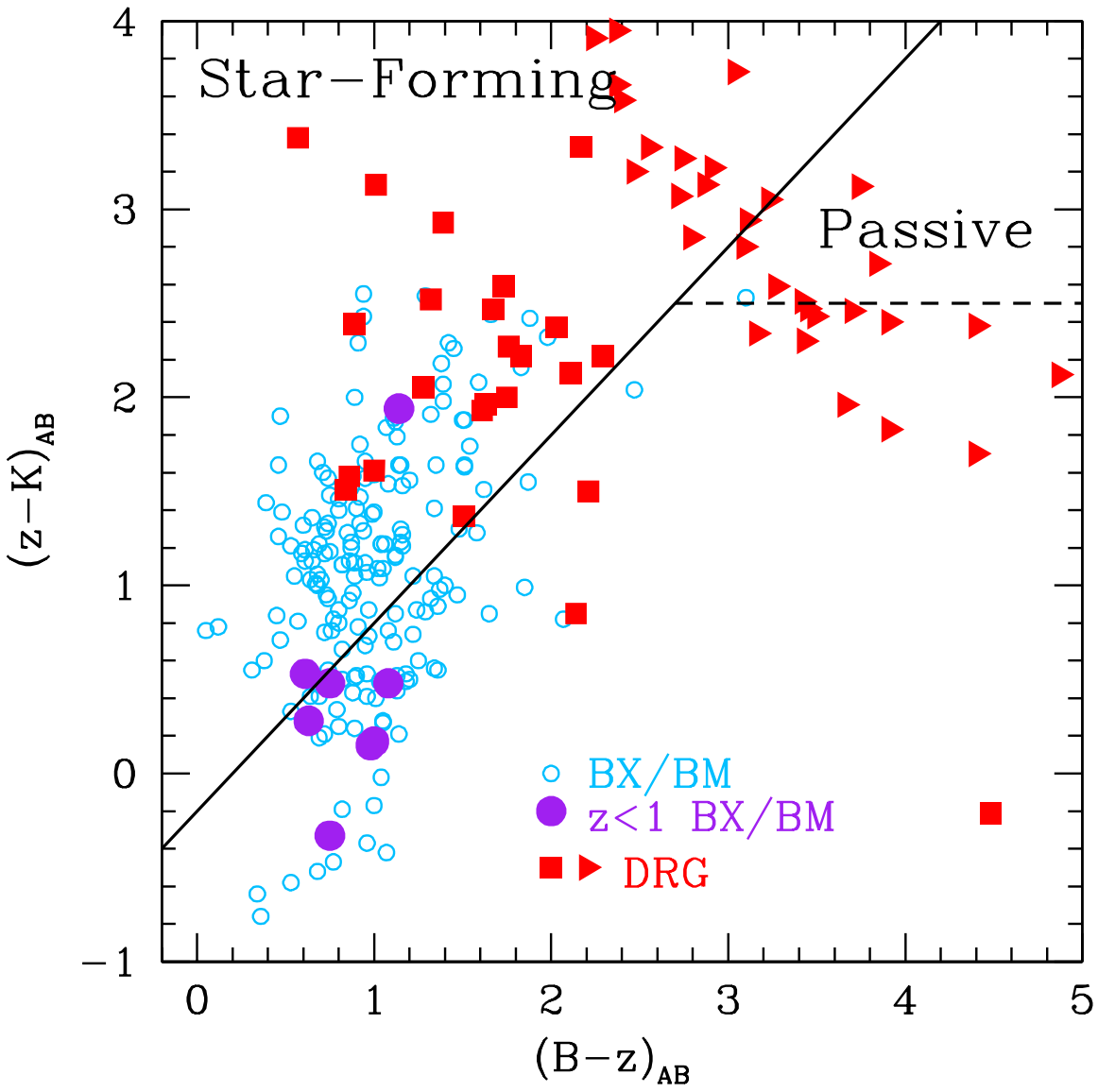

Figure 3.12 BzK colors of BX/BM galaxies (empty circles) and DRGs (filled squares) to $K_s = 21$. Large filled circles denote BX/BM objects with spectroscopically confirmed redshifts $z < 1$ (interlopers), most of which fall outside the BzK/SF selection window. Also shown is the expected region of color space for passively evolving $z > 1.4$ galaxies (Daddi et al. 2004a). Note the number of BX/BM galaxies that lie very close (e.g., within $\lesssim 0.2$ mag) of the BzK selection window. DRGs with B-band limits, shown by the triangles, cluster in the region expected for passively evolving $z > 1.4$ galaxies.

because we cannot measure photometry with infinite precision. The trend from lower (60%) to higher (80%) recovery rate shown in Figure 3.10a reflects the fact that a greater percentage of $K_s < 20$ BzK/SF galaxies have redder $G - \mathcal{R}$ colors (when compared with $K_s > 20$ BzK/SF galaxies) than required to satisfy the BX/BM criteria (Figure 3.11). There are some BzK/SF galaxies that have very red $G - \mathcal{R} \gtrsim 0.8$ colors. As we show in § 3.4, these red $G-\mathcal{R}$ galaxies would have an average bolometric SFR similar to BzK/SF galaxies with bluer $G-\mathcal{R}$ colors if they are at similar redshifts, $z \sim 2$. Therefore, if these red objects are at $z \sim 2$, then the correlation between $G - \mathcal{R}$ and reddening, as quantified by the Calzetti et al. (2000) law, would appear to fail. Photometric scatter will also reduce the effectiveness of the BzK criteria in selecting BX/BM galaxies (Figure 3.12). We can account for most of the photometric incompleteness using the more sophisticated analysis of Reddy et al. (2006a).

Our deep K-band data allow us to investigate the efficiency of BzK/SF selection to fainter K magnitudes than previously possible. Figure 3.13 shows the BzK colors of BX/BM galaxies with spectroscopic redshifts $1.4 < z < 2.6$ for three bins in K_s magnitude. The BzK/SF criteria were designed to select relatively massive galaxies with $K_s < 20$, but they become slightly less efficient in culling $K_s > 21$ galaxies: 10 of 49 ($\sim 20\%$) BX/BM galaxies with spectroscopic redshifts $1.4 < z < 2.6$ and $K_s > 21$ do not satisfy the BzK/SF criteria. Furthermore, we note that $\sim$ 11% (61/544) of BX/BM candidates that fall in the region with K-band data are undetected to $K_s = 22.5$ (3 σ). The K-band limits for these galaxies suggests they are younger star-forming systems with $(z - K)_{AB} \lesssim 1$, below which the BzK/SF criteria drop in efficiency, as discussed above. We remind the reader that many of the BzK/SF objects not appearing in the BX/BM sample may be missed by the BX/BM criteria simply because of photometric errors. BX/BM galaxies missed by the BzK/SF criteria may be missed not because of intrinsic differences in the objects, but simply because of photometric scatter or because of the difficulty in obtaining very deep K_s-band data.

Turning to $J - K_s > 2.3$ galaxies, we show the optical colors of DRGs with $\mathcal{R} < 25.5$ in Figure 3.11, and the near-IR colors of the 74% of DRGs with z-band detections in Figure 3.12. The optical criteria are particularly inefficient in selecting $J - K_s > 2.3$ sources: 9 of 73 (12%) of DRGs in the GOODS-N field satisfy BX, BM, or LBG selection.

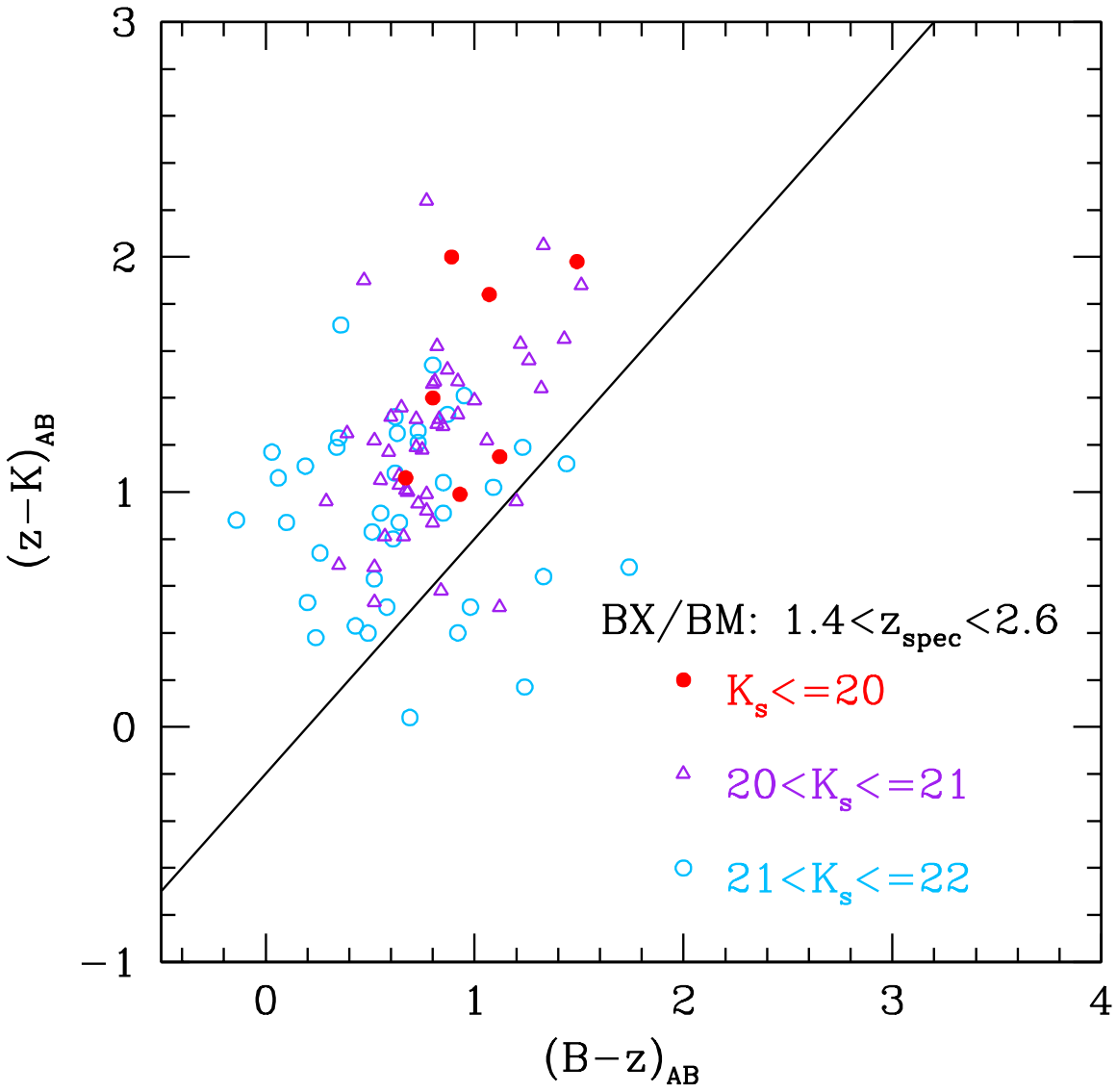

Figure 3.13 BzK colors of spectroscopically confirmed BX/BM galaxies with redshifts $1.4 < z < 2.6$ for different bins in $K_{\rm s}$ magnitude. BzK/SF selection appears to miss an increasing fraction of $K_{\rm s} > 21$ galaxies in this redshift range due to the narrowing BzK/SF selection window for objects with bluer $(z-K)_{\rm AB}$ colors. In addition, $\sim 19\%$ of BX/BM candidates have $K_{\rm s} > 22.0$ and are not shown.

This fraction is similar to the overall detection rate found by Erb et al. (2006c) for the four fields in the $z \sim 2$ optical survey with deep $J-$ and K-band data. The LBG criteria can be used to select some DRGs since $z \sim 2$ galaxies with a Calzetti reddened constant star formation SED with $E(B-V) \gtrsim 0.3$ are expected to lie in the color space occupied by $z \sim 3$ LBGs. A greater fraction ($\sim 30\%$) of DRGs satisfy the BzK/SF criteria (Figure 3.12) since these criteria select objects with developed spectral breaks and with redshifts that fall in the range probed by DRG selection (see Figure 3.1). We note that DRGs with B-band limits cluster in the region of color space expected for passively evolving $z > 1.4$ galaxies (Figure 3.12). These DRGs have little, if any, current star formation (see § 3.4.2).

3.3.3 Stacked X-ray Results

The X-ray data are not sufficiently sensitive to detect individual galaxies with SFR$\lesssim$ 190 $M_{\odot}$ yr^{-1} (3 σ). We can, however, stack the X-ray data for subsets of galaxies below the sensitivity threshold to determine their average X-ray emission. The influence of AGN in any X-ray stacking analysis is a concern. The softness of a stacked signal provides some circumstantial evidence for X-ray emission due primarily to star formation (e.g., van Dokkum et al. 2004, Daddi et al. 2004a, Laird et al. 2005). UV line signatures and radio emission can provide additional constraints on the presence of AGN (e.g., Reddy & Steidel 2004). We typically removed all directly detected X-ray sources from the optical and near-IR samples before running the stacking simulations, except as noted below and in Table 3.3 when considering X-ray detected sources which may be star-forming galaxies. Our method of excluding other X-ray detected sources ensures that luminous AGN do not contaminate the stacked signal. Indirect evidence suggests that less luminous AGN do not contribute significantly to the stacked signal. First, the stacked signal has no hard-band (HB; $2-8$ keV) detection indicating that the signal is softer than one would expect with a significant AGN contribution. Second, the availability of rest-frame UV spectra for many of the BX/BM objects provides an independent means of identifying AGN. There is one source whose spectrum shows high-ionization emission lines in the rest-frame UV, but no X-ray detection in the *Chandra* 2 Ms data. Removing this X-ray faint AGN source does not appreciably affect the stacked X-ray flux. In addition, Reddy & Steidel (2004) examined the very same BX/BM dataset used here and found a very good agreement between dust-

corrected UV, radio, and X-ray inferred SFRs for the sample, suggesting star formation as the dominant mechanism in producing the observed multi-wavelength emission. Finally, the local hosts of low luminosity AGN have stellar populations characteristic of passively evolving early-type galaxies (Kauffmann et al. 2003). In § 3.4.2 we show that passively evolving galaxies at $z \sim 2$ have little or no detectable X-ray emission, implying that low level accretion activity in these systems does little to alter the X-ray emission relative to that produced from star formation. The absence of X-ray emission from these passively evolving galaxies also suggests that low mass X-ray binaries contribute little X-ray emission in star-forming galaxies when compared with the emission produced from more direct tracers of the current star formation rate, such as high mass X-ray binaries.

Stacking results for the samples (to $K_{\rm s} = 22.5$) are summarized in Figure 3.14 and Table 3.2. The left panel of Figure 3.14 includes all photometrically selected BzK/SF and DRG galaxies, and all spectroscopically confirmed $z > 1$ BX/BM galaxies. The right panel includes only those BzK/SF galaxies with spectroscopic redshifts $z > 1$, all of which also satisfy the BX/BM criteria. All direct X-ray detections have been excluded in making Figure 3.14. The distributions do not change appreciably if we only consider the X-ray flux of BzK/SF galaxies spectroscopically confirmed to lie at $z > 1$ (Figure 3.14b). Removing the one spectroscopic $z > 1$ AGN undetected in X-rays does little to change the X-ray luminosity distributions. The luminosity distributions agree well between the three samples over a large range in $K_{\rm s}$ magnitude, with $K_{\rm s} < 20$ galaxies exhibiting the largest X-ray luminosities by a factor of 2 to 3 when compared with fainter $K_{\rm s} > 20.5$ galaxies.

3.4 Discussion

In this section we first present the X-ray inferred average bolometric SFRs for galaxies in the BX/BM, BzK/SF/PE, and DRG samples, and compare our results with other X-ray stacking analyses. Unless stated otherwise, we exclude hard-band X-ray AGN sources from the analysis of the SFRs. The SFRs are interpreted for galaxies as a function of their near-IR colors and we assess the ability of optical surveys to single out both heavily reddened and massive galaxies. We identify passively evolving galaxies at $z \sim 2$ from their red near-IR colors and discuss plausible star formation histories for these galaxies using the X-ray data as an additional constraint. Finally, we discuss the contribution of BX/BM, BzK/SF, and

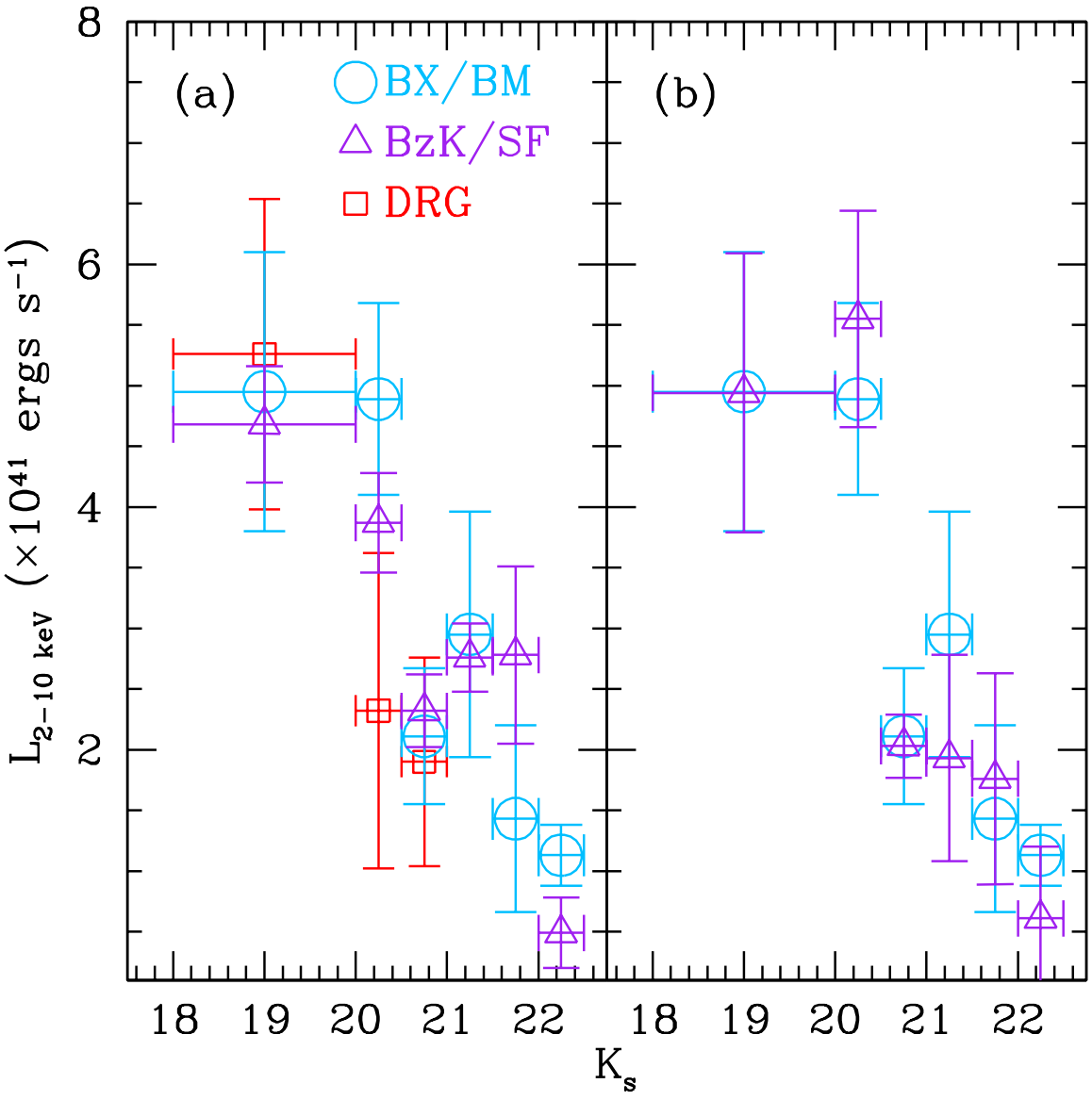

Figure 3.14 Stacked X-ray luminosity versus K_s magnitude for BX/BM galaxies with $z > 1$ (circles), BzK/SF galaxies (triangles), and DRGs (squares), excluding all directly detected X-ray sources. The left and right panels show the distributions for photometric and spectroscopically confirmed $z > 1$ BzK/SF galaxies, respectively. Sources without a spectroscopic redshift were assigned the mean redshift of the sample which they belong to, according to Figure 3.1. In all cases, we find the distributions consistent within the errors. We also find that $K_s < 20$ galaxies have average X-ray luminosities that are a factor of 2 to 3 times higher than that of $K_s > 20.5$ galaxies.

DRG galaxies to the star formation rate density at $z \sim 2$, taking into account the overlap between the samples and their respective redshift distributions.

3.4.1 Star Formation Rate Distributions

3.4.1.1 Star Formation Rates and Comparison with Other Studies

We estimated the SFRs for galaxies in our samples using the Ranalli et al. (2003) calibration between X-ray and FIR luminosity. This calibration reproduced the SFRs based on independent star formation tracers for $z \sim 2$ galaxies (Reddy & Steidel 2004), so we are confident in using it here. The SFR distributions for BX/BM, BzK, and DRG galaxies are shown in Figure 3.15, where we have added the five directly detected soft-band X-ray sources in Table 3.3 that may be star-forming galaxies. The SFRs are summarized in Table 3.2. The mean SFR of $K_{\rm s} < 20$ galaxies is $\sim 90 - 140$ $M_{\odot}$ yr^{-1}, and is a factor of 2 to 3 times larger than galaxies with $K_{\rm s} > 20.5$. For comparison, Daddi et al. (2004a) found an average SFR of K20 galaxies in the GOODS-South field of 190 $M_{\odot}$ yr^{-1} (including one likely star-forming galaxy directly detected in X-rays). This is somewhat higher than our value of 110 $M_{\odot}$ yr^{-1} for $K_{\rm s} < 20$ BzK/SF galaxies. This discrepancy could simply result from field-to-field variations, small number statistics, or the lower sensitivity of the X-ray data in the GOODS-South field compared to GOODS-North. With the *Chandra* 2 Ms data, we are able to exclude directly detected X-ray sources down to a factor of two lower threshold than was possible with the 1 Ms data in the GOODS-South field. If we add back those $K_{\rm s} < 20$ X-ray BzK/SF galaxies that would have been undetected in the 1 Ms data to the stacking analysis, we obtain an average SFR of 160 $M_{\odot}$ yr^{-1}, more in line with the Daddi et al. (2004a) value of 190 $M_{\odot}$ yr^{-1}.

A similar stacking analysis by Rubin et al. (2004) indicates that $K_{\rm s} < 22$ DRGs have SFRs of ~ 280 $M_{\odot}$ yr^{-1}, corrected for the difference in SFR calibration used here and in Rubin et al. (2004). This very high value is likely a result of the shallow X-ray data (74 ksec) considered in that study; the depth of their X-ray data precludes the removal of most of the X-ray sources that are directly detected in the 2 Ms X-ray survey. If we include those X-ray sources that would have been undetected in the 74 ksec data, assuming a mean redshift of $\langle z \rangle = 2.4$, the average SFR for the DRGs with $K_{\rm s} < 21$ is 250 $M_{\odot}$ yr^{-1}. Therefore, much of the difference in the SFRs can be attributed to unidentified AGN in the shallower X-ray

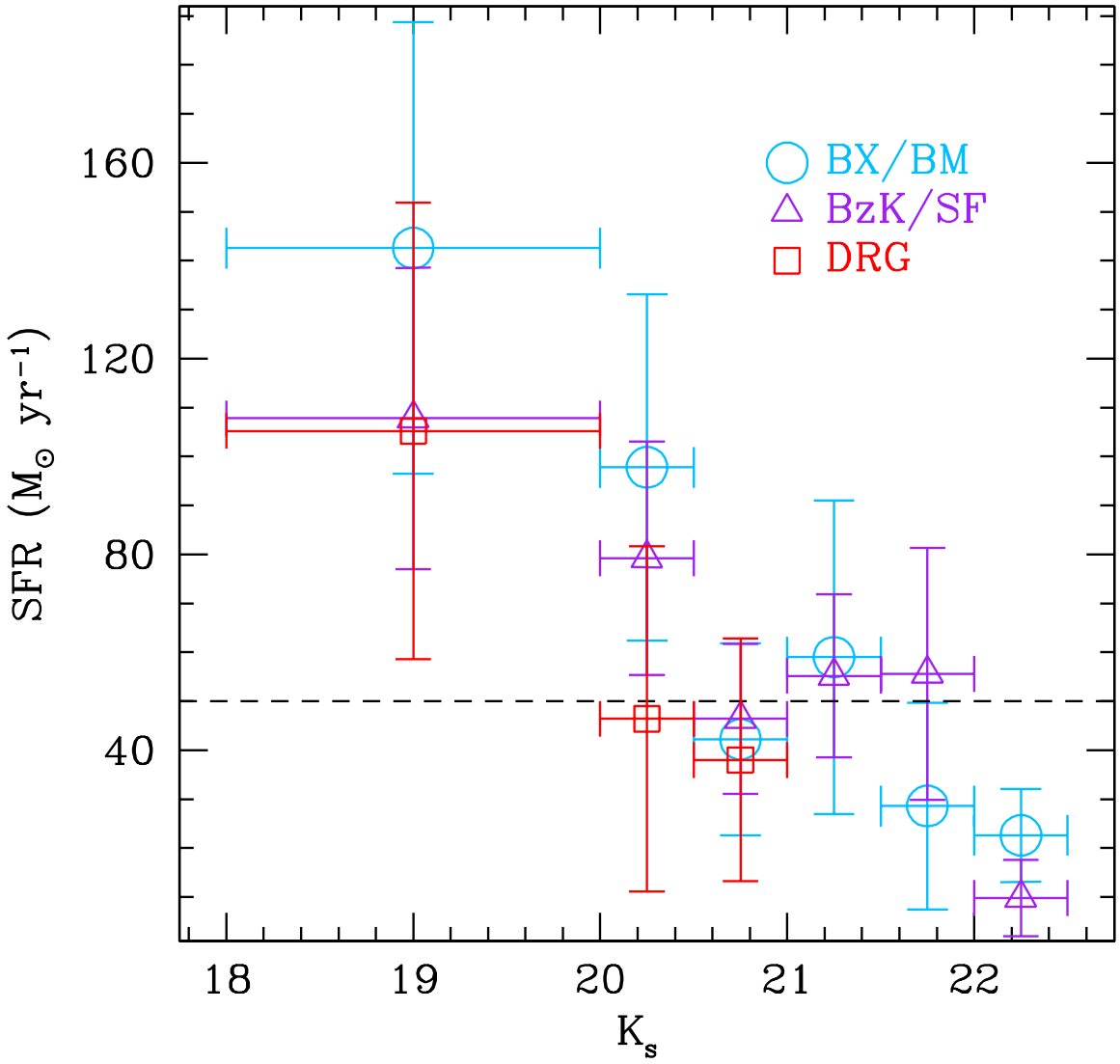

Figure 3.15 Star formation rates inferred from the X-ray luminosity using the Ranalli et al. (2003) calibration. We have added the five directly detected soft-band X-ray sources that may be star-forming (Table 3.3) to compute the average SFR. Circles, triangles and squares denote BX/BM, BzK, and DRG samples, respectively. The BX/BM points are for spectroscopically confirmed $z > 1$ galaxies, and we have assumed the mean redshifts for the BzK/SF and DRG samples as in Figure 3.14. Uncertainties in the star formation rates are dominated by scatter in the X-ray/FIR relation and the dispersion in the stacked X-ray estimates. The dashed horizontal line denotes the average SFR for the entire spectroscopic ($z > 1$) BX/BM sample of ~ 50 M$_\odot$ yr^{-1} from Reddy & Steidel (2004). Galaxies with $K_s < 20$ have inferred star formation rates a factor of $2-3$ higher than for $K_s > 20.5$ galaxies.

surveys contaminating estimates of the star formation rate. If Figure 3.15 is any indication, then adding DRGs with $21 < K_{\rm s} \leq 22$ to the stack would decrease this average SFR. Variance of the fraction of DRG/PE galaxies between fields may also affect the average SFRs: a greater fraction of DRG/PEs in the GOODS-N field, $\sim 25\%$ (3/13) of which have $K_{\rm s} < 20$, will lead to a lower *average* SFR for $K_{\rm s} < 20$ DRGs. As we show in § 4.4.2, there are clearly some number of very reddened galaxies with large SFRs (e.g., submillimeter galaxies) among DRGs (and among the BX/BM and BzK/SF samples). Regardless, these calculations underscore the importance of factoring in the differing sensitivity limits of the various X-ray surveys before comparing results. The strong dependence of SFR with $K_{\rm s}$ magnitude (Figure 3.15) also suggests that fair comparisons of the SFRs of galaxies selected in different surveys can only be made between objects with similar rest-frame optical luminosities.

Our analysis is advantageous as we are able to compare the SFRs of galaxies within the same field, employing the same multi-wavelength data (to the same sensitivity level) and the same photometric measurement techniques, for a consistent comparison. The inferred average SFRs of BzK/SF and DRG galaxies are remarkably similar to those of optically selected galaxies once the samples are restricted to similar $K_{\rm s}$ magnitudes. The previously noted discrepancies in X-ray inferred SFRs of BzK/SF, DRG, and BX/BM galaxies are therefore likely a result of a mismatch between X-ray survey limits and near-IR magnitude ranges. Field-to-field variations may also partly account for the previously observed discrepancies.

3.4.1.2 Dependence of SFR on $(z - K)_{\rm AB}$ Color

We began our analysis by noting the differences between the $(z - K)_{\rm AB}$ color distributions of optical and near-IR selected galaxies (Figure 3.7). Figure 3.15 indicates that despite these near-IR color differences, the BX/BM, BzK, and DRG galaxies have very similar *average* SFR distributions as a function of $K_{\rm s}$ magnitude. Another proxy for stellar mass is the $(z - K)_{\rm AB}$ or $\mathcal{R} - K_{\rm s}$ color (e.g., Shapley et al. 2005) as it directly probes the strength of the Balmer and 4000 Å breaks. Figure 3.16 shows the inferred average SFRs of optical and near-IR selected galaxies as a function of their $(z - K)_{\rm AB}$ color, excluding

all directly detected X-ray sources.[2] Within any single sample, objects with red $(z-K)_{\rm AB}$ colors up to $(z-K)_{\rm AB} \sim 3$ have the largest SFRs. The red $(z-K)_{\rm AB}$ color for these objects with high SFRs likely results from a developed spectral break (due to an older stellar population) combined with the effects of dust. In fact, Figure 3.17 illustrates the tendency for BX/BM objects with spectroscopic redshifts $z > 1$ and red $(z-K)_{\rm AB}$ colors to have larger attenuation, as parameterized by $E(B-V)$, on average, than those with bluer $(z-K)_{\rm AB}$ colors. The turnover in the inferred SFR around $(z-K)_{\rm AB} \sim 3$ is discussed in the next section.

Figure 3.16 suggests that optically selected BX/BM galaxies may have systematically higher SFRs than BzK and DRG galaxies with similar $(z-K)_{\rm AB}$ colors, perhaps indicating that the stacked sample for BzK/SF and DRG galaxies includes those that are passively evolving. This may be particularly true of DRGs, quite a few of which only have B-band limits and which cluster in the BzK color space occupied by passively evolving galaxies (Figure 3.12). We can assess the dispersion in SFRs by separately stacking galaxies that are expected to be currently star-forming based on their colors and those that are not. For example, the average SFR computed for BzK/SF galaxies that are *not* selected by the BX/BM criteria (of which $\sim 70\%$ are within 0.2 mag of the BX/BM selection windows) is $\sim 70\ M_{\odot}\ {\rm yr}^{-1}$, comparable to the average SFR of all BzK/SF galaxies with $K_{\rm s} < 21$. *In summary, star-forming BzK galaxies have similar SFRs regardless of whether or not they satisfy the* BX/BM *criteria.* The BX/BM criteria miss some BzK/SF galaxies either because of photometric scatter or because their optical colors are not indicative of their reddening. It is worth noting that photometric scatter works both ways: some sources with intrinsic colors satisfying the BX/BM criteria will be scattered *out* of the BX/BM selection windows and some whose colors do not satisfy the BX/BM criteria will be scattered *into* the BX/BM selection windows, although the two effects may not equilibrate (Reddy et al. 2006a). The incompleteness of the BX/BM and BzK/SF criteria with respect to all star-forming galaxies at $z \sim 2$ simply reflects our inability to establish perfect selection criteria immune to the effects of photometric scatter and SED variations while at the same time efficiently excluding interlopers (e.g., Adelberger et al. 2004). However, the advantage of *spectroscopic* optical surveys is that their selection functions can be quantified relatively

[2]Adding the five sources in Table 3.3 does not appreciably affect Figure 3.16

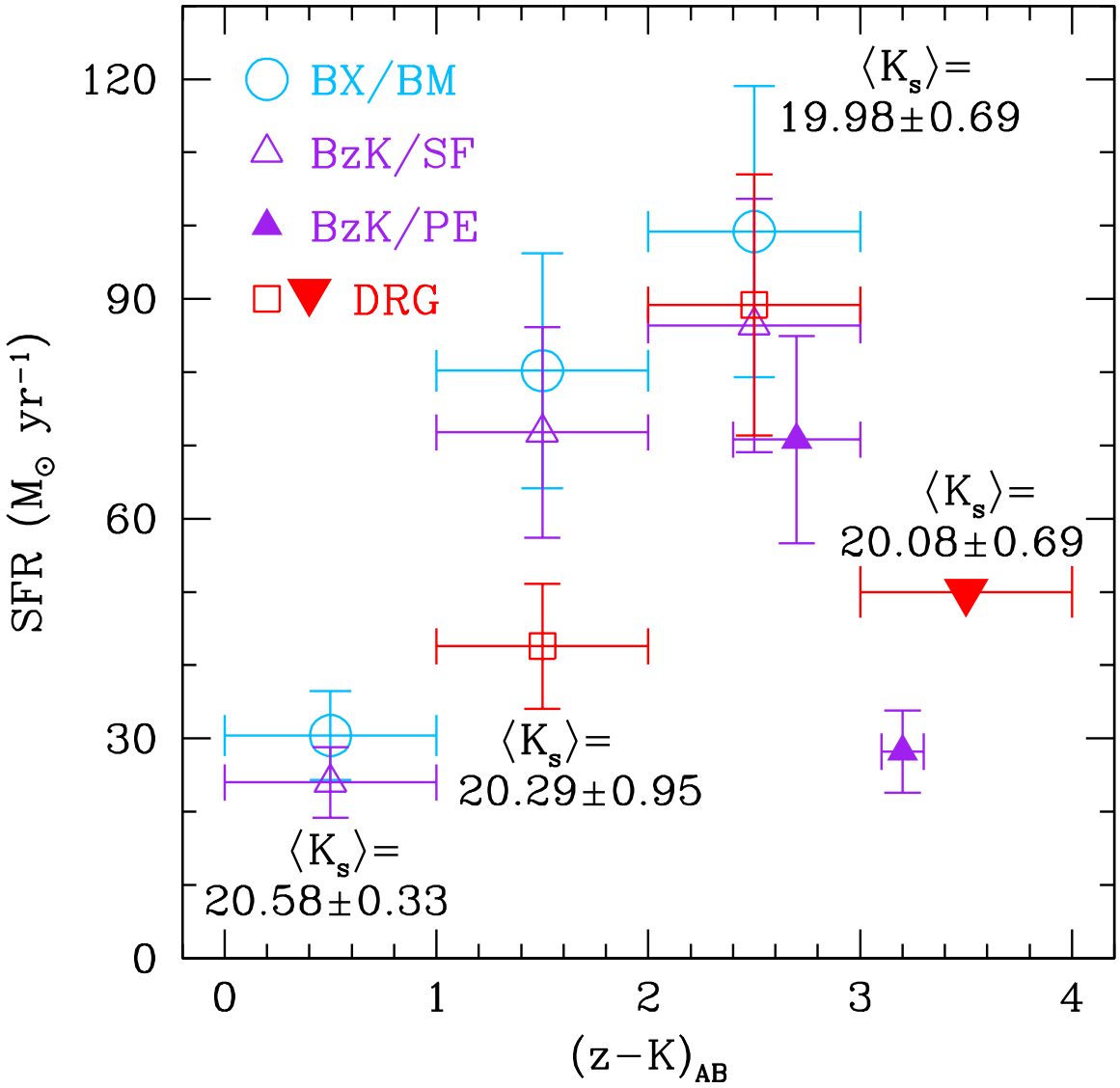

Figure 3.16 Star formation rates of $K_{\rm s} < 21$ galaxies as a function of $(z-K)_{\rm AB}$ color. Symbols are the same as in Figure 3.15. The small solid triangles denote the average SFR inferred for BzK galaxies that are selected to be passively evolving (BzK/PE galaxies) and the large inverted triangle indicates the limit in SFR found for the 13 DRGs with $(z-K)_{\rm AB} > 3.0$. Note the turnover in inferred SFR at $(z-K)_{\rm AB} \sim 3$. Also indicated are the average $K_{\rm s}$ magnitudes for sources in each bin of $(z-K)_{\rm AB}$ color.

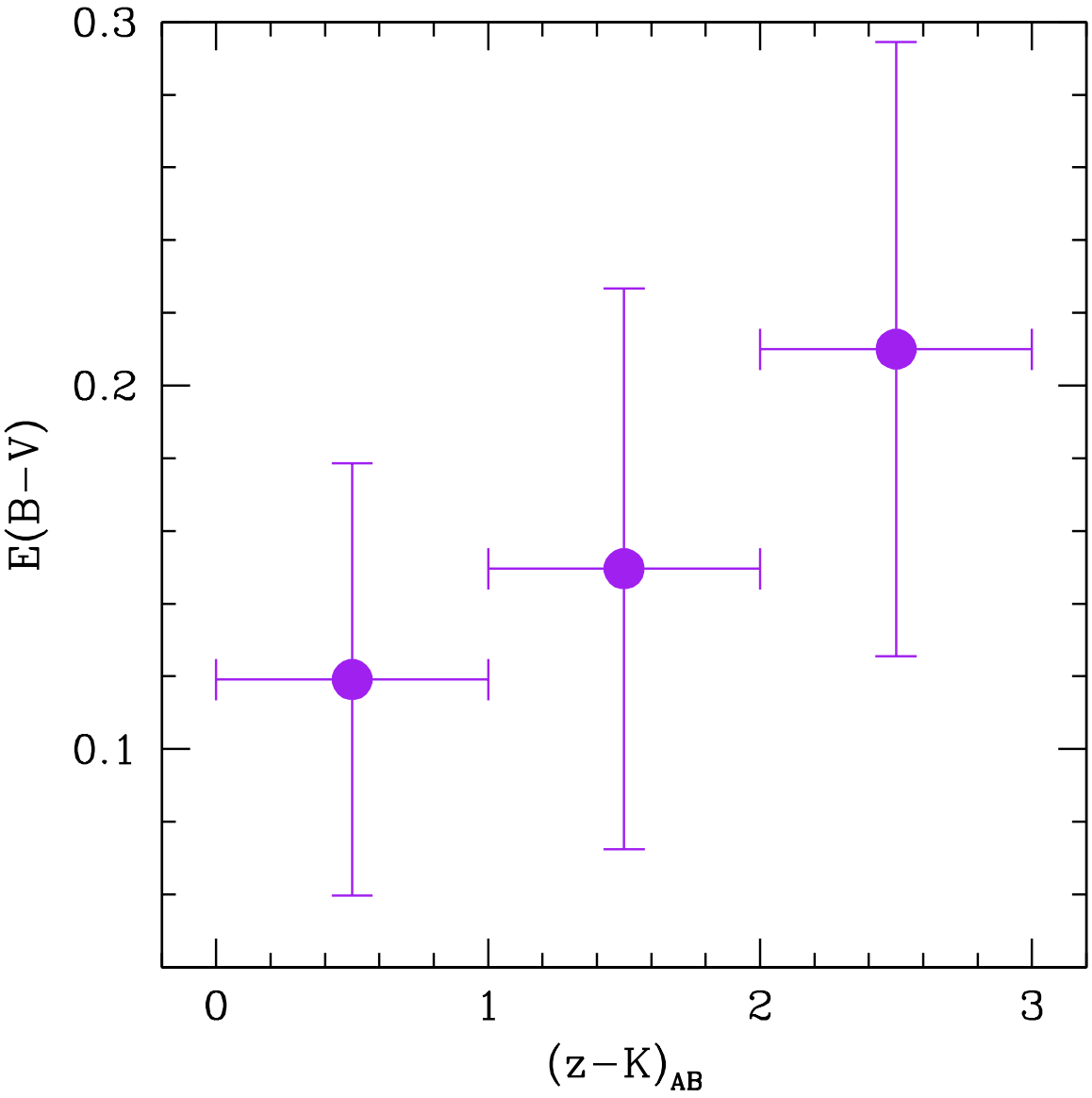

Figure 3.17 Attenuation, as parameterized by the rest-frame UV spectral slope, $E(B-V)$, as a function of $(z-K)_{\rm AB}$ color for spectroscopically confirmed BX/BM galaxies with $z > 1$. Errors in $E(B-V)$ represent the 1 σ dispersion of $E(B-V)$ values for each bin of $(z-K)_{\rm AB}$.

easily (e.g., Adelberger et al. 2004, Reddy et al. 2006a).

3.4.1.3 Optical Selection of Reddened Star-Forming Galaxies

Naively, one might interpret the inferred SFRs as a function of $(z-K)_{\rm AB}$ color combined with the results shown in Figure 3.8 to suggest that BX/BM selection may miss the most actively star-forming galaxies at $z\sim2$. We can interpret the similarity in SFRs of BX/BM and BzK/SF galaxies in the context of their reddening, as parameterized by their rest-frame UV spectral slopes, $E(B-V)$. Daddi et al. (2004a) show that the reddening vector is essentially parallel to the BzK limit defined by Equation 3.4, implying that BzK selection should be sensitive to galaxies with higher extinction (and presumably higher star formation rates) than found among BX/BM selected galaxies (i.e., $E(B-V)\geq0.3$). However, the similarity in the average SFRs of BX/BM and BzK/SF galaxies suggests several possibilities. First, we noted above that BzK/SF galaxies not selected by the BX/BM criteria have similar SFRs as those which do satisfy the BX/BM criteria.[3] Consequently, BzK/SF galaxies with large SFRs that do not satisfy the BX/BM criteria because they truly have $E(B-V)>0.3$ may not exist in sufficient numbers to significantly change the *average* SFRs for all BzK/SF galaxies which do not satisfy the BX/BM criteria. Adelberger & Steidel (2000) and Laird et al. (2005) find that optically selected galaxies with $z\gtrsim1$ show no correlation between their rest-frame UV luminosities and their obscuration, implying that on average the redder (more obscured) galaxies have higher bolometric SFRs than galaxies with less reddening. Therefore, the similarity in the average X-ray inferred SFRs of BX/BM and BzK/SF galaxies suggests that there are not large numbers of galaxies with $E(B-V)\gtrsim0.4$ (i.e., if there were a large number of such heavily reddened objects, their bolometric SFRs would imply X-ray luminosities large enough to be directly detected in the soft-band X-ray data, and very few likely star-forming galaxies at these redshifts are directly detected in the soft-band).

Second, studies of the UV emission from submillimeter galaxies (SMGs) suggest that heavily reddened galaxies may have similar rest-frame UV spectral properties, such as their

[3]Those BzK/SF galaxies with $G-\mathcal{R}\gtrsim1$ and blue $U_{\rm n}-G\lesssim1$ have optical colors that are similar to the colors expected for lower redshift ($z\lesssim1$) galaxies (e.g., Adelberger et al. 2004). So, if these galaxies are truly low redshift galaxies, then their inferred star formation rates would be even lower.

range in $E(B-V)$, as those which are forming stars at modest rates, implying that the correlation between $E(B-V)$ and bolometric SFR (e.g., from the Meurer et al. 1999 and Calzetti et al. 2000 laws) breaks down for the most actively star-forming galaxies (e.g., Chapman et al. 2005). Table 3.4 summarizes the properties of the nine *known* radio-selected SMGs with $S_{850\mu\mathrm{m}} \gtrsim 5$ mJy in the GOODS-N field that overlap with our near-IR imaging (Chapman et al. 2005; Wang et al. 2004). Also listed are two (pair) sources with $S_{850\mu\mathrm{m}} \sim 4$ mJy taken from Chapman et al. (2005) and Wang et al. (2004). Of the seven SMGs with redshifts $1.4 < z < 2.6$, three satisfy the BX/BM criteria. The detection rate of $\sim 40\%$ is similar to the detection rate of SMGs with BX/BM colors found by Chapman et al. (2005). The mean bolometric luminosity of the 5 SMGs is $\langle L_{\mathrm{bol}} \rangle \sim 9 \times 10^{12}$ $\mathrm{L}_{\odot}$ as inferred from their submillimeter emission, corresponding to an SFR of ~ 1500 $M_{\odot}$ yr^{-1} using the Kennicutt (1998a) relation.[4] Despite their large bolometric luminosities, the three submillimeter galaxies with redshifts in our sample have dust-corrected UV SFRs of $14-28$ $M_{\odot}$ yr^{-1}. In these cases, the UV emission may come from a relatively unobscured part of the galaxy or may be scattered out of the optically thick dusty regions (Chapman et al. 2005). The BzK/SF criteria cull 5 of the 7 SMGs with redshifts $1.4 < z < 2.6$. Therefore, at least in the small sample of SMGs examined here (irrespective of their X-ray properties), the BX/BM and BzK/SF samples host an approximately equal number of SMGs. Finally, as we show below, galaxies with the most extreme $(z-K)_{\mathrm{AB}}$ colors (i.e., $(z-K)_{\mathrm{AB}} > 3$) are red not because they are obscured by dust, but because they have little or no current star formation. It is therefore not surprising that such objects are not identified by criteria designed to select star-forming galaxies.

3.4.2 Passively Evolving Galaxies at $z \sim 2$

3.4.2.1 Near-IR Colors

We now turn to galaxies in our samples that appear to have little or no current star formation. DRGs have SFRs that are comparable to those of BzK/SF and BX/BM galaxies with similar near-IR colors for $(z-K)_{\mathrm{AB}} < 3$. However, stacking the 13 DRGs with $(z-K)_{\mathrm{AB}} \geq 3$ results in a non-detection with an upper limit of ~ 50 $M_{\odot}$ yr^{-1} (Figure 3.16). Stacking the X-ray emission from the 17 BzK/PE galaxies shows a similar turnover in the inferred

[4] As we discuss in § 3.4.4, some of the submillimeter flux may be coming from accretion activity

average SFR around $(z-K)_{\rm AB} \sim 3$ (Figure 3.16). The BzK colors of the DRGs (most of which only have B-band limits) lie in the BzK color space expected for passively-evolving galaxies (Figure 3.12). The stacking analysis confirms that these red DRGs and BzK/PE galaxies have little current star formation compared with DRGs and BzK/PE galaxies with bluer near-IR colors (Figure 3.16). A similar X-ray stacking analysis by Brusa et al. (2002) yields no detection for passive EROs in the K20 survey from the *Chandra* Deep Field South data.

The average $J-K_{\rm s}$ color of the 13 passively evolving DRGs (with $(z-K)_{\rm AB} > 3$) is $\langle J-K_{\rm s}\rangle = 2.98 \pm 0.59$, and is comparable to the average $J-K_{\rm s}$ color of DRGs with bluer $(z-K)_{\rm AB}$ colors, implying that the J-band is either in close proximity to the Balmer and 4000 Å breaks or the band encompasses the breaks completely. This will occur for galaxies with a mean redshift $\langle z\rangle \sim 1.88-2.38$ (Figure 3.3). In these cases, the $(z-K)_{\rm AB}$ color will be more effective than the $J-K_{\rm s}$ color in culling those galaxies with developed spectral breaks. The fraction of passively evolving DRGs inferred from their lack of X-ray emission is $13/54 \sim 24\%$, which is in reasonable agreement to the passively evolving DRG fraction of $\sim 30\%$ found by Förster Schreiber et al. (2004b) and Labbé et al. (2005).

Alternatively, galaxies with $2 < (z-K)_{\rm AB} < 3$ must still be forming stars at a prodigious rate, as indicated by their stacked X-ray flux. The similarity in average $K_{\rm s}$ magnitude between galaxies with $2 \leq (z-K)_{\rm AB} < 3$ and $(z-K)_{\rm AB} \geq 3$ (Figure 3.16) suggests they have similar masses, and the difference in $(z-K)_{\rm AB}$ color between the two samples simply reflects the presence of some relatively unobscured star formation in those galaxies with $2 \leq (z-K)_{\rm AB} < 3$.

3.4.2.2 Stellar Populations

Figure 3.18 further illustrates the differences between the star-forming and passively evolving galaxies in terms of some physical models. The left panel of Figure 3.18 shows the $(z-K)_{\rm AB}$ versus $(K-m_{3.6/4.5\mu{\rm m}})_{\rm AB}$ colors (near-IR/IRAC color diagram) for all galaxies, excluding direct X-ray detections. [5] Because the SEDs of (non-AGN) galaxies considered here are expected to be relatively flat in f_ν across the IRAC bands, we used 3.6 μm IRAC

[5] Labbé et al. (2005) propose a similar diagram to differentiate DRGs from other (e.g., star-forming) populations of $z \sim 2$ galaxies.

AB magnitudes for all sources that were not covered by the 4.5 μm imaging. Also shown in Figure 3.18a are synthetic colors for Bruzual & Charlot (2003) spectral templates at the mean redshifts of the BM ($\langle z \rangle \sim 1.7$) and BX ($\langle z \rangle \sim 2.2$) samples, assuming constant star formation, $E(B-V) = 0$ and 0.3, and a Calzetti et al. (2000) reddening law. The bulk of BX/BM and BzK/SF galaxies generally fall within the region of color space expected for constant star-forming galaxies with moderate extinction of $E(B-V) \sim 0.15$ and ages of ~ 1 Gyr. These values are consistent with those derived from detailed spectral modeling of BX/BM galaxies and LBGs by Shapley et al. (2005). Much of the scatter of star-forming galaxies to the left and right of the CSF models for $E(B-V) = 0.15 - 0.30$ is a result of photometric uncertainty, particularly in the $(K - m_{3.6/4.5\mu\mathrm{m}})_{\mathrm{AB}}$ color, since we include galaxies with formal IRAC uncertainties of 0.5 mag. In addition, some of the scatter for objects with blue $(z-K)_{\mathrm{AB}}$ colors arises from interlopers. The more interesting aspect of Figure 3.18a is that the constant star formation models cannot account for the colors of objects with $(z-K)_{\mathrm{AB}} \gtrsim 3$: these objects must have ages less than the age of the Universe at $z \sim 2$ (~ 3 Gyr) and simultaneously have modest $E(B-V)$—and hence modest current SFRs$\lesssim 190\ M_{\odot}\ \mathrm{yr}^{-1}$—such that they remain undetected as soft-band X-ray sources. The important result is that, similar to SED fitting, the X-ray stacking analysis allows us to rule out certain star formation histories. For the PE galaxies considered here, the X-ray data rule out the constant star formation models. The benefit of X-ray data is that we can quantify the current SFR independent of extinction and the degeneracies that plague SED fitting.

The only models that can account for the colors of objects with $(z-K)_{\mathrm{AB}} \gtrsim 3$ are those with declining star formation histories (right panel of Figure 3.18). For example, DRG/PEs at $z \sim 2.2$ have colors that can be reproduced by dust-free models ($E(B-V) = 0.0$) with star formation decay timescales between $\tau = 10$ Myr (instantaneous burst) and $\tau \sim 700$ Myr[6]. While the upper limit on the current average SFRs of DRG/PEs of $50\ M_{\odot}\ \mathrm{yr}^{-1}$ (Figure 3.16) does not help us further constrain the star formation history to a narrower range in τ, the fact that DRG/PEs are still detected at z-band suggests that single stellar population models with small τ are unrealistic (e.g., ages greater than 1 Gyr imply > 100 e-folding

[6]We rule out ages that are greater than the age of the Universe at $z \sim 2.2$, giving an upper limit on the age of ~ 3 Gyr.

times for the instantaneous burst model making such an object undetected at z-band). If there is ongoing low level star formation activity, then a two-component model with a underlying old stellar population and a recent star formation episode may be required (e.g., Yan et al. 2004).

The red $(z-K)_{\rm AB} > 3$ colors of BzK/PE galaxies can be reproduced by models with $\tau \sim 10-300$ Myr (for τ much larger than 300 Myr, the models over predict the current star formation rate). The X-ray data indicate that these BzK/PE galaxies have an average current SFR of $\sim 28\ M_{\odot}\ {\rm yr}^{-1}$. For an age of 1 Gyr and $\tau = 300$ Myr, this implies an "initial" SFR of $\sim 800\ M_{\odot}\ {\rm yr}^{-1}$ at $z \sim 2.4$. This initial SFR is comparable to that of SMGs and the implied formation redshift is close to the median redshift of SMGs ($z \sim 2.2$), suggesting SMGs could be plausible progenitors of BzK/PE galaxies if the single component model correctly described the star formation histories of these galaxies (e.g., Cimatti et al. 2004). The formation redshifts can be pushed back in time to significantly earlier epochs $z \gtrsim 3.5$ if one assumes a more physically motivated "truncated" star formation history that models the effects of feedback in halting star formation (Daddi et al. 2005b). Nonetheless, the simplistic example above illustrates how X-ray estimates of the bolometric SFRs of galaxies can be combined with the results of stellar population modeling to indicate the likely progenitors of such galaxies. In summary, we have demonstrated the utility of stacked X-ray data as a powerful constraint on the results from stellar population modeling. The X-ray data indicate that galaxies with $(z-K)_{\rm AB} \gtrsim 3$ have SEDs that are consistent with declining star formation history models. Other studies also show that the SEDs of BzK/PE galaxies can be adequately described by declining star formation history models (e.g., Daddi et al. 2005b). The deep X-ray data confirm these results and further allow us to constrain the current SFRs of passively evolving and star-forming galaxies independent of the degeneracies associated with stellar population modeling.

3.4.2.3 Space Densities

To conclude this section, we note that objects selected by their $J-K_{\rm s}$ colors appear to include a substantial number of passively evolving galaxies at redshifts $z \gtrsim 2$ (although, as we pointed out above, the $(z-K)_{\rm AB}$ color may be a more effective means of determining *which* DRGs are passively evolving). The space density implied by the 4 BzK/PE galaxies

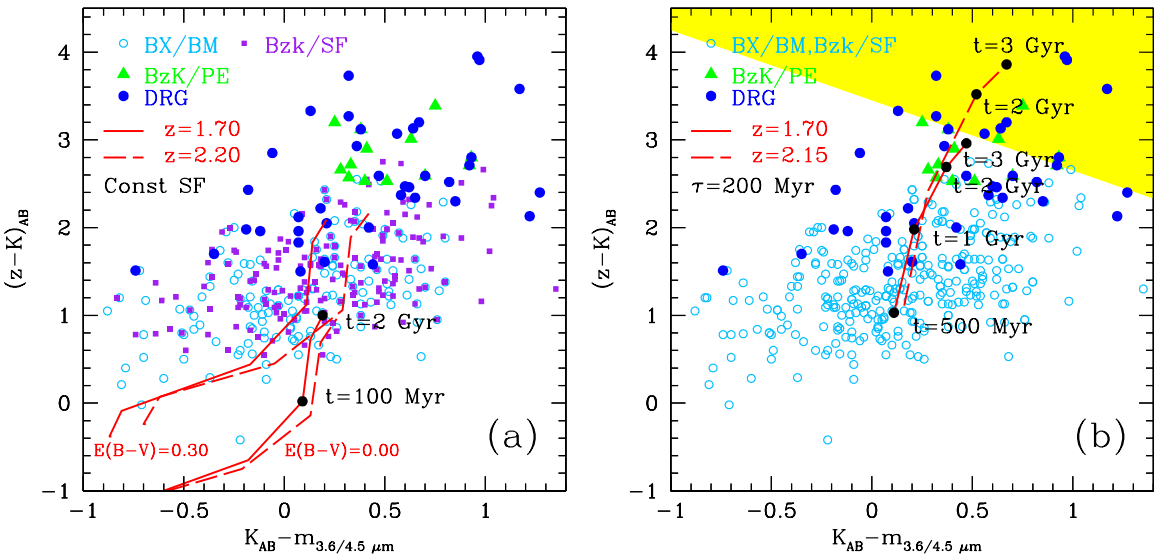

Figure 3.18 (a) $(z-K)_{\rm AB}$ versus $(K-m_{3.6/4.5\mu{\rm m}})_{\rm AB}$ colors for $K_{\rm s}<21$ galaxies in the BX/BM, BzK/SF, BzK/PE, and DRG samples. Also shown are Bruzual & Charlot (2003) spectral templates for ages 1 Myr to 3 Gyr at the mean redshifts of the BX ($\langle z\rangle\sim2.2$) and BM ($\langle z\rangle\sim1.7$) samples, assuming constant star formation, $E(B-V)=0.0$ and 0.3, and the Calzetti et al. (2000) reddening law. The models assume a Salpeter IMF from $0.1-100$ $M_\odot$ and solar metallicity. The photometric scatter is large given that we include galaxies with IRAC uncertainties up to 0.5 mag, and this accounts for the large spread in the $(K-m_{3.6/4.5\mu{\rm m}})_{\rm AB}$ colors of the star-forming candidates; (b) same as (a) except we show the spectral templates for a model with $\tau=200$ Myr and $E(B-V)=0.0$. The shaded region selects IRAC Extremely Red Objects (IEROs; Yan et al. 2004).

with $(z-K)_{\rm AB} > 3$ and $K_{\rm s} < 21$ is $\sim 3 \times 10^{-5}$ Mpc^{-3}, assuming a boxcar (or top-hat) selection function between redshifts $1.4 < z < 2.0$ and an area of ~ 72.3 arcmin^2. If we include all 17 BzK/PE galaxies (i.e., including those with $(z-K)_{\rm AB} < 3$ and those four that are directly detected in X-rays) with $K_{\rm s} < 21$, we find a space density of 1.3×10^{-4} Mpc^{-3}. Given the strong clustering observing for BzK/PE galaxies (e.g., Daddi et al. 2005b), our estimate is in good agreement with the value of 1.8×10^{-4} Mpc^{-3} obtained for the Daddi et al. (2005b) sample of *bona fide* BzK/PE objects in the Hubble Ultra Deep Field (UDF), an area that is 6 times smaller than the area considered in our analysis (i.e., 12.2 arcmin^2 in Daddi et al. (2005b) versus 72.3 arcmin^2 considered here).

All of the BzK/PE galaxies would have been detected with $K_{\rm s} < 21$ and $(z-K)_{\rm AB} > 3$, assuming the PE model shown in Figure 3.18b, if they were at the mean redshift assumed for DRG/PEs of $\langle z \rangle = 2.2$. The space density of the 13 DRG/PEs with $(z-K)_{\rm AB} > 3$ is $\sim 9 \times 10^{-5}$ to $K_{\rm s} = 21$, assuming a boxcar selection function between between redshifts $2.0 < z < 2.6$ and an area of ~ 72.3 arcmin^2. Here, we have assumed that the range in redshifts of DRG/PEs ($2.0 < z < 2.6$) is similar to that of all DRG galaxies based on the spectroscopic redshift distribution shown in Figure 3.1. Our estimate of the DRG/PE space density is comparable to that obtained by Labbé et al. (2005) after restricting their sample to $K_{\rm s} < 21$ (yielding 1 object over ~ 5 arcmin^2), and assuming a volume between redshifts $2.0 < z < 2.6$).

It is worth noting that the BzK/PE and DRG/PE populations appear to be highly clustered (e.g., Daddi et al. 2005b; van Dokkum et al. 2004) and this will likely affect their density estimates over small volumes. While the space densities derived here are in rough agreement with other studies, our estimates have been derived over a much larger volume (by a factor of $6-14$) than any previous study and will be less susceptible to variations in density due to clustering. We caution the reader that the density estimates may still be uncertain given that the redshift distribution of DRGs with $z \gtrsim 2.6$ is not well sampled, even in the large *spectroscopic* dataset of DRGs considered here.

Taken at face value, the density estimates derived above suggest a significant presence of passively evolving $K_{\rm s} < 21$ galaxies at redshifts $z \gtrsim 2$. This result contrasts with that of Daddi et al. (2005b) who argue for a rapid decrease in the number density of passively evolving galaxies at redshifts $z \gtrsim 2$ based on BzK/PE selection. The dropoff in space

density of passively evolving galaxies at redshifts $z \gtrsim 2$, as suggested by Daddi et al. (2005b), may be an artifact of the BzK/PE selection function that, based on previously published redshift distributions and shown in Figure 3.1, appears to miss passively evolving galaxies at redshifts $z \gtrsim 2$, even when using the very deep B-band of this study. Figure 3.12 shows that all of the DRGs that cluster around the BzK/PE selection window have limits in B-band and very few actually have limits that would for certain place them in the BzK/PE window. Photometric scatter for those galaxies with very faint (or no) B-band detections is likely to be significant for these galaxies. These results suggest that the depth of the B-band data is the determining factor in whether BzK/PE selection culls galaxies with redshifts $z \gtrsim 2$ or not. Because the depth of the photometry is an issue for the BzK/PE selection, it becomes difficult to accurately quantify with a single selection criteria the dropoff in space density of passively evolving galaxies between $z \lesssim 2$ and $z > 2$. We can avoid the need for excessively deep B-band data to select passively evolving galaxies with redshifts $z \gtrsim 2$ by simply selecting them using a single color, $J - K_{\rm s}$ or $(z - K)_{\rm AB}$. The stacked X-ray results show that a subsample of DRGs has very little star formation, suggesting that passively evolving galaxies have a significant presence at epochs earlier than $z = 2$. The inferred ages of DRGs would imply formation redshifts of $z \sim 5$ (Labbé et al. 2005).

We conclude this section by noting that there are several galaxies in the HS1700+643 sample of Shapley et al. (2005), and many more in optically selected samples in general (e.g., Erb et al. 2006c), that have old ages and early formation redshifts similar to those of the passively evolving BzK/PE and DRG/PE galaxies discussed here. In order to reproduce the observed SEDs for such objects, the current SFR must be much smaller (but still detectable in the case of optically selected galaxies) than the past average SFR.

3.4.3 Selecting Massive Galaxies

As discussed above, DRGs with $(z - K)_{\rm AB} > 3$ appear to be passively evolving based on their (lack of) stacked X-ray flux and their colors with respect to models with declining star formation histories. The X-ray data indicate that BzK/PE galaxies also appear to be well described by declining star formation histories, consistent with the SED modeling results of Daddi et al. (2005b). The stellar mass estimates of these PE galaxies will be presented elsewhere. Here, we simply mention that several existing studies of the stellar populations

of BzK/PE and DRG galaxies with $K_{\rm s} < 20$ indicate they have masses $\gtrsim 10^{11}$ M$_\odot$ (e.g., Daddi et al. 2005b; Förster Schreiber et al. 2004b). In addition, Yan et al. (2004) recently analyzed the stellar populations of IRAC-selected Extremely Red Objects (IEROs), selected to have $f_\nu(3.6\mu{\rm m})/f_\nu(z_{850}) > 20$ (or, equivalently, $(z{-}3.6\mu{\rm m})_{\rm AB} > 3.25$). Spectral modeling indicates these sources lie at redshifts $1.6 < z < 2.9$, are relatively old ($1.5 - 3.5$ Gyr), and require an evolved stellar population to fit the observed SEDs. Almost all of the PE galaxies with $(z-K)_{\rm AB} > 3$ satisfy the IERO criteria (shaded region of Figure 3.18b). Furthermore, the $\mathcal{R}$-band detections and limits for PEs with $(z-K)_{\rm AB} > 3$ imply $\mathcal{R}-K_{\rm s} \gtrsim 5.3$, satisfying the ERO criteria.

The inferred stellar masses of the Shapley et al. (2005) sample of optically selected galaxies in the HS1700+643 field are shown in Figure 3.19. For comparison, we also show the inferred stellar masses from the Yan et al. (2004) sample of IEROs.[7] Both the Shapley et al. (2005) and Yan et al. (2004) samples take advantage of the longer wavelength IRAC data to constrain the stellar masses, and the typical uncertainty in mass is $\sim 40\%$ for objects with $M^* < 10^{11}$ M$_\odot$ and $\leq 20\%$ for objects with $M^* > 10^{11}$ M$_\odot$. The IERO stellar masses have been multiplied by 1.7 to convert from a Chabrier to Salpeter IMF. The scatter in Figure 3.19 reflects the large ($\gtrsim 1$ magnitude) variation in the mass-to-light (M/L) ratio for objects with a given rest-frame optical luminosity in the BX and IERO samples. For magnitudes brighter than our DRG completeness limit of $K_{\rm s} = 21$, $\sim 16\%$ of BX galaxies have stellar masses $M^* > 10^{11}$ M$_\odot$. For $K_{\rm s} < 20$ BX galaxies, the fraction with $M^* > 10^{11}$ M$_\odot$ is $\sim 40\%$. So, while optically-selected BX galaxies have a lower *mean* stellar mass than IEROs, there is certainly a subsample of BX galaxies that have masses comparable to the most massive IERO galaxies. We note that the stellar mass distributions of $K_{\rm s} > 21$ BXs and IEROs do not overlap: the $\mathcal{R} - K_{\rm s}$ colors of IEROs are too red for them to be included in the optically-selected sample.

The X-ray stacking results indicate that BX/BM galaxies with $K_{\rm s} < 20$ have prodigious star formation rates, while IEROs (i.e., those DRGs with $(z - K)_{\rm AB} > 3$) have very little star formation. Therefore, a simple interpretation is that optical surveys include objects that are as massive ($M^* > 10^{11}$ M$_\odot$) as those selected in near-IR surveys, with the only requirement that the galaxies have some unobscured star formation. The range of star

[7] H. Yan, private communication

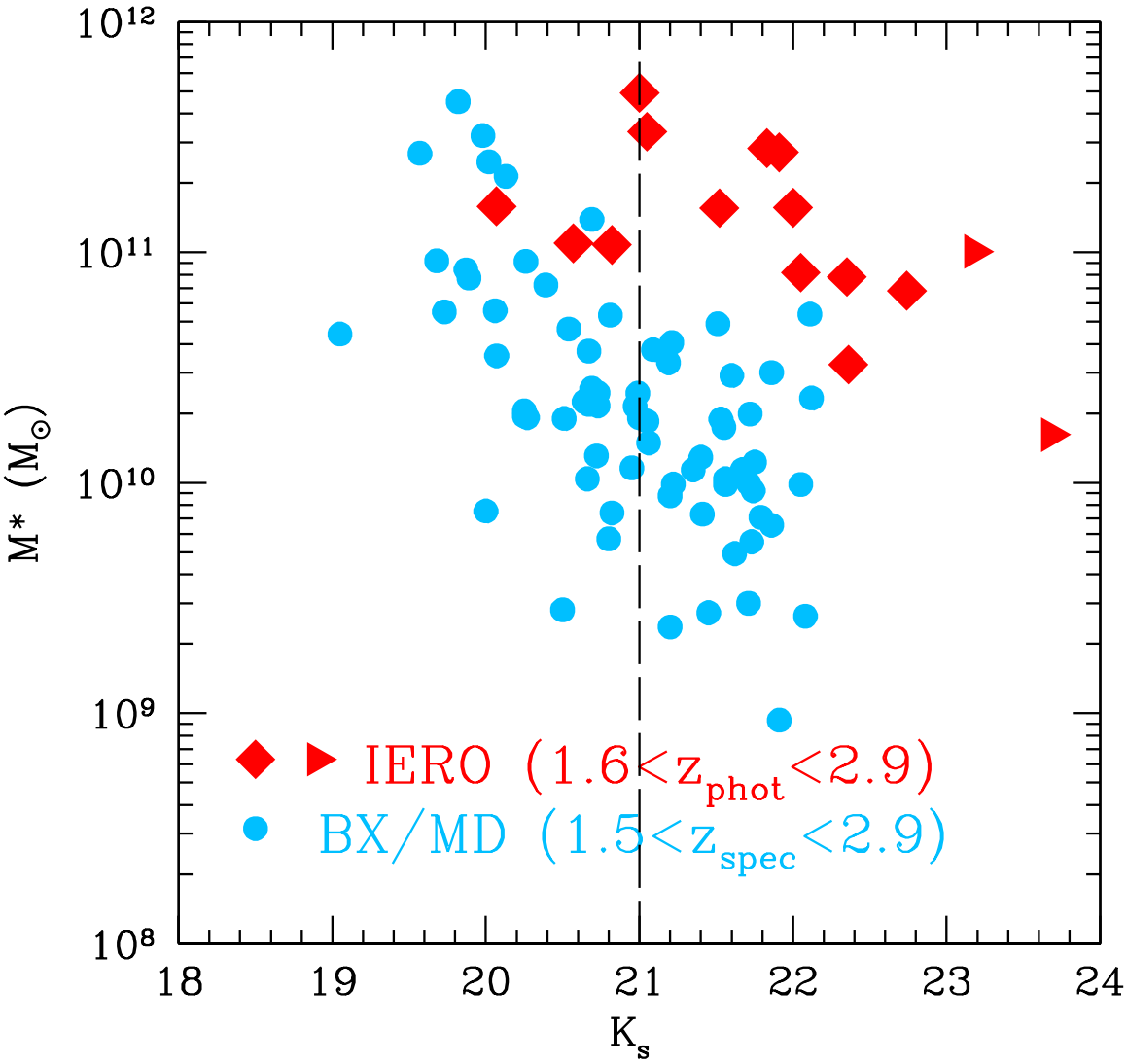

Figure 3.19 Inferred stellar masses of BX and "MD" objects from the Shapley et al. (2005) sample with spectroscopic redshifts $1.5 < z_{\rm spec} < 2.9$ (circles), and IEROs from the Yan et al. (2004) sample with photometric redshifts $1.6 < z_{\rm phot} < 2.9$ (squares, and triangles for those with $K_{\rm s}$-band limits). The stellar masses from Yan et al. (2004) have been multiplied by 1.7 to convert from a Chabrier to Salpeter IMF. The dashed vertical line denotes the limit brighter than which we are complete for IEROs (i.e., those DRGs with $(z-K)_{\rm AB} > 3$). A subset of BX galaxies have stellar masses similar to those of the IERO sample. The scatter in stellar masses reflects at least a magnitude variation in the M/L ratio of BX/MD and IERO objects at a given rest-frame optical luminosity.

formation rates (uncorrected for extinction) found for BX/BM galaxies is $3 - 60\ M_{\odot}\ \mathrm{yr}^{-1}$, and it is likely that massive galaxies with at least a little unobscured star formation can be BX/BM selected. This may be the only significant difference between optical and near-IR selected massive galaxies, and the difference in SFR may be temporal. These criteria typically fail to select passively evolving galaxies at $z \sim 2$ as they have already settled to a quiescent stage. This does not mean that such massive galaxies will never appear in optical surveys. For example, a subsequent accretion event at $z < 2$ could elevate the star formation activity in an otherwise passively evolving massive galaxy, thus bringing it into the optical sample. Nonetheless, the DRG and BzK/PE criteria add to the census of galaxies at $z \sim 2$ by selecting passively evolving galaxies that have stellar masses similar to the most massive galaxies selected in the rest-frame UV.

3.4.4 Star Formation Rate Density at $z \sim 2$

3.4.4.1 Contribution from Optical and Near-IR Selected Samples

We can roughly estimate the contribution of BX/BM, BzK/SF, and DRG/SF galaxies to the extinction-free star formation rate density (SFRD) at $z \sim 2$.[8] The BzK/SF criteria are designed to select galaxies with redshifts $1.4 < z < 2.6$. The similarity in surface densities, volumes probed, and SFRs of galaxies in the BzK/SF and BX/BM samples implies that their contribution to the SFRD will be comparable for objects with $K_{\mathrm{s}} < 22$. The redshift distribution of $K_{\mathrm{s}} < 21$ DRGs from within our own sample is reasonably well defined over this redshift range (cf., Figure 3.1), so we can estimate the added contribution of $\sim 80\%$ of the DRGs with redshifts $2.0 \lesssim z < 2.6$ to the SFRD between redshifts $1.4 < z < 2.6$. Figure 3.20 and Table 3.5 show the cumulative contribution to the SFRD of BzK/SF, BX/BM, and DRG/SF galaxies. The points in Figure 3.20 are not independent of each other due to the overlap between the samples (e.g., Figure 3.10). Also shown in Figure 3.20 by the shaded region is the inferred total SFRD assuming the overlap fractions of Figure 3.10 and counting all objects once. The results indicate that BX/BM selection would miss approximately one-third of the total SFRD from BX/BM and BzK/SF galaxies

[8] Although the BzK/PE galaxies do have detectable X-ray emission (e.g., Figure 3.16), their contribution to the SFRD is minimal given that their space density is a factor of 5 smaller than that of the BzK/SF and BX/BM galaxies to $K_{\mathrm{s}} = 21$ in the redshift range $1.4 < z < 2.0$.

to $K_{\rm s} = 22$ and DRG/SF $K_{\rm s} < 21$ galaxies combined. We remind the reader that much of the incompleteness of the BX/BM sample with respect to that of the BzK/SF sample (and vice versa) results from photometric scattering (e.g., Figures 3.11 and 3.12). Monte Carlo simulations can be used to quantify the biases of such photometric inaccuracy and thus correct for incompleteness (e.g., Reddy et al. 2006a). The total SFRD in the interval $1.4 < z < 2.6$ for BX/BM and BzK/SF galaxies to $K_{\rm s} = 22$ and DRG/SF galaxies to $K_{\rm s} = 21$, taking into account the overlap between the samples, is $\sim 0.10 \pm 0.02$ $M_{\odot}$ yr^{-1} Mpc^{-3}. Approximately 30% of this comes from galaxies with $K_{\rm s} < 20$ (Table 3.5). Optically-selected galaxies to $\mathcal{R} = 25.5$ and $K_{\rm s} = 22.0$ and BzK/SF galaxies to $K_{\rm s} = 22.0$ (with significant overlap between the two samples) account for $\sim$ 87% of the total SFRD quoted above. DRGs to $K_{\rm s} = 21$ that are not selected by the BX/BM or BzK/SF criteria contribute the remaining $\sim$ 13%. We note that the number $\sim 0.10 \pm 0.02$ $M_{\odot}$ yr^{-1} Mpc^{-3} does not include the five radio-selected SMGs to $S_{850\mu{\rm m}} \gtrsim 5$ mJy that are near-IR and/or optically-selected since we removed the directly detected hard-band X-ray sources in computing the SFRD. If we add these five radio-selected SMGs that are present in the optical and near-IR samples (all of which have $K_{\rm s} < 21$), then the total SFRD contributed by the BX/BM and BzK/SF objects to $K_{\rm s} = 22.0$ and DRG/SF galaxies to $K_{\rm s} = 21.0$ is $\sim 0.15 \pm 0.03$ $M_{\odot}$ yr^{-1} Mpc^{-3} (see next section).

3.4.4.2 Contribution from Radio-Selected Submillimeter Galaxies

We conclude this section by briefly considering the contribution of radio-selected submillimeter galaxies (SMGs) with $S_{850\mu{\rm m}} \gtrsim 5$ mJy to the SFRD. All but one of the radio-selected SMGs summarized in Table 3.4 are directly detected in either the soft- or hard-band and are likely associated with AGN. Stacking the X-ray emission for the five radio-selected SMGs with redshifts $1.4 < z < 2.6$ in Table 3.4 yields an average inferred SFR of ~ 2900 $M_{\odot}$ yr^{-1}, and this value should be regarded as an upper limit given that the X-ray emission is likely contaminated by AGN. On the other hand, the average bolometric luminosity of the five SMGs, as derived from their submillimeter flux, is $\langle L_{\rm bol} \rangle \sim 9 \times 10^{12}$ L$_{\odot}$. If we assume that 30% of $L_{\rm bol}$ arises from AGN (e.g., Chapman et al. 2005; Alexander et al. 2005), then the implied SFR is ~ 1000 $M_{\odot}$ yr^{-1}. If we take at face value the assertion that 30% of the bolometric luminosity of submillimeter galaxies comes from AGN, then this means the

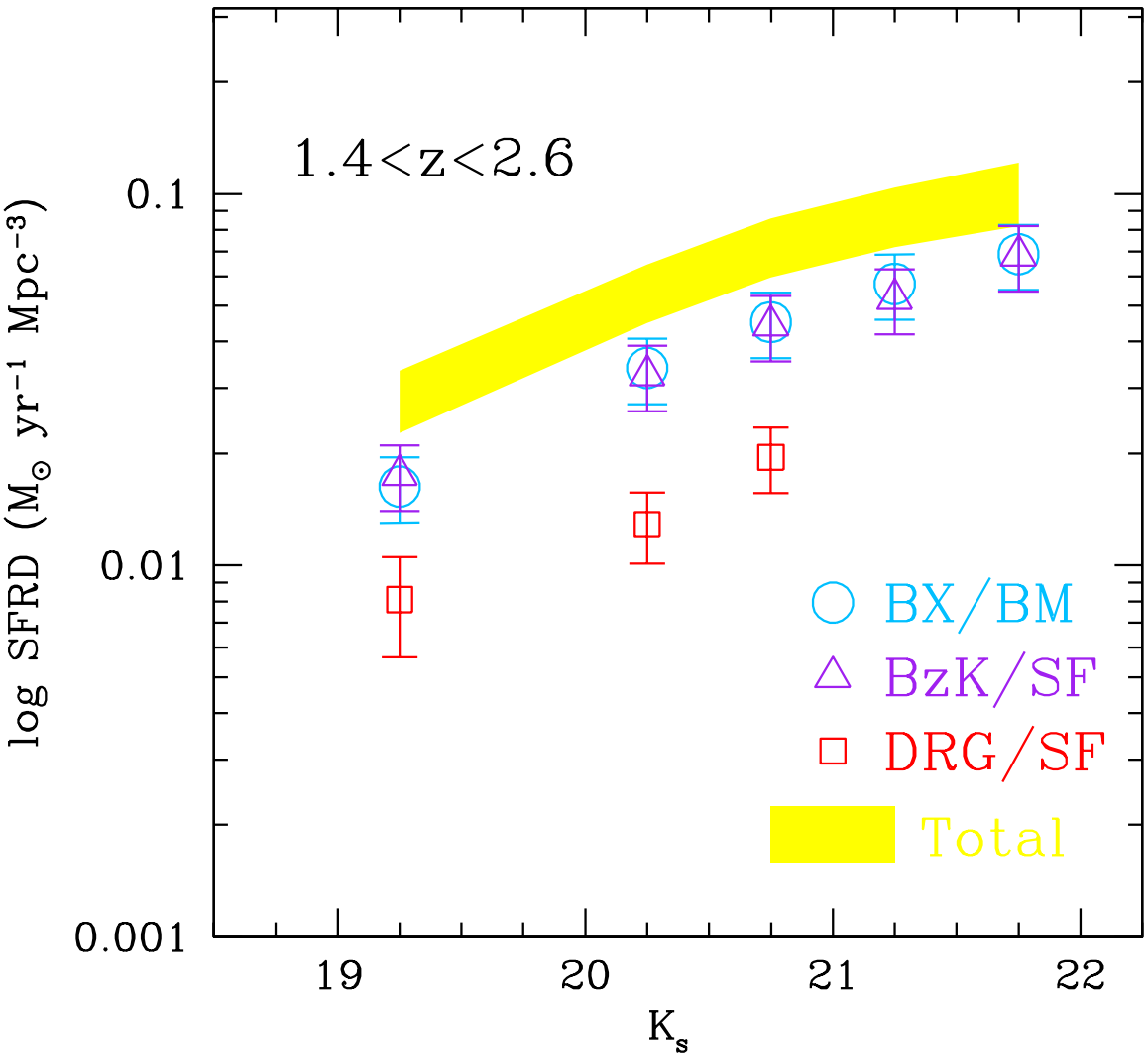

Figure 3.20 *Cumulative* star formation rate density (SFRD) as a function of $K_{\rm s}$ magnitude for BX/BM (circles), BzK/SF (triangles), and DRG/SF (squares) galaxies with redshifts $1.4 < z < 2.6$. The points are not independent of each other given the overlap between the samples. The shaded region denotes the total cumulative SFRD when counting overlap objects once. The total SFRD to $K_{\rm s} = 22$ includes DRGs with $K_{\rm s} < 21$. The error bars reflect the Poisson error and uncertainty in star formation rate added in quadrature, but do not reflect systematic errors associated with, e.g., photometric scattering.

X-ray emission would overestimate the average SFR of SMGs by a factor of ~ 3. In other words, only one-third of the X-ray emission from SMGs would result from star formation, and the remaining two-thirds would come from AGN.

To determine the *additional* SFRD provided by radio-selected SMGs with $S_{850\mu\mathrm{m}} \gtrsim 5$ mJy, we must account for their overlap with the optical and near-IR samples. The data in Table 3.4 show that there are four of nine SMGs that are not selected by the optical and/or near-IR criteria. All four of these galaxies have relatively low redshifts $z \lesssim 1$ and will obviously not contribute to the SFRD between redshifts $1.4 < z < 2.6$. Alternatively, of the five SMGs that are spectroscopically confirmed to lie at redshifts $1.4 < z < 2.6$, *all* are selected by either the BX/BM, BzK/SF, or DRG criteria (and sometimes by more than one set of criteria).

Because of the non-uniform coverage of the submillimeter observations, we must rely on the published submillimeter number counts to estimate the effective surface density probed by the nine radio-selected SMGs with $S_{850\mu\mathrm{m}} \gtrsim 5$ mJy listed in Table 3.4. According to the models shown in Figure 4 of Smail et al. (2002), we should expect to find ~ 0.25 sources arcmin^{-2} to $S_{850\mu\mathrm{m}} \sim 5$ mJy. Neglecting cosmic variance, the nine observed radio-selected SMGs to $S_{850\mu\mathrm{m}} \sim 5$ mJy then imply an effective surface area of ~ 36 arcmin^2. The spectroscopic redshifts compiled in Table 2 of Chapman et al. (2005) indicate that $\approx 44\%$ of the radio-selected SMGs to $S_{850\mu\mathrm{m}} \sim 5$ mJy lie at redshifts outside the range $1.4 < z < 2.6$. If we assume a Poisson distribution of sources, then the total number of SMGs to $S_{850\mu\mathrm{m}} \sim 5$ mJy could be as high $9 + \sqrt{9} = 12$. If we assume that the fraction of interlopers among the three unobserved objects is similar to the fraction of interlopers among objects that are observed, then we expect an upper limit of two SMGs with $S_{850\mu\mathrm{m}} \sim 5$ mJy that are unobserved and that lie between redshifts $1.4 < z < 2.6$. If we conservatively assume that these two sources are not selected by the optical and/or near-IR criteria, and they have bolometric SFRs of $\sim 1500\ M_\odot\ \mathrm{yr}^{-1}$ (similar to the average SFR found for the five spectroscopically confirmed radio-selected SMGs in Table 3.4), then the inferred *additional* SFRD provided by these two SMGs would be $\sim 3000\ M_\odot\ \mathrm{yr}^{-1}$ divided by the volume subtended by 36 arcmin^2 at redshifts $1.4 < z < 2.6$, or $\sim 0.022\ M_\odot\ \mathrm{yr}^{-1}\ \mathrm{Mpc}^{-3}$. We note that this should be treated as an upper limit for several reasons. First, we have assumed the maximum number of unobserved sources allowed by Poisson statistics. Second,

we have assumed an interloper fraction among these unobserved sources that is the same for the observed sources. In general, one might expect the contamination fraction to be higher among the general SMG population to $S_{850\mu\mathrm{m}} \sim 5$ mJy (where an accurate radio position may not be known) than would be inferred from the radio-selected SMG surveys. Finally, we have assumed that all of the unobserved sources cannot be selected by their optical and/or near-IR colors. Neglecting any overlap, radio-selected SMGs to $S_{850\mu\mathrm{m}} \sim 5$ mJy contribute $\sim 0.05\ M_{\odot}\ \mathrm{yr}^{-1}\ \mathrm{Mpc}^{-3}$ to the SFRD between redshifts $1.4 < z < 2.6$. However, our conservative calculation indicates that radio-selected SMGs to $S_{850\mu\mathrm{m}} \sim 5$ mJy that are not selected by optical (BX/BM) and/or near-IR (BzK and/or DRG) surveys make a small ($\lesssim 0.022\ M_{\odot}\ \mathrm{yr}^{-1}\ \mathrm{Mpc}^{-3}$ or $\lesssim 15\%$) *additional* contribution to the SFRD between redshifts $1.4 < z < 2.6$.

3.5 Conclusions

We have taken advantage of the extensive multi-wavelength data in the GOODS-North field to select galaxies at $z \sim 2$ based on their optical and near-IR colors and to compare them in a consistent manner. Our own ground-based optical and near-IR images are used to select galaxies based on their $U_{\mathrm{n}}G\mathcal{R}$, BzK, and $J - K_{\mathrm{s}}$ colors. Additional rest-frame UV spectroscopy for 25% of optically selected candidates allows us to quantify the redshift selection functions for the various samples. We use the deep *Chandra* 2 Ms X-ray data to determine the influence of AGN and estimate bolometric SFRs for galaxies in the optical and near-IR samples. We also use the deep *Spitzer*/IRAC data in the GOODS-North field in considering the stellar populations and masses of galaxies selected in different samples. Our analysis employs the same multi-wavelength data for a single field (GOODS-North), using the same photometric measurement techniques, for a consistent comparison between galaxies selected by their optical and near-IR colors. Our main conclusions are as follows:

1. Star-forming galaxies at $z \sim 2$ selected by their $U_{\mathrm{n}}G\mathcal{R}$ colors (i.e., BX/BM galaxies) and their BzK colors (i.e., BzK/SF galaxies) have optical and near-IR color distributions that indicate significant overlap ($\sim 70-80\%$) between the two samples. Photometric scatter could account for the colors of at least half of those galaxies missed by one set of criteria or the other. The BzK/SF criteria are less efficient in selecting (younger) $K_{\mathrm{s}} > 21$ galaxies at redshifts $1.4 < z < 2.6$, while the BX/BM criteria are less efficient in selecting near-IR

bright (e.g., $K_{\rm s} < 20$) objects. Distant red galaxies (DRGs; including both reddened star-forming and passively evolving galaxies) selected to have $J - K_{\rm s} > 2.3$ show near-IR colors that are $1-1.5$ magnitudes redder than for samples of star-forming galaxies. Criteria aimed at selecting passively evolving galaxies based on their BzK colors (i.e., BzK/PE galaxies) by design have red near-IR colors, but we find that the redshift distributions of BzK/PE galaxies and DRGs have very little overlap.

2. The deep X-ray data show that almost all of the directly detected X-ray sources in the samples have hard-band emission and X-ray/optical flux ratios indicating they are likely AGN. Much of this AGN contamination occurs for magnitudes $K_{\rm s} < 20$. We identify five objects that are detected in the soft-band X-ray data and are likely star-forming galaxies based on their absence in the hard-band X-ray data, optical magnitudes $R > 22$, and absence of obvious AGN features for those with spectra. We stacked the X-ray data for all likely star-forming galaxies (i.e., those undetected in X-rays and the five galaxies discussed above), excluding likely AGN. The stacking analysis shows that the star formation rate (SFR) distributions of BX/BM and BzK/SF galaxies and DRGs are very similar as a function of $K_{\rm s}$ magnitude. Galaxies with $K_{\rm s} < 20$ have average SFRs of $\sim 120\ M_{\odot}\ {\rm yr}^{-1}$, a factor of two to three higher than $K_{\rm s} > 20.5$ galaxies. Previous studies point to a similarity in the metallicities, clustering, and stellar masses of $K_{\rm s} < 20$ optical and near-IR selected galaxies (e.g., Shapley et al. 2004, Adelberger et al. 2005a). In this work we show that the bolometric SFRs of optical and near-IR selected galaxies are also very similar when subjected to a common near-IR magnitude.

3. Near-IR selection of star forming galaxies should be more immune to the effects of dust obscuration than optical surveys. However, the BX/BM, BzK/SF, and DRG samples show very similar SFRs as a function of near-IR color for galaxies with $(z - K)_{\rm AB} < 3$. The SFRs inferred for BzK/SF galaxies that are not optically-selected are very similar to BzK/SF galaxies that do satisfy the optical criteria, suggesting that star-forming galaxies in near-IR samples that are missed by optical criteria do not harbor large numbers of heavily reddened galaxies. Furthermore, the optical and BzK/SF samples host an approximately equal number of submillimeter galaxies (SMGs).

4. We identify a population of extremely red BzK and DRG galaxies with $(z-K)_{\rm AB} \gtrsim 3$. The stacked X-ray data indicate these red galaxies have little, if any, current star formation.

The absence of X-ray emission from these objects also suggests that low luminosity AGN and low mass X-ray binaries contribute little X-ray emission in star-forming galaxies compared with the emission produced from more direct tracers of the current star formation rate, such as high mass X-ray binaries. We further demonstrate the utility of deep X-ray data to constrain the stellar populations of these extremely red galaxies, and find that they must be described by declining star formation histories. Almost all of these passively evolving galaxies satisfy the IERO criteria of Yan et al. (2004). We find that optical selection includes a subset of galaxies with stellar masses similar to those inferred for IEROs, but which are forming stars at a prodigious rate. The stellar mass estimates from SED modeling (e.g., Yan et al. 2004, Förster Schreiber et al. 2004b) and bolometric SFR estimates from the deep X-ray data (this work) suggest that the presence or absence of star formation may be the only significant difference between optical and near-IR selected massive galaxies ($M^* > 10^{11}$ M$_\odot$), and the difference in SFR may be temporal.

5. We find evidence for a significant presence of passively evolving galaxies at redshifts $z \gtrsim 2$ compared with their space density at lower redshifts, $1.4 < z < 2.0$. Our analysis suggests that a single color technique using the $(z - K)_{\rm AB}$ or $J - K_{\rm s}$ color allows for a more practical method selecting passively evolving galaxies with $z \gtrsim 2$ than the BzK/PE criteria, as the latter would require excessively deep B-band data to accurately determine the space densities of passively evolving galaxies at $z \gtrsim 2$.

6. Finally, we consider the contribution of optical and near-IR selected galaxies to the SFRD at $z \sim 2$, taking into account the overlap between the samples and their respective redshift distributions. We find that BX/BM and BzK/SF galaxies to $K_{\rm s} = 22$, and DRG galaxies to $K_{\rm s} = 21$, account for an SFRD of $\sim 0.10 \pm 0.02$ $M_\odot$ yr^{-1} Mpc^{-3} between redshifts $1.4 < z < 2.6$. Approximately 87% of this total comes from optically-selected galaxies to $\mathcal{R} = 25.5$ and $K_{\rm s} = 22$ and near-IR selected BzK galaxies to $K_{\rm s} = 22$, and 13% from $K_{\rm s} < 21$ DRGs not selected by the BX/BM or BzK criteria. Of the known radio-selected SMGs to $S_{850\mu{\rm m}} \sim 4$ mJy in the GOODS-N field with redshifts $1.4 < z < 2.6$, $\gtrsim 80\%$ could be selected by the BX/BM, BzK, and/or DRG criteria.

We thank Scott Chapman for discussions regarding submillimeter galaxies in the GOODS-North field. Haojing Yan kindly provided stellar mass estimates for IEROs. We thank David Alexander for his suggestions regarding the use of the X-ray data, and Amy Barger for her

comments regarding Table 3.4. NAR, DKE, and CCS are supported by grant AST 03-07263 from the National Science Foundation and by the David and Lucile Packard Foundation. AES and KLA are supported by the Miller Foundation and the Carnegie Institute of Washington, respectively.

Table 3.1. Interloper Contamination of the BX/BM Sample

K_s Range	N_{phot}[a]	N_{spec}[b]	$N_{z<1}$[c]	$f_{z<1}$[d]
$K_s \leq 20.0$	61	18	7	0.39
$20.0 < K_s \leq 20.5$	58	23	2	0.09
$20.5 < K_s \leq 21.0$	82	30	3	0.10
$21.0 < K_s \leq 21.5$	101	32	2	0.06
$21.5 < K_s \leq 22.0$	141	29	3	0.10

[a]Number of photometric BX/BM candidates.

[b]Number of candidates with spectroscopic redshifts.

[c]Number of interlopers.

[d]Interloper fraction.

Table 3.2. Sample Properties

K_s Range	Sample	N_T[a]	N_X[b]	N_S[c]	$\langle z \rangle$[d]	$\langle L_{2.0-10\,\mathrm{keV}} \rangle$ ($\times 10^{41}$ ergs s^{-1})	$\langle \mathrm{SFR_x} \rangle$ ($M_\odot$ yr^{-1})
$18.0 < K_s \leq 20.0$	BX/BM[e]	11	4	10 (7)	1.75 (1.80)	7.13 ± 0.88 (4.95 ± 1.15)	143 (99)
	BzK/SF	77	24	45 (42)	1.97 (2.01)	5.39 ± 0.46 (4.68 ± 0.48)	108 (94)
	BzK/PE	14	3	11	1.74	3.07 ± 0.84	61
	DRG	20	5	14	2.48	5.26 ± 1.28	105
$20.0 < K_s \leq 20.5$	BX/BM [e]	21	0	21	2.03	4.89 ± 0.79	98
	BzK/SF	57	5	56 (55)	2.01 (2.01)	3.96 ± 0.40 (3.87 ± 0.41)	79 (77)
	BzK/PE	0	0	...	...	...	...
	DRG	20	7	13	2.48	2.32 ± 1.30	46
$20.5 < K_s \leq 21.0$	BX/BM [e]	27	0	27	1.99	2.11 ± 0.56	42
	BzK/SF	87	3	82 (81)	2.01 (2.01)	2.32 ± 0.30 (2.20 ± 0.30)	46 (44)
	BzK/PE	3	1	2	1.74	2.07 ± 1.54	41
	DRG	33	7	26	2.48	1.90 ± 0.86	38
$21.0 < K_s \leq 21.5$	BX/BM [e]	31	0	31	2.04	2.95 ± 1.01	59
	BzK/SF	99	2	97	2.01	2.76 ± 0.28	55
$21.5 < K_s \leq 22.0$	BX/BM [e]	26	0	26	2.22	1.43 ± 0.77	29

Table 3.2—Continued

K_s Range	Sample	N_T[a]	N_X[b]	N_S[c]	$\langle z \rangle$[d]	$\langle L_{2.0-10\,\mathrm{keV}} \rangle$ ($\times 10^{41}$ ergs s^{-1})	$\langle \mathrm{SFR_x} \rangle$ ($M_\odot$ yr^{-1})
	BzK/SF	148	0	148	2.01	2.78 ± 0.73	56
$22.0 < K_s \leq 22.5$	BX/BM [f]	93	0	93	2.04	1.13 ± 0.25	23
	BzK/SF	77	0	77	2.01	0.49 ± 0.29	10

*Note.—Values in parentheses are when we exclude all directly detected X-ray sources, including ones that may be star-forming galaxies (Table 3.3).

[a]Total number of sources in sample.

[b]Number of direct X-ray detections, corresponding to a minimum 3 σ flux of $f_{0.5-2.0\ \mathrm{keV}} \sim 2.5 \times 10^{-17}$ erg s^{-1} cm^{-2}.

[c]Number of stacked sources.

[d]Mean redshift of stacked sample. Sources without a spectroscopic redshift are assigned the mean redshift of the sample to which they belong, where the mean redshifts for the sample are specified in Figure 3.1.

[e]We only consider BX/BM galaxies that are spectroscopically confirmed to lie at redshifts $z > 1$, $\sim 25\%$ of the photometric sample of BX/BM galaxies.

[f]Photometric BX/BM galaxies.

Table 3.3. Possible Star-Forming Direct X-ray Detections

α (J2000.0)	δ (J2000.0)	Sample	z	$f_{0.5-2.0\ \mathrm{keV}}$[a] ($\times 10^{-15}$ erg s^{-1} cm^{-2})	K_s (Vega mag)	R[a] (mag)	$\log f_\mathrm{X}/f_\mathrm{R}$[b]
12:36:21.95	62:14:15.5	BzK/SF	1.38	0.02	18.95	23.1	-1.96
12:36:52.75	62:13:54.8	BX/BM	1.36	0.03	19.54	22.1	-2.18
12:36:53.46	62:11:40.0	BX/BM;BzK/SF	...	0.11	18.65	22.7	-1.38
12:36:56.89	62:11:12.1	BzK/SF	...	0.02	20.50	23.8	-1.68
12:37:03.70	62:11:22.6	BX/BM;BzK/SF	1.72	0.04	19.92	23.4	-1.54

[a]Soft-band fluxes are from Alexander et al. (2003) and *Cousins* R magnitudes are from Barger et al. (2003).

[b]Defined as $\log f_\mathrm{X}/f_\mathrm{R} = \log f_\mathrm{X} + 5.50 + R/2.5$ (Hornschemeier et al. 2001).

Table 3.4. Properties of Submillimeter Galaxies with K_s-band Data

α[a] (2000.0)	δ[a] (2000.0)	$S_{850\mu m}$[b] (mJy)	K_s (Vega mag)	z[c]	$f_{SB} \times 10^{-15}$[d] (erg s^{-1} cm^{-2})	$f_{HB} \times 10^{-15}$[d] (erg s^{-1} cm^{-2})	BX/BM[e]	BzK/SF[e]	DRG[e]	L_{bol}[f] ($\times 10^{12}$ L$_\odot$)
12:36:21.27	62:17:08.4	7.8 ± 1.9	20.62	1.988	...	...	yes	yes	yes	13.5
12:36:22.65	62:16:29.7	7.7 ± 1.3	19.85	2.466	...	1.14	yes	yes	no	11.6
12:36:29.13	62:10:45.8	5.0 ± 1.3	17.65	1.013	0.17	2.23	no	no	no	1.2
12:36:35.59	62:14:24.1	5.5 ± 1.4	18.62	2.005	0.21	2.48	no	yes	no	8.1
12:36:36.75	62:11:56.1	7.0 ± 2.1	18.41	0.557	1.62	2.01	no	no	no	0.12
12:36:51.76	62:12:21.3	4.6 ± 0.8	18.34	0.298	0.34	2.65	no	no	no	0.08
12:37:07.21	62:14:08.1	4.7 ± 1.5	20.05	2.484	0.09	0.91	no	no	yes	7.5
12:37:12.05	62:12:12.3	8.0 ± 1.8	20.65	2.914	0.03	0.37	no	no	yes	5.5
12:37:21.87	62:10:35.3	12.0 ± 3.9	17.59	0.979	0.05	2.11	no	no	no	0.53
12:37:11.98	62:13:25.7	4.2 ± 1.4	20.61	1.992	...	1.01	yes	yes	no	4.9
12:37:11.34	62:13:31.0	4.4 ± 1.4	18.65	1.996[g]	0.07	0.52	no	yes	no	...

Table 3.4—Continued

α[a] (2000.0)	δ[a] (2000.0)	$S_{850\mu m}$[b] (mJy)	K_s (Vega mag)	z[c]	$f_{SB} \times 10^{-15}$[d] (erg s^{-1} cm^{-2})	$f_{HB} \times 10^{-15}$[d] (erg s^{-1} cm^{-2})	BX/BM[e]	BzK/SF[e]	DRG[e]	L_{bol}[f] ($\times 10^{12}$ L$_\odot$)

[a]Radio coordinates are from Table 2 of Chapman et al. (2005). Five of these sources are also in Wang et al. (2004). The last source listed is only from Wang et al. (2004).

[b]$S_{850\mu m}$ fluxes are from Table 2 of Chapman et al. (2005). Two of the sources are measured by Chapman et al. (2005) to have $S_{850\mu m} \sim 4.6 - 4.7$ mJy, and are measured by Borys et al. (2003) and Wang et al. (2004) to have $S_{850\mu m} > 5$ mJy, and for fairness we include these in the table.

[c]Spectroscopic redshift from Chapman et al. (2005).

[d]Soft- and hard-band fluxes are from Alexander et al. (2003).

[e]This field indicates whether the submillimeter source satisfies the BX/BM, BzK/SF, and DRG selection criteria.

[f]Inferred bolometric luminosity from Chapman et al. (2005). The mean bolometric luminosity of the 6 submillimeter galaxies with spectroscopic redshifts $1.4 < z < 2.6$ is $\langle L_{bol} \rangle \sim 9 \times 10^{12}$ L$_\odot$.

[g]Redshift from Swinbank et al. (2004).

Table 3.5. Cumulative Contributions to the SFRD Between $1.4 < z < 2.6$

K_s Range	Sample[a]	z[b]	ρ[c] (arcmin^{-2})	SFRD[d] ($M_\odot$ yr^{-1} Mpc^{-3})
$K_s \leq 20.0$	BX/BM	1.4–2.6	0.44	0.016 ± 0.008
	BzK/SF	1.4–2.6	0.62	0.018 ± 0.004
	DRG/SF	2.0–2.6	0.15	0.008 ± 0.002
	BzK/SF—BX/BM	1.4–2.6	0.35	0.007 ± 0.002
	DRG/SF—BzK/SF—BX/BM	2.0–2.6	0.08	0.004 ± 0.001
	Total	2.0–2.6	0.87	0.027 ± 0.006
$K_s \leq 20.5$	BX/BM	1.4–2.6	1.13	0.034 ± 0.009
	BzK/SF	1.4–2.6	1.35	0.032 ± 0.006
	DRG/SF	2.0–2.6	0.30	0.013 ± 0.003
	BzK/SF—BX/BM	1.4–2.6	0.55	0.012 ± 0.002
	DRG/SF—BzK/SF—BX/BM	2.0–2.6	0.25	0.009 ± 0.002
	Total	2.0–2.6	1.93	0.055 ± 0.011
$K_s \leq 21.0$	BX/BM	1.4–2.6	2.15	0.045 ± 0.010
	BzK/SF	1.4–2.6	2.34	0.044 ± 0.009
	DRG/SF	2.0–2.6	0.58	0.020 ± 0.004
	BzK/SF—BX/BM	1.4–2.6	0.74	0.014 ± 0.002
	DRG/SF—BzK/SF—BX/BM	2.0–2.6	0.41	0.013 ± 0.002
	Total	2.0–2.6	3.30	0.072 ± 0.014
$K_s \leq 21.5$	BX/BM	1.4–2.6	3.17	0.057 ± 0.013
	BzK/SF	1.4–2.6	3.61	0.052 ± 0.010
	BzK/SF—BX/BM	1.4–2.6	1.71	0.017 ± 0.002
	Total[e]	2.0–2.6	5.29	0.087 ± 0.017

Table 3.5—Continued

K_s Range	Sample[a]	z[b]	ρ[c] (arcmin^{-2})	SFRD[d] ($M_\odot$ yr^{-1} Mpc^{-3})
$K_s \leq 22.0$	BX/BM	1.4–2.6	4.31	0.069 ± 0.015
	BzK/SF	1.4–2.6	4.93	0.068 ± 0.014
	BzK/SF—BX/BM	1.4–2.6	2.55	0.020 ± 0.003
	Total[e]	2.0–2.6	7.27	0.102 ± 0.021

[a]The BzK/SF—BX/BM sample represents the set of objects that are BzK/SF-selected, but not BX/BM-selected. Similarly, the DRG/SF—BzK/SF—BX/BM sample represents the set of DRGs that are not selected by either the BzK/SF or BX/BM criteria.

[b]Redshift range of sample.

[c]Surface density of photometric objects after removing interlopers and directly detected X-ray sources that are likely AGN. The number of BX/BM objects is calculated assuming the spectroscopic and interloper fractions from Table 3.1. The overlap fractions are taken from Figure 3.10. We assume a field area of ~ 72.3 arcmin^2 to compute surface densities.

[d]Assumes the average SFRs shown in Figure 3.15.

[e]This includes the contribution from the DRG/SF—BzK/SF—BX/BM sample for $K_s < 21$.

Chapter 4

STAR FORMATION AND EXTINCTION IN REDSHIFT $z \sim 2$ GALAXIES: INFERENCES FROM *SPITZER* MIPS OBSERVATIONS*†

Naveen A. Reddy,[a] Charles C. Steidel,[a] Dario Fadda,[b] Lin Yan,[b] Max Pettini,[c] Alice E. Shapley,[d] Dawn K. Erb,[e] & Kurt L. Adelberger[f]

[a]California Institute of Technology, MS 105–24,Pasadena, CA 91125

[b]*Spitzer* Science Center, California Institute of Technology, MS 220–6, Pasadena, CA 91126

[c]Institute of Astronomy, Madingley Road, Cambridge CB3 OHA, UK

[d]Department of Astrophysical Sciences, Peyton Hall-Ivy Lane, Princeton, NJ 08544

[e]Harvard-Smithsonian Center for Astrophysics, 60 Garden Street, Cambridge, MA 02138

[f]McKinsey & Company, 1420 Fifth Avenue, Suite 3100, Seattle, WA 98101

*Based, in part, on data obtained at the W. M. Keck Observatory, which is operated as a scientific partnership among the California Institute of Technology, the University of California, and NASA, and was made possible by the generous financial support of the W. M. Keck Foundation. Also based in part on observations made with the *Spitzer Space Telescope*, which is operated by the Jet Propulsion Laboratory, California Institute of Technology under a contract with NASA.

†A version of this chapter was published in *The Astrophysical Journal*, vol. 644.

Abstract

Using very deep *Spitzer* MIPS 24 μm observations, we present an analysis of the bolometric luminosities and UV extinction properties of more than 200 spectroscopically identified, optically selected (BX/BM) $z \sim 2$ galaxies in the GOODS-N field. The large spectroscopic sample of rest-UV selected galaxies is supplemented with photometrically identified near-IR-selected ("BzK" and "DRG") galaxies and sub-mm sources at similar redshifts in the same field, providing a representative collection of relatively massive ($M^* > 10^{10}$ M$_\odot$) galaxies at high redshifts. We focus on the redshift range $1.5 < z < 2.6$, for which the 24 μm observations provide a direct measurement of the strength of the mid-IR PAH features in the galaxy spectra; the rest-frame $5-8.5$ μm luminosities ($L_{5-8.5\mu\mathrm{m}}$) are particularly tightly constrained for the objects in our sample with precise spectroscopic redshifts. We demonstrate, using stacked X-ray observations and a subset of galaxies with Hα measurements, that $L_{5-8.5\mu\mathrm{m}}$ provides a reliable estimate of L_{IR} for most star-forming galaxies at $z \sim 2$. We show that the range of L_{IR} in the optical/near IR-selected samples considered extends from $\simeq 10^{10}$ L$_\odot$ to $> 10^{12}$ L$_\odot$, with a mean $\langle L_{\mathrm{IR}} \rangle \simeq 2 \times 10^{11}$ L$_\odot$. The LIRG population at $z \sim 2$ is essentially the same population of galaxies that are selected by their optical/near-IR colors. Objects with LIRG to ULIRG luminosities are present over the full range of stellar masses in the samples, from 2×10^9 M$_\odot$ to 5×10^{11} M$_\odot$. We use the MIPS 24 μm observations for an independent examination of dust extinction in high redshift galaxies, and demonstrate that, as in the local universe, the obscuration ($\frac{L_{\mathrm{IR}}}{L_{1600}}$) is strongly dependent on bolometric luminosity, and ranges in value from < 1 to ~ 1000 within the sample considered. However, the obscuration is ~ 10 times smaller at a given L_{bol} (or, equivalently, a similar level of obscuration occurs at luminosities ~ 10 times larger) at $z \sim 2$ than at $z \sim 0$. We show that the values of L_{IR} and obscuration inferred from the UV spectral slope β generally agree well with the values inferred from $L_{5-8.5\mu\mathrm{m}}$ for $L_{\mathrm{bol}} < 10^{12}$ L$_\odot$. As found previously by several investigators, for "ultraluminous" objects with $L_{\mathrm{bol}} > 10^{12}$ L$_\odot$ it is common for UV-based estimates to underpredict L_{IR} by a factor of $\sim 10 - 100$. Using the specific star formation rate of galaxies (SFR per unit stellar mass) as a proxy for cold gas fraction, we find a wide range in the evolutionary state of galaxies at $z \sim 2$, from galaxies that have just begun to form stars to those that have already accumulated most of their stellar mass and are about to become, or already are, passively-evolving.

4.1 Introduction

The most direct method currently available for tracing the bolometric luminosities of high redshift star-forming galaxies ($z \gtrsim 2$) has been from their submillimeter emission (e.g., Smail et al. 1997; Hughes et al. 1998; Barger et al. 1998). Unfortunately, current sensitivity limits of bolometers and submillimeter wave interferometers allow for only the most luminous starburst galaxies to be detected at high redshifts via their dust emission. Further compounding the problem is the coarse spatial resolution provided by such instruments, making it difficult to distinguish the counterpart(s) to the submillimeter emission for subsequent followup, although the recently developed method of radio-detection has been a breakthrough in alleviating this problem for most, but not all, bright submillimeter galaxies (e.g., Chapman et al. 2005). Regardless, the dust properties of the vast majority of star-forming galaxies at high redshift remained uninvestigated until recently.

The rest-frame far-infrared (FIR) wavelength region is still inaccessible for the *typical* galaxy at redshifts $z \gtrsim 1$, so we must look to other portions of the spectrum to directly examine dust properties. Our understanding of the mid-IR properties of local and high redshift galaxies advanced considerably with the launch of the *Infrared Space Observatory* (ISO), which was sensitive enough to detect the mid-IR emission of 10^{11} $L_{\odot}$ galaxies at $z \sim 1$ (e.g., Flores et al. 1999; Elbaz et al. 2002; Pozzi et al. 2004; Rowan-Robinson et al. 2004). These observations revealed the almost ubiquitous presence of mid-IR dust emission features in star-forming galaxies in both the local and $z \sim 1$ universe, and suggested the possibility of using the mid-IR dust emission of galaxies as a tracer of bolometric luminosity (Boselli et al. 1998; Adelberger & Steidel 2000; Dale et al. 2000; Helou et al. 2000; Förster Schreiber et al. 2003).

These advances now continue with the highly successful *Spitzer* Space Telescope, providing the same sensitivity as ISO in probing dust emission from 10^{11} $L_{\odot}$ galaxies at $z \sim 2$. The progress made with *Spitzer* is particularly important for studying galaxies at $z \sim 2$ because this epoch was until recently largely uninvestigated, yet is believed to be the most active in terms of star formation and the buildup of stellar and black hole mass (e.g., Dickinson et al. 2003b; Rudnick et al. 2003; Madau et al. 1996; Lilly et al. 1996; Steidel et al. 1999; Shaver et al. 1996; Fan et al. 2001; Di Matteo et al. 2003; Giavalisco et al. 1996). The sensitivity afforded by the *Spitzer* MIPS instrument allows us to examine the *typical*

L^* galaxy at $z \sim 2$, rather than a limited slice of the most luminous population, a problem that, as alluded to before, limits the usefulness of submillimeter observations.

It is fortuitous that the rest-frame mid-IR spectral features observed in local and $z \sim 1$ star-forming galaxies are redshifted into the *Spitzer* IRS spectral and MIPS imaging passbands at $z \sim 2$. The mid-IR spectral region from $3 - 15$ μm is rich with emission lines believed to arise from the stochastic heating of small dust grains by UV photons (see review by Genzel & Cesarsky 2000). These unidentified infrared bands (UIBs) are generally attributed to the C = C and C − H stretching and bending vibrational modes of a class of carbonaceous molecules called polycyclic aromatic hydrocarbons (PAHs; e.g., Puget & Leger 1989; Tielens et al. 1999), which we assume hereafter. In the typical spectrum of a star-forming galaxy, these PAH emission lines, along with various fine-structure metal and HI recombination lines (e.g., Sturm et al. 2000), are superposed on a mid-IR continuum thought to result from dust emission from very small grains, or VSGs (Desert et al. 1990). In star-forming galaxies, the global PAH emission is mainly attributed to UV radiation from OB stars and has been found to correlate with global star formation rate (e.g., Förster Schreiber et al. 2004b; Förster Schreiber et al. 2003; Roussel et al. 2001), although variations with ionizing intensity and metallicity are also observed (e.g., Engelbracht et al. 2005; Hogg et al. 2005; Alonso-Herrero et al. 2004; Helou et al. 2001; Normand et al. 1995).

Until now, the only way to estimate the bolometric luminosities of most galaxies at $z \sim 2$ independent of extinction was via their stacked X-ray and radio emission: unfortunately these data are not sufficiently sensitive to detect individual L^* galaxies at $z \sim 2$ (e.g., Reddy & Steidel 2004; Nandra et al. 2002; Brandt et al. 2001). The *Spitzer* data considered in this paper are useful in assessing the bolometric luminosities of galaxies on an individual basis. One is still limited because detailed mid-IR spectroscopy is feasible only for the most luminous galaxies at $z \sim 2$ (e.g., Yan et al. 2005; Houck et al. 2005), but L^* galaxies at $z \sim 2$ (with $L_{\rm bol} \sim 10^{11}$ $L_\odot$) can be detected in deep 24 μm images. We employ MIPS 24 μm data to study the rest-frame mid-IR properties of optical and near-IR selected galaxies at redshifts $1.5 \lesssim z \lesssim 2.6$. We describe the optical, near-IR, X-ray, and mid-IR data in § 4.2 and 4.3. Our large sample of spectroscopic redshifts for optically-selected galaxies allows us to very accurately constrain the rest-frame mid-IR fluxes of $z \sim 2$ galaxies. In § 4.4, we describe our method for estimating photometric redshifts for near-IR samples of galaxies where

spectroscopy is less feasible. The procedure for estimating infrared luminosities from MIPS data is outlined in § 4.5.1. We discuss the infrared luminosity distributions of 24 μm detected and undetected sources in § 4.5.2 and 4.5.3. The dust attenuation properties of optical and near-IR selected $z \sim 2$ galaxies and the correlation of these properties with bolometric luminosity are discussed in § 4.6 and § 4.7. The stellar populations and composite rest-frame UV spectral properties of faint 24 μm galaxies are discussed in § 4.8. In § 4.9 we examine in more detail the mid-IR properties of massive galaxies at $z \sim 2$. We conclude in § 4.10 by discussing the viability of optical and near-IR color criteria in selecting LIRGs and ULIRGs at $z \sim 2$ and what the *Spitzer* MIPS observations can reveal about the mass assembly of galaxies at high redshift. A flat ΛCDM cosmology is assumed with $H_0 = 70$ km s^{-1} Mpc^{-1} and $\Omega_\Lambda = 0.7$.

4.2 Sample Selection and Ancillary Data

4.2.1 Optical and Near-IR Selection

The star-forming galaxies studied here were drawn from the sample of $z \sim 2$ galaxies in the GOODS-N field selected based on their observed BX/BM colors to $\mathcal{R} = 25.5$ (Adelberger et al. 2004; Steidel et al. 2004). The optical images used for the selection of candidates cover an area $11'$ by $15'$. We refer to "BM" and "BX" galaxies as those that are selected to be at redshifts $1.5 \lesssim z \lesssim 2$ and $2.0 \lesssim z \lesssim 2.6$, respectively (Adelberger et al. 2004; Steidel et al. 2004). In addition to BX/BM galaxies, we also consider galaxies selected using the $z \sim 3$ LBG criteria (Steidel et al. 2003). The BX/BM and LBG candidates make up our BX/BM$-$, or optically-, selected sample. We obtained rest-frame UV spectra with the blue channel of the Low Resolution Imaging Spectrograph (LRIS-B) on Keck I for 386 BX/BM candidates. The numbers of candidates and spectroscopically confirmed galaxies in the BX/BM sample are summarized in Table 4.1. The *spectroscopic* redshift distribution of BX/BM galaxies in the GOODS-N field is shown in Figure 4.1. For efficiency, we preferentially targeted for spectroscopy those BX/BM candidates with $\mathcal{R}$-band magnitudes in the range $\mathcal{R} = 22.5 - 24.5$ (AB units) and gave lower priorities for fainter objects where redshift identification is more difficult from absorption lines and brighter objects where the contamination fraction (from low redshift interlopers) is larger. The star formation rate dis-

tribution of spectroscopically confirmed BX/BM galaxies is similar to that of all BX/BM galaxies in the targeted redshift range to $K_s = 21$ (Vega; Reddy et al. 2005; see also Steidel et al. 2004 for a discussion of spectroscopic bias of galaxy properties with respect to the photometric sample of BX/BM galaxies).

Our deep near-IR $J-$ and K-band imaging, in addition to publicly available deep optical imaging, allows us to select both star-forming galaxies and those with little current star formation in the GOODS-N field. Details of the optical and near-IR images are provided in Reddy et al. (2005). The near-IR selection of star-forming galaxies is done using the criteria of Daddi et al. (2004a), resulting in a "BzK/SF" sample (e.g., Daddi et al. 2004a; Reddy et al. 2005). The near-IR selected samples of galaxies with very little current star formation are constructed by considering the BzK and $J - K_s$ colors of candidates satisfying the BzK/PE and Distant Red Galaxy (DRG) criteria (e.g., Reddy et al. 2005; Daddi et al. 2004a; Franx et al. 2003). Approximately 70% of DRGs to $K_s = 21$ (Vega) have signatures of intense star formation (Papovich et al. 2006; Reddy et al. 2005; van Dokkum et al. 2004).[1] The $J-$ and K-band images cover a large area by near-IR standards ($\sim 8.5' \times 8.5'$), but are still less than half the area of the optical BX/BM images. The number of near-IR selected candidates and their surface densities are presented in Table 4.1. For the remaining analysis, we use AB units for optical (BX/BM) magnitudes and Vega units for near-IR (K_s) magnitudes.

4.2.2 X-Ray Data

The very deep *Chandra* X-ray data in the GOODS-N field (Alexander et al. 2003) allow for an independent means of assessing the presence of AGN in the samples, which can be quite significant for near-IR selected samples (Reddy et al. 2005). In addition, we can stack the X-ray data for those galaxies lying below the X-ray detection threshold to determine their average emission properties (e.g. Laird et al. 2005; Lehmer et al. 2005; Reddy & Steidel 2004; Nandra et al. 2002; Brandt et al. 2001). The X-ray data and stacking methods are discussed in detail in Reddy & Steidel (2004) and Reddy et al. (2005). The numbers of directly detected X-ray sources in each sample considered here are summarized in Table 4.1.

[1] In order to ensure our sample is complete, we only consider DRGs to $K_s = 21$.

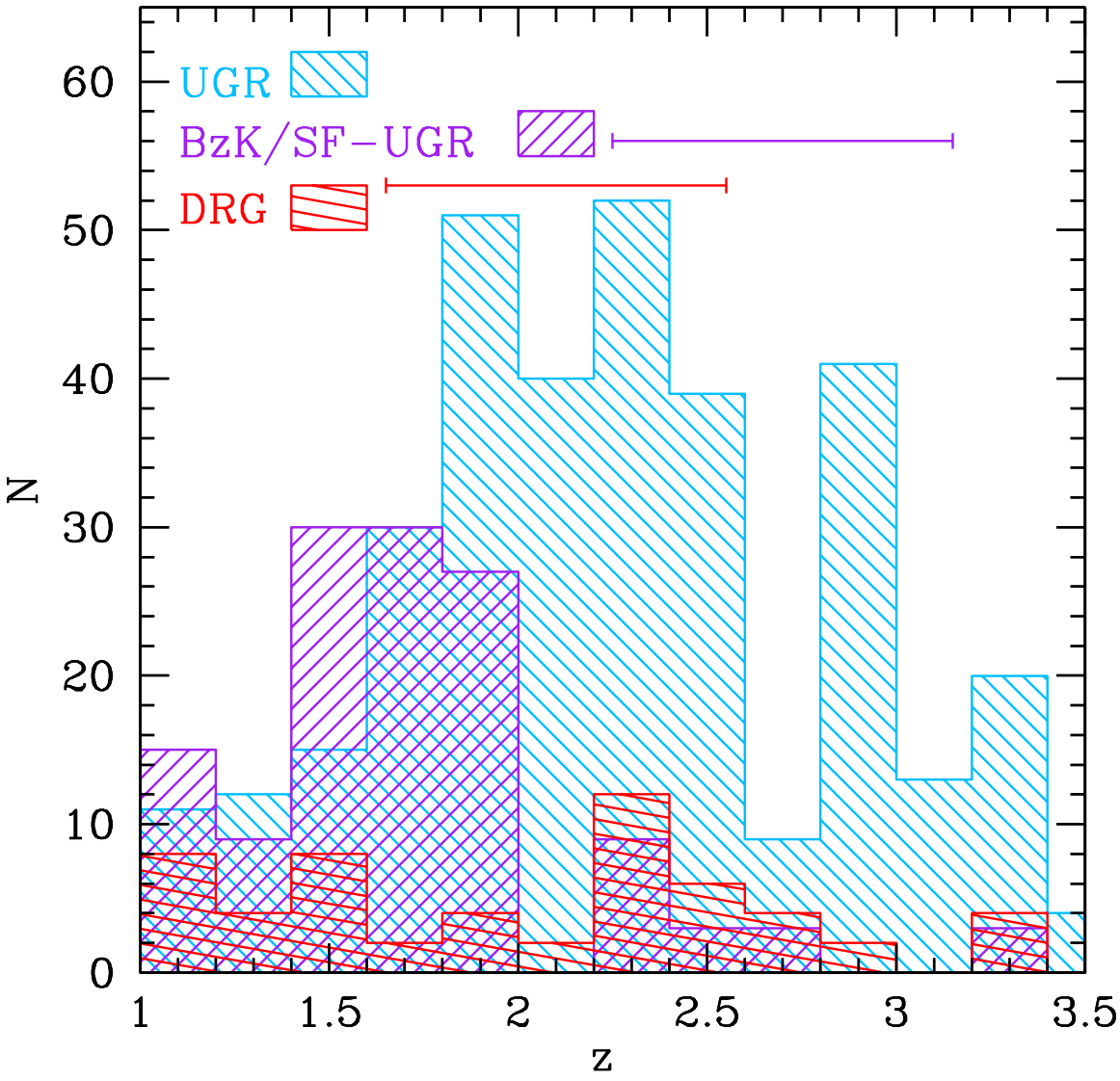

Figure 4.1 *Spectroscopic* redshift distribution of optically (i.e., BX/BM) selected galaxies, with typical error of $\sigma(z) = 0.002$. Also shown are arbitrarily normalized photometric redshift distributions of BzK/SF galaxies that do not satisfy the BX/BM criteria, and DRGs. The error bars indicate the average uncertainty in photometric redshifts ($\sigma(z) = 0.45$) for the near-IR selected BzK galaxies and DRGs.

4.3 Mid-IR Data

The mid-IR data are obtained from the *Spitzer* Multiband Imaging Photometer (MIPS) instrument. The 24 μm data were taken as part of the GOODS Legacy Survey (P.I.: M. Dickinson) between May 27 and June 6, 2004. They consist of 24 AORs (Astronomical Observation Requests) of approximately 3 hours each. The combined data reach a depth equivalent to $\sim$ 10 hours integration at any point in the mosaicked image. The data are publicly available since August 2004 in the *Spitzer* archive. The basic calibrated data (BCD) produced by the *Spitzer* pipeline were used as the starting point for the data reduction. As explained in detail by Fadda (2006), there were several artifacts that added noise to the images, hampering the detection of faint sources. These artifacts include image latencies from previous observations of bright objects or image dark spots present on the pick-off mirror that are projected in different positions by the cryogenic scan mirror during observations. Other variations come from the variable zodiacal light. We have corrected each BCD image for these effects using the procedure described by Fadda (2006). The final mosaic consists of 7198 BCDs combined using MOPEX (Makovoz & Marleau 2005). The final reduced 24 μm mosaic of the GOODS-N region has a pixel size of $1\farcs275$ and covers the entirety of our optical BX/BM images and the measured 3 σ depth is approximately 8 μJy. The large beam-size of MIPS ($\sim 5\farcs4$ at 24 μm) combined with the effects of blending make aperture photometry impractical. Instead, we have chosen to use a PSF fitting method to extract 24 μm fluxes for our galaxies, similar to the method used to extract IRAC fluxes for galaxies as discussed in Shapley et al. (2005).

We first compute an empirical PSF using a two-pass approach. In the first pass, we take the median flux profile of several tens of distinct MIPS point sources across the mosaic to create a rough empirical PSF. This PSF is then used to subtract sources in proximity to the tens of MIPS point sources in order to better determine the PSF profile out to larger radii. This is important for the MIPS PSF, which contains up to 20% of the point source flux in the Airy rings. The effects of source confusion are mitigated by employing the higher spatial resolution *Spitzer* IRAC data in the GOODS-N field to constrain the MIPS source positions. The empirical PSF, normalized to unit flux, is fit to these positions and the fluxes are extracted. The PSF used here extends to $15\farcs3$ radius, and we apply a 15% aperture correction based on the observed curves-of-growth of MIPS point source profiles from the

First Look Survey.

The number of MIPS detections ($> 3\ \sigma$) and non-detections in each sample are summarized in Table 4.1. Virtually all of the directly detected X-ray sources are detected at 24 μm and all have optical/X-ray flux ratios indicating that AGN dominate the X-flux (Reddy et al. 2005). Submillimeter galaxies are often associated with direct X-ray detections (e.g., Alexander et al. 2005; Reddy et al. 2005) even though their bolometric luminosities may still be dominated by star formation. Since we are primarily interested in the mid-IR emission as a tracer of star formation, we have excluded all directly detected X-ray sources (almost all of which are AGN; Reddy et al. 2005) for most of the analysis, unless they happen to coincide with a radio-detected SMG from the Chapman et al. (2005) (SC05) sample. We caution that the resulting sample of 9 SMGs is not meant to be uniform or complete: $\sim 40\%$ of SMGs are not associated with radio sources, either because of their higher redshifts or radio faintness (e.g., Chapman et al. 2005; Smail et al. 2002). Furthermore, the submillimeter observations are not uniform over the field. Nonetheless, it is of obvious interest at least to compare the mid-IR properties of this limited set of radio-detected SMGs to those of galaxies in other samples.

The MIPS 24 μm filter directly samples the rest-frame luminosity from $5 - 8.5$ μm ($L_{5-8.5\mu\mathrm{m}}$) for redshifts $1.5 \lesssim z \lesssim 2.6$. We used the mid-IR spectral shapes of star-forming galaxies (listed in Table 4.2) as templates in order to K-correct the 24 μm fluxes to determine $L_{5-8.5\mu\mathrm{m}}$. Figure 4.2 shows the expected 24 μm fluxes of the galaxies listed in Table 4.2 as a function of redshift. These galaxies were chosen to cover a large range in SFRs (from quiescent spiral galaxies to starbursts and LIRGs/ULIRGs). The mid-IR spectra are obtained from either ISO (for local galaxies; Förster Schreiber et al. 2004a) or *Spitzer* IRS (for $z \sim 2$ hyper-luminous galaxies; Yan et al. 2005) observations. Some properties of these galaxies are summarized in Table 4.2. The mid-IR spectrum of each galaxy is redshifted, convolved with the MIPS 24 μm filter, and the fluxes are normalized to have $L_{5-8.5\mu\mathrm{m}} = 10^{10}$ L$_\odot$ to produce the dotted curves in Figure 4.2. The small dispersion between the templates over redshifts $1.5 \lesssim z \lesssim 2.6$ reflects small changes in the broadband 24 μm fluxes of galaxies due to changes in the relative strengths of the various PAH emission lines and the ratio of PAH-to-continuum flux. The solid curve in the figure shows the average of all the template galaxies. The prominent peak at $z \approx 1.9$ is primarily due to the 7.7 μm feature shifting

into the MIPS 24 μm filter.

4.4 Photometric Redshifts of Near-IR Selected Galaxies

Figure 4.2 illustrates the sensitive dependence of the K-correction on the redshift (e.g., galaxies with a given observed $f_{24\mu\mathrm{m}}$ can have a factor of 3 spread in $L_{5-8.5\mu\mathrm{m}}$ depending on their redshift in the range $1.5 < z < 2.6$). Our large *spectroscopic* sample gives us the distinct advantage of knowing the *precise* redshifts for the optically selected galaxies, removing the added uncertainty introduced by photometric redshifts where the precise location of the PAH features with respect to the MIPS 24 μm filter is unknown, adding considerable uncertainty to the inferred infrared luminosities (e.g., Papovich et al. 2006). As we show below, the typical error in the photometric redshifts derived for near-IR selected galaxies (even when using data across a large baseline in wavelength, from UV through *Spitzer* IRAC), is $\sigma(z) \sim 0.5$. This error in redshift translates to at least a factor of three uncertainty in $L_{5-8.5\mu\ \mathrm{m}}$.

Nonetheless, photometric redshifts are the only practical option for optically faint galaxies where spectroscopy is not feasible. This is true for many of the DRGs and BzK/PE galaxies. We supplement our spectroscopic database of optically selected galaxies with photometric redshifts of near-IR selected galaxies. We made use of the HyperZ code to determine photometric redshifts (Bolzonella et al. 2000). To quantify the uncertainties in photometric redshifts, we tested the code on BX/BM galaxies with spectroscopic redshifts, fitting to the $U_{\mathrm{n}}BGV\mathcal{R}Iz + JK$ photometry. The $BVIz$ magnitudes are obtained from the v1.1 release of the GOODS ACS catalogs (Giavalisco et al. 2004b). Errors in the optical BX/BM and near-IR JK magnitudes are determined from Monte Carlo simulations described by Erb et al. (2006c) and Shapley et al. (2005).

The χ^2 between the modeled and observed colors was calculated for each galaxy for a number of different star formation histories (with exponential decay times τ = 10, 20, 50, 100, 200, 500, 1000, 2000, and 5000 Myr, and $\tau = \infty$) as a function of redshift. The best-fit photometric redshift is the redshift at which χ^2 is minimized. As a figure of merit of the

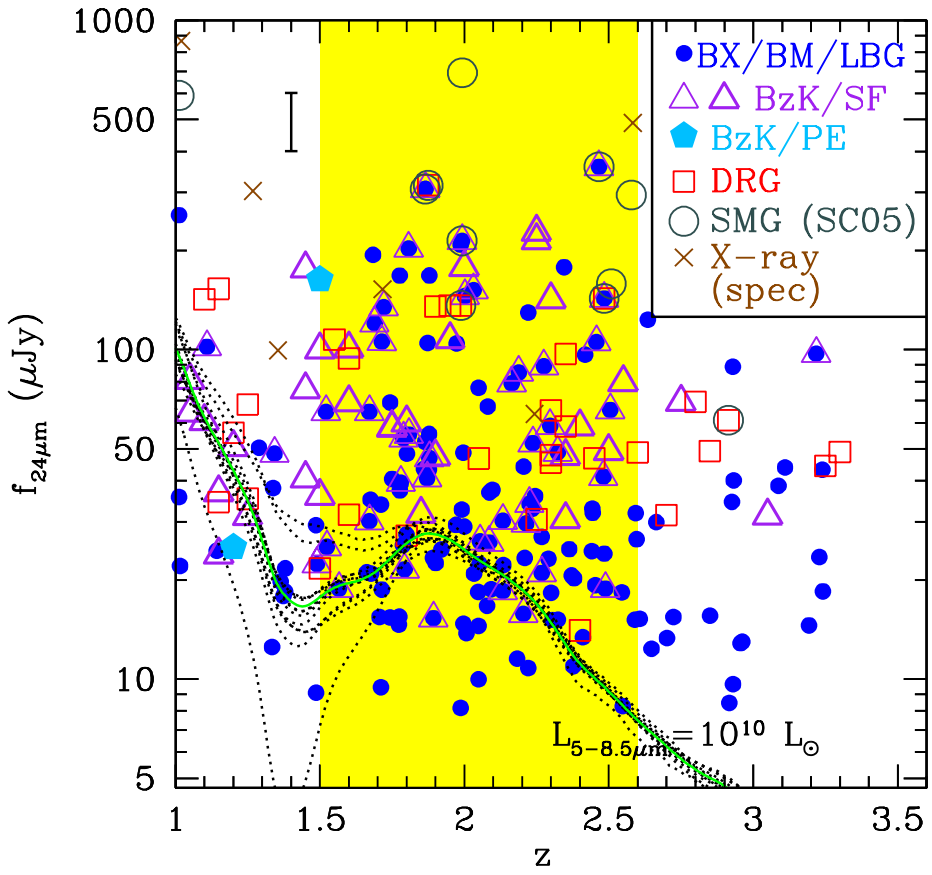

Figure 4.2 Expected 24 μm fluxes of the local and high redshift template galaxies summarized in Table 4.2 shown by the dotted curves, normalized so that $L_{5-8.5\mu\mathrm{m}} = 10^{10}$ $\mathrm{L}_\odot$. The solid curve is the average over all the templates. Also shown are the observed fluxes of BX/BM (small points) and BzK/SF galaxies (thin triangles) with spectroscopic redshifts; and BzK/SF (thick triangles), BzK/PE (solid pentagons), and DRGs (open squares) with photometric redshifts. The typical error in photometric redshifts of DRG and BzK galaxies is $\sigma(z) \sim 0.45$. Radio-detected submillimeter galaxies to $S_{850\mu\mathrm{m}} \sim 4.2$ mJy from Chapman et al. (2005) are shown by the open circles. We have removed directly detected X-ray sources in the samples above, except for those in the SMG sample. Crosses denote hard-band X-ray sources with spectroscopic redshifts in the BX/BM sample. The vertical error bar in the upper left-hand side of the figure shows the typical uncertainty in the 24 μm flux. The shaded region indicates the redshift range over which the MIPS 24 μm filter directly samples the rest-frame 7.7 μm PAH feature.

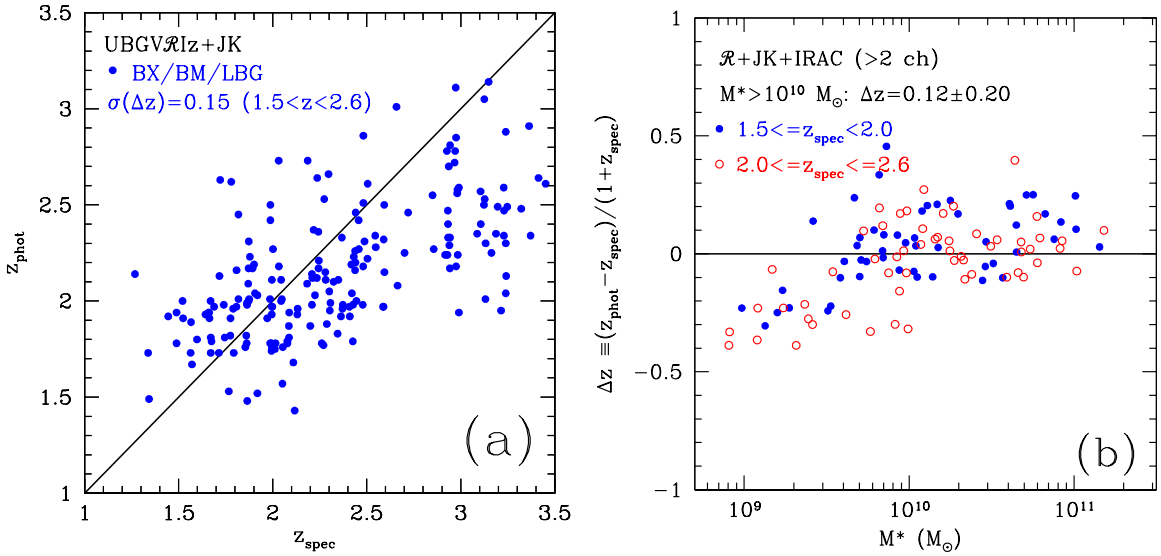

Figure 4.3 *Left panel:* Photometric versus spectroscopic redshifts for BX/BM galaxies. The solid line indicates $z_{\rm phot} = z_{\rm spec}$. *Right panel:* Δz, as defined in the text, as a function of stellar mass for galaxies with redshifts $1.5 \leq z < 2.0$ (solid circles) and $2.0 \leq z \leq 2.6$ (open circles). The figure only shows objects with $> 3\ \sigma$ detections in at least two IRAC channels.

resulting fit (and for easy comparison with other studies), we compute

$$\Delta z \equiv (z_{\rm phot} - z_{\rm spec})/(1 + z_{\rm spec}). \tag{4.1}$$

The results are shown in the left panel of Figure 4.3. The dispersion in Δz is $\sigma(\Delta z) \approx 0.15$ for galaxies with spectroscopic redshifts $1.5 < z < 2.6$. The actual error in redshift is typically $\sigma(z) \sim 0.45$. Both the Shapley et al. (2005) code (which uses Bruzual & Charlot (2003) models) and the Benítez (2000) code gave similar results. We found that adding *Spitzer* IRAC data does little to tighten the scatter between photometric and spectroscopic redshifts for most galaxies, reflecting the absence of any distinct features (e.g., strong spectral breaks) across the IRAC bands for $z \sim 2$ galaxies. We note from the left panel of Figure 4.3 that photometric redshifts systematically underestimate the true redshifts of $z > 3$ galaxies. This should not significantly affect our subsequent analysis since we only consider galaxies up to $z = 2.6$, and most of the BzK/SF and DRG galaxies have photometric redshifts $z_{\rm phot} \lesssim 2.5$.

The IRAC data are nonetheless a powerful tool in discerning the more massive galaxies from the less massive ones. Since most of the optically faint DRGs and BzK/PE galaxies are on average among the more massive galaxies at $z \sim 2$ (e.g., Figure 18 of Reddy et al. (2005)), we have incorporated the IRAC data in the photometric redshift fits. The right panel of Figure 4.3 shows Δz as a function of inferred stellar mass for BX/BM galaxies computed for the best-fit τ model, normalizing to the observed colors.[2] The scatter in Δz for galaxies with stellar masses $M^* \gtrsim 10^{10}$ $M_\odot$ is $\sigma(\Delta z) \sim 0.20$, and we will assume this value for the error in photometric redshifts of the DRG and BzK/PE galaxies. To extend the comparison presented by Reddy et al. (2005) between BX/BM and BzK selected samples of star-forming galaxies by examining their mid-IR properties, we compute photometric redshifts for BzK/SF galaxies that do not satisfy the BX/BM criteria. For the BzK/SF galaxies, we assume an error of $\sigma(\Delta z) \sim 0.15$, according to Figure 4.3a.

We obtained 51 secure photometric redshift fits for BzK/SF galaxies not selected by the BX/BM criteria (out of 95 such objects), and their (arbitrarily normalized) photometric redshift distribution is shown in Figure 4.1. Also shown is the (arbitrarily normalized) photometric redshift distribution for 28 (out of 49) non-X-ray-detected DRGs for which we were able to derive secure photometric redshifts $1 < z_{\rm phot} < 3.5$. The remaining DRGs either have $z_{\rm phot} < 1$ or $z_{\rm phot} > 3.5$ (and are irrelevant to the analysis considered below) or have photometry that was inconsistent with the Bruzual & Charlot (2003) models considered here, resulting in a large χ^2 value between the model and observed colors. The DRGs examined here appear to span a very large range in redshift from $z \sim 1 - 3.5$, a result similar to that found by Papovich et al. (2006) for DRGs in the GOODS-South field. We obtained good photometric redshift fits for only two of the BzK/PE galaxies: one at $z \sim 1.2$ and the other at $z \sim 1.5$. We reiterate that for purposes of redshift identification, we only assumed the photometric redshifts for those galaxies for which we were able to obtain good SED fits (i.e., with $\chi^2 \approx 1$) to the observed data. There were a number of objects for which the photometric redshift errors were relatively large ($\delta z/(1+z) \gtrsim 1$) or had derived redshifts that were much larger ($z > 4$) or smaller ($z < 1$) than of interest here, and we excluded such objects from our analysis. Hence, the photometric redshift distributions in Figure 4.1 should not be attributed to the populations as a whole. For the remaining analysis we

[2]We assume a Salpeter IMF in calculating the stellar mass.

consider only optically-selected galaxies with spectroscopic redshifts and near-IR selected galaxies with photometric redshifts between $1.5 \lesssim z \lesssim 2.6$ where the 24 μm fluxes directly trace the flux at rest-frame 7.7 μm. This is indicated by the shaded region in Figure 4.2.

4.5 Infrared Luminosities of Optical, Near-IR, and Submillimeter Selected Galaxies at $z \sim 2$

4.5.1 Inferring Infrared Luminosities from $L_{5-8.5\mu m}$

The conversion between $L_{5-8.5\mu\mathrm{m}}$ and infrared luminosity will largely depend on the assumed spectral template relating the mid-IR emission of galaxies to their total infrared luminosities. Fortunately, the deep X-ray data allow us to determine whether $L_{5-8.5\mu\mathrm{m}}$ scales with infrared luminosity (or star formation rate) independent of any assumed template, adopting the local empirical relationship between X-ray and FIR luminosity for star-forming galaxies. Figure 4.4 shows the ratio of $L_{5-8.5\mu\mathrm{m}}$ to stacked X-ray luminosity of (X-ray undetected) galaxies in bins of $L_{5-8.5\mu\mathrm{m}}$: we only considered optically-selected galaxies with spectroscopic redshifts since it is for these galaxies that we are able to constrain most accurately the rest-frame X-ray luminosities. Since X-ray emission is sensitive to star formation on timescales of $\gtrsim 100$ Myr (see § 4.6), Figure 4.4 shows results excluding galaxies with inferred ages < 100 Myr. Each bin contains $10 - 20$ sources except the faintest bin which includes 45 galaxies undetected at 24 μm with ages > 100 Myr. The X-ray data for galaxies in each bin were stacked using the procedure described in Reddy et al. (2005). The mean value of the mid-IR-to-X-ray luminosity ratio is $\langle L_{5-8.5\mu\mathrm{m}}/L_{2-10\ \mathrm{keV}}\rangle \approx 251 \pm 41$. The X-ray luminosities of local star-forming galaxies are found to tightly correlate with their infrared emission for galaxies with $10^8 \lesssim L_{\mathrm{FIR}} \lesssim 10^{12}$ $\mathrm{L}_\odot$ (e.g., Ranalli et al. 2003). Using the X-ray luminosity as a proxy for infrared luminosity therefore implies that the rest-frame mid-IR fluxes follow the total infrared luminosity (L_{IR}) for the vast majority of optically-selected galaxies at $z \sim 2$.[3] The mid-IR fluxes must also follow the infrared luminosity for most near-IR selected star-forming galaxies as well given the large overlap

[3]Another commonly used definition of L_{IR} is the total luminosity from $1-1000$ μm. This will differ from $L_{8-1000\mu\mathrm{m}}$ by only a few percent, and for the remaining analysis, we take $L_{\mathrm{IR}} \equiv L_{8-1000\mu\mathrm{m}}$, as defined by Sanders & Mirabel (1996).

$(70\% - 80\%)$ between optical and near-IR selected samples of $z \sim 2$ star-forming galaxies (Reddy et al. 2005). As we show below, the conversion we assume between rest-frame mid-IR and infrared luminosities reproduces the average infrared luminosities predicted from stacked X-ray analyses (§ 4.6.1).

To quantify the relationship between rest-frame mid-IR and total infrared luminosity with a minimum number of assumptions, we have made use of the data compiled by Elbaz et al. (2002), which include IRAS 60 and 100 μm measurements and *ISO* observations of 149 local star-forming galaxies with $L_{\rm IR}$ in the range $10^9 \lesssim L_{\rm IR} \lesssim 10^{12.6}$ $L_\odot$. The mean and dispersion of the IR/MIR flux ratio for the sample of 149 galaxies is $\langle \log(L_{\rm IR}/L_{5-8.5\mu{\rm m}}) \rangle = 1.24 \pm 0.35$. Note the large 1 σ dispersion of a factor of 2.2 in the IR/MIR flux ratio. The dispersion in the IR/MIR flux ratios between galaxies may be driven partly by changes in the mid-IR line strengths as the aromatic carriers are dehydrogenated and/or destroyed depending on the intensity of the ambient UV ionizing field (e.g., Alonso-Herrero et al. 2004; Helou et al. 2001; Dale et al. 2001; Normand et al. 1995). Metallicity effects and a changing distribution of dust with respect to HII regions also likely contribute to the observed factor of $2-3$ dispersion in the IR/MIR ratios. Nonetheless, the mean IR/MIR flux ratio is similar to that inferred from the Dale et al. (2001) template SED for a median $\log[f_\nu(60\mu m)/f_\nu(100\mu m)] \sim -0.20$. Based on the sample of 149 galaxies from Elbaz et al. (2002), we assume $L_{\rm IR} \approx 17.2 L_{5-8.5\mu{\rm m}}$ to convert $L_{5-8.5\mu{\rm m}}$ to $L_{\rm IR}$.

It is worth noting that the relationship between $L_{5-8.5\mu{\rm m}}$ and total IR luminosity for *local* star-forming galaxies may be described by a more complicated function, such as a two-power-law fit (e.g., Elbaz et al. 2002). These complicated relationships may not apply to galaxies at $z \sim 2$ for several reasons. First, the IR/MIR ratio may change depending on the relative contribution of older stellar populations in heating PAH and larger dust grains. The heating of dust by cooler stars is expected to be more prevalent for the less luminous local galaxies with older stellar populations, on average, than for $z \sim 2$ galaxies with relatively younger stellar populations. Second, it is found that $z \sim 2$ galaxies have metallicities that are on average 0.3 dex lower than those of local galaxies at a given stellar mass (Erb et al. 2006a). Therefore, the metallicity dependence of the IR/MIR ratio found for local galaxies (e.g., Engelbracht et al. 2005) suggests that we may not be able to ascribe the IR/MIR ratio for a galaxy of a given stellar mass at $z = 0$ to a galaxy at $z \sim 2$ with

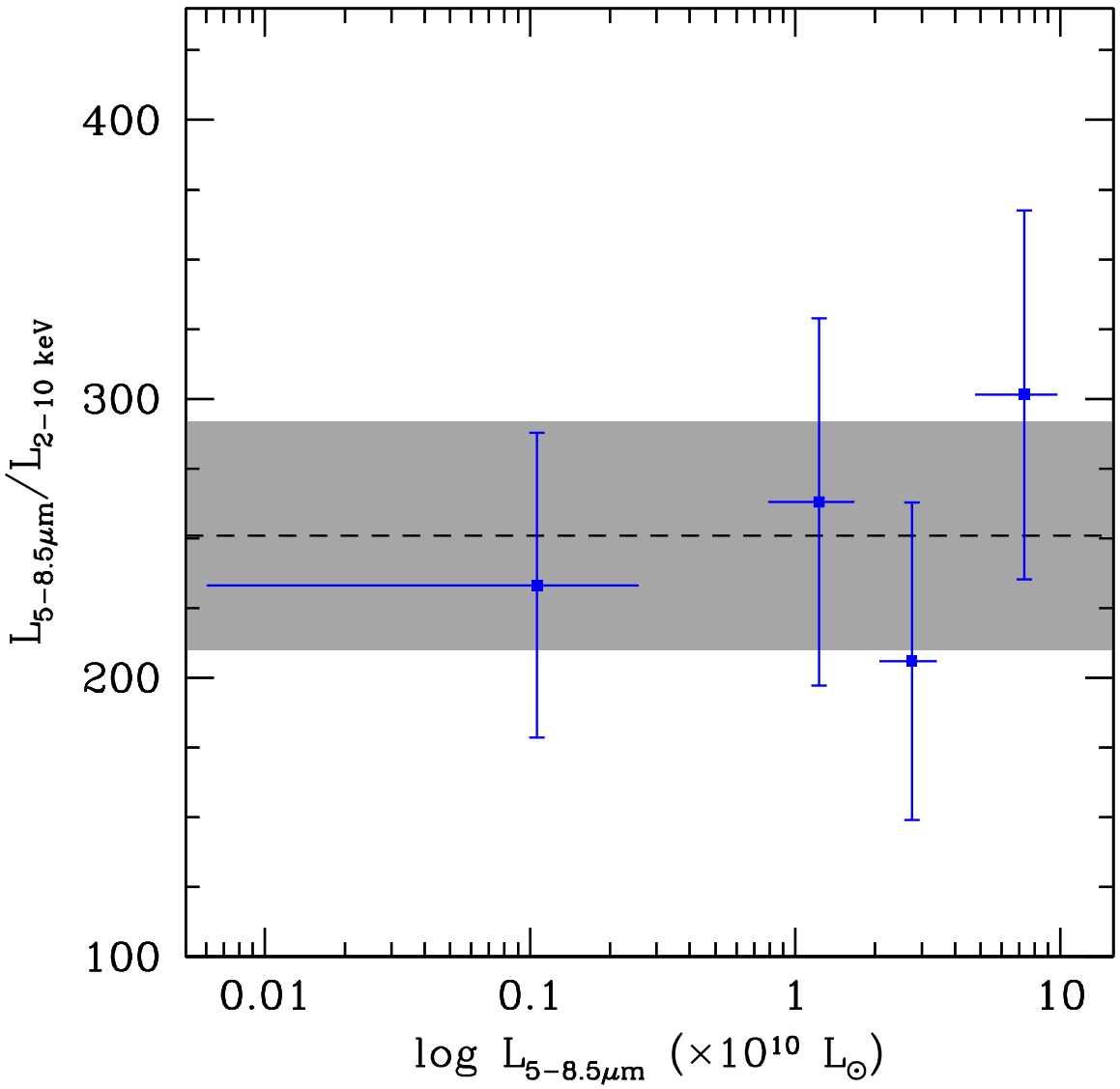

Figure 4.4 Ratio of $L_{5-8.5\mu\mathrm{m}}$ and stacked rest-frame $2-10$ keV X-ray luminosity in bins of $L_{5-8.5\mu\mathrm{m}}$ for galaxies with redshifts $1.5 < z < 2.6$ and those with inferred ages greater than 100 Myr. We have excluded sources directly detected in the *Chandra* 2 Ms data. The faintest bin is for galaxies undetected at 24 μm. Horizontal error bars indicate the 1 σ dispersion in $L_{5-8.5\mu\mathrm{m}}$ in each bin. Vertical error bars show the uncertainty in the mid-IR-to-X-ray luminosity ratio, computed as the uncertainty in the mean X-ray luminosity added in quadrature with the Poisson error in the mean mid-IR luminosity of galaxies in each bin. The dashed horizontal line and shaded region indicate the mean and 1 σ uncertainty of the mid-IR-to-X-ray luminosity ratio of $\sim 251 \pm 41$.

the same stellar mass. A third possibility, and one that is suggested by the results of this paper and other studies (e.g., Adelberger & Steidel 2000; Calzetti & Heckman 1999), is that the dust obscuration of galaxies at a given bolometric luminosity changes as function of redshift, a result that may reflect dust enrichment and/or a changing configuration of dust as galaxies age. Therefore, the relative distribution of PAH and larger dust grains within galaxies may also change as a function of redshift. Because of these uncertainties, and since the primary motivation of our study is to *independently* establish the validity of MIPS observations to infer the infrared luminosities of $z \sim 2$ galaxies, we adopted the simplest conversion that assumes only that the typical IR/MIR luminosity ratio for local galaxies with a wide range in infrared luminosity applies at $z \sim 2$. By taking an average over the local galaxies, we ensure that the derived $L_{\rm IR}$ is not more than a factor of $2-3$ away from that predicted using the IR/MIR ratio of any individual galaxy. As we show below, our constant conversion reproduces within the uncertainties the results that we obtain from stacked X-ray and dust-corrected UV estimates of $L_{\rm IR}$.

In addition to the stacked X-ray and dust-corrected UV estimates, we also have spectroscopic Hα observations for a small sample of 10 BX/BM galaxies in the GOODS-North field (Erb et al. 2006b) with clean (i.e., not blended) MIPS detections. Once corrected for extinction, the Hα fluxes of these galaxies provide estimates of their total (bolometric) luminosities, which we take to be the sum of the $L_{\rm IR}$ and observed 1600 Å luminosity (uncorrected for extinction):

$$L_{\rm bol} \equiv L_{\rm IR} + L_{1600}. \tag{4.2}$$

In Figure 4.5 we show the comparison between $L_{\rm bol}$ estimated from the sum of the MIPS-inferred $L_{\rm IR}$ and observed 1600 Å luminosity ($L_{\rm bol}^{\rm IR+UV}$) with $L_{\rm bol}$ estimated from the spectroscopic Hα observations ($L_{\rm bol}^{\rm H\alpha}$). The results indicate that within the uncertainties the two estimates of $L_{\rm bol}$ track each other very well (with a scatter of 0.2 dex) over the range of $L_{\rm bol}$ typical of galaxies in optical/near-IR selected samples (§ 4.7), at least for this limited sample of 10 objects. The agreement between the MIPS and Hα-inferred estimates suggests that our conversion relation between $L_{5-8.5\mu{\rm m}}$ and $L_{\rm IR}$ works reasonably well. Nonetheless, for comparison with our constant conversion relation, we also consider the effect on our results of assuming a two-power-law conversion suggested by Elbaz et al. (2002). As we

show below, assuming the two-power-law conversion does not change the main conclusions of our study.

The far-infrared luminosity ($L_{\rm FIR}$) is typically defined to be the luminosity from $40 - 120$ μm (Helou et al. 1988). Soifer et al. (1987) found $L_{\rm IR} \sim (1.91 \pm 0.17) \times L_{\rm FIR}$ for galaxies in their Bright Galaxy Sample. Modeling of the warm and cool components of the dust emission in UV-bright galaxies indicates a conversion factor of ~ 1.75 (Calzetti et al. 2000). We take a median value of ~ 1.80 in converting the inferred $L_{\rm IR}$ of galaxies to a FIR luminosity. Generally, uncertainties in the conversion between $L_{\rm IR}$ and $L_{\rm FIR}$ are much smaller than the uncertainties in converting $L_{5-8.5\mu{\rm m}}$ to $L_{\rm IR}$.

Hereafter we assume uncertainties in the total infrared luminosities as follows. For BX/BM galaxies and radio-selected SMGs with spectroscopic redshifts, we assume an uncertainty in $\log L_{\rm IR}$ of 0.3 dex, corresponding to the dispersion in the conversion between $L_{5-8.5\mu\ {\rm m}}$ and $L_{\rm IR}$. For near-IR selected BzK galaxies and DRGs, the photometric redshift error will add an additional 0.5 dex scatter. The total uncertainty in $\log L_{\rm IR}$ for BzK galaxies and DRGs with photometric redshifts is 0.6 dex.

4.5.2 Infrared Luminosity Distributions

Figure 4.2 summarizes the observed $f_{24\mu m}$ fluxes of galaxies as a function of redshift. In this figure, all direct X-ray detections were removed from the BX/BM, BzK and DRG samples, unless they happened to coincide with a radio-detected submillimeter galaxy (SMG) from Chapman et al. (2005), or unless they have spectroscopic redshifts in the BX/BM sample (crosses in Figure 4.2). The BX/BM and SMG samples include objects outside the region covered by our near-IR imaging. The overlap between the samples considered here is discussed extensively in Reddy et al. (2005). The observed 24 μm fluxes for objects in the various samples generally span a large range, from our sensitivity limit of ~ 8 μJy to $\gtrsim 200$ μJy.

For a more meaningful comparison, we have computed $L_{\rm IR}$ for galaxies using the prescription described in § 4.5.1. Figure 4.6 shows the distribution of $L_{\rm IR}$ as inferred from $L_{5-8.5\mu{\rm m}}$ for galaxies in the BX/BM, BzK/SF, DRG, and radio-detected SMG (Chapman et al. 2005) samples with either spectroscopic or photometric redshifts $1.5 < z < 2.6$. As in Figure 4.2, we have excluded directly detected X-ray sources from the distributions

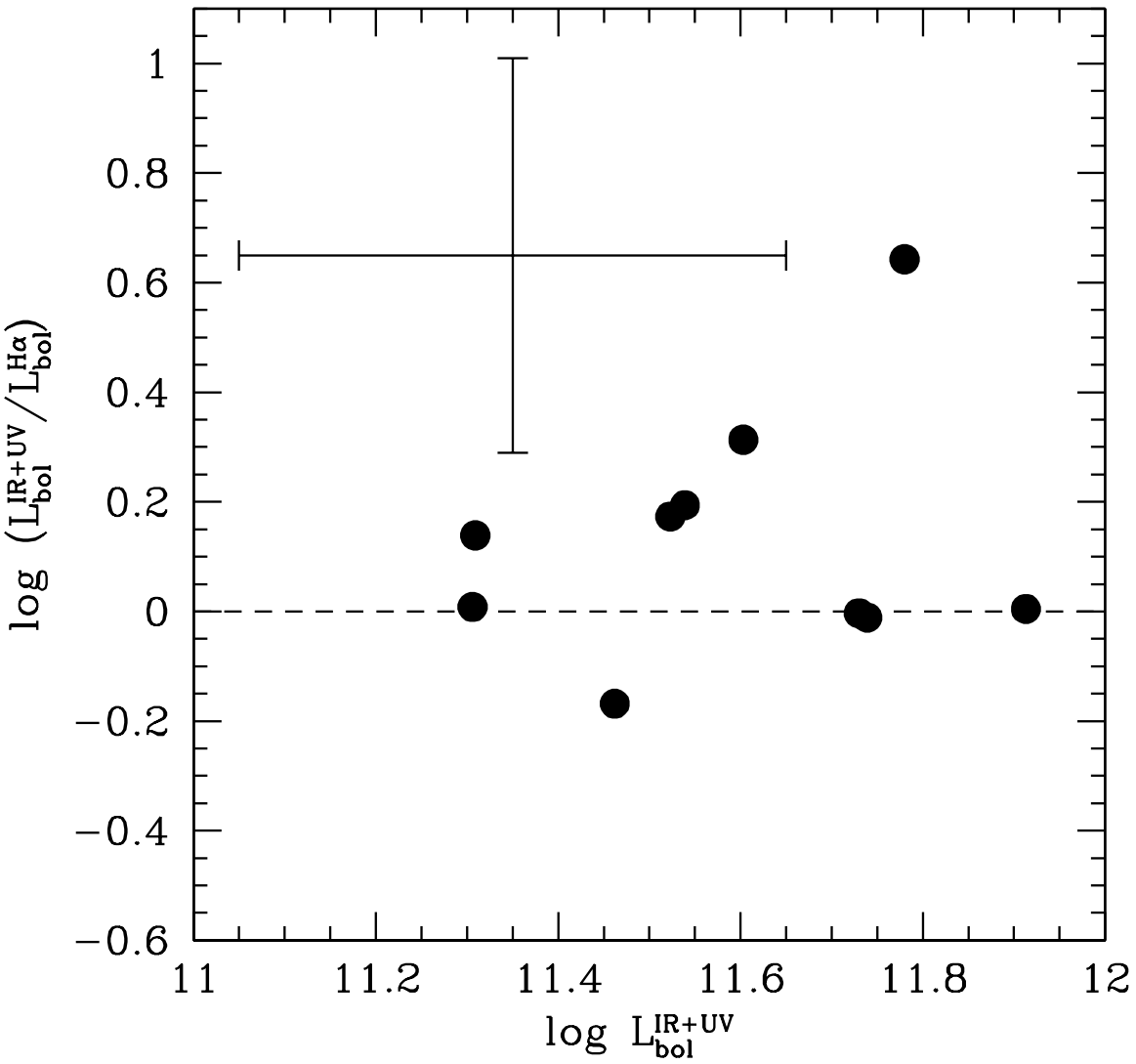

Figure 4.5 Comparison between MIPS-inferred $L_{\rm bol}^{\rm IR+UV}$ and Hα-inferred $L_{\rm bol}^{\rm H\alpha}$ for a sample of 10 BX/BM galaxies. The dispersion in the ratio of the two estimates is ~ 0.2 dex for the subsample considered here. The error bar shows the typical uncertainty of each point.

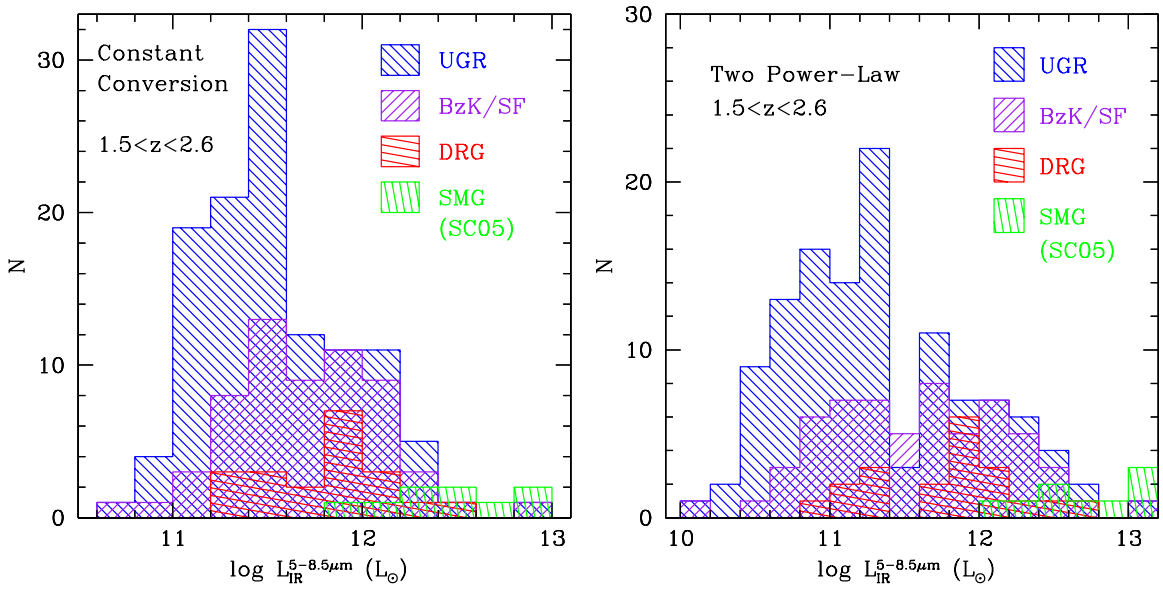

Figure 4.6 Distributions of $L_{\rm IR}$ as inferred from $L_{5-8.5\mu m}$ for galaxies in the BX/BM, BzK/SF, DRG, and radio-detected SMG (Chapman et al. 2005) samples with redshifts $1.5 < z < 2.6$ assuming our constant conversion between $L_{5-8.5\mu\rm m}$ and $L_{\rm IR}$ (*left panel*) and the two-power-law conversion of Elbaz et al. (2002) (*right panel*). We have excluded directly detected X-ray sources unless they happen to coincide with a radio-detected SMG.

unless they coincide with a radio-detected SMG source. We show the resulting distributions assuming the constant conversion and two-power-law conversion relations in the left and right panels, respectively. The distributions assuming the two-power-law conversion are bimodal. However, the distributions of observed UV luminosities and dust correction factors of BX/BM galaxies are approximately gaussian (e.g., Steidel et al. 2004; Reddy et al. 2006a). Assuming the Calzetti et al. (2000) law to convert the observed luminosities to dust-corrected luminosities then implies that the bolometric luminosity distribution of BX/BM galaxies should be gaussian, a result not in accordance with the bimodal distribution computed assuming the two-power-law conversion. More generally, we expect to find gaussian distributions of luminosity for galaxies in photometric surveys since such galaxies are typically selected on a continuous range of observed colors and/or magnitudes. The bimodality in Figure 4.6b is likely due to the sparse data used to establish the two-power-law relation for galaxies with $1 \times 10^{11} \lesssim L_{\rm IR} \approx\lesssim 5 \times 10^{11}$ L$_\odot$ (see Figure 5d of Elbaz et al. 2002). This range of $L_{\rm IR}$ happens to encompass the typical IR luminosity of $z \sim 2$ galaxies as inferred from X-ray and dust-corrected UV estimates (Reddy & Steidel 2004) and it is partly for this reason that we favored our simple constant conversion relationship.

Regardless of the conversion used, we find that the bulk of the galaxies in the BX/BM and BzK/SF samples and detected at 24 μm have inferred infrared luminosities comparable to those of local luminous infrared galaxies (LIRGs), with $10^{11} \lesssim L_{\rm IR} \lesssim 10^{12}$ L$_\odot$. Galaxies in the BX/BM sample with $f_{24\mu{\rm m}} \gtrsim 8$ μJy (corresponding to the 3 σ sensitivity limit) have $\langle L_{\rm IR} \rangle \sim 3.1 \times 10^{11}$ L$_\odot$ for the constant conversion and $\langle L_{\rm IR} \rangle \sim 2.1 \times 10^{11}$ L$_\odot$ for the two-power-law conversion (the two-power-law distribution is broader than that obtained using the constant conversion). Both the BX/BM and BzK/SF samples also host galaxies which, based on their inferred $L_{\rm IR}$, would be considered ultra-luminous infrared galaxies (ULIRGs) with $L_{\rm IR} \gtrsim 10^{12}$ L$_\odot$. Note that if we excluded all direct X-ray detections, including the submillimeter sources, the maximum inferred $L_{\rm IR}$ of BX/BM and BzK/SF galaxies is $\approx 2.5 \times 10^{12}$ L$_\odot$, an infrared luminosity that is similar to the detection limit of the *Chandra* 2 Ms data for a galaxy at $z \sim 2$ assuming the Ranalli et al. (2003) conversion between X-ray and FIR luminosity.

The BzK/SF sample distribution shown in Figure 4.6 includes galaxies that do not satisfy the BX/BM criteria (i.e., BzK/SF–BX/BM galaxies). These galaxies (to $K_{\rm s} = 21$)

have a mean IR luminosity that is identical to that of BX/BM galaxies to $K_{\rm s} = 21$. The average IR luminosity of BX/BM galaxies is ~ 1.8 times fainter than BzK galaxies since the BX/BM sample includes galaxies that extend to fainter $K_{\rm s}$ magnitudes than those in the BzK sample. Therefore, while the BzK/SF–BX/BM galaxies have redder $G-\mathcal{R}$ colors than required to satisfy the BX/BM criteria, it appears that their infrared luminosities are still comparable to those of BX/BM galaxies (see also the discussion in § 4.6), a result consistent with that obtained in X-ray stacking analyses (Reddy et al. 2005). Figure 4.6 indicates the DRG galaxies with photometric redshifts between $1.5 < z < 2.6$ also span a large range in $L_{\rm IR}$, from luminosities characteristic of LIRGs to ULIRGs. We find a luminosity distribution of DRGs to $K_{\rm s} = 21$ that is in good agreement with the $L_{\rm IR}$ distribution found by Papovich et al. (2006) for DRGs (to approximately the same depth) in the GOODS-South field.[4] We note that BX/BM galaxies and DRGs to $K_{\rm s} = 20$ have the same inferred $L_{\rm IR}$ as $K_{\rm s} < 20$ galaxies selected in other ways (e.g., using the BzK/SF criteria).

The inferred $L_{\rm IR}$ for the one BzK/PE selected galaxy with $z \sim 1.5$ is $\sim 1.2 \times 10^{12}$ L$_\odot$. The mean $f_{24\mu{\rm m}}$ flux of MIPS-detected (and non-X-ray-detected) BzK/PE galaxies without redshifts is $\langle f_{24\mu{\rm m}} \rangle \approx 81.4$ μJy which, at the mean redshift of BzK/PE galaxies (e.g., Reddy et al. 2005; Daddi et al. 2004a) of $z \sim 1.7$, corresponds to $L_{\rm IR} \sim 6 \times 10^{11}$ L$_\odot$. The 24 μm detection rate ($\sim 50\%$; Table 4.1) of non-X-ray-detected BzK/PE galaxies implies some contamination by star-forming galaxies; this is not unexpected given that photometric scattering can have a significant effect on samples constructed by color selection techniques (Reddy et al. 2005).

The radio-detected submillimeter galaxies to $S_{850\mu{\rm m}} \sim 4.2$ mJy analyzed here have inferred $L_{\rm IR}$ of $10^{12} \lesssim L_{\rm IR} \lesssim 10^{13}$ L$_\odot$, which can be directly compared with their bolometric luminosities calculated based on the submillimeter data presented by Chapman et al. (2005). The 850 μm inferred bolometric luminosities ($L_{\rm IR}^{850\mu m}$) are sensitive to the assumed characteristic dust temperature associated with a greybody fit to the dust SED and the emissivity. For example, a change in the assumed dust temperature from $T_{\rm d} = 36$ K (the median value for the sample of radio-detected SMGs in Chapman et al. 2005) to a cooler temperature of $T_{\rm d} = 31$ K results in a factor of ~ 5 decrease in the inferred FIR lumi-

[4]The DRG sample of Papovich et al. (2006) extends to $K_{\rm s} = 23.2$ in AB magnitudes, or $K_{\rm s} \sim 21.4$ in Vega magnitudes, over an area twice as large as studied here.

nosities. Figure 4.7 shows the comparison between 850 μm and 24 μm inferred bolometric luminosities of radio-detected SMGs. We also show the point corresponding to IRS9 from the Yan et al. (2005) sample of hyper-luminous $z = 2$ sources with IRS spectroscopy — this source has independent constraints on its FIR luminosity based on MIPS 70 and 160 μm and MAMBO millimeter measurements. The infrared luminosity of IRS9 is $L_{\rm IR} \sim 1.8 \times 10^{13}$ L$_\odot$ (constrained to within a factor of $2 - 3$) based on these multi-wavelength measurements (Yan et al. 2005).

Figure 4.7 shows that the IR/MIR flux ratio for IRS9 is comparable (to within ~ 1 σ) to those of the local star-forming galaxies listed in Table 4.2— these local galaxies are $1 - 3$ orders of magnitude fainter than IRS9. Judging the validity of our conversion for the hyper-luminous galaxies at $z \sim 2$ is difficult given that very few of these galaxies have independent constraints on their bolometric luminosities. On the other hand, the submillimeter (850 μm) inferred infrared luminosities of bright SMGs are systematically a factor of $2 - 10$ higher than predicted using our conversion between $L_{5-8.5\mu{\rm m}}$ and $L_{\rm IR}$. The crosses in Figure 4.7 demonstrate that the systematic offset cannot be completely accounted for if we assume a two-power-law conversion between $L_{5-8.5\mu{\rm m}}$ and $L_{\rm IR}$ — there are still 4 of 9 SMGs with $L_{\rm IR}^{850\mu m}$ that are a factor of 2 to 10 larger than predicted from their 24 μm fluxes, and the distribution of SMG points when considering the two-power law conversion is not symmetric about the line of equality (solid line in Figure 4.7). One possibility is that the submillimeter estimates are in fact correct and that our assumed conversion between mid-IR and IR luminosities does not apply to SMGs. The IRS sample considered here consists of just one hyper-luminous galaxy at $z = 2$, and if we ignore this galaxy then the systematic offset of SMGs may indicate a breakdown of our assumed conversion for the most luminous sources at redshifts $z \sim 2$ with $L_{\rm IR} \gtrsim 10^{13}$ L$_\odot$. The second possibility is that the submillimeter estimates overpredict the infrared luminosities of SMGs and that our MIR-to-IR conversion is correct. This may not be surprising since the conversion between submillimeter flux and bolometric luminosity is very sensitive to the assumed dust temperature, and a decrease in the assumed temperature of just a few degrees can reduce the inferred bolometric luminosity by a factor of $\sim 5 - 10$ (see example above). Finally, it is possible that neither the submillimeter or mid-IR inferred infrared luminosities of bright SMGs is correct. We note that it is common for these luminous galaxies to host

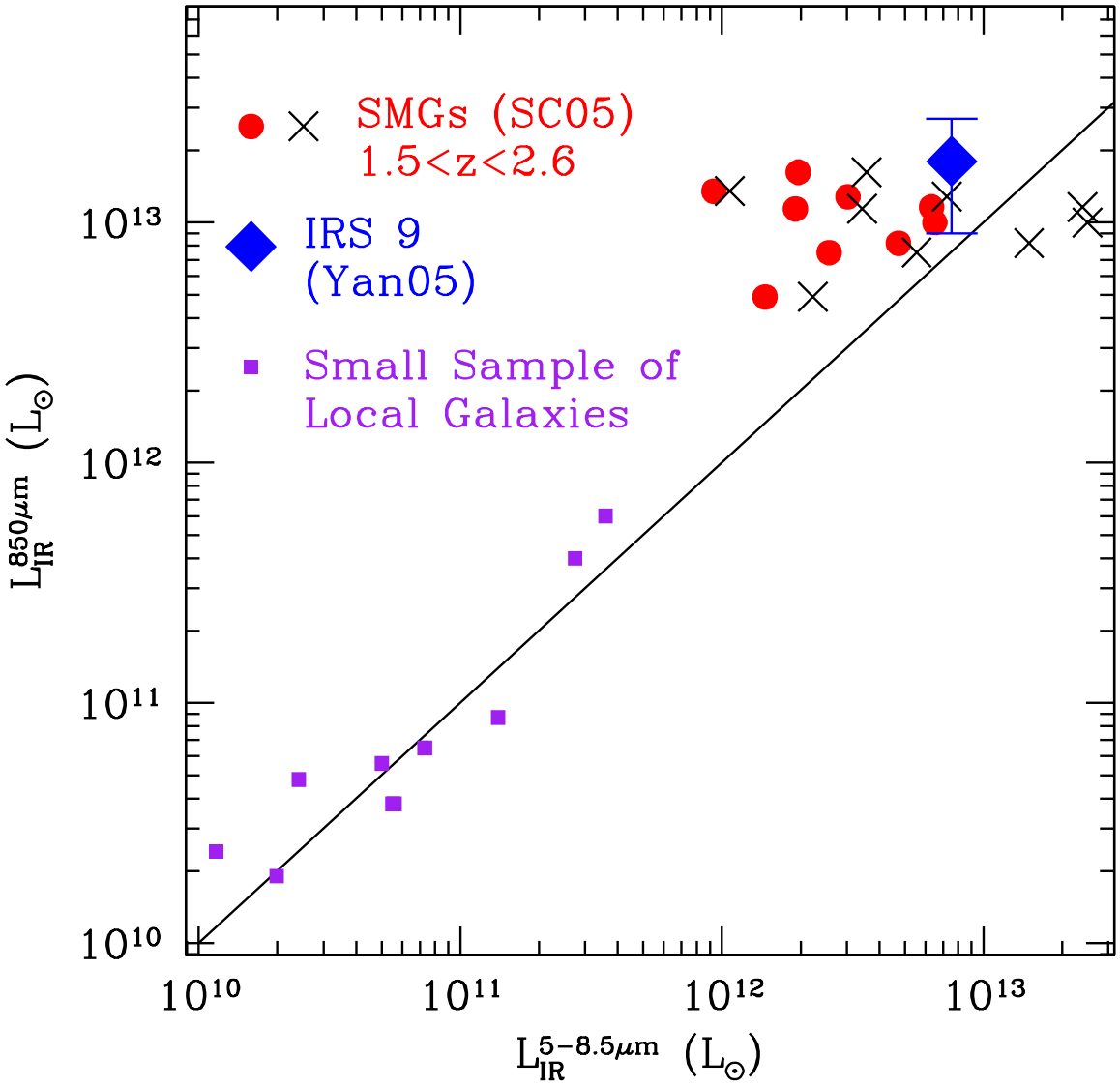

Figure 4.7 $L_{\rm IR}^{850\mu m}$, inferred from the submillimeter fluxes of radio-detected SMGs (Chapman et al. 2005), plotted against $L_{\rm IR}^{5-8.5\mu m}$ inferred from $L_{5-8.5\mu m}$ assuming a IR/MIR flux conversion of 17.2 (solid circles) and the two-power-law conversion of Elbaz et al. (2002) (crosses). The infrared luminosity of IRS9 is inferred from MIPS 24, 70, and 160μm data and MAMBO millimeter measurements (Yan et al. 2005). Also shown are the local star-forming templates listed in Table 4.2.

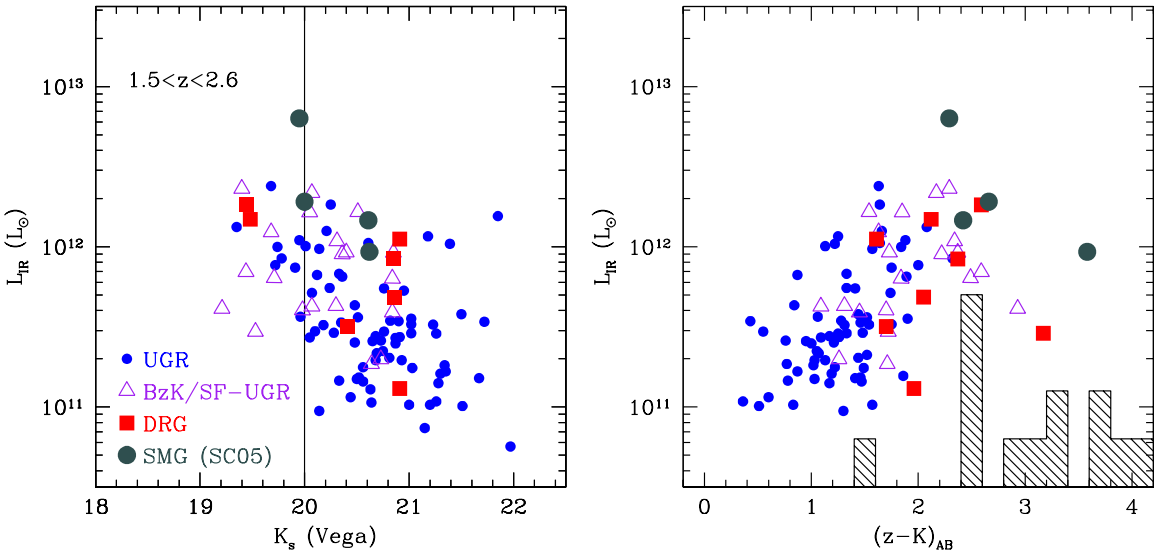

Figure 4.8 *Left panel:* Distribution of $L_{\rm IR}$ as a function of $K_{\rm s}$ for galaxies in the various samples. We have assumed a IR/MIR flux ratio of 17.2 for all galaxies including the radio-detected SMGs. *Right panel:* $L_{\rm IR}$ as a function of $(z-K)_{\rm AB}$ color. Symbols are the same as in the left panel. The arbitrarily normalized histogram indicates the distribution in $(z-K)_{\rm AB}$ color of DRGs and BzK/PE galaxies undetected at 24 μm.

AGN, and this can alter the observed mid-IR and IR fluxes beyond what would be expected given pure star formation (e.g., Armus et al. 2004; Fadda et al. 2002; Almaini et al. 1999; Fabian & Iwasawa 1999). As another example, Arp 220 has anomalously low PAH emission for its bolometric luminosity (when compared with other ULIRGs), suggesting that the galaxy contains a buried quasar and/or a heavily dust-enshrouded starburst such that the extinction at rest-frame 7 μm is no longer negligible (e.g., Haas et al. 2001; Charmandaris et al. 1997). *Spitzer* IRS observations of bright radio-detected SMGs will be useful in quantifying the relationship between the $5-8.5$ μm and bolometric luminosities of these ultraluminous sources.

A relevant line of investigation is to determine what the various optical and near-IR color and magnitude selections imply for the infrared luminosity distributions of the galaxies they select. Figure 4.8a shows the inferred $L_{\rm IR}$ of galaxies with redshifts $1.5 < z < 2.6$ as a function of $K_{\rm s}$ magnitude. We have assumed the IR/MIR flux ratio of 17.2 for the radio-detected SMGs shown in the figure. Galaxies with $K_{\rm s} < 20$ (e.g., K20 samples: Cimatti et al. 2002a; Cimatti et al. 2002b) have $\langle L_{\rm IR} \rangle \sim (1-2) \times 10^{12}$ L$_\odot$, similar to the value

found by Daddi et al. (2005a) for $K_{\rm s} < 20$ BzK-selected galaxies in the GOODS-N field. Alternatively, we find $\langle L_{\rm IR} \rangle \sim 5 \times 10^{11}$ L$_{\odot}$ for BX/BM, BzK, and DRG galaxies with $20 < K_{\rm s} < 21.0$. As stated in § 4.5.1, the uncertainties on any individual value of $\log L_{\rm IR}$ are 0.3 dex for BX/BM galaxies with spectroscopic redshifts and 0.6 dex for near-IR selected (BzK; DRG) galaxies with photometric redshifts. At any given $K_{\rm s}$ magnitude, the range in $L_{\rm IR}$ spans an order of magnitude assuming our constant conversion and larger than an order of magnitude assuming the two-power-law conversion of Elbaz et al. (2002). Finally we note that galaxies with $K_{\rm s} < 20$ at $z \sim 2$ that show some signature of star formation (i.e., those that are MIPS detected) generally have infrared luminosities that are a factor of two larger than those of galaxies with $20 < K_{\rm s} < 21$. As discussed elsewhere, there is also a population of massive galaxies with little detectable star formation (e.g., van Dokkum et al. 2004; Reddy et al. 2005).

We investigate this quiescent population of massive galaxies in the context of their star-forming counterparts by examining $L_{\rm IR}$ as a function of $(z-K)_{\rm AB}$ color (Figure 4.8b). The $(z-K)_{\rm AB}$ color probes the Balmer and 4000 Å breaks for galaxies at the redshifts of interest here, and is also sensitive to the current star formation rate (e.g., Reddy et al. 2005; Daddi et al. 2004a). Figure 4.8b shows that galaxies with redder $(z-K)_{\rm AB}$ color (up to $(z-K)_{\rm AB} \sim 3$) have higher inferred $L_{\rm IR}$ (and larger SFRs if the bolometric luminosity is attributed to star formation) on average than galaxies with bluer $(z-K)_{\rm AB}$ colors, a trend similar to that found when stacking X-ray data (Reddy et al. 2005). A more interesting result is indicated by the histogram that shows the distribution in $(z-K)_{\rm AB}$ color of DRGs and BzK/PE galaxies that are undetected at 24 μm. Of the 13 MIPS-undetected DRGs and BzK/PE galaxies, seven have $(z-K)_{\rm AB} > 3$. Reddy et al. (2005) found DRGs with $(z-K)_{\rm AB} \gtrsim 3$ to have little X-ray emission and had colors similar to those of IRAC Extremely Red Objects (IEROs; Yan et al. 2005). The lack of 24 μm detections for these red $(z-K)_{\rm AB}$ sources further supports the notion that they have little current star formation. It also rules out the possibility that they harbor Compton-thick obscured AGN as an explanation for their lack of X-ray emission, since we would then expect them to be bright at 24 μm.

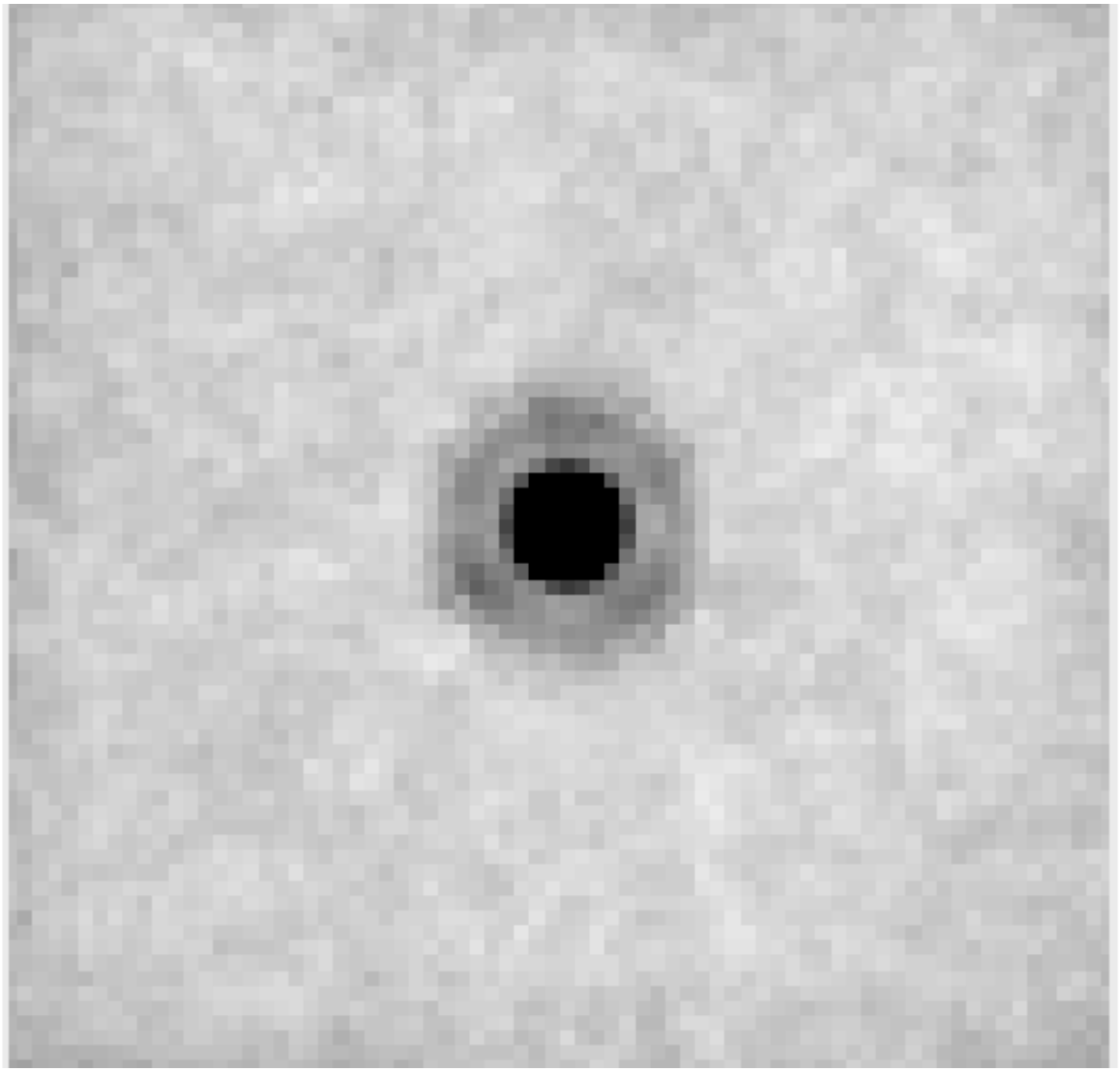

Figure 4.9 Stacked 24 μm flux of 48 isolated MIPS-undetected BX/BM galaxies ($f_{24\mu\mathrm{m}} \lesssim 8$ μJy) with spectroscopic redshifts $1.5 < z < 2.6$, indicating a mean flux per undetected galaxy of $\langle f_{24\mu m} \rangle \approx 3.30 \pm 0.48$ μJy.

4.5.3 Stacked 24 μm Flux

The high quality and depth of the MIPS data enable us to study the average properties of galaxies that are (individually) undetected at 24 μm by stacking their emission. The data were stacked by considering all galaxies undetected at 24 μm and X-ray wavelengths. To avoid contaminating the stacked signal, we only added galaxies to the stack if there were no bright MIPS sources within $\approx 5''$ of those galaxies. To ensure a clean signal, we extracted subimages around each undetected galaxy, subtracted all *detected* point sources within those subimages using the empirical PSF, and added the subimages together. The stacked flux was measured in a manner similar to the measurement of detected MIPS sources. Figure 4.9 shows the stacked image of 48 MIPS-undetected BX/BM galaxies with spectroscopic redshifts $1.5 < z < 2.6$. The mean flux per object is $\langle f_{24\mu\mathrm{m}} \rangle \approx 3.30 \pm 0.48$ μJy, where the error is the dispersion of the background in the *stacked* image. At a mean redshift of $\langle z \rangle = 2.05$, this flux corresponds to $L_{\mathrm{IR}} \approx 2 \times 10^{10}$ L$_{\odot}$. Combining this result with the mean L_{IR} of MIPS-detected BX/BM galaxies implies a mean across the entire sample, neglecting "confused" sources, of $\approx 2.3 \times 10^{11}$ L$_{\odot}$. This mean value does not change significantly if we add in directly detected X-ray sources (including radio-detected SMGs to $S_{850\mu\mathrm{m}} \sim 5$ mJy) because of their small number compared to the typical (less luminous) BX/BM galaxy. The mean value of $L_{\mathrm{IR}} \approx 2.3 \times 10^{11}$ L$_{\odot}$ is in excellent agreement with the average of $L_{\mathrm{IR}} \approx 3 \times 10^{11}$ L$_{\odot}$ found from stacked X-ray/radio and dust corrected UV estimates (Reddy & Steidel 2004). This suggests that the non-detection of galaxies at 24 μm is due to them having lower SFRs and not because they are deficient in PAH emission for a given L_{IR}. The advantage of the 24 μm data over X-ray/radio data is that we can estimate bolometric luminosities for individual L^* (LIRG) galaxies at $z \sim 2$ rather than ensembles of galaxies.

Combining our estimate of the MIPS-inferred average IR luminosity of BX/BM galaxies with the stacked radio results of Reddy & Steidel (2004), we find that the radio-IR relation appears valid on average for the sample. To quantify the radio-IR ratio for the sample, we compute the "q" parameter (Condon et al. 1991):

$$q \equiv \log(\frac{\mathrm{FIR}}{3.75 \times 10^{12}\ \mathrm{W\ m^{-2}}}) - \log(\frac{S_{1.4\ \mathrm{GHz}}}{\mathrm{W\ m^{-2}\ Hz^{-1}}}), \tag{4.3}$$

where $S_{1.4\ \mathrm{GHz}}$ is the rest-frame 1.4 GHz flux density in units of W m^{-2} Hz^{-1} and

$$\mathrm{FIR} \equiv 1.26 \times 10^{-14}(2.58 S_{60\ \mu\mathrm{m}} + S_{100\ \mu\mathrm{m}})\ \mathrm{W\ m^{-2}}, \tag{4.4}$$

where $S_{60\ \mu\mathrm{m}}$ and $S_{100\ \mu\mathrm{m}}$ are the IRAS 60 and 100 μm flux densities in Jy (Helou et al. 1988). The implied "q" value for the BX/BM sample is $\langle q \rangle \sim 2.5$ if we assume $\log[S_{60\ \mu\mathrm{m}}/S_{100\ \mu\mathrm{m}}] \sim 0.2$. This value of q is in excellent agreement with the value of $q \sim 2.4$ found for $\gtrsim 10^{11}$ L$_\odot$ galaxies in the IRAS 2 Jy sample (Yun et al. 2001). We also stacked the 24 μm data for undetected BzK/PE and DRG galaxies in the same manner as described above, which yielded a mean flux per object of $\langle f_{24\mu\mathrm{m}} \rangle \sim 2.72 \pm 1.65$ μJy. As noted in § 4.5.2, most of these sources have very red $(z-K)_{\mathrm{AB}}$ colors, and their low-level mid-IR and X-ray emission indicate they have low SFRs. Galaxies with $f_{24\mu\mathrm{m}} \lesssim 8$ μJy are discussed further below.

4.6 Dust Attenuation in Optical and Near-IR Selected Galaxies

Aside from inferring the infrared luminosity distributions, we can use the MIPS data to examine the relationship between dust extinction and rest-frame UV spectral slope. Meurer et al. (1999) found a relation between the rest-frame UV spectral slope, β, and the attenuation of local UV-selected starburst galaxies, parameterized by the ratio $L_{\mathrm{FIR}}/L_{1600}$, where L_{1600} is the rest-frame 1600 Å luminosity uncorrected for extinction. This relation appears to fail, however, for the most luminous starbursts such as ULIRGs (Goldader et al. 2002) and radio-detected SMGs (Chapman et al. 2005). A greater proportion of the star formation in galaxies with $L_{\mathrm{IR}} \gtrsim 10^{12}$ L$_\odot$ will be obscured by dust as compared with LIRG-type starbursts (e.g., see § 4.7). Therefore, whatever UV emission is able to escape from the optically thin regions of ULIRGs will constitute a lower fraction of the total bolometric luminosity. As a result, the rest-frame UV light can substantially underpredict (by a factor of $10-100$) the bolometric luminosities of the most luminous starbursts, such as radio-detected SMGs (Chapman et al. 2005). Normal ("quiescent") star-forming galaxies also appear to deviate from the Meurer et al. (1999) relation, such that $L_{\mathrm{FIR}}/L_{1600}$ is lower for a given amount of UV reddening than in starburst galaxies (e.g, Laird et al. 2005; Bell 2002) a result that may be tied to the varying ratio of current to past-average star formation rate of normal

star-forming galaxies (Kong et al. 2004). Alternatively, the star formation in local quiescent galaxies (i.e., those with low SFRs) is more distributed than in local starbursts so that a failure of the starburst reddening law may reflect a different distribution of dust with respect to the star forming regions in quiescent galaxies. Observations of radio-detected SMGs and quiescently star-forming galaxies suggests that the Meurer et al. (1999) and Calzetti et al. (2000) laws do not apply to these sources.

The rest-frame UV spectral and mid-IR data of $z \sim 2$ galaxies allow us to investigate how well the high redshift galaxies follow the local dust attenuation relation. The full SED modeling of BX/BM galaxies in the GOODS-N field yields estimates of the best-fit star formation history (τ), age, mass, SFR, and $E(B-V)$ color excess for each galaxy (Erb et al. 2006c; Shapley et al. 2005). The mean fractional uncertainty in $E(B-V)$ is $\langle \sigma_{\mathrm{E(B-V)}}/E(B-V) \rangle = 0.7$ as determined from Monte Carlo simulations. To convert $E(B-V)$ to β we assumed that 1 mag of extinction at 1600 Å ($A_{1600} = 1$) corresponds to $E(B-V) \approx 0.092$ (e.g., Calzetti et al. 2000). For most galaxies, the best-fit star formation history is close to that of a constant star formation history (with decay time-scale $\tau = \infty$). The most massive galaxies at $z \sim 2$ (with stellar masses $M^* \gtrsim 10^{11}$ $\mathrm{M}_\odot$) are generally better fit with declining star formation histories. We have assumed a CSF model for galaxies unless such a model provides a much poorer fit to the observed data than a declining star formation history.

4.6.1 Results for Optically Selected Galaxies

Figure 4.10 shows $L_{\mathrm{FIR}}/L_{1600}$ versus β for spectroscopically confirmed BX/BM galaxies with redshifts $1.5 < z < 2.6$. The FIR luminosity is computed from $L_{5-8.5\mu\mathrm{m}}$ using the procedure described in § 4.5.1. We estimated the rest-frame 1600 Å luminosity from either the U_{n}, G, or $\mathcal{R}$ magnitude depending on the redshift of the galaxy. The majority of BX/BM galaxies with inferred ages $\gtrsim 100$ Myr (solid circles) appear to agree well with Meurer et al. (1999) relation, shown by the solid curve.[5]

BX/BM galaxies with the youngest inferred ages ($\lesssim 100$ Myr; open circles) exhibit a large offset from the Meurer et al. (1999) relation in the sense that they exhibit redder UV

[5]Assuming the two-power-law conversion to compute L_{FIR} results in a similar distribution of points around the Meurer et al. (1999) relation but with larger scatter.

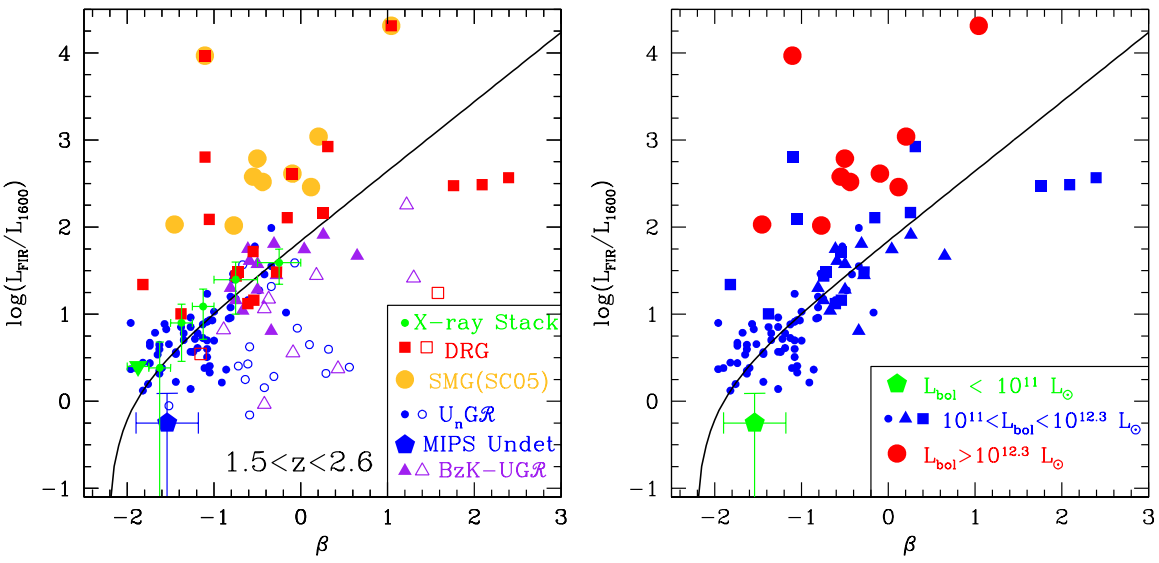

Figure 4.10 (*Left*) Dust absorption, parameterized by $F_{\rm FIR}/F_{1600}$, versus rest-frame UV spectral slope, β, for galaxies with redshifts $1.5 < z < 2.6$. Filled and open symbols respectively denote galaxies with inferred ages of > 100 Myr and < 100 Myr. The large pentagon shows the results for BX/BM galaxies undetected at 24 μm, using the stacked results of § 4.5.3. The horizontal and vertical error bars on this point reflect the dispersion about the mean β and mean $L_{\rm FIR}/L_{1600}$ of 24 μm undetected sources. The green points represent the results from an X-ray stacking analysis as described in the text. The solid line indicates the Meurer et al. (1999) relation found for local UV-selected starburst galaxies. (*Right*) Same as *left* panel, but excluding galaxies younger than 100 Myr and color-coding objects by $L_{\rm bol}$.

colors for a given dust obscuration than older galaxies that do follow the relation. Note that we have assumed a CSF model for the young galaxies shown in Figure 4.10. The inferred ages of these galaxies are typically smaller than 50 Myr, which is approximately the dynamical time across the galaxy. Assuming such small (and unrealistic ages) will cause us to overestimate $E(B-V)$ for these sources. The change in $E(B-V)$ that results from fixing the age of the young galaxies to 100 Myr ($\Delta E(B-V) = 0.09$) is not enough to completely account for the offset of the young galaxies from the Meurer et al. (1999) relation. This suggests that the Calzetti et al. (2000) law may not be applicable to these young galaxies because of a different configuration of dust with respect to the star-forming regions, in which case a grayer extinction law may be appropriate. As one example, the well-studied lensed Lyman Break Galaxy MS1512-cB58 has an inferred age of $\sim 70-100$ Myr and millimeter continuum observations suggest that its infrared luminosity is smaller than one would predict from its UV reddening (Baker et al. 2001). Regardless of the assumed extinction law, these young galaxies in the samples examined here have similar bolometric (sum of observed IR and UV) luminosities as older galaxies (see § 4.7).

The deep X-ray data in the GOODS-N field allow us to estimate (X-ray inferred) average infrared luminosities for well-defined samples of galaxies (e.g., Reddy et al. 2005; Laird et al. 2005; Nandra et al. 2002; Brandt et al. 2001). The green points in Figure 4.10 show the expected dust absorption inferred from the X-ray data as a function of β. These points were determined by stacking the X-ray data for non-X-ray-detected BX/BM galaxies (with ages > 100 Myr) in bins of β. We only considered stacking galaxies with ages > 100 Myr since the X-ray emission is sensitive to the star formation rate once O and B stars evolve to produce high mass X-ray binaries, which is roughly 10^8 years after the onset of star formation. The average X-ray flux per bin was converted to a FIR flux using the Ranalli et al. (2003) relation. Dividing the average FIR flux per bin by the average 1600 Å luminosity of objects in each bin yields the green points. The horizontal error bars indicate the bin width and the vertical error bars indicate the dispersion in stacked X-ray flux (computed using the procedure described in Reddy et al. (2005) and Reddy & Steidel (2004)) added in quadrature with the dispersion in the FIR/X-ray luminosity relation found by Ranalli et al. (2003). The X-ray results reproduce the Meurer et al. (1999) relation very well, providing an independent confirmation that typical BX/BM galaxies abide by the local dust obscuration relation for

starburst galaxies. The X-ray and mid-IR data indicate that the UV slope can be used to deduce the extinction corrections for these typical galaxies and that such galaxies have UV light that is only moderately extinguished in most cases. The agreement between the MIPS-inferred FIR luminosities and X-ray-inferred FIR luminosities (obtained with the empirically determined Ranalli et al. (2003) relation) suggests that the Ranalli et al. (2003) relation provides a reasonable description for most of the galaxies considered here. For comparison, adopting the Persic et al. (2004) relation would yield FIR luminosities five times in excess of those predicted from the 24 μm fluxes for the vast majority of $z \sim 2$ galaxies.

We compute the average dust obscuration of BX/BM galaxies undetected at 24 μm using the stacking results of § 4.5.3, and the result is denoted by the large pentagon in Figure 4.10. The stacked 24 μm FIR luminosity of MIPS undetected galaxies is divided by their average rest-frame 1600 Å luminosity. For these galaxies, L_{1600} is on average 1.6 times larger than their inferred $L_{\rm FIR}$ indicating they are significantly less obscured than galaxies detected at 24 μm. These undetected galaxies also have relatively blue rest-frame UV SEDs (as indicated by their average β) compared to 24 μm detected galaxies. Furthermore, the results of Figure 4.4 indicate these faint sources have lower X-ray emission than 24 μm detected galaxies. All of these observations combined suggest that galaxies are undetected at 24 μm because they have lower SFRs and are less obscured than galaxies with brighter 24 μm fluxes. We further explore the nature of these MIPS undetected sources in § 4.8.

4.6.2 Results for Near-IR and Submillimeter Selected Galaxies

Also shown in Figure 4.10 are BzK/SF galaxies to $K_{\rm s} = 21$ not satisfying the BX/BM criteria. As pointed out in § 4.5.2, these BzK/SF selected galaxies have inferred $L_{\rm IR}$ that are comparable to those of BX/BM galaxies to the same $K_{\rm s}$ limit, but of course with redder $G - \mathcal{R}$ colors and a $\mathcal{R} \sim 0.5$ mag fainter on average than BX/BM galaxies to the same $K_{\rm s}$ limit. The results of Figure 4.10 suggest that BzK/SF galaxies lying outside the color range selected by the BX/BM criteria also follow the Meurer et al. (1999) relation. Similar to the results found in § 4.6.1 for most BX/BM galaxies, the mid-IR data indicate that the UV light from most BzK/SF galaxies appears to be moderately extinguished and that the UV slope can be used to estimate their attenuation.

Almost all of the radio-detected SMGs considered here have inferred dust absorption factors (when we assume the 850 μm-inferred bolometric luminosities) that are at least a magnitude larger than predicted by the Meurer et al. (1999) relation for a given rest-frame UV slope. The discrepancy is not as substantial (i.e., it is reduced by a factor of $2-10$) if we inferred $L_{\rm IR}$ of the SMGs from their 24 μm fluxes assuming our conversion between MIR and IR luminosity. The BX/BM criteria are designed to select objects where followup spectroscopy is feasible, and this usually implies setting a limit to the allowed $E(B-V)$ (or β) of objects in the sample. However, given that at least half the galaxies with $L_{\rm bol} \gtrsim 10^{12}$ L$\odot$ have UV slopes comparable to that of the *typical* BX/BM galaxy, it is not uncommon to find such dust-obscured galaxies in optical surveys.

Of the limited sample of DRGs with photometric redshifts $1.5 < z < 2.6$, at least half lie above the local starburst attenuation law. We are able to find DRGs that agree with the Meurer et al. (1999) relation since the MIPS data studied here are significantly deeper (by a factor of ~ 5) than the data considered in Papovich et al. (2006). In particular, we find the surface density of DRGs between $1.5 < z < 2.6$ with $1 \lesssim \log(F_{\rm FIR}/F_{1600}) \lesssim 2$ of $\gtrsim 0.14$ arcmin^{-2} (this is a lower limit since there are number of DRGs without photometric redshifts, some of which may truly lie at redshifts $1.5 < z < 2.6$), which is at least a factor of 20 higher than in Papovich et al. (2006). Our results suggest that the DRG population consists of galaxies with a very wide range in star formation rate, from galaxies with little or no star formation (DRGs with very red $(z-K)_{\rm AB}$ colors; § 4.5.2) to those that are heavily obscured and rapidly forming stars.

4.6.3 Relationship between β and Obscuration as a Function of Luminosity

Figure 4.10b shows galaxies with ages > 100 Myr within the samples, color-coded by their $L_{\rm bol}$. Virtually all objects with $L_{\rm bol}$ in the range $10^{11} < L_{\rm bol} < 10^{12.3}$ L$_\odot$ have β that appear to reproduce their obscuration as inferred from the Meurer et al. (1999) and Calzetti et al. (2000) laws. There is some weaker evidence that the galaxies with the lowest SFRs (undetected at 24 μm) as indicated by the green pentagon in Figure 4.10b follow a different extinction law. More pronounced, however, is the systematic offset of the most luminous galaxies considered here with $L_{\rm bol} > 10^{12.3}$ L$_\odot$. These ultra-luminous galaxies have rest-

frame UV slopes that underpredict their obscuration by a factor of $10 - 100$. The main results of Figure 4.10b indicate that the relationship between UV reddening and obscuration is strongly dependent on the bolometric luminosity, but that most LIRG galaxies at $z \sim 2$ follow the local relation.

4.7 Relationship Between Dust Obscuration and Bolometric Luminosity

The bolometric luminosity of star-forming galaxies can be well-approximated by the sum of the IR and UV luminosities as indicated in Equation 4.5. Figure 4.11 shows $L_{\rm bol}$ as a function of dust obscuration for objects in the various samples assuming a constant conversion relation between mid-IR and total IR luminosity. Typical (LIRG) galaxies at $z \sim 2$ will have $L_{\rm bol} \approx L_{\rm IR}$ where $\sim 90\%$ of the bolometric luminosity is emitted in the infrared. The bolometric luminosity is strongly correlated with dust obscuration: galaxies with larger bolometric luminosities are more dust obscured than less luminous galaxies. The best-fit linear trend for spectroscopically confirmed BX/BM galaxies detected at 24 μm is

$$\log L_{\rm bol} = (0.62 \pm 0.06) \log \frac{L_{\rm IR}}{L_{1600}} + (10.95 \pm 0.07) \tag{4.5}$$

(solid line in Figure 4.11; we note that the two axes are not independent of each and may partly account for the tight scatter in the correlation). BX/BM galaxies undetected at 24 μm are indicated by the pentagon. These undetected galaxies have an average bolometric luminosity of $\langle L_{\rm bol} \rangle \sim 6 \times 10^{10}$ L$_\odot$ and have UV luminosities that are a factor of ~ 10 less dust obscured than the typical 24 μm detected BX/BM galaxy. Approximately half of the bolometric luminosity of these 24 μm undetected galaxies is emitted in the UV. Galaxies with inferred ages < 100 Myr (yellow symbols in Figure 4.11) have $L_{\rm bol}$ comparable to those of older galaxies at $z \sim 2$, suggesting that these young galaxies have similar IR/MIR ratios as older galaxies. Therefore, the deviation of the young galaxies from the Meurer et al. (1999) law as noted in § 4.6 suggests that we have overestimated $E(B-V)$ for these young sources and/or they may follow a steeper (e.g., SMC-like) extinction law.

We note that BX/BM galaxies with $K_{\rm s} < 21$ have bolometric luminosities and dust obscuration comparable to BzK galaxies to $K_{\rm s} = 21$ that are not optically selected. This

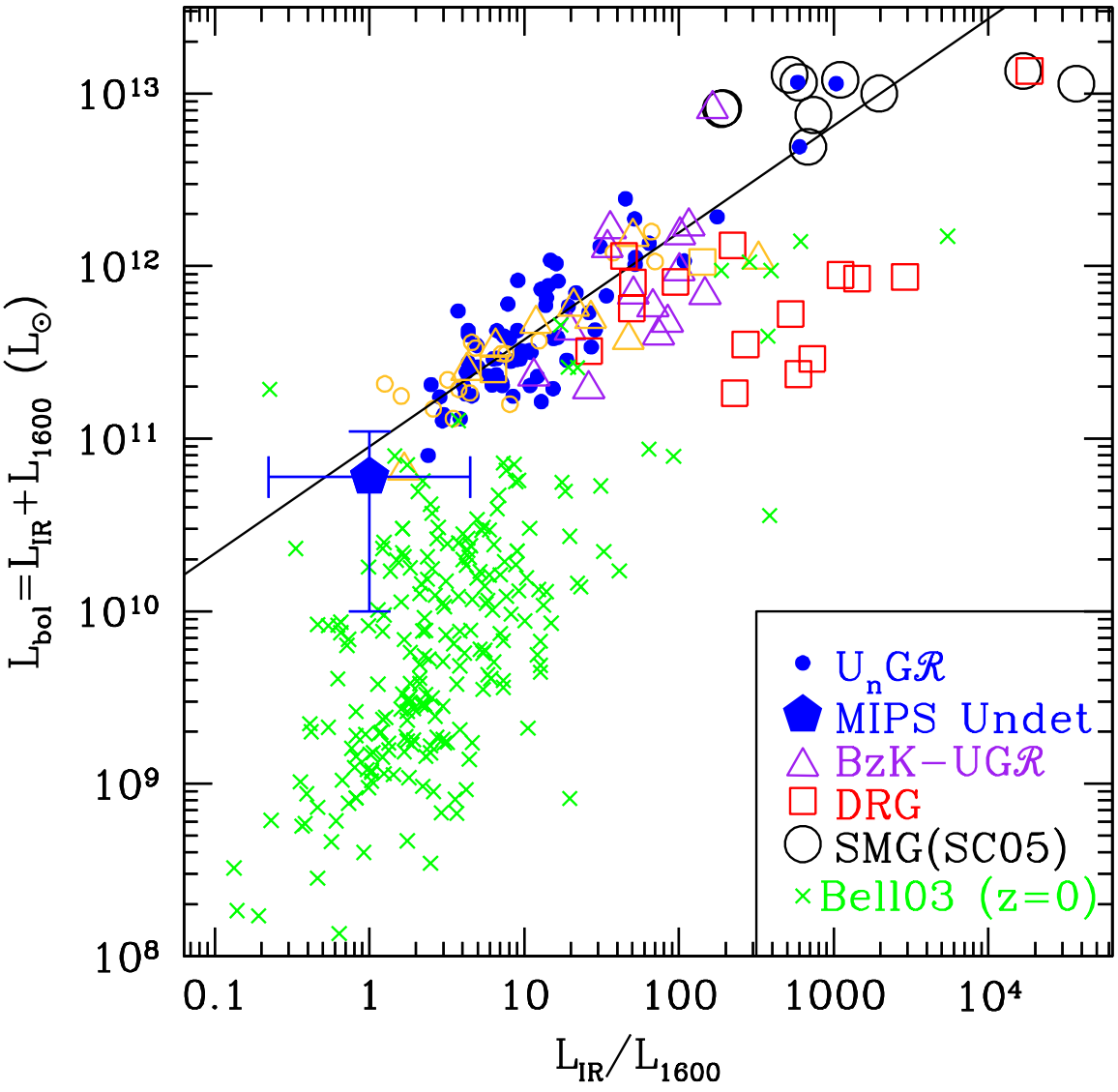

Figure 4.11 Bolometric luminosity, approximated as the sum of the IR and UV luminosities, versus dust obscuration. Shown are the distributions for $z \sim 2$ galaxies, and the solid line indicates the best-fit linear relation for spectroscopically confirmed BX/BM galaxies detected at 24 μm. For comparison, the pentagon denotes the result for galaxies in the BX/BM sample undetected at 24 μm, and the yellow symbols denote objects with inferred ages < 100 Myr. We also show local galaxies from the compilation of Bell (2003). Galaxies of a *given* bolometric luminosity are typically $8-10$ times less dust obscured at high redshift than at the present epoch.

implies that objects missed by optical selection but that appear in the near-IR selected BzK sample are not missed because they are more dust obscured, a result corroborated by X-ray stacking analyses (Reddy et al. 2005). The bright radio-detected SMGs have the highest inferred bolometric luminosities among all galaxies considered here, of order $\sim 10^{13}$ $L_{\odot}$ with dust-obscuration factors $\gtrsim 100$. Galaxies in the BX/BM, BzK, and radio-detected SMG samples detected at 24 μm mostly follow the linear relation denoted by the solid line in Figure 4.11. For SMGs, $L_{\rm bol} \approx L_{\rm IR}$, so assuming the submillimeter estimates of $L_{\rm IR}$ (rather than the mid-IR estimates shown in Figure 4.11) will move the SMGs in a direction parallel to the $z \sim 2$ trend.

DRGs detected at 24 μm span a large range in $L_{\rm IR}/L_{1600}$. About half the DRGs follow the linear trend established for optically selected galaxies at $z \sim 2$. The remaining half of DRGs have similar bolometric luminosities to those that follow the $z \sim 2$ trend, but the UV luminosities are a magnitude more attenuated than what we would have predicted from the Meurer et al. (1999) law. The SED analysis (§ 4.4) demonstrates that all of the DRGs which follow the $z \sim 2$ trend are all relatively young galaxies (ages $\lesssim 2$ Gyr) and have lower stellar masses ($M^* \lesssim 10^{11}$ $M_{\odot}$). In contrast, DRGs that are offset from the trend are all older (ages $\gtrsim 2$ Gyr) and all have masses $> 1.2 \times 10^{11}$ $M_{\odot}$. The offset could be explained naturally if the dust masses of galaxies increase as they age, a natural consequence of star formation. Note that if the massive, metal-rich DRGs have stronger PAH flux for a given IR luminosity than the younger galaxies, then this would serve only to increase the offset between the massive DRGs and the $z \sim 2$ trend. In fact, stacking the X-ray data for the younger and older DRGs indicates they have very similar bolometric luminosities, confirming the results obtained by inferring $L_{\rm IR}$ from the PAH flux. The results of Figure 4.11 suggest that much of the dust in galaxies with the largest stellar masses was produced by star formation prior to the episode currently heating the dust. Therefore, such galaxies will have larger dust obscuration for a given bolometric luminosity. Assuming the two-power-law conversion of Elbaz et al. (2002) would result in a $z \sim 2$ trend with a slope 20% larger than given in Equation 4.5, but with approximately the same intercept within the uncertainties, so our conclusions would be unchanged.

As galaxies are enriched with dust as they age, then we expect to see an even greater difference in dust obscuration between $z \sim 2$ galaxies and those at the present epoch.

To investigate this, we examined $L_{\rm bol}$ versus $L_{\rm IR}/L_{1600}$ for the sample of local galaxies compiled by Bell (2003), shown by crosses in Figure 4.11. The local sample includes the ULIRGs studied by Goldader et al. (2002). Unfortunately, the UV and IR data for local LIRG and ULIRGs are relatively sparse. However, of the small sample of local galaxies with $L_{\rm bol} \gtrsim 10^{11}$ L$_\odot$, almost all (10 of 11) lie to the right of the linear trend at $z \sim 2$ and at least half occupy the same region as the old, massive DRGs at $z \sim 2$. In fact, an interesting corollary to the above discussion is that massive, star-forming DRGs at $z \sim 2$ are more analogous to local ULIRGs than bright SMGs at $z \sim 2$, both in terms of bolometric luminosity *and* dust obscuration. Local ULIRGs undoubtedly carry a significant amount of dust into their current star formation episodes (e.g., Goldader et al. 2002), so it not surprising that they have similar dust-obscuration factors as massive, star-forming DRGs at $z \sim 2$. On the other hand, most galaxies lying on the $z \sim 2$ trend, including many bright SMGs, are likely undergoing their first major episode of star formation and have relatively low dust-to-gas ratios, unlike the more massive (offset) DRGs and local galaxies.

The offset between $z = 0$ and $z \sim 2$ galaxies can be seen at fainter bolometric luminosities where the local sample includes more galaxies ($10^{10} \lesssim L_{\rm bol} \lesssim 10^{11}$). Restricting our analysis to galaxies in the Bell (2003) sample with $L_{\rm bol}$ comparable to those of 24 μm undetected $z \sim 2$ galaxies, we find that the local sample is on average ~ 10 times more dust obscured than 24 μm undetected galaxies at $z \sim 2$. Further, recent GALEX results indicate that local near-UV selected galaxies with $L_{\rm bol} = 10^{11}$ L$_\odot$ have a mean dust-obscuration factor of ≈ 10; this is 8 times larger than the inferred dust obscuration of a $L_{\rm bol} = 10^{11}$ L$_\odot$ galaxy at $z = 2$ (Burgarella et al. 2005). To summarize, the important result from Figure 4.11 is that galaxies of a *given* bolometric luminosity are on average a factor of $8 - 10$ less dust obscured at $z \sim 2$ than at the present epoch, confirming the trend first noted by Adelberger & Steidel (2000) between galaxies at $z = 0$, $z \sim 1$, and $z \sim 3$; this result is also suggested by the work of Calzetti & Heckman (1999). Again, this result could be anticipated if successive generations of star formation add to already existing dust within galaxies and/or if the dust distribution within galaxies becomes more compact with time (e.g., via the effects of mergers, which tend to drive gas and dust to the central kpc of the system). The net result of dust enrichment and a more compact distribution of dust (e.g., after a merger event) is an increase in the dust column density towards star-forming

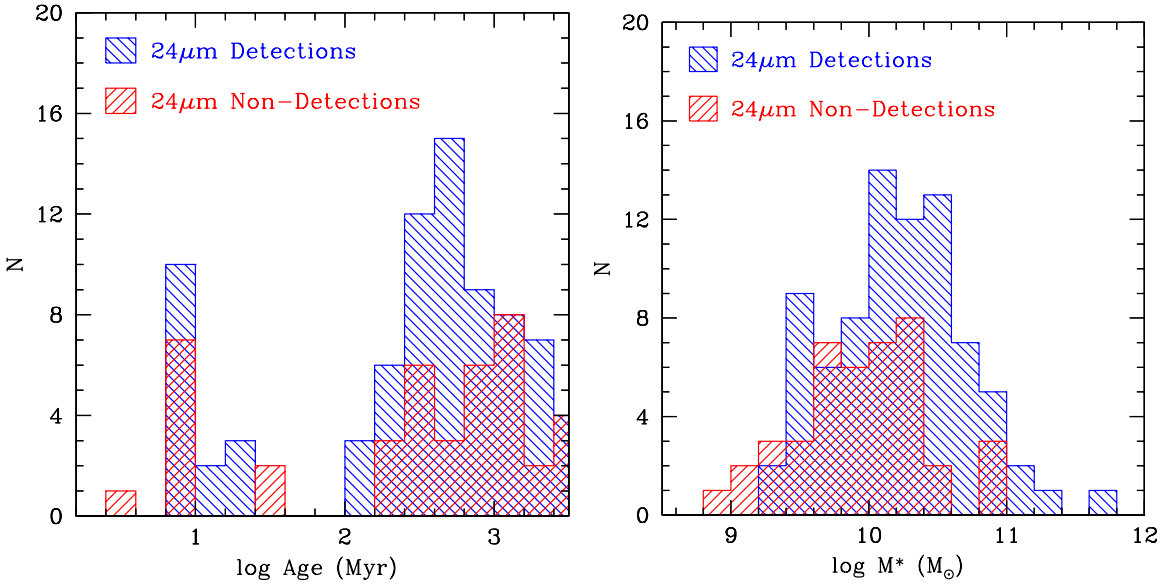

Figure 4.12 Histograms of the age (left panel) and mass (right panel) distributions for 24 μm detected and non-detected BX/BM galaxies with redshifts $1.5 < z < 2.6$. The age distributions of detected and non-detected BX/BM galaxies are similar. The mean of the mass distributions are offset such that undetected galaxies have $\langle \log M^* \rangle$ that is 0.4 dex lower than that of 24 μm detected galaxies.

regions. The relationship between dust obscuration and $L_{\rm bol}$ (i.e., Eq 4.5) indicates that for the mean $L_{\rm bol}$ of the BX/BM selected sample of galaxies of $L_{\rm bol} \sim 2.3 \times 10^{11}$ L$_\odot$, the average dust obscuration is $\langle L_{\rm IR}/L_{1600} \rangle \approx 4.6$. This factor is in excellent agreement with the mean attenuation of $4.5 - 5.0$ inferred from stacked X-ray analyses (Reddy & Steidel 2004). One would observe a factor of $4 - 5$ attenuation in a galaxy one order of magnitude less luminous at $z = 0$ than at $z \sim 2$. The implication is that, while it is true that a larger fraction of star formation at high redshifts occurs in dustier systems, the dust obscuration we observe for galaxies of a given $L_{\rm bol}$ has less of an impact on observations of high redshift galaxies than one would have surmised on the basis of present day galaxies.

4.8 Properties of 24 μm Faint Galaxies

4.8.1 Ages and Masses of Faint 24 μm Galaxies

In addition to the information gleaned from the stacking analysis described above, we also have detailed information on the stellar populations of galaxies with faint mid-IR emission. Optical and near-IR selected galaxies undetected at 24 μm appear to have a distribution in ages that is similar to that of 24 μm detected galaxies (left panel of Figure 4.12), so young ages cannot explain why they are undetected at 24 μm. Alternatively, although we find a large range in inferred stellar mass of galaxies with $f_{24\mu\mathrm{m}} < 8$ μJy, the *mean* stellar mass of undetected objects is 0.4 dex lower in $\log M^*$ than 24 μm detected galaxies (right panel of Figure 4.12). Regardless of these small differences in the stellar populations of 24 μm detected and undetected sources, the X-ray data indicate that the primary reason why galaxies are undetected at 24 μm is because they have lower SFRs (Figure 4.4). We demonstrate in the next section how the rest-frame UV spectral properties of galaxies can be used to interpret their 24 μm emission.

4.8.2 Composite UV Spectra

A unique advantage of our optical BX/BM selection is the efficiency with which we are able to obtain rest-frame UV spectra for these galaxies, and this spectroscopy allows for an independent probe of the physical conditions in the ISM. While the S/N of any individual spectrum is typically too low to accurately measure interstellar absorption line widths, we can take advantage of the large number of spectra by stacking them to create a higher S/N composite spectrum. To investigate differences in the ISM as a function of infrared luminosity, we constructed composite UV spectra for (a) the top quartile of 24 μm detected BX/BM galaxies, and (b) all BX/BM galaxies undetected at 24 μm. In order to stack the spectra, we first de-redshifted them by the systemic redshift. The systemic redshift was inferred from a weighted combination of the measured absorption and/or emission line redshifts, following the procedure of Adelberger et al. (2003). We used the Rix et al. (2004) prescription to normalize the composite spectra to the underlying stellar continua. The detected and undetected composite spectra consist of 39 and 73 galaxies, respectively, and are shown in Figure 4.13. For comparison, the mean 24 μm flux of MIPS detected and

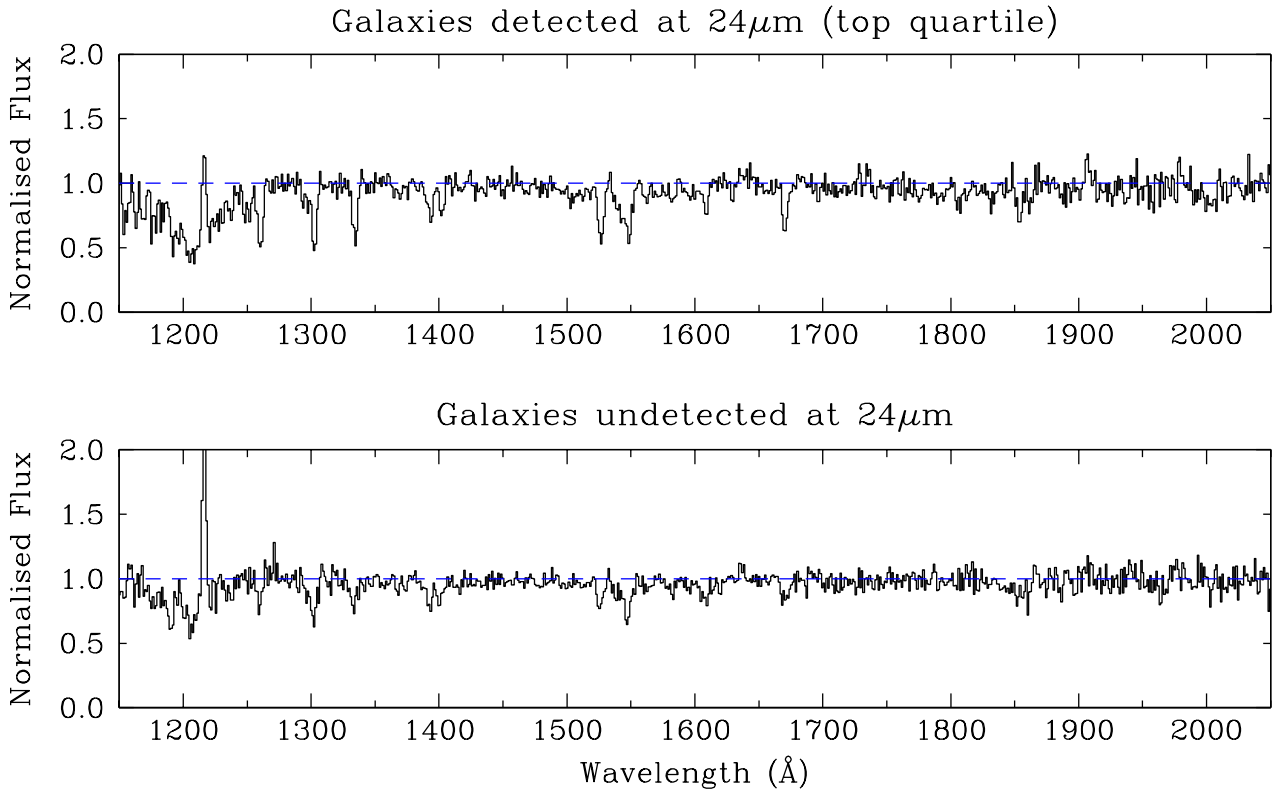

Figure 4.13 Normalized composite UV spectra for the 39 galaxies in the top quartile of 24 μm detected BX/BM galaxies (top) with $\langle f_{24\mu\mathrm{m}} \rangle \sim 100$ μJy and 73 BX/BM galaxies undetected at 24 μm (bottom) with $\langle f_{24\mu\mathrm{m}} \rangle \sim 3$ μJy.

undetected galaxies is $\langle f_{24\ \mu\mathrm{m}} \rangle \sim 100$ μJy and ~ 3 μJy, respectively; both subsamples have $\langle z \rangle \sim 2.1$. Table 4.3 lists the measured rest-frame equivalent widths of several interstellar absorption lines in the composite spectra. The primary difference between the rest-frame UV spectra of 24 μm detected and undetected galaxies is that the latter have interstellar absorption lines that are a factor of 2 weaker than the lines in the 24 μm detected galaxies. Because the line strengths are controlled by the combination of the velocity spread in outflowing interstellar material and the covering fraction of optically thick material, this indicates that galaxies weak in mid-IR emission are likely to have more quiescent ISM than 24 μm-bright galaxies, a result expected if those galaxies undetected by MIPS have lower SFRs, and hence lower energy input into the ISM and a lower level of dust enrichment, than 24 μm detected galaxies.

Comparing the mid-IR detections with non-detections, we find the latter have significantly stronger Lyα emission than the former. The emergent Lyα profiles of galaxies will

depend strongly on a number of physical parameters including the spectrum of UV radiation (i.e., the stellar IMF), presence of outflows, and dust covering fraction. Neglecting all of these effects, galaxies with larger SFRs will have stronger Lyα emission. However, given that the bolometric luminosity of star-forming galaxies scales with dust obscuration (e.g., Figure 4.11), we might expect 24 μm detected galaxies to have larger dust column densities than undetected galaxies; this may partly explain the absence of Lyα emission in 24 μm detected galaxies. In addition, the velocity spread of the ISM will also affect the emergent Lyα profile: the larger velocity spread in 24 μm detected galaxies, as indicated by their stronger interstellar absorption lines, implies most Lyα photons will have larger scattering path-lengths and are more likely to be attenuated by dust and/or scattered out of resonance (e.g., Hansen & Peng Oh 2005; Adelberger et al. 2003).

Finally, we note that the stacked X-ray analysis of 24 μm undetected galaxies confirms they have lower SFRs than 24 μm detected galaxies. Therefore, galaxies are undetected at rest-frame $5 - 8.5$ μm primarily because they have lower SFRs and not because they are deficient in mid-IR PAH luminosity for a given $L_{\rm IR}$. If such undetected galaxies had depressed MIR/IR flux ratios, we would not have expected to see as large a difference in the strengths of their interstellar absorption lines as compared with 24 μm detected galaxies.

4.9 Mid-IR Properties of Massive Galaxies at $z \sim 2$

The epoch between $z = 3$ and $z = 1$ appears to be the most active in terms of the buildup of stellar mass (e.g., Dickinson et al. (2003b), see also § 4.1), but significant numbers of massive galaxies ($M^* \gtrsim 10^{11}$ L$_\odot$) already appear to be in place by redshifts $z \sim 2$. The subsequent evolution of these massive galaxies and their relation to the local population of massive and passively evolving elliptical galaxies is an important question. It is useful to determine, therefore, what the mid-IR properties of massive galaxies tell us about their bolometric luminosities.

Figure 4.14 shows the bolometric luminosity of galaxies in the BX/BM, BzK, and DRG samples as a function of best-fit stellar mass. The mass modeling comes from the SED analysis where we have fit for the R+$JK_{\rm s}$+IRAC photometry assuming a constant star formation (CSF) model. As discussed elsewhere, the stellar mass is the most well-determined parameter from the SED analysis and is relatively insensitive to the assumed star formation

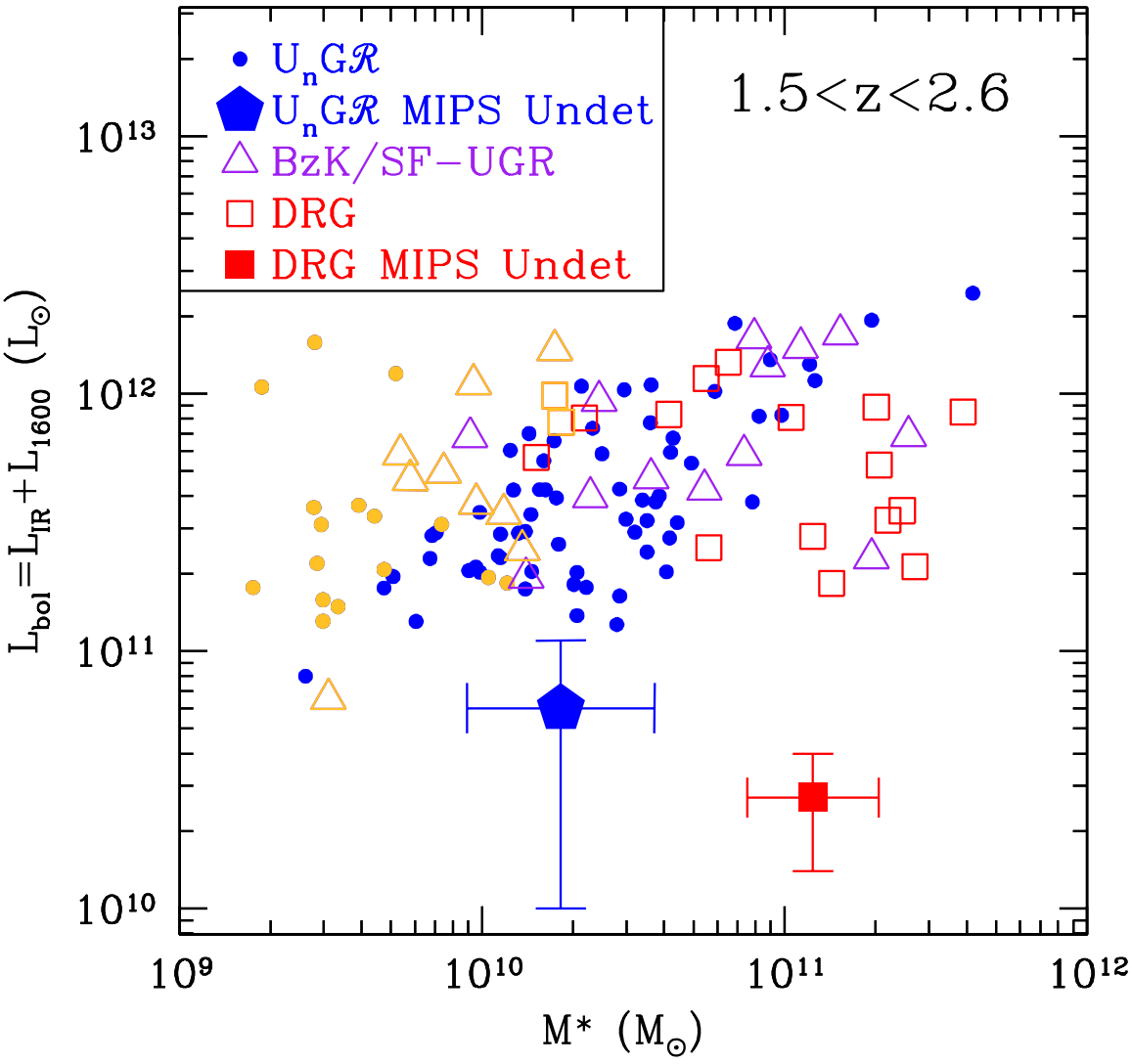

Figure 4.14 Inferred $L_{\rm bol}$ as a function of best-fit stellar mass assuming a CSF model for galaxies in the BX/BM, BzK, and DRG samples. We assumed a IR/MIR ratio of 17.2 to convert $L_{5-8.5\mu{\rm m}}$ to $L_{\rm IR}$. The large solid pentagon and square denote results for undetected BX/BM and the seven undetected DRG galaxies, respectively. The light gray (yellow) symbols indicate 24 μm detected galaxies with inferred ages $\leq$ 100 Myr.

history (Shapley et al. 2005; Papovich et al. 2001). There are several interesting aspects worth considering in Figure 4.14. First, we note that galaxies with the youngest inferred ages ($\lesssim$ 100 Myr) have low stellar masses ($M^* \lesssim 2 \times 10^{10}$ M$_\odot$) and span a large range in bolometric luminosity from LIRG- to ULIRG-type galaxies. Among BX/BM galaxies with spectroscopic redshifts $1.5 < z < 2.6$, we note a trend of increasing $L_{\rm bol}$ with stellar mass; BX/BM galaxies with $M^* \gtrsim 10^{11}$ M$_\odot$ have infrared luminosities typical of ULIRGs. The BzK/SF and DRG criteria cull $M^* \gtrsim 10^{11}$ M$_\odot$ galaxies with a large range in bolometric luminosity, from 10^{11} L$_\odot$ to $\gtrsim 10^{12}$ L$_\odot$. Optically selected sources undetected at 24 μm have stellar masses similar to those of detected BX/BM galaxies, but with $L_{\rm bol}$ a factor of ~ 10 lower. As noted before, the 24 μm emission from these galaxies appears to be primarily dependent on their current star formation rate. Finally, we note that DRGs undetected at 24 μm have similar stellar masses as those that are detected ($M^* \gtrsim 10^{11}$ M$_\odot$), but are on average 40 times less bolometrically luminous. As noted in § 4.5.2, these 24 μm-undetected DRGs have very red $(z-K)_{\rm AB}$ colors. Their faint 24 μm emission corroborates the results of X-ray stacking analyses that indicate these galaxies have very little current star formation (Reddy et al. 2005).

The results of Figure 4.14 suggest that galaxies with large stellar masses at $z \sim 2$ span a large range in bolometric luminosity, from galaxies with little star formation to ULIRG-type systems. The range is likely larger than what one would infer from Figure 4.14 since we have excluded directly detected X-ray sources that may be heavily star-forming galaxies and/or host AGN. Figure 4.14 suggests that $\gtrsim$ 70% of massive galaxies ($M^* > 10^{11}$ M$_\odot$) with redshifts $1.5 < z < 2.6$ in optical and near-IR surveys have $L_{\rm bol} \gtrsim 3 \times 10^{11}$ L$_\odot$ (or SFRs $\gtrsim 20$ $M_\odot$ yr^{-1}, assuming the SFR calibration of Kennicutt 1998a). Our results imply that most $1.5 < z < 2.6$ galaxies with large stellar masses ($M^* \gtrsim 10^{11}$ M$_\odot$) have levels of star formation that exceed those of LIRGs.

4.10 Discussion

4.10.1 Selection of LIRGs and ULIRGs at $z \sim 2$

In § 4.5.2 we showed that optical and near-IR selected samples to $\mathcal{R} = 25.5$, or $K_{\rm s} = 22$, host galaxies with a wide range in infrared luminosity, from a few times 10^{10} L$_\odot$ up to the

most luminous objects at these redshifts with $L_{\rm IR} > 10^{12}$ L$_\odot$. Typical galaxies in these samples have infrared luminosities in the range $10^{11} < L_{\rm IR} < 10^{12}$ L$_\odot$, similar in luminosity to, but with dust obscuration a factor of ~ 10 lower than (see § 4.7), local LIRGs. One advantage of optical (i.e., rest-frame UV) selection of LIRGs and ULIRGs at high redshift is that it allows for the kind of efficient spectroscopic followup necessary to accurately interpret the nature of 24 μm emission from these galaxies. As shown in § 4.4, the K-correction depends sensitively on redshift such that even for "good" photometric redshift estimates with $\delta z/(1+z) \sim 0.1$, the corresponding uncertainty in the rest-frame $5-8.5$ μm luminosity increases by a factor of 5. A unique aspect of our study combining the optical sample with MIPS observations is that the spectroscopic database can be used to assess the physical conditions of the ISM in galaxies as function of $L_{\rm bol}$, providing an additional method for probing the detailed nature of 24 μm galaxies at $z \sim 2$ (§ 4.8.2). Aside from the constraints on the mid-IR luminosities possible with spectroscopic redshifts, precise positions of sources from higher spatial resolution and shorter wavelength data enable the de-blending of most $z \sim 2$ galaxies. The de-blending procedure made possible by optical, near-IR, and *Spitzer* IRAC observations enable accurate identification and photometry of faint galaxies well below the MIPS 24 μm confusion limit and will provide a more complete "census" of the LIRG population at redshift $z \sim 2$ than possible using MIPS observations alone.

Further, selection by optical colors gives important information on the *unobscured* component of the star formation in galaxies and complements well the information on the obscured component probed by the 24 μm observations. Objects with lower star formation rates will have bolometric luminosities that are typically dominated by the observed UV emission and objects with larger star formation rates will have bolometric luminosities that are dominated by the observed IR emission. The transition between the UV and IR dominated regimes (i.e., where $L_{\rm IR} = L_{1600}$) at $z \sim 2$ occurs for galaxies with $L_{\rm IR} \approx 10^{11}$ L$_\odot$, or about $0.3L^*$ (Figure 4.11). A comparison with the $z = 0$ sample of Bell (2003) shows that the bolometric luminosities begin to be dominated by IR emission (i.e., $L_{\rm IR}/L_{1600} > 1$) for galaxies that are 2 orders of magnitude more luminous at $z \sim 2$ than at the present epoch. As discussed in § 4.7, this is plausibly explained as a result of higher dust-to-gas ratios in the local galaxies. More generally, galaxies of a given dust obscuration are anywhere

from 2 to 100 times more luminous at $z \sim 2$ than locally (Figure 4.11), with the greatest difference for galaxies with relatively low $L_{\rm IR}/L_{1600} \lesssim 20$. The implication of these observations is that while it is certainly true that a larger fraction of the star formation at high redshifts occurs in dustier galaxies, selection via rest-frame UV colors (and performing followup spectroscopy) is easier at high redshift than locally for galaxies at a given bolometric luminosity. Optical selection is therefore arguably the most promising and spectroscopically efficient method for selecting LIRGs (which undoubtedly accounts for a significant fraction of the star formation rate density and far-infrared background; e.g., Adelberger & Steidel 2000) at $z \sim 2$.

As demonstrated in § 4.5.2 and in Reddy et al. (2005), ULIRGs and SMGs at these redshifts also often appear in optical and near-IR selected samples; $\sim$ 50% of the most luminous SMGs have enough unobscured star formation that they satisfy the $z \sim 2$ optical criteria (Chapman et al. 2005). Accounting for the obscured portion of star formation in these ultraluminous sources of course requires the longer wavelength data since rest-frame UV slopes underpredict their $L_{\rm IR}$ (§ 4.6). In some sense, 24 μm observations are a more powerful method of estimating $L_{\rm bol}$ of these ultra-luminous sources since their detection significance at 24 μm is typically $50 - 100$ times larger and the beamsize is a factor of 9 smaller than at 850 μm. The ability to uniformly cover large areas of the sky with MIPS observations provides an additional advantage over current submillimeter surveys which suffer from areal and depth incompleteness, thus making it difficult to constrain the volumes probed. Using 24 μm observations to assess the global energetics of ultraluminous sources of course requires that we accurately calibrate the $L_{5-8.5\mu{\rm m}}/L_{\rm IR}$ ratios for these objects.

We have demonstrated that the typical galaxy in optical and near-IR samples of $z \sim 2$ galaxies has $L_{\rm IR}$ corresponding to that of LIRGs. A related issue is whether most LIRGs at $z \sim 2$ can be selected by their rest-frame UV or optical colors. A direct comparison of the number counts of MIPS sources to the number of 24 μm detected BX/BM and BzK galaxies to 8 μJy (the GOODS-N MIPS 24 μm 3 σ sensitivity limit) is not possible since (a) we primarily relied on the $K_{\rm s}$-band data to de-blend sources in the 24 μm imaging and (b) the redshift distribution of MIPS sources to 8 μJy is not yet well established. Nonetheless, including both optical and near-IR selected LIRGs at $z \sim 2$ ensures that

we must be reasonably "complete" for both optically-bright (and 24 μm-faint) LIRGs in the optical sample and optically-faint (and 24 μm-bright) LIRGs in the near-IR selected BzK and DRG samples. Galaxies with LIRG luminosities will predominantly have near-IR magnitudes bright enough to be considered in our analysis (i.e., $K_{\rm s} \lesssim 21$ according to the left panel of Figure 4.8). Objects not selected by these various criteria will likely either fall at different redshifts, not have LIRG luminosities, and/or may be scattered out of the color selection windows due to photometric error (e.g., Reddy et al. 2005). As an example of one form of photometric scatter, in the course of the $z \sim 3$ Lyman Break Galaxy Survey, we relied on BX/BM photometry based on images of the HDF-North field taken at the Palomar Hale 5 m Telescope (Steidel et al. 2003). We subsequently imaged a larger portion of the GOODS-North field using the Keck I Telescope (Steidel et al. 2004). Our photometric analysis indicates that of the BX/BM objects to $\mathcal{R} = 25.5$ identified in the Palomar imaging, about 76% were recovered as BX/BM objects in the Keck imaging. A small fraction of the remaining 24% were recovered using LBG selection. The level of scatter between different photometric realizations in other fields is also typically $\sim 25\%$ and is mostly due to the narrow photometric windows used to select BX/BM galaxies. Regardless of these photometric effects, it is highly unlikely that there exist large numbers of LIRGs at $z \sim 2$ with such different optical and near-IR properties that they would be completely absent from all the samples considered here. Finally, our knowledge of the exact positions of optical and near-IR selected galaxies from the higher spatial resolution $K_{\rm s}$-band and IRAC data allows us to mitigate the effects of confusion (see § 4.3), so we should be reasonably complete for galaxies that are detected at 24 μm to 8 μJy but which might otherwise be confused with brighter sources. It is therefore reasonable to conclude that the LIRG population at $z \sim 2$ is essentially the same population of galaxies that are selected in optical and near-IR samples.

4.10.2 Mass Assembly at High Redshift

We demonstrated that LIRGs and ULIRGs are present over the full range of stellar mass, from $\sim 2 \times 10^9$ M$_\odot$ to 5×10^{11} M$_\odot$, for galaxies in the samples considered here (Figure 4.14). To assess the significance of the current star formation in the buildup of stellar mass, we have computed the specific star formation rate, ϕ, defined as the SFR per unit stellar

mass. We show the observed ϕ for galaxies in our sample as function of stellar mass in Figure 4.15. The correlation between ϕ and M^* could have been predicted from Figure 4.14 since the range of $L_{\rm bol}$ is similar over the range of M^* considered here. We also note that the correlation is accentuated since (a) ϕ is not independent of M^* and (b) there are presumably galaxies with low ϕ and low M^* that would be missing from the optical and near-IR samples (irrespective of the MIPS detection limit). Furthermore, the upper envelope of points in Figure 4.15 is defined by our cut to exclude luminous AGN based on the *Chandra* X-ray data. Nonetheless, we find that star-forming galaxies with large stellar masses $M^* \gtrsim 10^{11}$ M$_\odot$ without AGN signatures have specific SFRs that are 1 to 2 orders of magnitude lower than those of young galaxies (yellow symbols), implying that the current star formation contributes more significantly to the buildup of stellar mass in low mass galaxies than high mass galaxies at $z \sim 2$. This change in specific SFR as a function of mass has been observed at later epochs as well (e.g., Bell et al. 2005). The shifting of the relationship to lower specific SFRs at later epochs for galaxies with large stellar masses has been referred to as "downsizing" (Cowie et al. 1996).

The most massive, star-forming DRGs at these redshifts with large dust-to-gas ratios (see Figure 4.11) also have the lowest ϕ for MIPS-detected galaxies at $z \sim 2$. Papovich et al. (2006) demonstrate that the integrated specific SFR of these massive DRGs at $z \sim 2$ is ~ 2 magnitudes larger than for galaxies with similar masses ($M^* > 10^{11}$ M$_\odot$) at lower redshifts $0.3 \leq z < 0.5$, based on a comparison with the COMBO-17 sample (Bell et al. 2005). This decrease in ϕ suggests that $M^* > 10^{11}$ M$_\odot$ galaxies have built up most of their stellar mass by $z \sim 2$. In fact, the mass-doubling time becomes increasingly large for these massive galaxies if we assume the case of an exponentially declining star formation model. In this case, ϕ will evolve with time t as

$$\phi(t) = \frac{(1+f)\exp(-t/\tau)}{\tau[1-\exp(-t/\tau)]}, \tag{4.6}$$

where f is the ratio of the gas mass that is lost due to outflows to that formed in stars and τ is the star formation decay timescale as defined in § 4.4. Given some initial SFR, a CSF model (i.e., with $\tau = \infty$) will track straight through the points corresponding to galaxies with $M^* \gtrsim 10^{11}$ M$_\odot$, but such a model would predict a ϕ at $z \sim 0.4$ that is ~ 5 times larger than observed at $z \sim 0.4$ in the COMBO-17 survey (Bell et al. 2005). Therefore, a

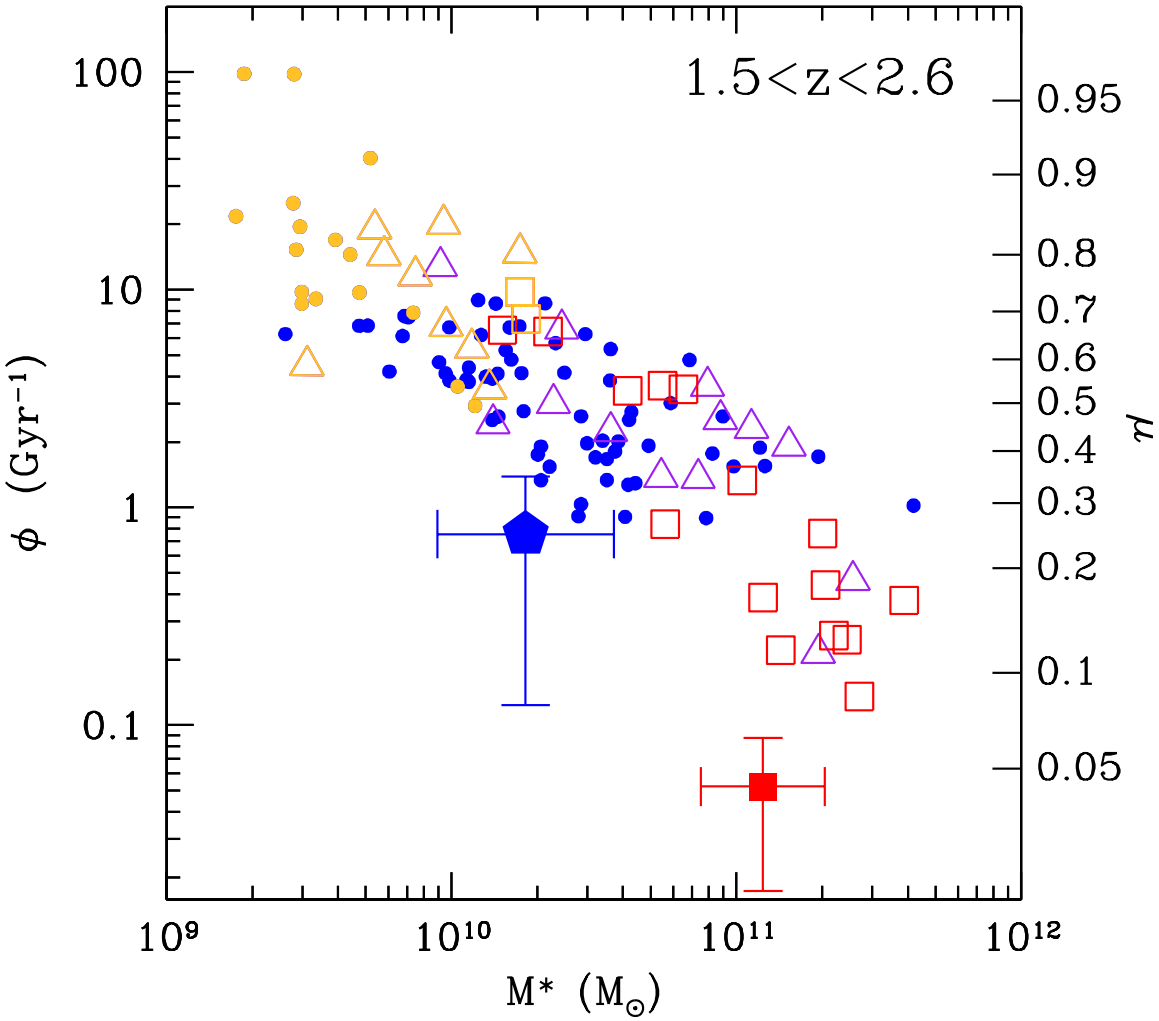

Figure 4.15 Specific SFR, ϕ, as a function of stellar mass for galaxies in the samples considered here. Symbols are the same as in Figure 4.14 (yellow symbols indicate galaxies with inferred ages $\lesssim$ 100 Myr). The right-hand axis indicates the gas fraction μ associated with galaxies of a given ϕ.

declining star formation history may be more appropriate for describing the future evolution of galaxies with large stellar masses at $z \sim 2$. In particular, Erb et al. (2006a) find that a model that assumes a super-solar yield of metals (i.e., ratio of mass of metals ejected into the ISM to mass of metals locked in long-lived stars) of $y = 1.5$ $Z_{\odot}$ and an outflow rate of 4 $\times$ SFR ($f = 4$) appears to best-fit the observed metallicities of BX/BM galaxies at $z \sim 2$ as a function of gas fraction. If all star-forming galaxies at $z \sim 2$ follow a similar evolutionary track as the $M^* > 10^{11}$ $M_{\odot}$ galaxies (i.e., follow an exponentially declining star formation history with large outflow rate), then the scatter of galaxies with a given specific SFR simply reflects the range in the final stellar masses and dark matter halo masses (see also discussion in Erb et al. 2006a).

We can directly relate the specific SFR ϕ with the cold gas fraction, $\mu \equiv M_{\rm gas}/(M_{\rm gas} + M^*)$. If we assume that the SFR is proportional to the cold gas mass, $M_{\rm gas}$, to the 1.4 power according to the Schmidt law (Kennicutt 1998b), then

$$\phi \propto \frac{M_{\rm gas}^{1.4}}{M^*}. \tag{4.7}$$

It then follows that

$$\phi = C \frac{\mu^{1.4}}{1-\mu}, \tag{4.8}$$

where C is a constant that depends on the constant of proportionality between the SFR and gas mass surface densities in the Schmidt law and the total gas mass at virialization (i.e., when star formation commences). There is a one-to-one correspondence between the specific SFR, ϕ, and gas fraction, μ, such that galaxies with large specific SFRs will have a larger fraction of cold gas than galaxies with small specific SFRs. Erb et al. (2006c) demonstrate that μ decreases as a function of stellar mass for a large sample of BX/BM galaxies with Hα spectroscopy, with a mean μ across the sample of $\langle \mu \rangle \sim 0.5$. The mean specific SFR for these galaxies is $\langle \phi \rangle \sim 3$ Gyr^{-1}. Using these mean values to estimate C, we show the range of μ on the right-hand axis of Figure 4.15. Young galaxies with ages less than 100 Myr in our sample also have the largest gas fractions ($\mu \sim 0.6 - 0.9$) and largest specific SFRs (Figure 4.15) compared with older galaxies at $z \sim 2$. These results strongly suggest that the young galaxies have large reservoirs of cold gas and have just begun forming stars. Similarly,

galaxies with the largest stellar masses have lower specific SFRs and therefore lower cold gas fractions ($\mu \sim 0.1 - 0.3$) and are likely to cease star formation in a relatively short time. The correlation between ϕ and M^* revealed by Figure 4.15 is actually expected from the trend between μ and M^* inferred from the Hα spectroscopic analysis of Erb et al. (2006c). Furthermore, Erb et al. (2006a) find a tight trend between metallicity and gas fraction such that galaxies with lower μ are more metal-rich. These galaxies will therefore be more dust-obscured since metallicity is directly proportional to dust-to-gas ratio. Our analysis confirms our expectation that the most dust-obscured objects at $z \sim 2$ (i.e., the DRGs with the largest dust-to-gas ratios, Figure 4.11) also have low gas fractions as demonstrated in Figure 4.15. Figure 4.15 indicates that the trend in gas fraction versus stellar mass (or, metallicity versus gas fraction) found for BX/BM-selected galaxies with Hα spectroscopy (Erb et al. 2006a) also applies to galaxies selected by their near-IR colors.

Combining the optical and near-IR samples, we find a wide range in the evolutionary state of galaxies at $z \sim 2$, from those that are just starting to form stars to those which have already accumulated most of their stellar mass and are about to become passive or already are. Almost all DRGs with the reddest $(z - K)_{\rm AB}$ color ($(z - K)_{\rm AB} > 3$) are undetected at 24 μm and in the deep *Chandra* X-ray data (e.g., see right panel of Figure 4.8, and Figure 16 in Reddy et al. 2005). The specific SFRs of these red DRGs are the lowest observed for the $z \sim 2$ galaxies considered here; they have cold gas fractions of less than 5%, confirming that they have essentially shut off star formation by $z \sim 2$. The star-forming DRGs with $M^* > 10^{11}$ M$_\odot$ (which are dusty and metal-rich as inferred from their large dust-to-gas ratios; cf. Figure 4.11) are likely to reach this passively-evolving state by redshifts $z \lesssim 1.5$. A simple model that assumes a high outflow rate proportional to the SFR and exponentially declining star formation history (i.e., the model that appears to best-fit the observed metallicities of galaxies as function of gas fraction; Erb et al. 2006a) is sufficient to explain the presence of galaxies with large stellar masses and little star formation by $z \sim 2$ without invoking AGN feedback, despite the fact that a large AGN fraction of $\sim 25\%$ is observed among galaxies with large stellar masses (Reddy et al. 2005).

4.11 Conclusions

We use *Spitzer* MIPS data to examine the bolometric luminosities and extinction properties of optical and near-IR selected galaxies at redshifts $1.5 \lesssim z \lesssim 2.6$ in the GOODS-North field. At these redshifts, the mid-IR ($5 - 8.5$ μm) features associated with polycyclic aromatic hydrocarbon (PAH) emission, which are ubiquitous in local and $z \sim 1$ star-forming galaxies, are shifted into the MIPS 24 μm filter. Extensive multi-wavelength data in the GOODS-North field, including very deep *Chandra* X-ray data, allow us to test the validity of inferring the bolometric luminosities of high redshift galaxies from their rest-frame $5 - 8.5$ μm emission. Galaxies at $z \sim 2$ are selected by their optical (BX/BM) and near-IR (BzK and $J - K_{\rm s}$) colors, and for comparison we also consider radio-detected submillimeter galaxies (SMGs; Chapman et al. 2005). The optically-selected sample is advantageous because we have knowledge of the precise redshifts of $\gtrsim 300$ galaxies from spectroscopy, allowing for the most accurate estimates of the rest-frame mid-IR luminosities of $z \sim 2$ galaxies. In addition to our spectroscopic sample, we use deep optical, near-IR, and *Spitzer* IRAC data to derive photometric redshifts for BzK galaxies and those with red $J - K_{\rm s} > 2.3$ colors (Distant Red Galaxies; DRGs). The principle conclusions of this study are as follows:

1. Using local templates to K-correct the observed 24 μm fluxes, we find that the rest-frame $5 - 8.5$ μm luminosity ($L_{5-8.5\mu{\rm m}}$) of $z \sim 2$ galaxies correlates well with their stacked X-ray emission. A subset of galaxies with Hα measurements have Hα-inferred bolometric luminosities that correlate very well with their $L_{5-8.5\mu{\rm m}}$-inferred bolometric luminosities (with a scatter of 0.2 dex). These observations suggest that $L_{5-8.5\mu{\rm m}}$ provides a reliable estimate of $L_{\rm IR}$ for most star-forming galaxies at $z \sim 2$.

2. We find that the optical and near-IR selected $z \sim 2$ galaxies span a very wide range in infrared luminosity from LIRG to ULIRG objects. We find a mean infrared luminosity of $\langle L_{\rm IR} \rangle \sim 2 \times 10^{11}$ L$_\odot$ for galaxies in the optical and near-IR samples, in excellent agreement with the value obtained from a stacked X-ray analysis. The optical and near-IR selected star-forming galaxies likely account for a significant fraction of the LIRG population at $z \sim 2$. Galaxies with $K_{\rm s} < 20$ have $L_{\rm IR}$ greater than 2 times that of galaxies with $K_{\rm s} > 20.5$. Non-AGN galaxies with the reddest near-IR colors ($(z - K)_{\rm AB} > 3$) are mostly undetected at 24 μm suggesting they have low SFRs, a conclusion supported by stacked X-ray analyses.

3. We demonstrate using 24 μm and X-ray stacking analyses that galaxies undetected

to $f_{24\mu m} \sim 8$ μJy are faint because they have lower SFRs and/or lower obscuration than 24 μm detected galaxies, and not because they are deficient in PAH emission at a given $L_{\rm IR}$. We infer that typically half of the bolometric luminosity of these 24 μm undetected galaxies is emitted in the UV. Comparing the rest-frame UV composite spectra of 24 μm undetected galaxies with those in the top quartile of detected objects shows that the latter have low-ionization interstellar absorption lines that are ~ 2 times stronger than the former, indicating some combination of more turbulent interstellar media and a larger neutral gas covering fraction. This is consistent with our conclusion that galaxies undetected at 24 μm have lower SFRs than 24 μm detected galaxies, and therefore a lower input of kinetic energy and dust into their ISM.

4. The 24 μm (and deep X-ray) data indicate that galaxies whose current star formation episodes are older than 100 Myr and have infrared luminosities $10^{10} \lesssim L_{\rm IR} \lesssim 10^{12}$ L$_\odot$ appear to follow the local relation between rest-frame UV slope and dust obscuration, implying that such galaxies at $z \sim 2$ have moderate amounts of dust extinction and that their UV slopes can be used to infer their extinction. Galaxies younger than 100 Myr have rest-frame UV colors that are redder than expected given their inferred $L_{\rm IR}$, indicating they may obey a steeper extinction law. These young galaxies have the lowest stellar masses, but span the same range in bolometric luminosity as galaxies with larger stellar masses.

5. Galaxies with $L_{\rm bol} \gtrsim 10^{12}$ L$_\odot$, including radio-detected SMGs, are typically ~ 10 to 100 times more dust obscured than their UV spectral slopes would indicate, assuming their 850 μm-inferred infrared luminosities. The 24 μm inferred infrared luminosities of radio-detected SMGs are systematically a factor of $2-10$ times lower than those predicted by their 850 μm fluxes; adopting the 24 μm estimates implies dust attenuation factors that are $\sim 5-50$ times larger than their UV spectral slopes would indicate. Regardless, such galaxies will often be blue enough to satisfy the BX/BM criteria, so finding these dust obscured galaxies in optical surveys is not uncommon.

6. A comparison between the dust obscuration in $z \sim 2$ and $z = 0$ galaxies suggests that galaxies of a *given* bolometric luminosity are much less dust obscured (by a factor of $\sim 8-10$) at high redshift than at the present epoch. This result is expected (a) as galaxies age and go through successive generations of star formation and dust production and (b) if the distribution of dust and star formation in galaxies becomes more compact over time

(e.g., through mergers or interactions) resulting in greater dust column densities towards star-forming regions. We find that star-forming Distant Red Galaxies (DRGs) with stellar masses $M^* \gtrsim 10^{11}$ $M_\odot$ and ages $\gtrsim 2$ Gyr have bolometric luminosities and dust-obscuration factors similar to those of local ULIRGs, suggesting that such DRGs, like local ULIRGs, carry relatively large amounts of dust into their current episodes of star formation.

7. Galaxies with the largest stellar masses at $z \sim 2$ ($M^* \gtrsim 10^{11}$ $M_\odot$) also span a large range in bolometric luminosity, from those that have red near-IR colors ($(z-K)_{\rm AB} > 3$) with little current star formation to those ULIRG objects found among optical and near-IR selected massive galaxies. Our results suggest $\gtrsim 70\%$ of massive galaxies ($M^* \gtrsim 10^{11}$ $M_\odot$) in optical and near-IR surveys with redshifts $1.5 < z < 2.6$ have $L_{\rm bol} \gtrsim 3 \times 10^{11}$ $L_\odot$ (SFRs $\gtrsim 20$ $M_\odot$ yr^{-1}), comparable to and exceeding the luminosity of LIRGs.

8. Similar to lower redshift studies, we find a trend between specific SFR (SFR per unit stellar mass) and stellar mass at $z \sim 2$, which indicates that the observed star formation contributes more to the buildup of stellar mass in galaxies with low stellar masses than in those with larger stellar masses at $z \sim 2$. This trend between specific SFR and stellar mass indicates a strong decrease in cold gas fraction as function of stellar mass, consistent with results from near-IR spectroscopic observations, and suggests that galaxies with large stellar masses ($M^* > 10^{11}$ $M_\odot$) at $z \sim 2$ will quickly cease star formation. Combining optical and near-IR selected samples, we find a large range in the evolutionary state of galaxies at $z \sim 2$, from those that have just begun to form stars and that have large gas fractions to those that are old, massive, and have little remaining cold gas.

We thank Natascha Förster Schreiber and Helene Roussel for providing their ISO spectra of local galaxies, and David Elbaz for providing an electronic catalog of the mid-IR and IR luminosities of local star-forming galaxies. We also thank the referee, Emeric Le Floc'h, for useful comments. The work presented here has been supported by grant AST 03-07263 from the National Science Foundation and by the David and Lucile Packard Foundation. We made use of the NASA/IPAC Extragalactic Database (NED), which is operated by the Jet Propulsion Laboratory, California Institute of Technology, under contract with NASA.

Table 4.1. Properties of the Samples

Sample	Limits	N_c[a]	N_x[b]	ρ[c] (arcmin^{-2})	N_s[d]	$\langle z \rangle$[e]	N_g[f]	f_m[g]
BX/BM (BX/BM/LBG)	$\mathcal{R} < 25.5$	1571	23	10.2 ± 0.3	313	2.25 ± 0.33	219	0.65
BzK/SF	$K_s < 21.0$	221	32	3.1 ± 0.2	53	2.09 ± 0.34	82	0.82
BzK/PE	$K_s < 21.0$	17	4	0.24 ± 0.06	0	1.70 ± 0.20	13	0.54
DRG[h]	$K_s < 21.0$	73	19	1.0 ± 0.1	5	2.48 ± 0.35	24	0.71

[a]Number of candidates.

[b]Number of directly detected X-ray sources, including spectroscopically confirmed galaxies.

[c]Surface density of candidates. Errors are computed assuming Poisson statistics.

[d]Number of spectroscopically confirmed objects with $z > 1.5$. Note that we only obtained spectra for those BzK and DRG galaxies that satisfy the BX/BM criteria.

[e]Mean redshift of sample for $z > 1.5$. For the BzK/PE sample, this is the mean redshift of the *photometric* redshift distribution observed for BzK/PE galaxies (e.g., Daddi et al. 2004a;Reddy et al. 2005). For the DRGs, this is the mean redshift of the *spectroscopic* redshift distribution observed for DRGs with $z > 1.5$ in four of the fields of the $z \sim 2$ optical survey (Reddy et al. 2005).

[f]Number of non-AGN galaxies (i.e., those with no direct X-ray detections) with spectroscopic redshifts $1.5 < z < 2.6$. For the BzK/SF sample, this number includes both spectroscopically confirmed BzK/SF galaxies (all of which are in the BX/BM sample) and those with secure photometric redshifts. For the BzK/PE sample, this includes all candidates without direct X-ray detections. For the DRG sample, this number includes galaxies with photometric redshifts $1.5 < z < 2.6$.

[g]Fraction of MIPS 24 μm detections to 8 μJy (3 σ) among the N_g galaxies.

[h]The DRG sample includes both star-forming galaxies and those with little star formation. As discussed in Reddy et al. (2005), those with spectra (i.e., those DRGs that also satisfy the BX/BM criteria) are likely to be currently forming stars.

Table 4.2. Local Template Galaxies

Name[a]	z[b]	$L_{\rm IR}$ ($\times 10^{10}$ L$_\odot$)
M82	0.000677	4.8
NGC253	0.000811	1.8
M83	0.001711	1.9
M51	0.002000	2.4
NGC1808	0.003319	3.8
NGC1097	0.004240	3.8
NGC1365	0.005457	8.7
NGC520	0.007609	6.5
NGC7714	0.009333	5.6
NGC3256	0.009386	40
NGC6240	0.024480	60
IRS9	1.83	1800

[a]All galaxies are compiled from Förster Schreiber et al. (2004a) and Roussel et al. (2001), except for IRS9 and NGC7714 which are taken from Yan et al. (2005). The bolometric luminosity of IRS9 is constrained within a factor of 2 to 3 (Yan et al. 2005).

[b]Redshifts for local galaxies are obtained from NASA/IPAC Extragalactic Database (NED).

Table 4.3. Interstellar Absorption Line Wavelengths and Equivalent Widths for 24 μm Detected and Undetected BX/BM Galaxies

Line	$\lambda_{\rm trans}$[a]	Detected W_λ[b]	Undetected W_λ[b]
Si II	1260.4	2.58	0.99
OI + Si II	1303.3	2.27	1.58
C II	1334.5	2.05	0.94
Si II	1526.7	2.36	1.32
Fe II	1608.5	0.87	1.15
Al II	1670.8	1.85	1.15
Al III	1854.7	1.66	0.55
Al III	1862.8	0.81	0.64

[a]Transition wavelength in Å.

[b]Measured rest-frame equivalent width in Å.

¿

Chapter 5

A SPECTROSCOPIC SURVEY OF REDSHIFT $1.4 \lesssim Z \lesssim 3.0$ GALAXIES IN THE GOODS-NORTH FIELD: SURVEY DESCRIPTION, CATALOGS, AND PROPERTIES*†

Naveen A. Reddy,[a] Charles C. Steidel,[a] Dawn K. Erb,[b] Alice E. Shapley,[c] & Max Pettini,[d]

[a]California Institute of Technology, MS 105–24,Pasadena, CA 91125

[b]Harvard-Smithsonian Center for Astrophysics, 60 Garden Street, Cambridge, MA 02138

[c]Department of Astrophysical Sciences, Peyton Hall-Ivy Lane, Princeton, NJ 08544

[d]Institute of Astronomy, Madingley Road, Cambridge CB3 OHA, UK

*Based on data obtained at the W. M. Keck Observatory, which is operated as a scientific partnership among the California Institute of Technology, the University of California, and NASA, and was made possible by the generous financial support of the W. M. Keck Foundation.

†A version of this chapter was submitted to *The Astrophysical Journal*.

Abstract

We present the results of a spectroscopic survey with the Low Resolution Imaging Spectrograph on the Keck I telescope of more than 280 star-forming galaxies and AGN at redshifts $1.4 \lesssim z \lesssim 3.0$ in the GOODS-North field. Candidates are selected by their BX/BM colors using the "BM" and "BX" criteria to target redshift $1.4 \lesssim z \lesssim 2.5$ galaxies and the Lyman break criteria to target redshift $z \sim 3$ galaxies; combined, these samples account for $\sim 25-30\%$ of the R and K_s-band counts to $\mathcal{R} = 25.5$ and $K_s(\mathrm{AB}) = 24.4$, respectively. The sample of 212 BM/BX galaxies and 74 LBGs is presently the largest spectroscopic sample of galaxies at $z > 1.4$ in GOODS-N. Extensive multi-wavelength data, including our very deep ground-based near-IR imaging to $K_s(\mathrm{AB}) = 24.4$, allow us to investigate the stellar populations, stellar masses, bolometric luminosities (L_{bol}), and extinction of $z \sim 2$ galaxies. Deep *Chandra* X-ray and *Spitzer* IRAC and MIPS data indicate that the sample includes galaxies with a wide range in L_{bol}, from $\simeq 10^{10}$ $\mathrm{L}_\odot$ to $> 10^{12}$ $\mathrm{L}_\odot$, and 4 orders of magnitude in dust obscuration ($L_{\mathrm{bol}}/L_{\mathrm{UV}}$). The sample includes galaxies with a large dynamic range in evolutionary state, from very young galaxies (ages $\simeq 50$ Myr) with small stellar masses ($M^* \simeq 10^9$ $\mathrm{M}_\odot$) to evolved galaxies (ages > 2 Gyr) with stellar masses comparable to the most massive galaxies at these redshifts ($M^* > 10^{11}$ $\mathrm{M}_\odot$). *Spitzer* data indicate that the optical sample includes some fraction of the obscured AGN population at high redshifts: at least 3 of 11 AGN in the $z > 1.4$ sample are undetected in the deep X-ray data but exhibit power-law SEDs longward of ~ 2 μm (rest-frame) indicative of obscured AGN. The results of our survey indicate that rest-frame UV selection and spectroscopy presently constitute the most time-wise *efficient* method of culling large samples of high redshift galaxies with a wide range in intrinsic properties, and the data presented here will add significantly to the multi-wavelength legacy of the GOODS survey.

5.1 Introduction

Rapid advances in our understanding of galaxy evolution have been prompted by the recognition that observations covering the full spectrum are necessary to adequately interpret the physical nature of galaxies. Multi-color *Hubble Space Telescope* (*HST*) imaging of two otherwise inconspicuous fields in the high Galactic latitude sky (Williams et al. 1996, 2000)

marked the inception of a decade dominated by large-scale multi-wavelength surveys. The two *Hubble* Deep Fields are now encompassed or near other areas of the sky that are the focus of a number of space and ground-based observations both within and peripheral to the *Great Observatories Origins Deep Survey* (GOODS; Dickinson et al. 2003a). Included among these data are the deepest *Chandra* X-ray observations (Alexander et al. 2003), *HST* ACS optical imaging (Giavalisco et al. 2004b), *Spitzer* IR to far-IR imaging (Dickinson et al., in prep; Chary et al., in prep), *GALEX* far and near-UV imaging (Schiminovich et al. 2003), ground-based optical and near-IR imaging and spectroscopy (Capak et al. 2004; Cowie et al. 2004; Vanzella et al. 2005), and radio/submillimeter observations (Richards 2000; Pope et al. 2005).

Despite the easy access to broadband photometry and subsequent insights into galaxy evolution made possible by multi-wavelength surveys such as GOODS, important issues regarding survey completeness and the physical conditions in galaxies and their surrounding intergalactic medium can only be investigated spectroscopically. Spectroscopy of galaxies in blind flux-limited surveys can be quite inefficient and expensive, particularly if one only wants to study galaxies at certain cosmological epochs. However, we have shown that the technique of photometric pre-selection can allow one to cull large samples of galaxies in particular redshift ranges over a large range in redshift $1.0 \lesssim z \lesssim 4$ (e.g., Adelberger et al. 2004; Steidel et al. 2004, 2003, 1995; Steidel & Hamilton 1993), which can then be efficiently followed up using multi-object optical spectrographs such as the Low Resolution Imaging Spectrograph (LRIS) on the 10 m Keck telescope. Near-UV sensitive spectrographs such as the blue arm of LRIS (LRIS-B) on Keck and the Focal Reducer/low dispersion Spectrograph (FORS) on the VLT have significantly extended our capabilities by allowing for spectroscopy of key features that fall shortward of the OH emission forest for redshifts $1.4 \lesssim z \lesssim 3$, a particularly active epoch in the context of galaxy evolution and the buildup of stellar and black hole mass. To take advantage of extensive multi-wavelength data, we included the GOODS-North (GOODS-N, hereafter) field in our ongoing survey to select and spectroscopically follow up large samples of galaxies at redshifts $1.4 \lesssim z \lesssim 3.0$ (Steidel et al. 2004). In the interest of public dissemination of data, we present in this paper the results of our spectroscopic survey of $1.4 \lesssim z \lesssim 3.0$ star-forming galaxies in the GOODS-N field including associated photometry and spectroscopic redshifts. Information on the galaxies, including

their photometric measurements and errors and stellar population fits, are available at the following public website: http://www.astro.caltech.edu/∼drlaw/GOODS/.

The outline of this paper is as follows. In § 5.2 we briefly describe the optical imaging, photometry, and spectroscopy. To supplement these, we have also obtained the deepest wide-area near-IR J and K-band imaging in the GOODS-North field, and these data are also presented in § 5.2. The spectroscopic results and associated catalog are presented in § 5.3. We describe the *Spitzer* IRAC and MIPS data (taken from the GOODS-N public release; Dickinson et al. in prep. and Chary et al. in prep.) for our spectroscopic sample of galaxies in § 5.4. Ground-based photometry and *Spitzer* IRAC data, together with spectroscopic redshifts, enable the modeling of the stellar populations of galaxies given certain simplifying assumptions. Our modeling procedure and results are discussed in § 5.5. In § 5.6 we describe a few characteristics of the sample of star-forming galaxies and AGN to demonstrate the wide range in intrinsic properties of UV-selected galaxies at high redshift. A flat ΛCDM cosmology is assumed with $H_0 = 70$ km s^{-1} Mpc^{-1} and $\Omega_\Lambda = 0.7$. All magnitudes are on the AB (Oke & Gunn 1983) system.

5.2 Data and Sample Selection

5.2.1 Optical and Near-IR Imaging and Photometry

The imaging, photometry, color selection, and spectroscopic observations of galaxies in the fields of our $z \sim 2$ survey are described in several other papers published by our group (Steidel et al. 2003, 2004; Adelberger et al. 2004; Reddy et al. 2005). Specific details regarding the GOODS-N optical imaging are presented in Reddy et al. (2005) and summarized below for convenience.

The optical images used to photometrically pre-select candidate galaxies at redshifts $1.4 \lesssim z \lesssim 3.0$ in the GOODS-N field were obtained in April 2002 and 2003 with the KPNO and Keck I telescopes. The KPNO MOSAIC U-band image obtained from the GOODS team (PI: Giavalisco) was transformed to $U_{\rm n}$ magnitudes (Steidel et al. 2004). The Keck I G- and $\mathcal{R}$-band images were taken with the LRIS instrument (Oke et al. 1995; Steidel et al. 2004) and were oriented to ensure maximum overlap with the GOODS *Spitzer* Legacy and *Hubble* Treasury programs. The images cover $11' \times 15'$ with FWHM $\sim 0\farcs7 - 1\farcs1$ to a limiting

magnitude of ~ 27.5 measured within a $1''$ aperture ($3\,\sigma$) in the BX/BM bands. This depth ensures we are complete to $\mathcal{R} = 25.5$, neglecting photometric scatter, for galaxies whose colors satisfy our $z \sim 2-3$ color criteria. The optical imaging reduction and photometry were done following the procedures described in Steidel et al. (2003, 2004). The images were astrometrically calibrated using the SDSS database. Source detection is done at $\mathcal{R}$-band, and $G-\mathcal{R}$ and $U_{\rm n}-G$ colors are computed by applying the $\mathcal{R}$-band isophotal apertures to images in the other filters.

We have obtained very deep wide-area near-IR imaging at $J-$ and $K_{\rm s}$-band in the GOODS-N field from observations with the Wide Field Infrared Camera (WIRC; Wilson et al. 2003) on the Palomar Hale 5 m telescope. The images, taken under photometric conditions with $\sim 1\farcs0$ FWHM, reach a depth of $K_{\rm s} \sim 24.4$ and $J \sim 25.0$ over the central $8\farcm7 \times 8\farcm7$ of the GOODS-N field. The near-IR imaging reduction procedure is described in detail by Erb et al. (2006c). Near-IR magnitudes were calibrated in Vega magnitudes and converted to AB units assuming the following conversions: $K_{\rm s}(AB) = K_{\rm s}(Vega) + 1.82$ and $J(AB) = J(Vega) + 0.90$. Figure 5.1 shows the area imaged in the near-IR with respect to our optical image of the GOODS-N field.

Photometric errors for both optical and near-IR magnitudes were determined from Monte Carlo simulations. We added large numbers of simulated galaxies with known magnitudes to our images and then recovered them using the same photometric method used to detect actual galaxies. Comparing the input magnitudes with those recovered then yields an estimate of the bias and uncertainty in our photometry. The Monte Carlo method is discussed in more detail by Shapley et al. (2005). The typical errors in the optical and near-IR magnitudes range from 0.05 to 0.3 mag.

5.2.2 Photometric Selection

We selected galaxies in different redshift ranges between $1.4 \lesssim z \lesssim 3.4$ using the "BM," "BX," "C," "D," and "MD" selection criteria (Steidel et al. 2003; Adelberger et al. 2004; Steidel et al. 2004). The C, D, and MD criteria are used to select Lyman Break Galaxies (LBGs) at redshifts $2.7 \lesssim z \lesssim 3.3$ (Steidel et al. 2003)[1]. The "BM" and "BX" criteria were

[1]Note that we did not select "M" galaxies in GOODS-N as was done in other fields of the $z \sim 3$ survey (Steidel et al. 2003).

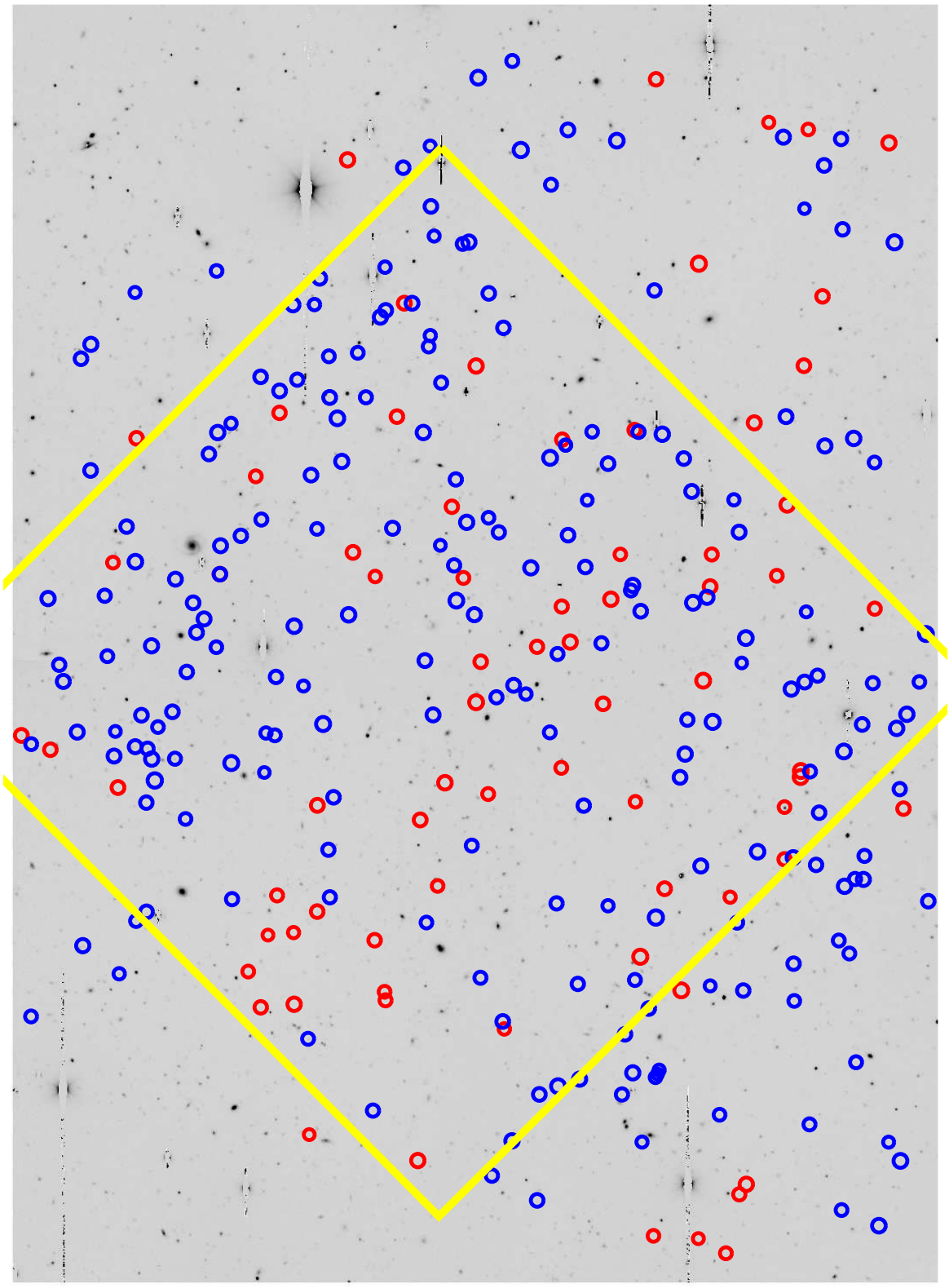

Figure 5.1 Positions of BX/BM (blue circles) and LBG (red circles) galaxies with spectroscopic redshifts $z > 1.4$ overlaid on our $10' \times 15'$ optical $\mathcal{R}$-band image of the GOODS-N field. The yellow box ($8.5' \times 8.5'$) indicates the region with deep J and K_s *Palomar* imaging.

designed to cull galaxies at redshifts $1.4 \lesssim z \lesssim 2.0$ and $2.0 \lesssim z \lesssim 2.5$, respectively, with approximately the same range of UV luminosity and intrinsic UV color as the $z \sim 3$ LBGs (Adelberger et al. 2004; Steidel et al. 2004). The various selection criteria considered here are shown in Figure 5.2. We only considered candidates to $\mathcal{R} = 25.5$ to ensure a sample of galaxies that are bright enough such that optical spectroscopy is feasible.[2] This limit corresponds to an absolute magnitude 0.6 mag fainter at $z \sim 2.2$ than at $z \sim 3$. We also excluded from the sample those candidates with $\mathcal{R} < 19$ since almost all of these objects are stars. Optical selection yielded 1360 BM/BX and 192 C/D/MD candidates in the $11' \times 15'$ area of the GOODS-N field. Combined, the BX/BM and C/D/MD candidates constitute $\sim 30\%$ of the $\mathcal{R}$-band counts to $\mathcal{R} = 25.5$. The number of candidates and their surface densities are listed in Table 5.1. Approximately 50% of these candidates lie in the region imaged at J and K_s. The remainder of this paper focuses on those galaxies that have been spectroscopically confirmed to lie at redshifts $z > 1.4$, as described in the next section.

5.2.3 Optical Spectroscopy

We took advantage of the multi-object capabilities of the Keck LRIS instrument to obtain spectroscopy for the photometrically selected candidates. In its upgraded double-armed capacity, LRIS makes use of a dichroic to send light to both a red and blue arm. The commissioning of the blue arm of LRIS (LRIS-B) allowed, for the first time, the ability to obtain very sensitive near-UV spectroscopic observations at wavelengths as short as ~ 3100 Å, essentially to the atmospheric transmission limit. The wavelength range from the atmospheric cutoff up to ~ 5500 Å is particularly useful for probing the rich set of interstellar and stellar lines between Lyα and C IV ($\lambda 1548, 1550$) for galaxies in the so-called spectroscopic desert, between redshifts $1.4 \lesssim z \lesssim 2.5$. As shown previously in Adelberger et al. (2004) and Steidel et al. (2004), combining photometric selection of BM and BX candidates with the near-UV sensitivity of LRIS-B allows for the wholesale spectroscopy of large numbers of galaxies in this redshift range; this in turn enables us to focus our study on

[2] A few objects were candidates based on photometry of our *Palomar* images of the GOODS-N field (Steidel et al. 2003), but failed to satisfy the photometric selection criteria based on the newer *Keck* images. These objects are indicated in subsequent tables by their notation as presented in Steidel et al. (2003) or, in the case of BM/BX objects, by the letters "BX" or "BM" followed by no more than three numerical digits. The photometric values for these objects are the ones based on the new photometry.

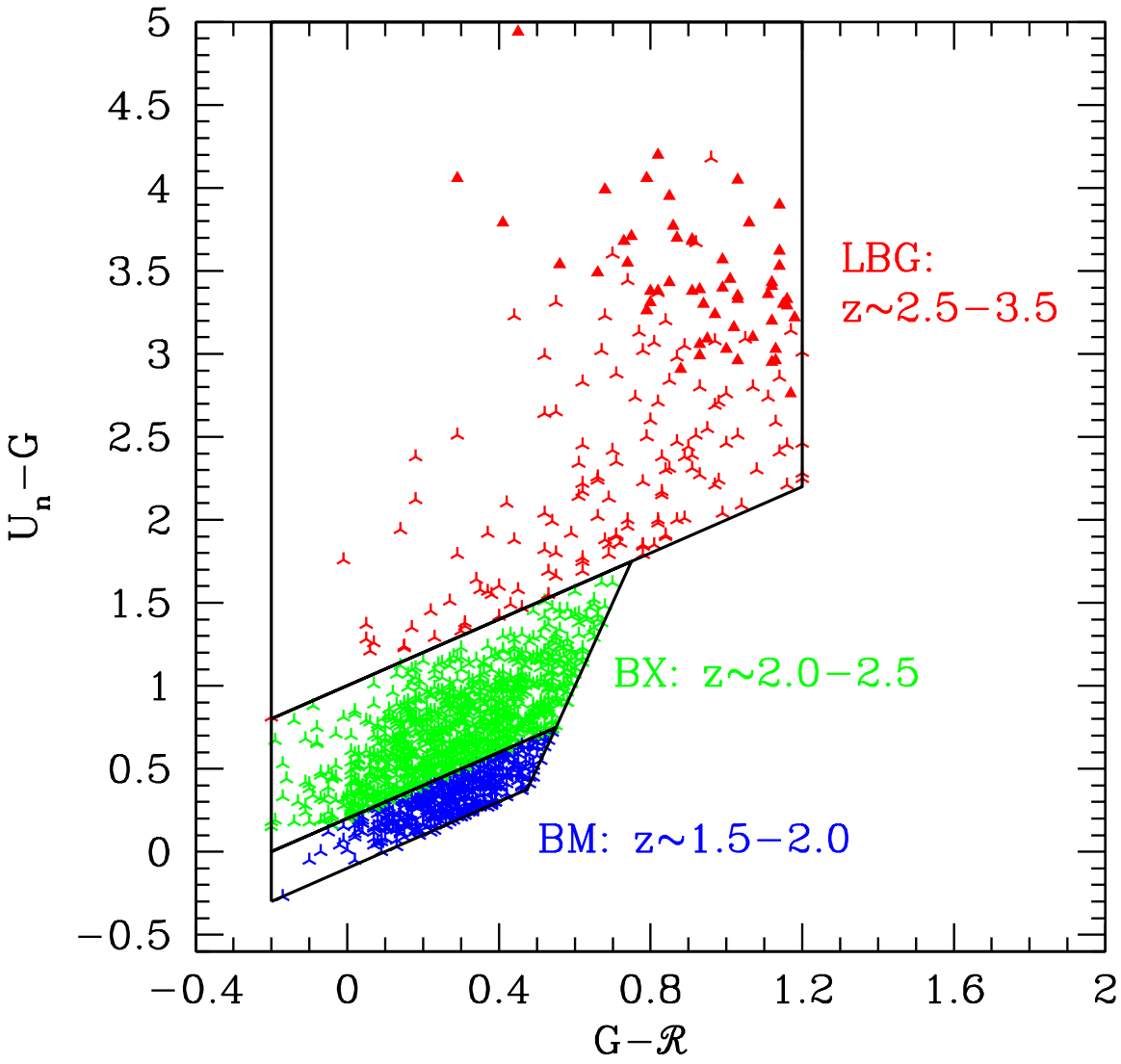

Figure 5.2 BX/BM colors of candidates in the GOODS-N field selected using the LBG and BM/BX selection criteria. Upward triangles indicate "C" candidates with no detection in $U_{\rm n}$.

an epoch that was particularly active in terms of star formation and accretion activity (e.g., Dickinson et al. 2003b; Chapman et al. 2003; Fan et al. 2001; Madau et al. 1996; Shaver et al. 1996; Schmidt et al. 1995).

The instrumental setup used for spectroscopy in the GOODS-N field varied during the course of the $z \sim 2$ survey; the various setups are described in more detail by Steidel et al. (2004). We selected dichroic filters designed to split the incoming beam at 5600 Å or 6800 Å. To provide maximum throughput between 3100 and 4000 Å, we used a 400 groove mm^{-1} grism blazed at 3400 Å on LRIS-B, resulting in a dispersion of 1.09 Å per pixel. For simultaneous observations on the red-side of LRIS (LRIS-R), we used a 400 groove mm^{-1} grating blazed at 8500 Å, providing wavelength coverage up to 9500 Å. We typically obtained simultaneous blue and red side spectroscopic observations between 3100 and 9500 Å, with slight variations due to the relative placement of slits in the telescope focal plane.

The slit masks used for spectroscopy cover $8' \times 5'$ on the sky. For a minimum slit length of $9''$ (adopted in order to ensure good background subtraction), we are able to include $30-35$ slits, in addition to $4-5$ star boxes used to accurately align each mask. We set the width of each slit to $1''.2$ and this, combined with a typical seeing of $0''.8$, yields a typical resolution of 5 Å for point sources. To obtain the optimum mix of objects on any given slit mask, we assigned each candidate a weight primarily based on its optical magnitude. We gave larger weights to objects with $\mathcal{R} = 23.5 - 24.5$ and lower weights for fainter objects where absorption line spectroscopy is more difficult and brighter objects where the foreground ($z \lesssim 1.0$) interloper fraction is larger. Nonetheless, we filled "blank" areas of the masks with filler objects that included these fainter and brighter objects. We particularly included some bright ($\mathcal{R} < 23.5$) objects on masks since at least some of these are intrinsically bright $z \sim 2-3$ galaxies and are most suitable for detailed follow up spectroscopic studies. To support other projects being conducted by our group, we also deliberately targeted objects within the BX/BM sample that had interesting multi-wavelength properties, such as those identified with 850 μm or 24 μm emission, as well as those with unusually red near-IR colors. We also designed masks to overlap as much as possible with the near-IR imaging. Because of this, $\sim$ 73% of spectroscopically confirmed galaxies with $z > 1.4$ lie in the K_s-band region, even though $\sim$ 50% of BX/BM candidates lie in the same region (see Figure 5.1).

We typically obtained three exposures of 1800 sec per mask, for a total exposure of

5400 sec. The range in optical magnitudes implies a large range in the S/N of the spectra. At the minimum, however, we found 5400 sec to be sufficient to obtain redshifts, and a few objects were observed on more than one mask. The spectroscopic success rate per mask is primarily a function of the weather conditions (e.g., cirrus, seeing) at the time of observation, with a 90% success rate of obtaining redshifts in the best conditions; these redshifts, for the most part, fell within the targeted redshift ranges. This suggests that the redshift distribution for the spectroscopic and photometric samples are similar, and there are not large numbers of galaxies whose true redshifts are far from those expected based on their observed BX/BM colors. Details of the spectral reduction techniques are described in Steidel et al. (2003). We identified redshifts based on the presence of a number of low-ionization interstellar absorption lines (e.g., Si II λ1260, O I+S II λ1303, C II λ1334, Si II λ1526, Fe II λ1608, Al II λ1670, and Al III λ1854, 1862), stellar wind features (e.g., N V λ1238, 1242, S IV λ1393, 1402, and C IV λ1548, 1550), the C III λ1909 nebular emission line, or Lyα emission or absorption. A few examples of spectra are shown in Steidel et al. (2003, 2004). Spectroscopically confirmed galaxies with $1.4 < z < 3.0$ are shown with respect to the $\mathcal{R}$-band image of the GOODS-N field in Figure 5.1.

Comparison with nebular redshifts derived from Hα spectroscopy indicates that Lyα emission is almost always redshifted, and interstellar absorption lines are almost always blueshifted, with respect to the systemic (nebular) redshift of the galaxy. These systematic offsets have been interpreted as the result of outflows (e.g., Adelberger et al. 2003, 2005b; Pettini et al. 2001; Shapley et al. 2003). Adelberger et al. (2005b) present linear least-squares fits to the systemic redshifts of galaxies given their Lyα and interstellar absorption redshifts based on a sample of 138 objects with near-IR spectroscopy (Erb et al. 2006c; Pettini et al. 2001).

5.3 Spectroscopic Results and Catalog

Our spectroscopic sample in the GOODS-N field presently includes 212 BM/BX and 74 C/D/MD galaxies with secure spectroscopic redshifts $z > 1.4$ (Table 5.2). The total sample includes 347 objects with secure spectroscopic redshifts, including 40 interlopers with $z < 1$. We also include 41 objects with uncertain redshifts in Table 5.2, denoted by a colon (":") in the redshift field (for consistency with Steidel et al. 2003), for a total of 388 objects.

Table 5.1 lists the statistics for the individual samples, including the numbers of candidates observed, the interloper fractions, and mean redshifts. The primary source of contamination in the LBG sample is from K dwarfs in the Galactic halo. Star-forming galaxies at redshift $\langle z \rangle = 0.17 \pm 0.09$ contaminate the BX sample since their Balmer breaks mimic the Lyα forest decrement. These interlopers can be easily excluded using K_s-band photometry (e.g., the BzK criteria; Daddi et al. 2004b), but we have not imposed any additional criteria other than the observed optical magnitudes and colors. The main "contaminants" of the BM sample occur from galaxies with redshifts $1.0 < z < 1.4$; these galaxies have BX/BM colors very similar to those of BM objects, and the narrow BM color selection window implies that photometric scatter and Lyα perturbations on the BX/BM colors can have a significant impact on the observed redshift distribution of BM galaxies (Reddy et al., in prep.). Throughout this paper we consider objects with $z < 1.4$ to be contaminants. The AGN/QSO (as identified from either their X-ray, UV, or *Spitzer* IRAC or MIPS emission) with $z > 1.4$ make up $\sim 4\%$ of the sample (see § 5.6.2 for further discussion).

For consistency, we compared redshifts for objects in common with the Team Keck Treasury Redshift Survey (TKRS; Wirth et al. 2004; Cowie et al. 2004). We note that the TKRS survey is based primarily upon observations with the DEIMOS intrument on Keck II, and so the TKRS redshift selection function rapidly declines above $z \sim 1.2$ as the emission and absorption lines used for redshift identifiction (including [N II], [S II], [O III], [O II] emission features and Calcium H and K absorption features) are shifted out of the DEIMOS spectral range. The overlap between the BX/BM and TKRS samples is small given that the two surveys target different redshifts (TKRS is better at identifying galaxies at $z \lesssim 1.2$ and our BX/BM selection is better at identifying galaxies at $z \gtrsim 1.4$).

There are 64 objects with redshifts in the BX/BM catalog that are also in the TKRS database. Of these, 52 were previously published in other surveys of the GOODS-N field (Cowie et al. 2004; Cohen et al. 1996, 2000; Cohen 2001; Barger et al. 2000, 2003; Wirth et al. 2004; Phillips et al. 1997; Lowenthal et al. 1997; Dawson et al. 2001; Steidel et al. 2003, 1996; Dickinson 1998) and/or have agreement in redshift between the BX/BM and TKRS samples. Upon further inspection of the 12 objects with discrepant redshifts, we adopted the TKRS redshift for 6 of them (BX1202, BX1371, BMZ1010, BMZ1100, BMZ1121, and BMZ1208); the redshifts for these 6 galaxies are all below $z < 1.4$ where the DEIMOS-

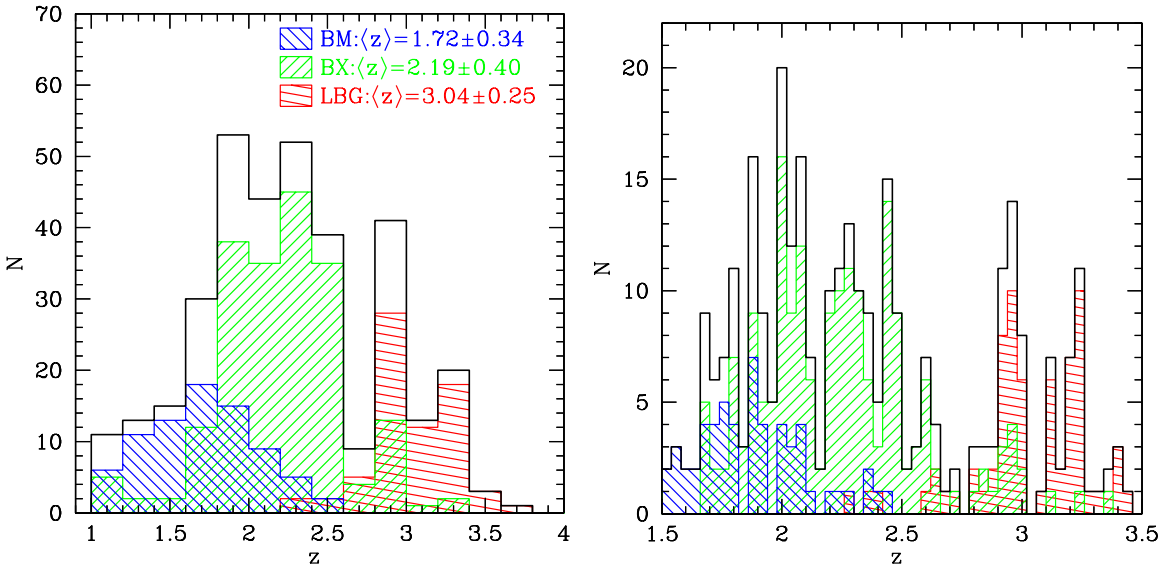

Figure 5.3 (*Left*) Redshift histogram of spectroscopically confirmed BM/BX and LBG galaxies in the GOODS-N field with $z > 1$. The solid line indicates the total distribution of BM, BX, and LBG galaxies. (*Right*) Redshift histogram with higher resolution bins, $\delta z = 0.04$, emphasizing the large-scale structure in GOODS-N.

determination was found to be secure and where our BM selection function drops off. Five of the objects had the correct redshifts in our catalog (BX1299, BX1319, BX1805, BMZ1119, and BMZ1375). For the remaining object, BX1214, we were able to rule out the Cohen et al. (2000) redshift of $z = 2.500$, but were unable to confidently assign a redshift based on our LRIS spectrum.

The redshift distributions of BM/BX and LBG galaxies with $z_{\rm spec} > 1$ are shown in Figure 3.1, where the right panel emphasizes large-scale structure in the GOODS-N field. The redshift over-density at $z = 2.95$ is prominent, and was also noted in the LBG survey (Steidel et al. 2003). We also note a possible overdensity at $z = 2.00$, which corresponds to an overdensity of 5 submillimeter galaxies as noted by Blain et al. (2004). However, we caution that Figure 3.1 only presents raw numbers, and we have not accounted for the selection function and relative fractions of candidates observed. Therefore, the significance of any "over-densities" appearing in Figure 3.1 is not quantified.

5.4 *Spitzer* IRAC and MIPS Data

To aid in understanding the stellar populations and extinction of $z \sim 2$ galaxies, we compiled *Spitzer* IRAC and MIPS photometry for our sample of BX/BM-selected galaxies using the public *Spitzer* data in the GOODS-N field (Dickinson et al., in prep; Chary et al., in prep). The IRAC photometry was performed by fitting an empirical point spread function (PSF) determined from the IRAC images to the spatial positions of sources from the higher resolution K_s-band data. This method mitigates the effects of confusion by allowing for the deblending of partially resolved sources in the IRAC images, and is similar to the method employed by the GOODS team for extracting photometry (Dickinson et al., in prep; Chary et al., in prep). We extracted the MIPS 24 μm fluxes of BX/BM galaxies using a similar procedure; the spatial positions of sources from the IRAC data were used to deblend and extract the 24 μm fluxes (Reddy et al. 2006b). Photometric errors were computed from the dispersion of extracted fluxes for 100 PSFs fit to random blank regions around each galaxy. Since the IRAC and MIPS data are background-limited, the errors will be dominated by the background noise for all but the brightest galaxies at these wavelengths. The IRAC channel $1-4$ magnitudes and MIPS 24 μm fluxes are listed in Table 5.2. We do not give fluxes for those galaxies that were either undetected or were badly blended with a nearby bright source. Of the 212 BX/BM galaxies with secure spectroscopic redshifts $z > 1.4$, only 2 ($< 1\%$) are undetected at 3.6 μm to the GOODS IRAC depth. Of the 74 LBGs, 11 ($\approx 15\%$) are undetected at 3.6 μm. The MIPS detection fraction is $\approx 65\%$ for BX/BM galaxies, decreasing to a $\approx 53\%$ for the LBGs, to a limiting 3 σ flux of $f_{24\mu\mathrm{m}} \approx 8$ μJy.

5.5 Stellar Population Modeling

The combination of multi-wavelength photometry and spectroscopic redshifts allows us to better constrain the stellar populations of UV-selected galaxies than if we only had photometric redshifts. To demonstrate the wide range in stellar populations of UV-selected galaxies at redshifts $z \sim 2-3$, we fit the BX/BMJK_s + IRAC magnitudes with Bruzual & Charlot (2003) models assuming a Salpeter (1955) IMF and solar metallicity. The assumption of solar metallicity is a reasonable approximation for most galaxies in the BX/BM-selected sample (Erb et al. 2006a). The models were corrected for the effects of IGM opacity before

comparing to the observed magnitudes. In fitting the stellar populations, we assumed an exponentially declining star formation history with decay timescales τ = 10, 20, 50, 100, 200, 500, 1000, 2000, and 5000 Myr, and $\tau = \infty$ (constant star formation, CSF, model). We also assumed a varying amount of reddening, or $E(B-V)$, from 0.0 to 0.7. The best-fit model was taken to be the combination of τ, age, and $E(B-V)$ that gave the lowest χ^2 value with respect to the observed magnitudes. The star formation rate (SFR) and stellar mass are determined from the normalization of the model to the observed magnitudes. Even with spectroscopic redshifts, there is considerable uncertainty in the best-fit parameters, with the exception of the total stellar mass M^* which is generally robust to changes in the assumed star formation history (e.g., Papovich et al. 2001; Shapley et al. 2001, 2005; Erb et al. 2006c). The best-fit stellar population parameters for both a CSF and τ model for each galaxy are collected in Table 5.4. Monte Carlo simulations indicate that the typical fractional uncertainties associated with the best-fit parameters (when including IRAC data in the fits) are $\langle \sigma_x / \langle x \rangle \rangle$ = 0.6, 0.4, 0.5, and 0.2 in $E(B-V)$, age, SFR, and stellar mass, respectively (Erb et al. 2006c). For completeness we have included the best-fit SFRs from the fitting in Table 5.4, but we note that we have several other *independent* multi-wavelength measures of the SFRs for these galaxies (e.g., from dust-corrected UV, Hα, and 24 μm data) that are unaffected by the degeneracies associated with stellar population modeling.

Aside from the systematic errors resulting from the degeneracy between star formation history and the best-fit parameters, there are additional caveats to the SED results. Around 30 objects had optical through IRAC photometry which is inconsistent with the stellar population models considered here; these objects exhibit large J/$K_{\rm s}$ *and* IRAC magnitude residuals with respect to the best-fit stellar population (and have $\chi^2 > 10$), and often give unrealistically young ages ($<$ 10 Myr) and large SFRs ($>$ 2000 $M_\odot$ yr^{-1}). We do not present the SED results for these galaxies. In addition to these 30, there are 4 galaxies that fit the optical and IRAC data well, but have large $K_{\rm s}$ residuals with respect to the best-fit stellar population (i.e., a $K_{\rm s}$ magnitude more than 3 σ away from the best-fit). Three of these four galaxies have redshifts $2.0 \leq z \leq 2.5$ where the $K_{\rm s}$ magnitude may be contaminated by emission from Hα+[N II]. The four galaxies with large $K_{\rm s}$ residuals are indicated by the notation "$K_{\rm s}$" in Table 5.4. Also, we noted a few objects with 8 μm excesses when compared with the best-fit stellar population, many of which have large 24 μm

fluxes ($f_{24\mu\mathrm{m}} > 100$ μJy) indicating they may be obscured AGN (see Table 5.6). We do not present SED fitting results for any of the sources which may have AGN based on their 8 μm and 24 μm excesses and/or X-ray/optical emission. Finally, we did not perform SED fitting for galaxies without photometry longward of $\mathcal{R}$-band or that had redshifts $z < 1$. The best-fit SED parameters for the remaining 254 galaxies are listed in Table 5.4. Note that the SFRs and stellar masses (M^*) in Table 5.4 assume a Salpeter (1955) IMF from 0.1 to 100 $M_\odot$. Assuming the Chabrier (2003) IMF with a shallower faint-end slope results in SFRs and stellar masses a factor of 1.8 lower than listed in Table 5.4. We also note that a number of galaxies have inferred ages < 50 Myr, which are unlikely given the dynamical timescale of ~ 50 Myr for star formation in galaxy-sized objects. The SED parameters for these galaxies with extremely young *inferred* ages should be taken with caution.

5.6 The Diverse Properties of Optically Selected Galaxies at High Redshift

5.6.1 Star-Forming Galaxies

Of the best-fit SED parameters, the stellar mass is the least uncertain and is generally robust to changes in the assumed star formation history, as can be seen by comparing columns 6 and 11 in Table 5.4. Figure 5.4 shows the distribution of stellar masses for BX/BM-selected galaxies with redshifts $z > 1$, assuming a constant star formation history. Table 5.5 shows the median and mean stellar masses and dispersion (assuming a CSF history) for galaxies in the various samples. While the mean stellar mass of the sample is $\langle M^* \rangle \approx 1.1 \times 10^{10}$ $M_\odot$, there is large dispersion about this mean of a factor of 3.4. This mean stellar mass is a factor of ~ 2 lower than found in Shapley et al. (2005) and Erb et al. (2006c), partly because we included galaxies undetected to $K_\mathrm{s} = 24.1$ in the sample considered here (as long as they had IRAC data to constrain the stellar mass), and these faint K_s galaxies on average have lower stellar masses than K_s-detected galaxies. Further, we have included BM galaxies which have a mean stellar mass that is a factor of ≈ 2 lower than than the mean stellar mass for BX galaxies and LBGs (Table 5.5). This difference in mean stellar mass likely reflects the fact that BM galaxies have a lower mean redshift ($z = 1.72 \pm 0.32$; Figure 5.3) than BX galaxies and LBGs, and therefore we are able to probe down to fainter absolute

magnitudes and are sensitive to lower mass galaxies.

Regardless, the sample includes galaxies with a wide range in ages, from young galaxies with ages comparable to the dynamical timescale for star formation of ~ 50 Myr to those that are older than 2 Gyr. In fact, the BX/BM sample includes galaxies which are as old (> 2 Gyr) and as massive ($M^* > 10^{11}$ M$_\odot$) as galaxies found at $z \sim 2$ in near-IR selected samples (e.g., the distant red galaxies, or DRGs, of Franx et al. 2003).[3] In particular, Shapley et al. (2005) and Reddy et al. (2005) have shown that while the typical stellar mass of near-IR selected DRGs with $K_s \lesssim 21.8$ is larger by an order of magnitude than the *typical* stellar mass of BX/BM-selected galaxies to $\mathcal{R} = 25.5$, the actual range in stellar mass probed by DRG selection does not appear to significantly exceed the range in stellar mass of BX/BM-selected galaxies (although we note that DRG selection appears to be much more efficient is selecting galaxies with $M^* \gtrsim 10^{11}$ M$_\odot$ at $z \sim 2-3$; e.g., van Dokkum et al. 2006). Further, SED analysis of the optically-selected DRGs (as indicated in Table 5.2 by the notation "DRG" in the last column) with fainter near-IR magnitudes ($K_s \gtrsim 22.8$) have stellar masses that are comparable to the stellar masses of typical BX/BM-selected galaxies ($10^9 \lesssim M^* \lesssim 10^{11}$ M$_\odot$). These observations suggest that the presence of unobscured star formation in a galaxy has little bearing on its total stellar mass, particularly since such star formation would contribute negligibly to the stellar mass of galaxies that are already massive (M$^* > 10^{11}$ M$_\odot$; e.g., Reddy et al. 2006b; Erb et al. 2006b; Papovich et al. 2006). While optical selection allows us to very efficiently follow up galaxies spanning over 2 orders of magnitude in age and stellar mass at redshifts $z \gtrsim 1.4$, other techniques are required to assess the total stellar mass budget at these redshifts (e.g., van Dokkum et al. 2006; Reddy et al. 2005).

While the $E(B-V)$ and SFRs determined from SED modeling are more uncertain than the inferred stellar masses, we have several independent methods of assessing the extinction and SFRs in $z \sim 2$ galaxies, made possible by the extensive multi-wavelength data in the GOODS-N field. The exquisite, photon-limited *Chandra* X-ray data in the GOODS-N field, currently the deepest X-ray data ever taken (Alexander et al. 2003), allow for stacking analyses to estimate the average emission properties of galaxies (Brandt et al. 2001; Nandra

[3]Optically selected galaxies which satisfy the DRG criteria ($J-K_s > 2.3$ in Vega magnitudes, or $J-K_s > 1.38$ in AB) are indicated by "DRG" in the last column of Table 5.2.

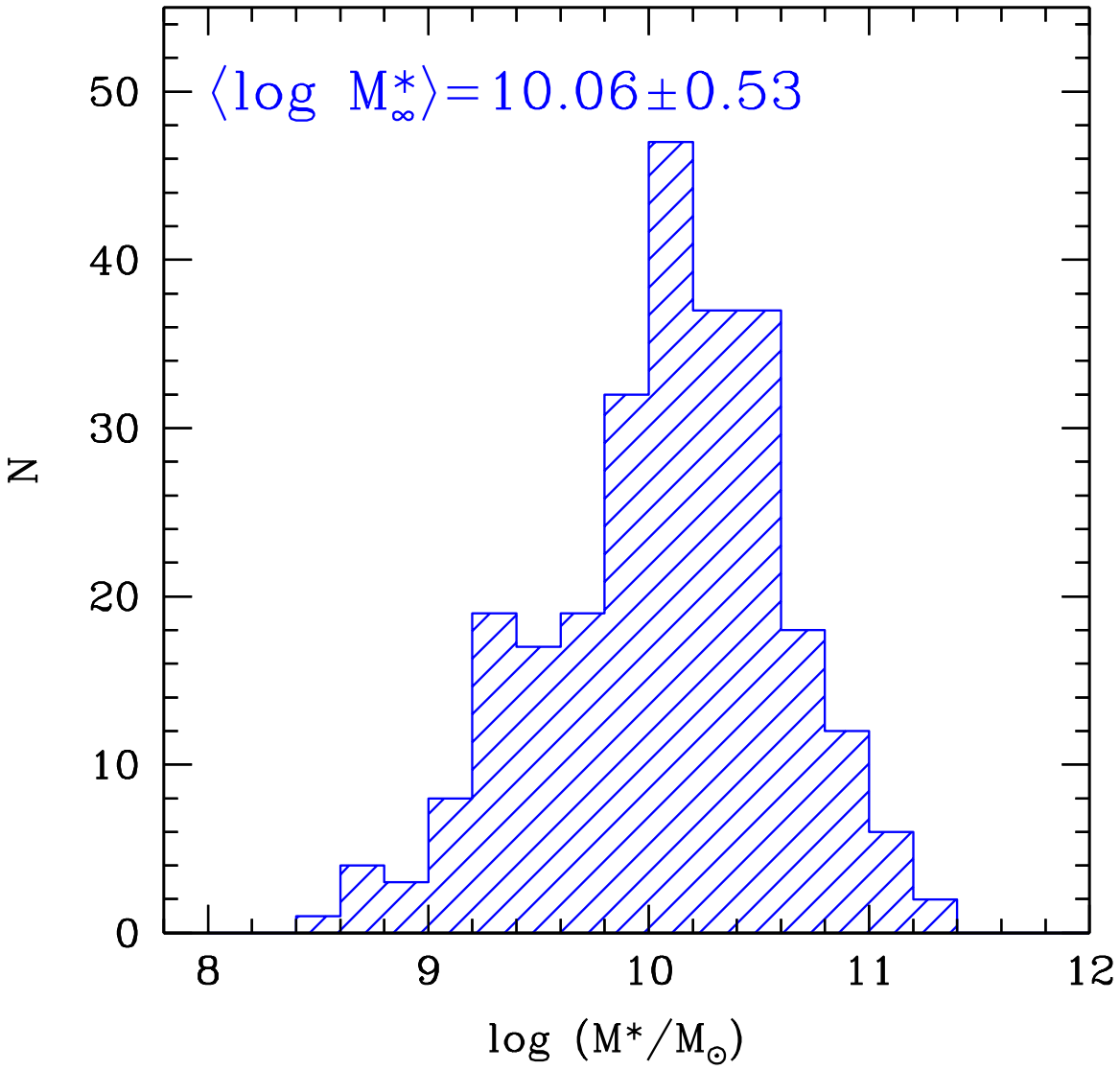

Figure 5.4 Stellar mass distribution of BX/BM-selected galaxies with redshifts $z > 1$, assuming a constant star formation (CSF) model. Assuming a best-fit exponentially declining star formation history (τ model) results in a stellar mass distribution that is virtually identical to the one shown here, with a mean and dispersion in log space of $\langle \log M^*_\tau \rangle = 10.08 \pm 0.51$.

et al. 2002; Reddy & Steidel 2004; Reddy et al. 2005). Based on the stacking analyses of Nandra et al. (2002) and Reddy & Steidel (2004), the mean SFRs of $z \sim 2-3$ BX/BM-selected galaxies is $\sim 50\ M_{\odot}\ \mathrm{yr}^{-1}$, with mean attenuation factors, defined as the ratio between the bolometric SFR and UV-based SFR (uncorrected for extinction), of $4.5-5.0$.

The X-ray data allow us to determine the average extinction and SFRs of galaxies over the entire range of redshifts probed by the BX/BM and LBG criteria. However, important progress has been made in determining the individual properties of galaxies in a narrower redshift range, $1.5 \lesssim z \lesssim 2.6$, where the *Spitzer* MIPS 24 μm band is sensitive to the 7.7 μm polycyclic aromatic hydrocarbon (PAH) dust emission ubiquitous in local and high redshift star-forming galaxies (Reddy et al. 2006b; Papovich et al. 2006). Reddy et al. (2006b) demonstrate that the 24 μm emission of $z \sim 2$ galaxies can be used as a tracer of the SFR or total infrared luminosity (L_{IR}), particularly for galaxies with spectroscopic redshifts where we are able to accurately constrain the K-corrections from 24 μm flux to rest-frame $5-8.5$ μm luminosity. The MIPS data indicate that BX/BM-selected galaxies at redshifts $1.5 \lesssim z \lesssim 2.6$ span more than 3 orders of magnitude in L_{IR}, from those which are undetected to the 3 σ sensitivity limit of 8 μJy for MIPS data in the GOODS field, to those which have L_{IR} comparable to the most luminous star-forming galaxies at these redshifts, the submillimeter galaxies (Smail et al. 1997; Hughes et al. 1998; Barger et al. 1998; Chapman et al. 2005). The mean infrared luminosity for BX/BM-selected galaxies is $\langle L_{\mathrm{IR}} \rangle \simeq 2 \times 10^{11}$ L$_{\odot}$, assuming that the rest-frame infrared emission ($L_{5-8.5\mu\mathrm{m}}$) as probed by MIPS observations scales with infrared luminosity as $L_{\mathrm{IR}} \approx 17.2 L_{5-8.5\mu\mathrm{m}}$ as determined from local templates (see Reddy et al. 2006b), and this value of $\langle L_{\mathrm{IR}} \rangle$ inferred from MIPS is in excellent agreement with X-ray and dust-corrected UV-based estimates. More generally, the BX/BM-selected sample includes galaxies over 4 orders of magnitude in dust obscuration ($L_{\mathrm{bol}}/L_{\mathrm{UV}}$), from those galaxies with little dust and whose UV luminosity is comparable to L_{IR}, to those that are heavily dust-obscured and have attenuation factors $\gtrsim 1000$.

Aside from the large dynamic range in SFRs and extinction of BX/BM-selected galaxies, the sample also hosts galaxies with a wide range in morphology and kinematics (Erb et al. 2003, 2006c; Law et al., in prep.), from disk-like galaxies with signatures of rotation, as inferred from Hα spectral data (e.g., Forster Schreiber et al. 2006), to those galaxies that appear irregular and/or are merging. UV-selected samples efficiently target the redshift

range where the morphological transformation of galaxies from irregular at high redshift to the Hubble sequence at low redshifts ($z \lesssim 1.4$) takes place. The deep Hubble ACS data in the GOODS-N field (Giavalisco et al. 2004b) combined with our extensive rest-frame UV spectroscopic database make it possible to study in detail the correlation between morphological structure and the SFRs, extinction, masses, and spectral properties of high redshift galaxies (Law et al., in prep.).

5.6.2 AGN

The combination of X-ray, observed optical, 8 μm, and 24 μm data, along with spectroscopic redshifts, allows for a powerful probe of AGN activity among BX/BM-selected galaxies. We classified objects as AGN based on one or more of the following criteria: (a) the presence of high ionization UV lines (identical to the method used in Steidel et al. 2002 and Shapley et al. 2005); (b) direct detection in the *Chandra* 2 Ms data (Alexander et al. 2003) and an X-ray-to-optical flux ratio indicative of AGN (e.g., see Hornschemeier et al. 2001 and Reddy et al. 2005); or (c) an 8 and 24 μm flux excess above what one would expect from a simple star-forming population. Table 5.6 lists the 11 AGN with confirmed redshifts $z > 1.4$ which have emission indicative of AGN.

MD31 is the most unusual source: it has an X-ray counterpart within $1\farcs5$ of the optical position, but shows no evidence of AGN from the rest-UV (observed optical) spectrum nor from *Spitzer* observations. The SED analysis indicates that MD31 is best-fit with an ~ 2 Gyr old population with a modest $E(B-V) \sim 0.17$ and SFR~ 60 $M_\odot$ yr^{-1} assuming the CSF model, and thus is not expected to be bright in X-rays as a result of star formation alone (i.e., the 2 Ms X-ray sensitivity implies a detection threshold of ~ 480 $M_\odot$ yr^{-1} at the redshift of MD31, $z = 2.981$). Examination of the deep ACS imaging in the GOODS field reveals no other optical counterpart within $1\farcs5$ of MD31. If the X-ray counterpart is indeed associated with accretion activity in MD31, then the X-ray detection fraction of AGN with $z > 1.4$ in our sample is 7/11, or 64%. On the other hand, the fraction of AGN showing 8 μm and/or 24 μm excesses is 9/11, or 82%. While the object statistics are insufficient to judge the efficiency of AGN detection in the X-ray versus IR, we note that the IRAC and MIPS integration time for any given object in the GOODS-N field is ~ 10 hours, whereas the X-ray integrations required to detect faint AGN at redshifts $z \gtrsim 1.4$ is on the order of

a megasecond or larger. The possible difference in AGN detection fraction and especially integration time between the IR and X-ray observations suggest that deep IR imaging may be a more efficient method of finding AGN at high redshifts. In this case, the 8 μm and 24 μm data indicate at least an additional three AGN that are unidentified in X-rays. For comparison, while our optical spectra have integration times of 5400 s, a factor of 370 times shorter than the X-ray integration time (2 Ms), we can still detect $\approx 73\%$ of AGN based on their rest-frame UV emission lines.

The properties of the three X-ray undetected AGN with $z > 2$ are worth further consideration: these AGN are BX1637, BX160, and MD74. Figure 5.5 shows the observed optical through 24 μm SEDs of these AGN, as well as BM1156, which is very weakly detected in X-rays, and demonstrates the power-law behavior at observed wavelengths longer than $\lambda \sim 2$ μm, indicative of warm dust population. The three X-ray undetected AGN are also not detected in the deep radio imaging of the HDF (Richards 2000), placing a 3 σ upper limit on their observed 1.4 GHz flux of $f_{1.4\ \mathrm{GHz}} < 24$ μJy. However, all three have disturbed and/or extended rest-frame UV morphologies from deep ACS imaging (Giavalisco et al. 2004b), suggesting the obscured AGN in these systems may be triggered by merger activity. The non-detection of these three AGN (even when stacking them) in both the soft ($0.5 - 2.0$ keV) and full ($2.0 - 8.0$ keV) X-ray bands of *Chandra* makes it difficult to constrain their column densities. Nonetheless, these three AGN have a mean spectroscopic redshift of $\langle z_{AGN} \rangle \approx 2.5$, and if we assume the AGN have intrinsic photon index of $\Gamma = 2.0$ (e.g., Alexander et al. 2005), then we cannot rule out the possibility that these could be Compton-thick AGN with column densities $N_{\mathrm{H}} > 10^{24}$ cm^{-2}. Comparison with the 8 μm and 24 μm fluxes of Mrk 463 and Mrk 1014, two infrared luminous AGN (Armus et al. 2004), suggests that BX1637 and MD74 could have total infrared luminosities in the range $5 \times 10^{12} \lesssim L_{\mathrm{IR}} \lesssim 2 \times 10^{13}$ L$_{\odot}$. Constraints on the 850 μm fluxes of these two AGN could narrow the range of possible L_{IR}, but unfortunately submillimeter observations do not cover the region containing these two AGN. BX160 is covered in published 850 μm imaging and is undetected to $S_{850} \sim 1.5$ mJy (Wang et al. 2004), suggesting an upper limit on the infrared luminosity of $\sim 10^{12.5}$ L$_{\odot}$. We caution, however, that the lack of data across the Raleigh-Jeans tail of the dust SEDs makes it difficult to accurately constrain the dust temperatures and hence total bolometric luminosities of these sources.

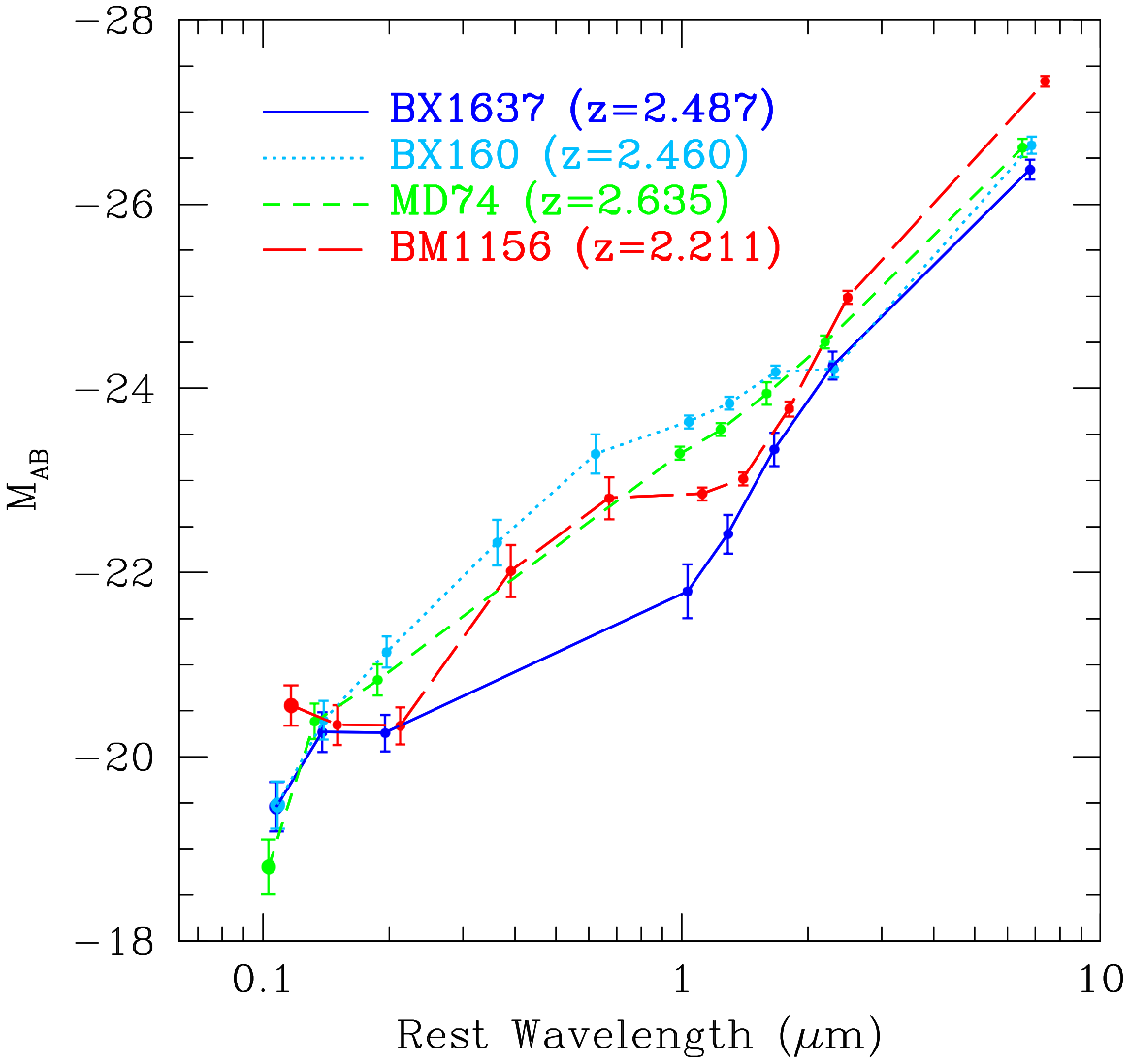

Figure 5.5 Spectral energy distributions of the three X-ray undetected AGN (BX1637, BX160, and MD74) and one faint X-ray detected AGN (BM1156) at $z = 2.211 - 2.635$ in the spectroscopic BX/BM sample, from observed optical through 24 μm. All four exhibit a power law slope at long wavelengths ($\lambda \gtrsim 2$ μm rest-frame) indicative of a warm dust population.

The presence of obscured AGN at high redshifts has been postulated based on the expected fraction of high column density AGN ($N_{\rm H} > 10^{23}$ cm^{-2}) at $z \gtrsim 1.4$ in simulations that model the contribution to the X-ray background (Comastri & Fiore 2004; Gilli 2004). While high column density AGN may be unidentifiable as AGN based on their optical spectra alone, the fact that some fraction of their host galaxies are optically bright ($\mathcal{R} < 25.5$) and fall within optically-selected samples bodes well for determining their spectroscopic redshifts. Accurate spectroscopic redshifts are particularly important for constraining AGN column densities ($N_{\rm H}$); the inferred $N_{\rm H}$ depends strongly on the assumed redshift, $N_{\rm H}(z) \approx N_{\rm H}(0)(1+z)^{2.6}$ (Alexander et al. 2005).

In summary, of the 11 AGN with $z > 1.4$ in our optically-selected sample, 7/11 (64%) are detected in X-rays to 2 Ms, 9/11 (82%) are detected with 8 and/or 24 μm excesses, and 8/11 (73%) have rest-frame UV signatures of AGN. Even in the deepest X-ray image available, there is still a considerable number of AGN that remain undetected, and we must incorporate other techniques, e.g., optical spectra and 8 and 24 μm data, to fully account for the census of AGN.

5.7 Summary

We have presented the results of a spectroscopic survey of redshift $1.4 \lesssim z \lesssim 3.0$ star-forming galaxies in the GOODS-North field, made possible by efficient UV (BX/BM) color selection and the unique multi-object capabilities of the LRIS instrument on the Keck I telescope. Our sample consists of 212 redshifts for galaxies at redshifts $1.4 \lesssim z \lesssim 2.5$ selected using the BM and BX criteria of Adelberger et al. (2004) and Steidel et al. (2004), and 30 new redshifts (of a total of 74) for Lyman break galaxies at redshifts $2.5 \lesssim z \lesssim 3.5$. Our deep optical and near-IR imaging, supplemented by publicly available *Spitzer* IRAC and MIPS data (Dickinson et al., in prep; Chary et al., in prep), allow us to measure the stellar populations, stellar masses, star formation rates, and dust extinction for galaxies in our sample (e.g., Erb et al. 2006c; Shapley et al. 2003, 2005; Reddy & Steidel 2004; Reddy et al. 2005, 2006b; Steidel et al. 2004). These analyses indicate that the BX/BM-selected sample consists of galaxies which span two orders of magnitude in age and stellar mass, and 4 orders of magnitude in dust obscuration ($L_{\rm bol}/L_{\rm UV}$). Included are galaxies with bolometric star formation rates ranging from $\sim 5\ M_\odot$ yr^{-1} to $> 1000\ M_\odot$ yr^{-1}. We further

identify at least 3 of 11 AGN in our sample that appear to be heavily dust-obscured based on their power-law SEDs longward of 2 μm (rest-frame) and lack of detection in the deep *Chandra* 2 Ms data (Alexander et al. 2003). A compilation of the multi-wavelength data for these 11 AGN indicates that optical and *Spitzer* data are able to more efficiently (in terms of integration time) select AGN at $z > 1.4$ than X-ray data, but optical spectra and *Spitzer* and *Chandra* data are all required to fully account for the census of AGN at high redshifts. The photometry and SED fitting results for galaxies in our sample are available at http://www.astro.caltech.edu/∼drlaw/GOODS/.

Large spectroscopic samples at high redshifts allow for a number of other detailed investigations such as the galaxy and AGN/QSO luminosity functions (Steidel et al. 1999; Adelberger & Steidel 2000; Shapley et al. 2001; Hunt et al. 2004, Reddy et al. in prep.); metallicities (Pettini et al. 1998, 2001; Shapley et al. 2004; Erb et al. 2006a); signatures of galaxy feedback and IGM metal enrichment (Adelberger et al. 2003); and accurate clustering analyses (Adelberger et al. 2005a,b). This large range in galaxy evolution studies highlights the exquisite versatility and efficiency of optically-selected samples in addressing many fundamental issues in cosmology.

We thank David Law for setting up the website where the galaxy photometry and SED fits are available to the public. We are grateful to the staff of the Keck and Palomar Observatories for their help in obtaining the data presented here. This work has been supported by grant AST 03-07263 from the National Science Foundation and by the David and Lucile Packard Foundation.

Table 5.1. Sample Statistics to $\mathcal{R} = 25.5$

Candidates	$N_{\rm cand}$[a]	$\rho_{\rm cand}$[b] (arcmin^{-2})	$N_{\rm obs}$[c]	$N_{z>1}$[d]	$f_{z>1}$[e]	$N_{z>1.4}$[f]	$\langle z \rangle$[g]
BM	470	3.13 ± 0.14	67	63	0.94	49	1.72 ± 0.34
BX	890	5.93 ± 0.20	205	170	0.83	163	2.19 ± 0.40
C	55	0.37 ± 0.05	26	26	0.97	26	3.11 ± 0.21
D	59	0.39 ± 0.05	23	23	0.98	23	3.05 ± 0.22
MD	78	0.52 ± 0.06	26	25	0.96	25	2.96 ± 0.30
Total	1552	10.35 ± 0.26	347	307	0.88	286	2.25 ± 0.57

[a]Number of photometric candidates.

[b]Surface density of photometric candidates to $\mathcal{R} = 25.5$.

[c]Number of objects with secure spectroscopic identifications.

[d]Number of objects with secure redshifts $z > 1$.

[e]Fraction of spectroscopically observed objects with $z > 1$. The foreground ($z < 1$) contamination rates of the C, D, and MD samples are very low ($< 5\%$) and we assume the interloper fractions derived over all fields of the $z \sim 3$ Lyman Break Galaxy survey (Steidel et al. 2003). For the BM and BX samples, we assume foreground contamination fractions derived from the GOODS-N field, which are similar to those derived in other fields of the $z \sim 2$ survey (Steidel et al. 2004).

[f]Number of objects with $z > 1.4$

[g]Mean and standard deviation of redshift distribution for objects with $z > 1$.

Table 5.2. GOODS-N BX/BM Galaxies with Spectroscopic Redshifts

Name	α (J2000.0)	δ (J2000.0)	$z_{\rm em}$[a]	$z_{\rm abs}$[b]	Type[c]	$\mathcal{R}$[d] (mag)	$G-\mathcal{R}$ (mag)	$U_{\rm n}-G$[e] (mag)	J[f] (mag)	$K_{\rm s}$[f] (mag)	Notes[g]
BX1035	12:36:13.03	62:10:21.1	...	2.236	GAL	23.46	0.37	0.68	...	...	
BX1040	12:36:17.81	62:10:11.2	2.469	2.466	GAL	24.84	0.22	0.68	...	...	
BX1042	12:35:50.89	62:13:33.5	2.613	2.601	GAL	24.83	0.50	1.16	...	...	
BX1050	12:36:18.80	62:10:37.4	...	2.322	GAL	24.71	0.40	0.73	...	...	
BX1051	12:35:52.97	62:13:36.8	...	2.098	GAL	24.23	0.14	0.57	...	...	
BX1055	12:35:59.59	62:13:07.5	2.496	2.486	GAL	24.09	0.24	0.81	...	...	
BX1060	12:36:06.40	62:12:29.1	...	2.081	GAL	24.22	0.43	0.84	...	...	
BX1064	12:36:30.34	62:09:45.3	...	2.086	GAL	24.20	0.28	0.61	23.60	22.63	
BX1065	12:36:09.84	62:11:39.0	...	2.701	GAL	24.01	0.43	1.04	...	...	
BX1069	12:36:45.82	62:08:08.2	0.000	0.000	STAR	21.95	0.38	0.77	...	...	
BX1071	12:36:20.10	62:11:12.6	...	1.996	GAL	24.41	0.27	0.76	23.71	24.10	
BX1073	12:36:43.35	62:08:19.6	0.087	0.087	GAL	20.59	0.40	0.82	...	...	
BX1074	12:36:19.38	62:11:25.5	1.754	1.745	GAL	24.01	0.13	0.40	22.74	21.92	
BX1075	12:36:14.45	62:11:52.1	...	2.221	GAL	24.08	0.35	1.04	...	...	
BX1080	12:36:18.39	62:11:39.2	...	2.390	GAL	24.38	0.51	1.15	...	...	S03-D7
BX1081	12:36:15.19	62:12:07.6	...	1.801	GAL	24.23	0.23	0.60	...	...	
BX1084	12:36:13.57	62:12:21.5	...	2.437	GAL	23.24	0.26	0.72	...	...	
BX1085	12:36:13.33	62:12:16.3	...	2.236	GAL	24.50	0.33	0.87	...	...	
BX1086	12:36:13.42	62:12:18.8	2.444	2.444	GAL	24.64	0.41	1.09	...	...	z from Hα

Table 5.2—Continued

Name	α (J2000.0)	δ (J2000.0)	$z_{\rm em}$[a]	$z_{\rm abs}$[b]	Type[c]	$\mathcal{R}$[d] (mag)	$G-\mathcal{R}$ (mag)	$U_{\rm n}-G$[e] (mag)	J[f] (mag)	$K_{\rm s}$[f] (mag)	Notes[g]
BX1089	12:36:00.64	62:13:59.4	...	2.049	GAL	24.23	0.16	0.83	...	...	
BX1100	12:36:39.65	62:09:48.4	...	2.079	GAL	23.20	0.17	0.61	22.85	22.11	
BX1104	12:36:18.35	62:12:22.2	2.445	2.438	GAL	24.03	0.18	0.78	...	...	
BX1106	12:36:27.56	62:11:29.8	...	2.917	GAL	24.61	0.65	1.52	> 25.0	24.05	S03-oMD28
BX1112	12:36:15.65	62:13:05.3	0.170	...	GAL	24.26	0.21	0.87	...	...	
BX1116	12:36:09.05	62:13:59.1	...	2.048	GAL	24.10	0.13	0.62	...	...	
BX1120	12:36:07.62	62:14:16.6	0.169	...	GAL	24.64	0.43	1.31	...	...	
BX1121	12:36:13.24	62:13:39.6	1.878	1.878	GAL	23.80	0.13	0.46	...	...	
BX1125	12:36:25.00	62:12:23.6	2.222	...	GAL	25.20	0.18	0.94	> 25.0	> 24.4	
BX1126	12:36:11.91	62:13:58.7	...	:1.942	GAL	24.59	0.07	0.32	...	...	
BX1129	12:36:56.94	62:08:48.7	...	1.973	GAL	22.80	0.21	0.58	...	...	
BX1130	12:36:33.17	62:11:34.1	0.080	...	GAL	20.65	0.30	0.84	20.50	20.20	B03-173
BX1132	12:36:03.91	62:15:08.3	...	:2.112	GAL	24.41	0.45	0.98	...	...	
BX1140	12:36:08.51	62:14:48.0	1.487	...	GAL	24.69	0.10	0.36	...	...	
BX1145	12:36:10.12	62:14:49.2	...	2.325	GAL	25.40	0.17	0.51	...	...	
BX1157	12:36:18.30	62:14:09.1	2.083	2.078	GAL	24.14	0.14	0.34	...	...	
BX1161	12:36:59.39	62:09:21.9	...	1.891	GAL	23.71	0.37	0.59	...	...	
BX1164	12:36:24.20	62:13:32.6	2.598	2.588	GAL	24.49	0.22	0.85	> 25.0	> 24.4	
BX1166	12:36:20.32	62:14:04.9	1.334	...	GAL	24.54	0.09	0.30	22.95	23.13	

Table 5.2—Continued

Name	α (J2000.0)	δ (J2000.0)	$z_{\rm em}$[a]	$z_{\rm abs}$[b]	Type[c]	$\mathcal{R}$[d] (mag)	$G-\mathcal{R}$ (mag)	$U_{\rm n}-G$[e] (mag)	J[f] (mag)	$K_{\rm s}$[f] (mag)	Notes[g]
BX1169	12:36:28.27	62:13:15.3	...	1.871	GAL	23.82	0.14	0.43	23.04	22.30	
BX1170	12:36:31.94	62:12:51.8	2.445	2.441	GAL	24.26	0.35	1.04	23.23	22.58	
BX1172	12:36:54.35	62:10:18.3	2.811	2.802	GAL	24.50	0.55	1.19	> 25.0	> 24.4	S03-D2
BX1174	12:36:47.82	62:11:06.1	2.349	...	GAL	24.37	0.19	0.49	24.40	23.72	
BX1178	12:36:33.52	62:12:51.8	0.000	0.000	STAR	23.23	0.01	0.42	23.38	22.64	
BX1183	12:37:08.51	62:08:54.7	2.043	:2.039	GAL	24.67	0.37	1.00	...	...	
BX1185	12:36:12.60	62:15:30.0	2.207	2.203	GAL	24.99	0.47	0.96	...	...	
BX1186	12:36:13.20	62:15:26.2	...	2.079	GAL	25.02	0.22	0.53	...	...	
BX1192	12:36:16.83	62:15:14.3	...	1.996	GAL	24.22	0.15	0.86	...	...	
BX1197	12:36:18.89	62:15:06.8	2.599	2.587	GAL	24.13	0.17	0.80	> 25.0	> 24.4	
BX1201	12:36:14.13	62:15:41.8	...	2.000	GAL	24.00	0.18	0.71	...	...	
BX1204	12:36:21.73	62:14:52.6	2.209	2.200	GAL	24.27	0.32	1.13	23.27	22.38	
BX1208	12:36:41.67	62:12:38.7	2.589	...	GAL	24.44	0.30	0.79	23.66	23.99	
BX1209	12:36:37.07	62:13:11.8	0.348	...	GAL	24.63	0.30	0.88	> 25.0	23.07	
BX1214	12:36:44.65	62:12:27.2	...	:1.879	GAL	23.99	0.23	0.60	22.67	22.10	
BX1217	12:37:08.47	62:09:47.1	...	:2.170	GAL	24.73	0.27	0.89	23.40	22.82	
BX1218	12:36:41.69	62:12:58.0	...	:2.054	GAL	23.88	0.11	0.35	23.23	22.50	
BX1220	12:36:30.85	62:14:18.2	0.136	0.136	GAL	24.86	0.41	0.81	23.51	22.45	
BX1222	12:37:02.99	62:10:34.1	2.446	2.438	GAL	24.53	0.26	0.75	> 25.0	24.14	S03-MD18

Table 5.2—Continued

Name	α (J2000.0)	δ (J2000.0)	$z_{\rm em}$[a]	$z_{\rm abs}$[b]	Type[c]	$\mathcal{R}$[d] (mag)	$G-\mathcal{R}$ (mag)	$U_{\rm n}-G$[e] (mag)	J[f] (mag)	$K_{\rm s}$[f] (mag)	Notes[g]
BX1223	12:36:18.22	62:15:51.6	:1.865	...	GAL	25.07	0.25	0.48	23.55	21.81	DRG
BX1228	12:36:20.19	62:15:40.6	1.999	1.995	GAL	24.03	0.39	0.65	23.12	23.33	
BX1229	12:36:33.23	62:14:11.0	1.343	1.343	GAL	23.80	0.12	0.36	23.06	22.57	
BX1233	12:36:36.76	62:13:51.3	2.856	...	GAL	24.67	0.37	0.86	> 25.0	23.37	S03-D12; DRG
BX1238	12:36:54.39	62:11:55.4	...	2.261	GAL	24.57	0.30	0.65	24.00	23.33	
BX1240	12:37:06.77	62:10:23.1	...	2.282	GAL	24.01	0.14	0.68	24.06	23.63	
BX1243	12:37:06.66	62:10:35.2	...	:2.037	GAL	23.99	0.27	0.52	23.21	22.99	
BX1244	12:37:02.55	62:11:05.0	...	1.012	GAL	23.68	0.07	0.27	> 25.0	> 24.4	
BX1245	12:36:16.28	62:16:30.4	2.097	2.089	GAL	23.82	-0.05	0.34	...	...	
BX1250	12:36:32.11	62:14:50.9	1.856	1.853	GAL	24.68	0.04	0.40	24.06	23.39	
BX1252	12:37:07.71	62:10:37.6	...	2.931	GAL	24.12	0.60	1.57	24.56	23.72	
BX1253	12:36:23.62	62:15:55.9	...	1.933	GAL	24.51	0.18	0.38	> 25.0	> 24.4	
BX1260	12:37:13.31	62:10:14.9	...	:1.714	GAL	24.98	0.50	1.02	22.97	21.60	
BX1264	12:37:09.38	62:10:46.3	2.942	...	GAL	24.76	0.14	0.80	> 25.0	23.75	S03-oMD24
BX1265	12:36:33.35	62:15:04.4	2.437	2.431	GAL	23.93	0.17	1.02	24.27	22.74	S03-oMD51; DRG
BX1267	12:36:22.67	62:16:21.6	1.996	1.996	GAL	23.90	0.13	0.51	22.84	22.17	
BX1269	12:37:10.37	62:10:49.2	...	2.275	GAL	23.53	0.45	1.00	22.97	21.96	
BX1270	12:36:51.42	62:13:00.6	0.089	0.089	GAL	22.93	0.28	0.95	22.81	22.89	
BX1274	12:37:11.35	62:10:44.2	2.599	2.594	GAL	24.29	0.25	0.93	24.02	23.87	

Table 5.2—Continued

Name	α (J2000.0)	δ (J2000.0)	$z_{\rm em}$[a]	$z_{\rm abs}$[b]	Type[c]	$\mathcal{R}$[d] (mag)	$G-\mathcal{R}$ (mag)	$U_{\rm n}-G$[e] (mag)	J[f] (mag)	$K_{\rm s}$[f] (mag)	Notes[g]
BX1277	12:37:18.60	62:09:55.5	...	2.268	GAL	23.87	0.14	0.61	22.89	23.08	
BX1279	12:36:19.45	62:17:01.1	0.995	...	GAL	24.79	-0.19	0.19	> 25.0	> 24.4	
BX1281	12:37:03.39	62:11:53.5	...	2.410	GAL	25.16	0.32	0.70	> 25.0	23.89	S03-D8
BX1283	12:37:16.29	62:10:23.3	...	2.427	GAL	24.59	0.24	0.60	23.46	22.72	
BX1284	12:36:44.08	62:14:09.9	2.276	2.270	GAL	24.37	0.01	0.61	23.77	22.97	
BX1287	12:36:20.64	62:16:57.9	...	1.675	GAL	23.05	0.05	0.34	22.17	22.58	
BX1288	12:37:11.14	62:11:04.5	2.301	...	GAL	24.16	0.10	0.58	23.29	23.50	
BX1289	12:36:33.67	62:15:32.9	...	2.488	GAL	24.15	0.34	1.16	23.47	22.64	
BX1290	12:36:35.55	62:15:21.8	2.980	...	GAL	24.69	0.39	0.79	> 25.0	> 24.4	S03-oMD54
BX1291	12:37:00.11	62:12:25.2	...	2.052	GAL	23.56	0.30	0.80	23.49	23.17	
BX1293	12:36:46.52	62:14:07.5	0.128	...	GAL	24.22	0.33	0.67	23.53	23.43	
BX1296	12:36:20.91	62:17:09.5	1.989	1.988	GAL	24.15	0.26	0.59	22.82	21.75	
BX1297	12:37:13.08	62:11:02.2	...	2.274	GAL	24.53	0.35	0.82	23.25	22.00	
BX1299	12:36:53.24	62:13:22.2	1.654	1.649	GAL	23.49	0.36	0.61	23.38	22.32	
BX1300	12:36:54.76	62:13:14.7	:2.288	:2.288	GAL	24.55	0.21	0.65	24.08	23.34	
BX1303	12:37:11.20	62:11:18.7	2.305	2.304	GAL	24.72	0.11	0.81	24.24	22.85	DRG
BX1305	12:36:50.12	62:14:01.0	2.238	2.231	GAL	24.77	0.14	0.72	23.35	23.00	
BX1307	12:36:48.33	62:14:16.7	...	2.002	GAL	23.30	0.20	0.74	22.69	21.83	
BX1311	12:36:30.54	62:16:26.1	2.490	2.479	GAL	23.29	0.21	0.81	22.94	22.30	

Table 5.2—Continued

Name	α (J2000.0)	δ (J2000.0)	$z_{\rm em}$[a]	$z_{\rm abs}$[b]	Type[c]	$\mathcal{R}$[d] (mag)	$G-\mathcal{R}$ (mag)	$U_{\rm n}-G$[e] (mag)	J[f] (mag)	$K_{\rm s}$[f] (mag)	Notes[g]
BX1312	12:37:02.27	62:12:43.2	0.107	0.107	GAL	22.72	0.46	1.04	22.32	22.71	
BX1313	12:37:04.04	62:12:33.8	2.637	2.632	GAL	24.31	0.42	0.99	> 25.0	> 24.4	
BX1315	12:36:30.10	62:16:35.9	...	1.671	GAL	23.77	0.19	0.41	22.62	22.06	
BX1316	12:37:20.70	62:10:40.7	2.088	...	GAL	24.26	0.20	0.55	23.16	22.41	
BX1317	12:36:25.36	62:17:08.0	1.792	1.787	GAL	23.28	0.16	0.41	22.44	21.78	
BX1319	12:37:04.26	62:12:39.5	1.109	1.109	GAL	23.33	0.31	0.62	22.54	21.82	
BX1321	12:36:48.31	62:14:26.5	0.139	...	—	19.22	0.32	0.91	18.72	18.46	B03-251
BX1322	12:37:06.54	62:12:24.9	2.449	2.438	GAL	23.72	0.31	0.57	24.01	22.77	
BX1324	12:37:12.95	62:11:44.5	1.821	1.815	GAL	24.38	0.46	1.03	22.85	22.15	
BX1326	12:36:35.71	62:16:14.9	2.984	...	GAL	24.49	0.40	0.73	> 25.0	23.90	
BX1327	12:36:57.51	62:13:44.2	2.209	...	GAL	24.05	0.21	0.44	23.13	22.51	
BX1329	12:36:54.62	62:14:07.7	...	:1.987	GAL	24.69	-0.04	0.45	23.95	23.79	
BX1330	12:36:48.91	62:14:50.9	...	2.363	GAL	23.73	0.05	0.61	23.66	22.72	
BX1332	12:37:17.13	62:11:39.9	2.218	2.209	GAL	23.64	0.32	0.92	23.35	22.50	
BX1334	12:36:46.64	62:15:17.0	3.371	...	GAL	25.11	0.46	1.19	> 25.0	23.22	S03-M28; DRG
BX1335	12:36:44.69	62:15:31.2	...	:2.453	AGN?	25.15	0.28	0.94	23.74	22.84	
BX1339	12:36:25.09	62:17:56.8	1.993	1.984	GAL	24.60	-0.05	0.48	...	...	
BX1343	12:37:08.77	62:12:57.8	...	2.268	GAL	23.98	0.17	0.82	22.88	22.57	
BX1348	12:37:05.84	62:13:29.3	1.923	1.919	GAL	24.76	0.05	0.29	23.84	23.89	

Table 5.2—Continued

Name	α (J2000.0)	δ (J2000.0)	$z_{\rm em}$[a]	$z_{\rm abs}$[b]	Type[c]	$\mathcal{R}$[d] (mag)	$G-\mathcal{R}$ (mag)	$U_{\rm n}-G$[e] (mag)	J[f] (mag)	$K_{\rm s}$[f] (mag)	Notes[g]
BX1349	12:36:57.27	62:14:29.7	...	1.873	GAL	24.29	0.41	0.74	22.93	22.18	
BX1350	12:37:05.50	62:13:34.6	...	:2.830	GAL	24.56	0.45	1.14	> 25.0	> 24.4	S03-MD37
BX1351	12:36:59.40	62:14:04.7	0.089	0.089	GAL	20.17	0.45	1.01	19.69	19.83	
BX1353	12:36:31.15	62:17:39.9	...	:2.505	GAL	24.28	0.24	0.61	22.92	22.03	
BX1354	12:37:17.25	62:12:20.3	2.088	2.088	GAL	24.98	-0.10	0.38	> 25.0	> 24.4	
BX1355	12:36:43.16	62:16:20.1	...	2.307	GAL	24.09	0.13	1.07	23.77	22.98	
BX1358	12:36:59.46	62:14:27.7	2.943	...	GAL	24.83	0.49	1.45	> 25.0	23.73	
BX1361	12:36:30.47	62:17:53.9	...	:1.849	GAL	25.48	-0.04	0.22	> 25.0	23.43	DRG
BX1362	12:36:42.57	62:16:29.4	...	1.664	GAL	24.55	0.05	0.28	23.56	22.83	
BX1363	12:37:27.40	62:11:12.7	...	2.297	GAL	23.82	0.33	0.76	22.89	22.15	
BX1364	12:37:23.74	62:11:41.2	...	2.183	GAL	24.27	0.22	0.74	23.56	22.82	
BX1368	12:36:48.24	62:15:56.2	2.446	2.440	GAL	23.79	0.30	0.96	23.34	22.45	
BX1371	12:37:16.57	62:12:45.2	0.947	...	GAL	24.23	0.30	0.95	23.84	23.79	
BX1374	12:36:57.90	62:15:07.0	0.116	0.116	GAL	23.80	0.26	0.88	23.27	23.41	
BX1376	12:36:52.96	62:15:45.5	2.434	2.426	GAL	24.48	0.01	0.70	24.05	23.95	
BX1378	12:37:02.02	62:14:43.4	...	1.971	GAL	23.90	0.33	0.66	23.14	22.75	
BX1387	12:36:56.32	62:15:52.4	...	2.324	GAL	24.77	0.17	0.61	23.72	23.89	
BX1388	12:36:44.84	62:17:15.8	...	2.032	GAL	24.55	0.27	0.99	22.63	21.77	
BX1391	12:37:13.87	62:13:54.9	...	1.906	GAL	24.06	0.35	0.57	23.14	22.98	

Table 5.2—Continued

Name	α (J2000.0)	δ (J2000.0)	$z_{\rm em}$[a]	$z_{\rm abs}$[b]	Type[c]	$\mathcal{R}$[d] (mag)	$G-\mathcal{R}$ (mag)	$U_{\rm n}-G$[e] (mag)	J[f] (mag)	$K_{\rm s}$[f] (mag)	Notes[g]
BX1392	12:37:25.92	62:12:06.4	0.089	...	GAL	21.58	0.37	0.94	21.27	21.23	
BX1397	12:37:04.12	62:15:09.8	...	2.133	GAL	24.12	0.14	0.76	22.85	22.69	
BX1399	12:37:18.30	62:13:32.6	...	2.033	GAL	25.22	0.23	0.73	23.91	23.49	
BX1400	12:37:06.09	62:15:01.5	:3.239	...	GAL	23.77	0.52	1.21	23.17	23.41	
BX1401	12:37:02.93	62:15:22.5	...	2.481	GAL	23.47	0.41	0.87	22.38	21.73	
BX1403	12:37:25.12	62:12:49.5	...	:1.706	GAL	24.63	0.32	0.52	> 25.0	> 24.4	
BX1408	12:36:57.40	62:16:18.2	...	2.482	GAL	24.83	0.64	1.47	24.13	22.68	S03-MD40; DRG
BX1409	12:36:47.41	62:17:28.7	...	2.237	GAL	24.66	0.49	1.17	23.28	21.89	DRG
BX1420	12:36:50.87	62:17:12.4	...	2.133	GAL	23.79	0.45	1.01	22.84	22.34	
BX1425	12:37:17.96	62:14:17.6	...	1.864	GAL	24.65	0.02	0.28	23.44	23.66	
BX1427	12:37:33.28	62:12:33.8	...	2.548	GAL	24.54	0.39	0.85	...	...	
BX1431	12:36:58.48	62:16:45.5	2.006	1.996	GAL	24.00	0.09	0.45	> 25.0	23.13	DRG
BX1434	12:37:16.80	62:14:38.8	...	1.994	GAL	24.49	0.26	0.51	23.62	23.21	
BX1439	12:36:53.66	62:17:24.3	2.191	2.186	GAL	23.90	0.26	0.79	22.78	21.54	
BX1443	12:36:44.87	62:18:37.9	...	1.684	GAL	23.33	0.31	0.57	...	...	
BX1446	12:36:43.42	62:18:55.3	2.326	2.315	GAL	24.21	0.16	0.71	...	...	
BX1451	12:37:13.22	62:15:31.7	...	2.245	GAL	24.58	0.40	0.86	23.54	22.84	
BX1458	12:37:26.95	62:14:03.6	...	1.864	GAL	24.84	0.35	0.68	23.19	23.05	
BX1460	12:36:56.80	62:17:25.5	3.137	3.131	GAL	24.70	0.41	1.30	24.39	23.68	

Table 5.2—Continued

Name	α (J2000.0)	δ (J2000.0)	$z_{\rm em}$[a]	$z_{\rm abs}$[b]	Type[c]	$\mathcal{R}$[d] (mag)	$G-\mathcal{R}$ (mag)	$U_{\rm n}-G$[e] (mag)	J[f] (mag)	$K_{\rm s}$[f] (mag)	Notes[g]
BX1461	12:36:49.54	62:18:33.2	2.107	2.107	GAL	24.77	0.23	0.63	...	...	
BX1476	12:37:19.55	62:15:20.8	1.930	1.927	GAL	25.19	0.15	0.37	> 25.0	24.42	
BX1479	12:37:15.42	62:16:03.9	2.383	2.371	GAL	24.39	0.16	0.79	23.77	23.12	
BX1480	12:37:25.43	62:14:56.2	...	2.545	GAL	24.28	0.53	1.13	24.06	23.32	
BX1485	12:37:28.12	62:14:39.9	...	2.548	GAL	23.29	0.35	0.96	22.96	22.02	
BX1495	12:37:24.88	62:15:22.4	2.251	2.244	GAL	24.98	0.20	0.73	> 25.0	23.32	DRG
BX1501	12:37:41.58	62:13:22.2	1.879	1.875	GAL	23.78	0.16	0.46	...	...	
BX1504	12:37:41.90	62:13:33.7	2.869	2.858	GAL	24.34	0.52	1.42	...	...	
BX1505	12:36:59.12	62:18:35.8	1.012	...	GAL	24.49	0.11	0.34	...	...	
BX1510	12:37:27.13	62:15:28.3	...	:2.072	GAL	24.90	0.15	0.57	23.54	23.98	
BX1514	12:37:14.93	62:16:59.8	...	2.135	GAL	24.90	0.29	0.56	23.48	> 24.4	
BX1525	12:37:24.15	62:16:11.6	1.689	1.689	GAL	24.15	0.28	0.56	22.44	21.56	
BX1529	12:37:01.68	62:18:48.6	0.232	...	GAL	24.31	0.27	0.51	...	...	
BX1530	12:37:22.85	62:16:27.6	...	2.421	GAL	24.40	0.25	0.84	24.18	23.19	
BX1535	12:37:07.18	62:18:30.1	...	2.299	GAL	24.31	0.33	0.97	...	...	
BX1542	12:36:55.06	62:20:05.2	1.018	...	GAL	24.72	0.11	0.31	...	...	
BX1544	12:37:14.85	62:17:47.3	...	:2.486	GAL	24.27	0.24	1.13	...	...	
BX1548	12:37:00.49	62:19:30.3	0.223	...	GAL	23.79	0.46	0.89	...	...	
BX1557	12:37:27.17	62:16:31.7	...	1.776	GAL	23.74	0.31	0.80	22.99	23.00	

Table 5.2—Continued

Name	α (J2000.0)	δ (J2000.0)	$z_{\rm em}$[a]	$z_{\rm abs}$[b]	Type[c]	$\mathcal{R}$[d] (mag)	$G-\mathcal{R}$ (mag)	$U_{\rm n}-G$[e] (mag)	J[f] (mag)	$K_{\rm s}$[f] (mag)	Notes[g]
BX1559	12:37:29.41	62:15:40.1	...	2.408	GAL	24.19	0.07	0.59	23.84	23.53	
BX1564	12:37:23.47	62:17:20.0	...	2.218	GAL	23.28	0.27	1.01	22.21	21.44	
BX1567	12:37:23.17	62:17:23.9	...	2.225	GAL	23.50	0.18	1.05	22.31	22.00	DLA
BX1568	12:36:54.06	62:20:48.1	...	1.787	GAL	23.46	0.08	0.44	...	...	
BX1572	12:36:58.51	62:20:29.3	...	1.782	GAL	24.32	0.25	0.59	...	...	
BX1574	12:37:25.95	62:17:10.1	...	1.808	GAL	24.24	0.22	0.66	22.66	22.33	
BX1579	12:37:38.93	62:15:41.0	0.190	...	GAL	22.98	0.38	0.62	...	...	
BX1586	12:37:24.91	62:17:40.8	...	:1.901	GAL	24.44	0.41	0.82	23.54	23.10	
BX1588	12:37:02.54	62:20:20.9	...	2.221	GAL	23.22	0.30	1.17	> 25.0	> 24.4	
BX1591	12:37:28.21	62:17:22.6	2.050	2.048	GAL	24.45	0.21	0.52	23.03	22.97	
BX1605	12:37:21.51	62:18:30.6	1.977	1.970	GAL	23.89	-0.07	0.19	...	...	
BX1616	12:37:32.75	62:17:27.6	...	2.205	GAL	25.29	0.13	0.35	...	...	
BX1617	12:37:04.16	62:20:50.8	2.323	2.317	GAL	25.15	0.15	0.68	...	...	
BX1630	12:37:25.95	62:18:32.5	2.222	2.217	GAL	24.35	0.03	0.52	...	...	
BX1636	12:37:20.03	62:19:23.1	2.306	2.295	GAL	24.08	0.44	1.16	...	...	
BX1637	12:37:04.82	62:21:11.5	2.487	...	GAL	24.92	-0.01	0.81	...	...	
BX1641	12:37:08.89	62:20:44.7	1.433	...	GAL	24.20	0.01	0.26	...	...	
BX1642	12:37:32.40	62:17:50.8	2.010	2.004	GAL	24.29	0.25	0.46	...	...	
BX1650	12:37:24.11	62:19:04.7	2.100	2.094	GAL	23.24	0.18	0.74	...	...	

Table 5.2—Continued

Name	α (J2000.0)	δ (J2000.0)	$z_{\rm em}$[a]	$z_{\rm abs}$[b]	Type[c]	$\mathcal{R}$[d] (mag)	$G-\mathcal{R}$ (mag)	$U_{\rm n}-G$[e] (mag)	J[f] (mag)	$K_{\rm s}$[f] (mag)	Notes[g]
BX1655	12:37:32.30	62:18:16.3	0.157	...	GAL	24.37	0.41	1.21	...	...	
BX1669	12:37:48.40	62:16:34.8	0.118	...	GAL	23.24	0.35	0.96	...	...	
BX1676	12:37:36.68	62:18:02.1	0.188	...	GAL	23.49	0.42	0.80	...	...	
BX1694	12:37:33.82	62:18:46.3	2.009	2.005	GAL	23.66	0.11	0.53	...	...	
BX1708	12:37:32.65	62:19:10.6	...	1.987	GAL	24.50	0.45	1.00	...	...	
BX1782	12:36:57.46	62:08:38.0	0.177	0.177	GAL	22.27	0.43	0.75	...	...	
BX1790	12:36:59.31	62:09:31.2	...	2.990	GAL	23.81	0.62	1.17	22.58	23.20	
BX1796	12:36:27.51	62:14:18.8	0.089	...	GAL	22.70	0.49	0.70	22.43	22.15	
BX1805	12:36:38.64	62:14:21.8	0.306	0.306	GAL	22.80	0.48	0.80	21.66	21.10	
BX1808	12:36:59.54	62:12:14.2	...	:1.943	GAL	24.09	0.43	0.68	23.33	23.38	
BX1815	12:37:15.22	62:11:02.6	0.000	0.000	STAR	19.64	0.54	1.08	19.48	19.87	
BX1816	12:36:44.13	62:14:50.7	...	:2.095	GAL	24.25	0.53	0.87	23.16	22.00	
BX1817	12:36:23.27	62:16:43.2	1.862	1.858	GAL	24.54	0.46	0.76	23.66	22.69	
BX1820	12:37:19.43	62:11:13.8	...	2.457	GAL	24.11	0.65	1.35	23.07	22.07	
BX1821	12:37:12.63	62:12:10.4	...	2.590	GAL	24.79	0.60	1.11	23.93	23.54	
BX1822	12:37:05.74	62:13:03.2	0.109	...	GAL	22.05	0.59	1.14	22.03	21.91	
BX1823	12:37:15.40	62:12:17.9	...	1.818	GAL	24.65	0.49	0.78	22.24	21.33	
BX1826	12:37:17.38	62:12:46.8	...	2.929	GAL	24.67	0.52	1.02	23.99	23.78	
BX1827	12:36:56.63	62:15:19.0	1.988	...	GAL	24.84	0.56	1.12	24.48	23.28	

Table 5.2—Continued

Name	α (J2000.0)	δ (J2000.0)	$z_{\rm em}$[a]	$z_{\rm abs}$[b]	Type[c]	$\mathcal{R}$[d] (mag)	$G-\mathcal{R}$ (mag)	$U_{\rm n}-G$[e] (mag)	J[f] (mag)	$K_{\rm s}$[f] (mag)	Notes[g]
BX1828	12:37:16.22	62:13:24.3	...	:2.967	GAL	24.09	0.66	1.40	23.35	23.45	
BX1833	12:37:11.13	62:14:33.8	0.000	0.000	STAR	22.12	0.59	1.02	22.30	22.01	
BX1841	12:37:02.63	62:16:33.9	...	2.373	GAL	24.70	0.47	1.04	23.46	23.12	
BX1848	12:37:25.86	62:14:42.4	2.648	...	GAL	25.05	0.45	0.81	> 25.0	> 24.4	
BX1851	12:37:29.99	62:15:59.5	0.215	...	GAL	22.96	0.48	0.72	22.31	22.07	
BX1856	12:37:22.40	62:17:18.0	0.232	...	GAL	23.03	0.51	0.82	22.51	22.34	
BX1860	12:37:30.81	62:16:54.7	...	:2.504	GAL	24.80	0.51	0.85	> 25.0	23.71	
BX28	12:37:17.78	62:09:37.8	0.229	...	GAL	23.74	0.61	0.78	23.54	23.11	
BX82	12:37:05.37	62:10:45.3	1.023	...	GAL	24.41	0.58	0.19	23.29	22.94	
BX84	12:37:13.74	62:10:42.0	2.166	2.161	GAL	24.15	0.22	0.80	> 25.0	> 24.4	
BX150	12:37:14.98	62:12:07.9	2.281	2.273	GAL	24.64	0.54	0.53	> 25.0	> 24.4	
BX160	12:37:20.07	62:12:23.0	2.462	2.458	AGN	24.02	0.74	0.92	22.83	21.87	
BX184	12:37:19.28	62:13:00.6	1.998	...	GAL	24.22	0.70	0.99	23.42	23.46	
BX274	12:36:53.60	62:15:25.0	0.000	0.000	STAR	18.57	0.33	0.96	18.48	18.96	
BX283	12:37:24.35	62:15:58.3	0.129	...	GAL	23.41	0.44	0.84	> 25.0	> 24.4	
BX289	12:37:00.47	62:16:04.9	0.941	...	GAL	24.49	0.69	0.22	23.39	23.25	
BX305	12:36:37.13	62:16:28.7	...	2.482	GAL	24.28	0.79	1.30	23.63	21.96	DRG
BX308	12:37:02.66	62:16:34.0	...	2.376	GAL	24.87	0.46	0.95	> 25.0	> 24.4	
BX313	12:36:29.66	62:16:45.1	...	2.323	GAL	24.34	0.42	0.60	> 25.0	> 24.4	

Table 5.2—Continued

Name	α (J2000.0)	δ (J2000.0)	$z_{\rm em}$ [a]	$z_{\rm abs}$ [b]	Type[c]	$\mathcal{R}$[d] (mag)	$G-\mathcal{R}$ (mag)	$U_{\rm n}-G$[e] (mag)	J[f] (mag)	$K_{\rm s}$[f] (mag)	Notes[g]
BX341	12:36:22.26	62:17:30.9	2.117	2.117	GAL	23.56	0.71	0.27	23.77	22.73	
BM1008	12:35:47.95	62:12:52.3	1.801	1.798	GAL	23.58	0.24	0.25	...	...	
BM1010	12:36:08.08	62:10:44.7	...	1.346	GAL	24.03	0.16	0.18	...	...	
BM1011	12:35:51.57	62:12:42.0	1.677	1.677	GAL	23.90	0.28	0.33	...	...	
BM1017	12:36:11.72	62:10:39.3	...	:2.371	GAL	24.58	0.17	0.20	...	...	
BM1030	12:35:55.26	62:14:01.2	1.143	1.142	GAL	24.29	0.20	0.37	...	...	
BM1048	12:36:11.63	62:13:18.3	1.381	1.379	GAL	23.50	0.23	0.23	...	...	
BM1053	12:36:18.48	62:12:45.9	1.460	1.457	GAL	24.99	0.09	-0.02	...	...	
BM1061	12:36:15.82	62:13:26.0	2.089	...	GAL	25.37	0.02	-0.05	...	...	
BM1063	12:36:21.37	62:12:52.9	...	2.087	GAL	24.46	0.20	0.39	23.14	22.84	
BM1064	12:36:32.06	62:11:40.0	...	1.524	GAL	23.57	0.18	0.28	22.54	22.55	
BM1069	12:36:11.63	62:14:16.5	...	2.028	GAL	24.43	0.27	0.36	...	...	
BM1072	12:36:04.15	62:15:21.0	1.143	...	GAL	23.48	0.10	0.29	...	...	
BM1074	12:36:28.77	62:12:39.4	0.880	...	GAL	24.32	0.11	0.00	23.63	23.42	
BM1083	12:36:06.67	62:15:50.7	2.414	...	QSO	23.34	0.25	0.26	...	...	B03-77
BM1092	12:36:13.42	62:15:17.7	1.479	...	GAL	24.07	0.12	0.31	...	...	
BM1095	12:36:24.64	62:14:18.6	1.450	1.445	GAL	24.31	-0.01	0.15	23.17	23.66	
BM1098	12:36:51.16	62:11:28.0	...	1.671	GAL	23.76	0.20	0.37	22.77	22.47	
BM1099	12:37:03.45	62:10:09.1	...	:1.662	GAL	24.67	0.23	0.35	23.73	23.16	

Table 5.2—Continued

Name	α (J2000.0)	δ (J2000.0)	$z_{\rm em}$[a]	$z_{\rm abs}$[b]	Type[c]	$\mathcal{R}$[d] (mag)	$G-\mathcal{R}$ (mag)	$U_{\rm n}-G$[e] (mag)	J[f] (mag)	$K_{\rm s}$[f] (mag)	Notes[g]
BM1119	12:37:03.70	62:11:22.6	...	1.717	GAL	23.29	0.28	0.32	22.30	21.74	B03-327
BM1121	12:36:58.38	62:12:13.9	1.020	1.020	GAL	23.11	0.26	0.22	22.52	22.15	
BM1122	12:37:02.62	62:11:56.7	1.994	1.986	GAL	23.96	0.17	0.33	24.18	24.00	
BM1132	12:36:53.07	62:13:44.3	...	:1.901	GAL	23.76	0.26	0.40	23.13	22.63	
BM1135	12:36:49.76	62:14:14.9	...	1.872	GAL	23.57	0.29	0.43	22.44	21.76	
BM1136	12:36:52.75	62:13:54.8	1.355	...	GAL	22.15	0.16	0.23	21.53	21.36	B03-272
BM1139	12:37:22.12	62:10:46.6	1.919	...	GAL	24.10	0.25	0.18	24.37	23.17	
BM1144	12:36:43.72	62:15:46.2	...	:1.660	GAL	25.09	0.22	0.40	23.47	22.92	
BM1146	12:37:10.65	62:12:56.2	...	:1.926	GAL	24.30	0.09	0.06	23.88	23.29	
BM1148	12:36:46.15	62:15:51.1	2.053	2.045	GAL	23.38	0.20	0.29	24.43	23.08	
BM1149	12:36:34.79	62:17:10.1	1.631	1.629	GAL	24.58	0.02	0.16	> 25.0	> 24.4	
BM1153	12:36:48.46	62:15:59.5	2.450	2.439	GAL	24.64	0.32	0.47	23.83	22.85	
BM1155	12:37:23.98	62:12:12.1	2.024	2.015	GAL	23.99	0.08	0.15	23.25	23.50	
BM1156	12:37:04.34	62:14:46.3	2.211	...	AGN	24.62	-0.01	-0.21	22.94	22.15	S03-oMD49
BM1158	12:37:18.58	62:13:15.0	...	1.521	GAL	23.35	0.28	0.48	22.19	21.94	
BM1159	12:37:13.32	62:13:56.4	...	1.016	GAL	22.87	0.10	0.08	22.13	22.03	
BM1160	12:36:55.63	62:16:01.9	1.364	...	GAL	24.36	0.28	0.36	23.43	23.41	
BM1161	12:37:08.76	62:14:31.5	2.045	...	GAL	24.94	0.15	0.04	> 25.0	23.68	
BM1163	12:37:26.98	62:12:24.5	1.876	1.872	GAL	24.72	0.23	0.43	23.80	23.56	

Table 5.2—Continued

Name	α (J2000.0)	δ (J2000.0)	$z_{\rm em}$[a]	$z_{\rm abs}$[b]	Type[c]	$\mathcal{R}$[d] (mag)	$G-\mathcal{R}$ (mag)	$U_{\rm n}-G$[e] (mag)	J[f] (mag)	$K_{\rm s}$[f] (mag)	Notes[g]
BM1171	12:36:40.34	62:18:53.8	...	2.082	GAL	24.71	0.28	0.36	...	...	
BM1172	12:37:02.84	62:16:20.5	1.866	1.862	GAL	24.23	0.13	0.15	23.55	23.49	
BM1174	12:36:56.40	62:17:09.8	...	:1.670	GAL	24.97	0.11	0.14	25.0	> 24.4	
BM1175	12:37:26.35	62:13:38.5	1.778	1.767	GAL	23.94	0.25	0.30	23.28	23.02	
BM1180	12:37:27.22	62:13:52.9	...	1.598	GAL	23.55	0.20	0.28	22.21	21.84	
BM1181	12:37:01.75	62:16:53.0	1.747	1.740	GAL	22.56	0.25	0.35	22.03	22.26	
BM1190	12:37:06.87	62:17:02.1	1.020	...	QSO	19.81	0.15	-0.02	19.37	19.06	B03-344
BM1193	12:37:19.33	62:15:59.1	...	:1.564	GAL	24.36	0.20	0.17	22.93	23.30	
BM1195	12:37:35.59	62:14:05.9	...	1.289	GAL	23.97	0.28	0.37	...	...	
BM1196	12:37:18.75	62:16:15.0	1.863	...	—	24.62	-0.07	0.00	> 25.0	> 24.4	
BM1197	12:37:19.39	62:16:21.0	...	1.566	GAL	23.76	0.20	0.34	22.61	22.38	
BM1198	12:37:24.06	62:16:05.8	...	1.780	GAL	23.65	0.24	0.43	23.21	22.73	
BM1200	12:37:30.85	62:15:29.6	...	2.078	GAL	23.79	0.26	0.41	23.86	22.45	DRG
BM1201	12:37:21.09	62:16:41.9	1.001	...	GAL	24.24	0.09	0.00	23.12	23.26	
BM1204	12:37:18.29	62:17:09.1	...	1.489	GAL	23.64	0.08	0.19	22.79	22.65	
BM1205	12:37:42.45	62:14:19.5	1.711	1.711	GAL	24.44	0.11	-0.05	...	...	
BM1207	12:37:16.19	62:17:30.3	1.083	...	GAL	23.95	0.23	0.26	23.19	23.18	
BM1209	12:37:30.87	62:15:55.1	...	1.775	GAL	23.44	0.29	0.40	> 25.0	22.46	DRG
BM1211	12:37:43.19	62:14:49.6	0.960	...	GAL	24.47	0.21	0.15	...	...	

Table 5.2—Continued

Name	α (J2000.0)	δ (J2000.0)	$z_{\rm em}$[a]	$z_{\rm abs}$[b]	Type[c]	$\mathcal{R}$[d] (mag)	$G-\mathcal{R}$ (mag)	$U_{\rm n}-G$[e] (mag)	J[f] (mag)	$K_{\rm s}$[f] (mag)	Notes[g]
BM1212	12:37:24.28	62:17:20.8	...	:1.379	GAL	23.65	0.10	0.26	22.83	23.36	
BM1226	12:37:11.63	62:19:58.2	1.355	...	GAL	24.32	0.28	0.39	...	...	
BM1289	12:37:00.02	62:07:46.2	2.380	...	GAL	24.34	0.45	0.59	...	...	
BM1293	12:36:58.59	62:08:28.2	:2.300	...	GAL	24.91	0.50	0.66	...	...	
BM1299	12:37:01.33	62:08:44.6	...	1.595	GAL	23.31	0.44	0.51	...	...	
BM1303	12:36:39.51	62:11:40.4	...	1.721	GAL	24.75	0.46	0.45	23.56	22.43	
BM1324	12:36:16.00	62:15:58.2	0.322	0.322	GAL	22.80	0.36	0.52	...	...	
BM1326	12:36:53.46	62:11:40.0	...	1.268	GAL	22.31	0.28	0.19	21.46	20.47	B03-277
BM1334	12:37:12.15	62:10:29.6	...	1.893	GAL	23.74	0.43	0.58	22.47	21.96	
BM1335	12:37:07.82	62:10:57.6	...	1.489	GAL	23.16	0.51	0.55	22.02	21.47	
BM1339	12:37:09.12	62:11:28.5	...	1.338	GAL	23.17	0.36	0.31	22.40	22.00	
BM1345	12:37:17.39	62:10:46.7	0.202	...	GAL	22.54	0.37	0.53	21.57	20.87	
BM1358	12:37:01.24	62:15:20.5	...	1.807	GAL	24.07	0.46	0.64	22.33	21.17	
BM1362	12:37:07.09	62:14:56.0	...	:1.711	GAL	23.24	0.48	0.64	22.32	21.87	
BM1369	12:37:07.79	62:15:25.0	...	1.879	GAL	24.56	0.43	0.61	> 25.0	23.21	DRG
BM1375	12:36:58.58	62:17:15.3	2.113	2.106	GAL	23.91	0.30	0.31	22.92	22.75	
BM1376	12:37:13.85	62:15:38.3	...	:1.278	GAL	23.35	0.46	0.40	22.30	22.12	
BM1384	12:37:23.15	62:15:38.0	2.243	...	AGN	23.98	0.49	0.45	22.79	21.69	B03-409
BM1396	12:37:38.38	62:15:09.0	1.743	1.743	GAL	23.66	0.45	0.52	...	...	

Table 5.2—Continued

Name	α (J2000.0)	δ (J2000.0)	$z_{\rm em}$[a]	$z_{\rm abs}$[b]	Type[c]	$\mathcal{R}$[d] (mag)	$G-\mathcal{R}$ (mag)	$U_{\rm n}-G$[e] (mag)	J[f] (mag)	$K_{\rm s}$[f] (mag)	Notes[g]
BM1413	12:37:41.39	62:16:45.9	...	:1.391	GAL	22.93	0.42	0.35	...	...	
BM35	12:37:00.80	62:11:34.0	...	1.875	GAL	23.49	0.43	0.17	22.70	22.68	
BM63	12:37:13.75	62:14:09.0	:1.912	...	GAL	24.48	0.30	0.21	23.87	> 24.4	
BM69	12:37:17.68	62:14:35.9	:1.991	:1.991	GAL	25.12	0.31	0.27	> 25.0	> 24.4	
BM70	12:37:20.05	62:14:57.1	1.997	1.994	GAL	24.05	0.37	0.15	23.11	23.33	
BM72	12:37:22.00	62:15:03.3	...	1.571	GAL	24.72	0.34	0.18	23.27	23.33	
C2	12:35:59.42	62:11:19.9	...	2.991	GAL	25.24	0.80	> 1.46	...	...	
C11	12:36:47.88	62:10:31.9	...	2.990	GAL	24.59	0.86	> 2.05	> 25.0	23.46	S03-M7; DRG
C12	12:36:51.54	62:10:41.7	...	2.975	GAL	24.41	1.14	> 1.95	24.2	23.18	S03-M9
C14	12:36:54.95	62:11:43.8	...	2.973	GAL	25.30	1.07	> 1.13	> 25.0	23.79	
C16	12:36:44.07	62:13:11.0	...	2.929	GAL	23.99	1.14	> 2.37	23.26	22.25	S03-M18
C17	12:37:09.73	62:10:16.6	...	3.384	GAL	24.75	1.16	> 1.59	> 25.0	> 24.4	
C18	12:36:23.89	62:15:48.8	3.230	...	GAL	25.15	0.56	> 1.79	23.96	23.36	
C20	12:36:24.29	62:15:51.7	2.981	...	GAL	25.28	0.93	> 1.29	> 25.0	> 24.4	
C29	12:36:48.86	62:15:02.6	3.115	3.105	GAL	24.72	0.73	> 2.05	> 25.0	23.13	S03-oC38; DRG
C30	12:36:51.87	62:15:15.4	3.334	3.321	GAL	24.32	0.79	> 2.39	> 25.0	23.56	S03-C24; DRG
C33	12:36:49.01	62:15:42.5	3.136	3.125	GAL	23.77	0.45	> 3.28	23.68	23.65	S03-D15
C35	12:36:43.09	62:16:36.0	...	3.363	GAL	24.71	0.91	> 1.88	> 25.0	23.53	S03-M32; DRG
C40	12:37:06.19	62:15:10.1	3.246	3.239	GAL	24.53	0.85	> 2.12	23.95	23.28	S03-M27

Table 5.2—Continued

Name	α (J2000.0)	δ (J2000.0)	$z_{\rm em}$[a]	$z_{\rm abs}$[b]	Type[c]	$\mathcal{R}$[d] (mag)	$G-\mathcal{R}$ (mag)	$U_{\rm n}-G$[e] (mag)	J[f] (mag)	$K_{\rm s}$[f] (mag)	Notes[g]
C41	12:37:21.63	62:13:50.4	3.148	...	GAL	25.14	0.29	> 2.07	> 25.0	23.87	S03-C18
C42	12:36:51.29	62:18:15.0	...	3.411	GAL	24.46	1.06	> 1.98	...	...	
C48	12:36:51.81	62:19:06.0	...	3.206	GAL	24.89	0.99	> 1.62	...	...	
C53	12:37:23.38	62:16:23.9	3.103	...	GAL	25.04	0.94	> 1.52	> 25.0	> 24.4	
C54	12:37:05.98	62:19:04.0	3.217	...	GAL	25.34	0.41	> 1.75	...	...	
S03-C5	12:36:23.88	62:09:43.0	...	:2.664	GAL	24.65	0.71	0.89	24.10	23.54	S03-C5
S03-C7	12:36:37.64	62:10:47.4	...	2.658	GAL	24.36	0.95	1.23	24.41	23.09	S03-C7
S03-C8	12:36:26.95	62:11:27.0	2.993	2.983	GAL	24.38	0.85	1.81	23.59	23.96	S03-C8
S03-C17	12:36:51.17	62:13:48.9	3.163	...	GAL	24.84	0.60	0.92	> 25.0	23.91	S03-C17
S03-C26	12:37:03.26	62:16:35.0	...	3.239	GAL	23.95	1.31	2.85	23.58	22.66	S03-C26
S03-oC14	12:36:50.36	62:10:55.3	2.928	...	GAL	25.61	0.36	1.21	...	...	S03-oC14
S03-oC26	12:36:34.83	62:12:53.6	3.182	...	GAL	25.63	0.40	1.66	...	...	S03-oC26
S03-oC29	12:36:45.35	62:13:46.7	3.161	...	GAL	25.49	0.64	1.59	...	...	S03-oC29
S03-oC34	12:36:33.49	62:14:17.9	3.413	...	QSO	25.32	1.05	1.58	24.21	22.92	S03-oC34; B03-176
D8	12:35:59.84	62:12:08.7	3.300	...	GAL	25.10	0.93	2.80	...	...	
D14	12:36:45.02	62:09:40.6	2.983	2.975	GAL	24.97	0.37	1.92	24.69	23.97	S03-MD10
D16	12:36:17.49	62:13:10.1	2.930	...	GAL	25.06	-0.01	1.76	...	...	S03-D11
D19	12:36:41.84	62:11:07.1	3.199	3.187	GAL	24.45	0.68	3.23	24.03	23.33	S03-MD22
D20	12:36:49.46	62:10:18.5	3.247	...	GAL	25.26	0.76	2.74	24.45	23.22	

Table 5.2—Continued

Name	α (J2000.0)	δ (J2000.0)	$z_{\rm em}$[a]	$z_{\rm abs}$[b]	Type[c]	$\mathcal{R}$[d] (mag)	$G-\mathcal{R}$ (mag)	$U_{\rm n}-G$[e] (mag)	J[f] (mag)	$K_{\rm s}$[f] (mag)	Notes[g]
D23	12:36:19.37	62:15:01.9	3.128	3.123	GAL	23.78	0.62	2.45	23.47	22.96	S03-C22
D25	12:36:46.94	62:12:26.2	2.970	...	GAL	24.25	0.14	1.94	> 25.0	> 24.4	S03-D10
D26	12:36:14.69	62:16:22.9	2.975	...	GAL	25.48	0.29	1.79	...	...	
D28	12:36:47.79	62:12:55.7	...	2.932	GAL	24.02	0.95	2.55	23.38	22.35	S03-M17
D29	12:37:16.91	62:10:02.1	3.451	...	GAL	24.09	0.82	3.37	24.06	23.66	S03-C6
D32	12:36:42.39	62:14:49.0	2.962	...	GAL	24.87	0.18	2.38	> 25.0	> 24.4	S03-D14
D34	12:36:37.14	62:15:48.0	2.975	2.970	GAL	25.46	0.62	2.22	> 25.0	24.21	S03-C25
D35	12:36:53.62	62:14:10.3	3.196	...	GAL	24.88	1.00	2.76	24.04	23.5	S03-M22
D38	12:36:39.27	62:17:13.1	2.944	2.936	GAL	24.48	0.71	2.35	23.92	23.32	S03-C27
D39	12:37:00.54	62:14:41.9	...	2.987	GAL	24.82	0.61	2.14	24.60	> 24.4	
D41	12:36:43.42	62:17:51.8	3.228	...	GAL	24.77	0.84	3.20	24.19	23.46	
D45	12:36:58.98	62:17:14.2	3.134	3.127	GAL	23.58	1.05	3.09	21.86	20.92	S03-C28
D47	12:37:24.37	62:14:31.9	3.193	3.188	GAL	25.16	0.44	3.23	> 25.0	> 24.4	
D55	12:36:55.29	62:19:47.9	3.251	3.239	GAL	23.92	1.14	2.86	...	...	
S03-D3	12:36:47.70	62:10:53.2	...	2.943	GAL	24.18	0.81	1.47	23.68	23.60	S03-D3
S03-D6	12:37:12.27	62:11:37.8	2.925	...	GAL	25.40	0.14	2.00	...	...	S03-D6
S03-oD3	12:36:48.31	62:09:51.7	2.729	2.720	GAL	24.52	0.68	0.62	> 25.0	24.13	S03-oD3
S03-oD12	12:36:20.51	62:14:17.8	2.418	...	GAL	24.59	0.58	0.74	24.18	23.67	S03-oD12
MD4	12:35:56.54	62:11:26.1	2.867	...	GAL	25.22	0.38	1.55	...	...	

Table 5.2—Continued

Name	α (J2000.0)	δ (J2000.0)	$z_{\rm em}$[a]	$z_{\rm abs}$[b]	Type[c]	$\mathcal{R}$[d] (mag)	$G-\mathcal{R}$ (mag)	$U_{\rm n}-G$[e] (mag)	J[f] (mag)	$K_{\rm s}$[f] (mag)	Notes[g]
MD6	12:36:02.68	62:10:59.8	3.246	3.241	GAL	24.38	0.87	2.00	...	...	
MD13	12:35:59.63	62:12:00.6	...	2.974	GAL	24.01	0.91	2.31	...	...	
MD27	12:36:42.96	62:09:58.1	3.661	...	GAL	25.48	1.00	2.46	22.86	21.04	DRG
MD31	12:36:22.58	62:13:06.5	2.981	...	GAL	24.92	0.53	1.69	24.57	23.13	S03-C14; B03-133; DRG
MD33	12:36:25.56	62:13:50.5	...	2.932	GAL	24.40	0.68	1.88	23.42	23.38	
MD34	12:36:41.25	62:12:03.1	3.222	3.214	GAL	24.26	0.91	2.39	24.17	22.78	S03-C11; DRG
MD39	12:36:22.94	62:15:26.7	2.583	...	QSO	20.48	-0.23	0.78	20.19	20.07	B03-137
MD43	12:36:40.87	62:13:58.5	...	3.087	GAL	24.04	0.66	2.02	23.01	22.42	S03-D13
MD48	12:37:06.64	62:14:00.2	...	2.926	GAL	24.89	0.69	1.79	24.01	23.36	S03-M21
MD49	12:37:25.45	62:12:00.9	...	2.850	GAL	23.95	0.62	1.75	24.01	22.96	
MD50	12:36:51.43	62:16:08.3	3.238	3.234	GAL	24.77	0.99	2.04	> 25.0	> 24.4	
MD54	12:37:32.35	62:13:11.2	2.939	...	GAL	25.10	0.54	1.99	...	...	
MD55	12:37:16.11	62:15:26.5	...	2.956	GAL	24.86	0.69	2.13	> 25.0	> 24.4	
MD74	12:37:01.27	62:21:32.6	2.635	...	GAL	24.45	0.45	1.58	...	...	
MD75	12:37:37.09	62:17:04.6	...	2.790	GAL	24.03	1.08	2.30	...	...	
MD78	12:37:07.72	62:21:00.3	2.812	...	GAL	24.83	0.27	1.51	...	...	
MD79	12:37:10.91	62:20:44.7	...	:2.291	GAL	24.44	0.35	1.58	...	...	
MD83	12:37:21.57	62:20:11.0	...	3.213	GAL	24.35	0.62	1.77	...	...	
S03-MD3	12:36:33.05	62:09:03.3	2.898	...	GAL	23.94	0.87	1.48	...	...	S03-MD3

Table 5.2—Continued

Name	α (J2000.0)	δ (J2000.0)	$z_{\rm em}$[a]	$z_{\rm abs}$[b]	Type[c]	$\mathcal{R}$[d] (mag)	$G-\mathcal{R}$ (mag)	$U_{\rm n}-G$[e] (mag)	J[f] (mag)	$K_{\rm s}$[f] (mag)	Notes[g]
S03-MD12	12:37:19.86	62:09:54.9	2.647	...	AGN	24.36	0.72	0.92	23.41	22.11	S03-MD12; B03-398
S03-MD45	12:37:14.18	62:16:28.6	:2.345	...	GAL	23.63	0.57	0.82	22.00	21.50	S03-MD45
S03-oMD19	12:36:37.00	62:10:43.8	...	3.241	GAL	24.04	0.68	1.48	23.75	22.72	S03-oMD19
S03-oMD56	12:36:38.40	62:15:39.5	0.000	0.000	STAR	23.24	0.82	1.45	23.40	23.75	S03-oMD56
S03-M16	12:37:17.38	62:12:46.8	...	2.939	GAL	24.67	0.52	1.02	23.99	23.78	S03-M16
S03-M23	12:37:02.68	62:14:25.9	...	3.214	GAL	24.61	1.09	2.43	...	...	S03-M23
S03-M25	12:36:50.80	62:14:44.5	...	3.106	GAL	24.70	0.82	1.69	> 25.0	23.85	S03-M25
S03-M35	12:36:45.18	62:16:52.1	...	3.229	GAL	24.05	1.24	3.12	23.34	22.57	S03-M35

[a]Emission line redshift. An entry with a colon indicates the redshift is uncertain. A blank entry indicates that an emission line redshift could not be measured.

[b]Absorption line redshift. An entry with a colon indicates the redshift is uncertain. A blank entry indicates that an absorption line redshift could not be measured.

[c]Source type, either galaxy ("GAL"), "AGN," "QSO," or "STAR."

[d]$\mathcal{R}$ magnitude in AB units.

[e]Upper limits given for galaxies undetected in $U_{\rm n}$.

[f]A blank entry indicates the object did not lie in the region with near-IR imaging.

[g]Galaxies in common with the LBG survey in the HDF-N are indicated by their names ("S03-XXX") as given in Steidel et al. (2003). Galaxies with X-ray counterparts within $1.5''$ are indicated by their names ("B03-XXX") in the spectroscopic follow up to the *Chandra* 2 Ms survey by Barger et al. (2003). Galaxies satisfying the distant red galaxy (DRG) criteria of Franx et al. (2003) are indicated by "DRG."

Table 5.3. *Spitzer* Photometry

Name	$m_{3.6\mu m}$ (mag)	$m_{4.5\mu m}$ (mag)	$m_{5.8\mu m}$ (mag)	$m_{8.0\mu m}$ (mag)	$f_{24\mu m}$ (μJy)
BX1035	22.48 ± 0.09	22.47 ± 0.13	22.11 ± 0.14	22.59 ± 0.28	32.95 ± 6.32
BX1040	22.94 ± 0.12	23.27 ± 0.21	...	...	...
BX1042	23.09 ± 0.07	23.03 ± 0.10	23.13 ± 0.19	22.88 ± 0.18	15.23 ± 4.31
BX1050	23.49 ± 0.09	23.51 ± 0.08	23.46 ± 0.30	...	...
BX1051	23.07 ± 0.19	...	...	...	203.87 ± 14.45
BX1055	23.12 ± 0.10	23.23 ± 0.14	...	...	...
BX1060	21.74 ± 0.07	21.73 ± 0.08	21.93 ± 0.19	...	67.27 ± 8.32
BX1064	23.00 ± 0.07	23.11 ± 0.08	23.16 ± 0.17	23.76 ± 0.32	25.99 ± 5.48
BX1065	22.41 ± 0.07	22.60 ± 0.15	...	...	13.32 ± 3.90
BX1069	23.37 ± 0.08	24.01 ± 0.16	...	...	...
BX1071	22.84 ± 0.10	23.06 ± 0.21	...	...	...
BX1073	21.71 ± 0.07	22.15 ± 0.07	22.66 ± 0.10	22.56 ± 0.24	41.19 ± 6.68
BX1074	22.11 ± 0.07	22.09 ± 0.07	22.00 ± 0.23	...	40.52 ± 6.51
BX1075	22.47 ± 0.11	22.49 ± 0.15	22.30 ± 0.22	...	10.80 ± 3.53
BX1080	22.55 ± 0.07	22.53 ± 0.07	22.72 ± 0.23	23.02 ± 0.35	47.34 ± 7.02
BX1081	22.25 ± 0.07	22.33 ± 0.07	22.66 ± 0.24	22.79 ± 0.20	48.32 ± 7.14
BX1084	22.29 ± 0.07	22.33 ± 0.07	22.19 ± 0.15	22.63 ± 0.18	54.30 ± 7.51
BX1085	23.38 ± 0.09	23.52 ± 0.15	23.47 ± 0.32	...	...
BX1086	23.25 ± 0.12	23.24 ± 0.13	...	...	...
BX1089	21.92 ± 0.07	21.95 ± 0.07	21.94 ± 0.17	21.83 ± 0.26	76.67 ± 9.22
BX1100	22.22 ± 0.11	22.26 ± 0.16	22.19 ± 0.26	...	84.35 ± 9.29
BX1104	23.03 ± 0.07	23.08 ± 0.07	23.26 ± 0.30	23.12 ± 0.28	24.47 ± 5.23
BX1106	23.07 ± 0.11	23.16 ± 0.21	22.88 ± 0.26	22.93 ± 0.32	8.47 ± 1.34
BX1112	24.18 ± 0.09	24.77 ± 0.21	...	...	...
BX1116	22.59 ± 0.07	22.66 ± 0.07	22.50 ± 0.15	23.06 ± 0.14	18.38 ± 5.06
BX1120	24.95 ± 0.21	...	...	...	...
BX1121	21.77 ± 0.07	21.78 ± 0.07	22.07 ± 0.14	22.22 ± 0.14	55.47 ± 7.76
BX1125	24.00 ± 0.14	24.37 ± 0.24	...	...	...
BX1126	23.61 ± 0.16	23.74 ± 0.25	...	...	...
BX1129	21.52 ± 0.07	21.60 ± 0.07	21.46 ± 0.09	22.00 ± 0.13	104.43 ± 10.33

Table 5.3—Continued

Name	$m_{3.6\mu m}$ (mag)	$m_{4.5\mu m}$ (mag)	$m_{5.8\mu m}$ (mag)	$m_{8.0\mu m}$ (mag)	$f_{24\mu m}$ (μJy)
BX1130	21.05 ± 0.07	20.99 ± 0.07	21.15 ± 0.07	21.57 ± 0.07	152.77 ± 13.66
BX1132	22.72 ± 0.07	22.64 ± 0.07	22.53 ± 0.13	...	...
BX1140	22.62 ± 0.08	22.74 ± 0.12	22.71 ± 0.32	...	9.09 ± 2.86
BX1145	24.13 ± 0.15	24.23 ± 0.15	...	...	...
BX1157	21.99 ± 0.07	22.00 ± 0.07	21.62 ± 0.16	21.84 ± 0.22	...
BX1161	21.85 ± 0.07	21.87 ± 0.07	22.24 ± 0.15	22.47 ± 0.19	23.33 ± 5.29
BX1164	24.05 ± 0.16	24.43 ± 0.21	...	...	...
BX1166	23.28 ± 0.18	23.55 ± 0.35	...	...	12.52 ± 3.64
BX1169	22.47 ± 0.07	22.45 ± 0.07	22.54 ± 0.21	23.14 ± 0.33	40.73 ± 7.68
BX1170	22.38 ± 0.07	22.49 ± 0.12	22.06 ± 0.30	...	32.93 ± 6.10
BX1172	24.05 ± 0.24	24.31 ± 0.23	...	...	...
BX1174	23.07 ± 0.17	23.36 ± 0.24	...	...	...
BX1178	24.01 ± 0.24	...	...	...	...
BX1183	23.25 ± 0.15	23.51 ± 0.34	...	...	...
BX1185	22.54 ± 0.07	22.46 ± 0.08	22.41 ± 0.15	22.52 ± 0.19	44.14 ± 6.85
BX1186	24.66 ± 0.25	24.53 ± 0.34	...	...	...
BX1192	21.52 ± 0.07	21.56 ± 0.07	21.47 ± 0.15	21.67 ± 0.22	111.62 ± 10.67
BX1197	22.73 ± 0.12	22.76 ± 0.17	...	...	31.90 ± 6.83
BX1201	22.94 ± 0.07	22.99 ± 0.07	23.04 ± 0.27	...	29.01 ± 5.52
BX1204	22.51 ± 0.07	22.62 ± 0.07	22.76 ± 0.15	23.21 ± 0.28	15.79 ± 4.41
BX1208	23.76 ± 0.13	24.17 ± 0.32	...	...	...
BX1209	23.96 ± 0.12	23.93 ± 0.13	...	...	13.09 ± 5.38
BX1214	22.05 ± 0.07	21.96 ± 0.07	21.97 ± 0.08	22.39 ± 0.14	46.90 ± 6.95
BX1217	23.23 ± 0.07	23.24 ± 0.09	23.27 ± 0.30	23.44 ± 0.33	...
BX1218	22.40 ± 0.07	22.40 ± 0.12	22.67 ± 0.19	22.97 ± 0.33	26.21 ± 5.28
BX1220	21.92 ± 0.07	21.91 ± 0.07	21.99 ± 0.07	22.56 ± 0.13	...
BX1222	24.43 ± 0.35	24.41 ± 0.32	...	...	...
BX1223	21.17 ± 0.07	20.92 ± 0.07	20.51 ± 0.07	20.79 ± 0.14	307.42 ± 17.60
BX1228	22.94 ± 0.08	23.10 ± 0.11	23.05 ± 0.22	...	14.73 ± 4.13
BX1229	22.42 ± 0.07	22.40 ± 0.09	22.31 ± 0.22	22.34 ± 0.28	48.37 ± 9.40

Table 5.3—Continued

Name	$m_{3.6\mu m}$ (mag)	$m_{4.5\mu m}$ (mag)	$m_{5.8\mu m}$ (mag)	$m_{8.0\mu m}$ (mag)	$f_{24\mu m}$ (μJy)
BX1233	22.75 ± 0.07	22.61 ± 0.07	22.20 ± 0.09	...	...
BX1238	22.97 ± 0.07	22.91 ± 0.07	23.21 ± 0.20	...	...
BX1240	23.19 ± 0.11	23.19 ± 0.17	...	...	...
BX1243	22.68 ± 0.07	22.71 ± 0.15	22.67 ± 0.22	...	...
BX1244	22.35 ± 0.09	22.48 ± 0.23	22.70 ± 0.32	...	35.69 ± 6.25
BX1245	22.91 ± 0.08	22.91 ± 0.11	...	...	18.75 ± 4.63
BX1250	22.86 ± 0.07	22.86 ± 0.07	22.95 ± 0.13	...	...
BX1252	23.53 ± 0.21	...	...	...	...
BX1253	22.49 ± 0.07	22.53 ± 0.07	23.13 ± 0.20	23.18 ± 0.33	...
BX1260	21.51 ± 0.07	21.45 ± 0.07	21.34 ± 0.08	21.83 ± 0.11	105.68 ± 10.42
BX1264	...	...	...	...	...
BX1265	23.20 ± 0.07	23.27 ± 0.07	23.42 ± 0.26	23.33 ± 0.36	...
BX1267	23.45 ± 0.30	...	...	...	48.69 ± 7.22
BX1269	21.85 ± 0.07	21.78 ± 0.08	21.77 ± 0.20	22.15 ± 0.22	89.06 ± 9.46
BX1270	23.97 ± 0.07	24.35 ± 0.10	...	...	...
BX1274	22.80 ± 0.16	23.02 ± 0.24	...	...	26.57 ± 5.20
BX1277	23.11 ± 0.07	23.28 ± 0.13	...	...	27.04 ± 5.83
BX1279	23.79 ± 0.18	24.15 ± 0.17	...	...	40.68 ± 8.92
BX1281	23.84 ± 0.15	24.11 ± 0.26	...	...	13.39 ± 3.94
BX1283	22.69 ± 0.08	22.69 ± 0.08	23.31 ± 0.21	23.18 ± 0.36	...
BX1284	23.28 ± 0.12	23.33 ± 0.17	23.10 ± 0.28	...	...
BX1287	22.60 ± 0.07	22.50 ± 0.08	22.68 ± 0.12	23.27 ± 0.36	35.08 ± 6.41
BX1288	23.15 ± 0.08	23.31 ± 0.10	23.57 ± 0.29	...	...
BX1289	22.76 ± 0.07	22.77 ± 0.07	22.90 ± 0.13	22.91 ± 0.16	18.82 ± 4.53
BX1290	23.81 ± 0.28	24.16 ± 0.30	...	...	...
BX1291	23.05 ± 0.14	23.15 ± 0.12	23.19 ± 0.24	23.71 ± 0.34	22.36 ± 5.34
BX1293	21.07 ± 0.07	21.09 ± 0.07	21.06 ± 0.07	20.79 ± 0.07	199.25 ± 14.50
BX1296	21.19 ± 0.07	20.96 ± 0.07	20.67 ± 0.09	21.00 ± 0.14	263.66 ± 16.42
BX1297	21.89 ± 0.07	21.85 ± 0.07	21.76 ± 0.12	22.19 ± 0.23	...
BX1299	22.94 ± 0.08	22.96 ± 0.07	23.49 ± 0.26	...	18.70 ± 5.07

Table 5.3—Continued

Name	$m_{3.6\mu m}$ (mag)	$m_{4.5\mu m}$ (mag)	$m_{5.8\mu m}$ (mag)	$m_{8.0\mu m}$ (mag)	$f_{24\mu m}$ (μJy)
BX1300	22.93 ± 0.14	23.06 ± 0.19	...	...	...
BX1303	23.55 ± 0.18	23.35 ± 0.14	...	...	15.12 ± 3.96
BX1305	22.80 ± 0.09	22.76 ± 0.11	22.68 ± 0.26	22.76 ± 0.31	73.11 ± 8.89
BX1307	21.69 ± 0.07	21.61 ± 0.07	21.34 ± 0.09	21.44 ± 0.26	145.53 ± 12.20
BX1311	22.65 ± 0.10	22.74 ± 0.12	22.60 ± 0.17	...	24.03 ± 5.06
BX1312	23.86 ± 0.16	...	...	...	45.43 ± 9.19
BX1313	23.68 ± 0.07	23.71 ± 0.25	...	...	...
BX1315	21.79 ± 0.07	21.75 ± 0.07	21.91 ± 0.07	22.05 ± 0.17	64.79 ± 8.16
BX1316	22.04 ± 0.07	21.99 ± 0.09	21.79 ± 0.22	...	...
BX1317	22.26 ± 0.07	22.25 ± 0.07	22.32 ± 0.14	22.50 ± 0.17	53.91 ± 7.66
BX1319	21.34 ± 0.07	21.23 ± 0.07	21.17 ± 0.07	21.46 ± 0.09	102.06 ± 10.40
BX1321	19.37 ± 0.07	19.74 ± 0.07	19.73 ± 0.07	17.68 ± 0.07	434.77 ± 21.43
BX1322	23.25 ± 0.14	23.28 ± 0.16	...	...	31.95 ± 5.97
BX1324	21.79 ± 0.07	21.70 ± 0.07	21.90 ± 0.13	22.09 ± 0.16	142.97 ± 12.16
BX1326	23.81 ± 0.12	24.17 ± 0.18	...	...	...
BX1327	22.92 ± 0.07	23.00 ± 0.07	22.98 ± 0.16	23.45 ± 0.23	23.31 ± 5.20
BX1329	24.46 ± 0.25	...	...	...	8.17 ± 2.53
BX1330	22.91 ± 0.07	22.95 ± 0.07	22.86 ± 0.11	...	24.80 ± 5.38
BX1332	22.50 ± 0.08	22.53 ± 0.11	22.41 ± 0.13	...	29.66 ± 5.62
BX1334	...	...	...	...	...
BX1335	22.90 ± 0.07	22.89 ± 0.07	22.67 ± 0.15	22.88 ± 0.15	19.29 ± 4.60
BX1339	23.06 ± 0.09	23.03 ± 0.12	22.63 ± 0.31	...	...
BX1343	22.45 ± 0.07	22.51 ± 0.07	22.45 ± 0.34	...	21.00 ± 5.39
BX1348	23.88 ± 0.23	...	...	...	24.78 ± 5.65
BX1349	21.61 ± 0.07	21.45 ± 0.07	21.49 ± 0.09	21.68 ± 0.09	104.76 ± 10.36
BX1350	...	...	...	...	...
BX1351	21.53 ± 0.07	21.90 ± 0.07	21.98 ± 0.07	21.55 ± 0.07	...
BX1353	21.82 ± 0.07	21.75 ± 0.07	21.92 ± 0.20	22.14 ± 0.22	65.65 ± 8.38
BX1354	24.50 ± 0.20	...	...	...	...
BX1355	22.34 ± 0.07	22.53 ± 0.11	22.94 ± 0.15	...	...

Table 5.3—Continued

Name	$m_{3.6\mu m}$ (mag)	$m_{4.5\mu m}$ (mag)	$m_{5.8\mu m}$ (mag)	$m_{8.0\mu m}$ (mag)	$f_{24\mu m}$ (μJy)
BX1358	24.11 ± 0.12	24.25 ± 0.11	...	...	...
BX1361	24.22 ± 0.20	...	...	...	...
BX1362	22.08 ± 0.07	22.34 ± 0.07	...	...	...
BX1363	22.58 ± 0.07	22.59 ± 0.07	22.52 ± 0.14	22.76 ± 0.29	58.75 ± 7.76
BX1364	22.65 ± 0.07	22.64 ± 0.12	22.78 ± 0.19	23.14 ± 0.31	11.53 ± 3.71
BX1368	22.35 ± 0.07	22.60 ± 0.16	22.43 ± 0.29	22.40 ± 0.33	70.96 ± 8.69
BX1371	24.49 ± 0.24	24.95 ± 0.35	...	...	...
BX1374	24.13 ± 0.13	...	...	...	...
BX1376	23.93 ± 0.09	24.05 ± 0.18	...	...	...
BX1378	22.42 ± 0.07	22.40 ± 0.07	22.43 ± 0.10	23.15 ± 0.18	29.37 ± 5.53
BX1387	23.61 ± 0.08	23.60 ± 0.08	23.40 ± 0.31	23.13 ± 0.23	15.16 ± 4.45
BX1388	21.55 ± 0.07	21.43 ± 0.07	21.23 ± 0.07	21.54 ± 0.13	151.74 ± 12.35
BX1391	22.46 ± 0.07	22.45 ± 0.07	22.52 ± 0.09	23.19 ± 0.19	...
BX1392	22.48 ± 0.07	22.85 ± 0.07	23.35 ± 0.30	23.04 ± 0.15	...
BX1397	22.47 ± 0.07	22.36 ± 0.07	22.30 ± 0.12	22.50 ± 0.16	30.24 ± 5.93
BX1399	22.73 ± 0.10	22.84 ± 0.13	22.51 ± 0.31	...	20.89 ± 5.04
BX1400	23.79 ± 0.09	24.10 ± 0.11	...	...	...
BX1401	21.76 ± 0.07	21.57 ± 0.07	21.35 ± 0.10	21.60 ± 0.13	41.17 ± 6.76
BX1403	22.85 ± 0.10	22.82 ± 0.16	...	...	15.44 ± 4.29
BX1408	22.49 ± 0.07	22.38 ± 0.07	22.28 ± 0.11	22.63 ± 0.12	31.36 ± 6.06
BX1409	22.23 ± 0.07	22.22 ± 0.08	22.10 ± 0.18	22.34 ± 0.20	52.06 ± 7.44
BX1420	22.06 ± 0.07	22.13 ± 0.07	...	...	18.50 ± 4.54
BX1425	23.30 ± 0.07	23.28 ± 0.07	23.50 ± 0.33	...	...
BX1427	22.98 ± 0.08	22.97 ± 0.08	22.82 ± 0.21	...	8.27 ± 2.22
BX1431	23.11 ± 0.16	23.25 ± 0.34	...	...	...
BX1434	23.14 ± 0.19	23.18 ± 0.27	...	...	...
BX1439	21.91 ± 0.07	21.82 ± 0.09	21.82 ± 0.12	22.05 ± 0.21	85.29 ± 9.45
BX1443	20.85 ± 0.07	20.67 ± 0.07	20.81 ± 0.07	20.93 ± 0.07	194.03 ± 14.01
BX1446	23.08 ± 0.13	23.00 ± 0.15	...	...	...
BX1451	22.37 ± 0.10	22.23 ± 0.08	22.36 ± 0.28	22.47 ± 0.28	35.95 ± 6.08

Table 5.3—Continued

Name	$m_{3.6\mu m}$ (mag)	$m_{4.5\mu m}$ (mag)	$m_{5.8\mu m}$ (mag)	$m_{8.0\mu m}$ (mag)	$f_{24\mu m}$ (μJy)
BX1458	22.63 ± 0.13	22.78 ± 0.23	...	...	52.44 ± 7.46
BX1460	23.30 ± 0.12	23.72 ± 0.21	23.18 ± 0.35	...	...
BX1461	23.54 ± 0.11	23.48 ± 0.08	...	23.77 ± 0.36	...
BX1476	22.46 ± 0.07	23.04 ± 0.11	...	...	...
BX1479	23.03 ± 0.12	23.08 ± 0.17	22.68 ± 0.34	...	10.95 ± 3.60
BX1480	22.65 ± 0.08	22.54 ± 0.09	22.52 ± 0.19	22.80 ± 0.28	18.33 ± 4.32
BX1485	21.36 ± 0.07	21.32 ± 0.09	21.19 ± 0.16	21.30 ± 0.17	315.88 ± 17.89
BX1495	23.48 ± 0.23	23.40 ± 0.27	...	...	...
BX1501	22.19 ± 0.09	22.16 ± 0.09	22.28 ± 0.21	22.74 ± 0.36	43.26 ± 7.11
BX1504	23.75 ± 0.22	23.71 ± 0.13	23.55 ± 0.34	...	...
BX1505	22.93 ± 0.10	22.94 ± 0.14	22.57 ± 0.32	22.00 ± 0.21	256.18 ± 16.16
BX1510	23.52 ± 0.15	23.50 ± 0.25	...	...	...
BX1514	22.68 ± 0.09	22.51 ± 0.08	22.96 ± 0.34	22.80 ± 0.25	22.18 ± 4.98
BX1525	21.59 ± 0.07	21.41 ± 0.07	21.55 ± 0.12	21.60 ± 0.11	120.42 ± 11.09
BX1529	...	...	...	...	...
BX1530	23.41 ± 0.15	23.33 ± 0.17	...	22.83 ± 0.33	...
BX1535	23.18 ± 0.07	23.17 ± 0.09	23.27 ± 0.35	23.46 ± 0.26	...
BX1542	23.34 ± 0.19	23.70 ± 0.32	...	...	...
BX1544	...	...	...	...	...
BX1548	23.95 ± 0.17	24.71 ± 0.31	...	...	...
BX1557	21.64 ± 0.07	21.73 ± 0.07	21.29 ± 0.08	22.85 ± 0.20	167.90 ± 13.04
BX1559	23.10 ± 0.28	23.08 ± 0.18	...	...	85.77 ± 9.67
BX1564	21.77 ± 0.07	21.69 ± 0.07	21.57 ± 0.10	21.98 ± 0.20	74.79 ± 8.86
BX1567	21.96 ± 0.07	21.86 ± 0.07	21.79 ± 0.11	22.03 ± 0.19	34.10 ± 6.21
BX1568	22.68 ± 0.08	22.63 ± 0.09	22.68 ± 0.23	23.30 ± 0.26	25.51 ± 5.93
BX1572	23.43 ± 0.07	23.47 ± 0.07	23.63 ± 0.31	...	...
BX1574	22.00 ± 0.07	21.90 ± 0.07	22.08 ± 0.14	22.12 ± 0.19	55.27 ± 7.64
BX1579	23.65 ± 0.24	24.17 ± 0.26	...	...	58.13 ± 8.14
BX1586	23.02 ± 0.17	23.02 ± 0.12	...	...	22.50 ± 5.15
BX1588	21.58 ± 0.07	21.48 ± 0.07	21.24 ± 0.11	21.52 ± 0.20	129.66 ± 11.55

Table 5.3—Continued

Name	$m_{3.6\mu m}$ (mag)	$m_{4.5\mu m}$ (mag)	$m_{5.8\mu m}$ (mag)	$m_{8.0\mu m}$ (mag)	$f_{24\mu m}$ (μJy)
BX1591	23.17 ± 0.08	23.24 ± 0.07	23.49 ± 0.26	...	9.98 ± 1.97
BX1605	23.29 ± 0.07	23.36 ± 0.17	...	...	...
BX1616	23.79 ± 0.30	...	...	...	...
BX1617	23.96 ± 0.10	23.99 ± 0.09	...	23.37 ± 0.31	...
BX1630	23.40 ± 0.11	23.49 ± 0.07	...	23.54 ± 0.32	...
BX1636	21.93 ± 0.07	21.82 ± 0.07	21.66 ± 0.14	21.82 ± 0.27	71.21 ± 8.51
BX1637	23.38 ± 0.29	22.76 ± 0.21	21.84 ± 0.18	20.93 ± 0.15	109.43 ± 10.77
BX1641	23.79 ± 0.10	23.93 ± 0.16	...	...	...
BX1642	22.97 ± 0.09	22.95 ± 0.09	...	...	...
BX1650	22.10 ± 0.07	22.05 ± 0.07	21.95 ± 0.11	22.42 ± 0.24	37.54 ± 6.45
BX1655	24.55 ± 0.09	24.92 ± 0.22	...	...	...
BX1669	23.22 ± 0.07	23.41 ± 0.07	...	23.44 ± 0.34	...
BX1676	23.58 ± 0.07	23.81 ± 0.29	...	...	50.98 ± 9.29
BX1694	22.50 ± 0.07	22.58 ± 0.07	22.28 ± 0.11	...	13.78 ± 4.30
BX1708	21.46 ± 0.07	21.23 ± 0.07	21.03 ± 0.07	21.34 ± 0.08	208.29 ± 14.57
BX1782	22.64 ± 0.15	23.17 ± 0.23	...	...	30.34 ± 5.59
BX1790	23.20 ± 0.21	23.09 ± 0.18	...	...	...
BX1796	22.43 ± 0.07	22.93 ± 0.07	22.71 ± 0.14	...	...
BX1805	21.99 ± 0.07	22.37 ± 0.07	22.67 ± 0.09	22.59 ± 0.20	95.24 ± 10.31
BX1808	23.01 ± 0.12	23.29 ± 0.36	...	...	...
BX1815	21.13 ± 0.07	21.68 ± 0.07	22.08 ± 0.07	22.81 ± 0.14	...
BX1816	21.42 ± 0.07	21.26 ± 0.07	21.25 ± 0.11	21.62 ± 0.21	...
BX1817	21.65 ± 0.07	21.77 ± 0.09	21.75 ± 0.31	...	43.43 ± 7.41
BX1820	21.64 ± 0.07	21.49 ± 0.07	21.27 ± 0.12	21.32 ± 0.08	105.56 ± 10.50
BX1821	23.28 ± 0.21	23.44 ± 0.28	22.87 ± 0.33	...	15.13 ± 4.83
BX1822	22.78 ± 0.07	23.24 ± 0.07	23.03 ± 0.27	...	...
BX1823	20.88 ± 0.07	20.76 ± 0.07	20.78 ± 0.09	21.02 ± 0.14	127.39 ± 11.44
BX1826	23.49 ± 0.13	23.52 ± 0.27	...	...	31.96 ± 6.87
BX1827	23.42 ± 0.09	23.46 ± 0.13	...	...	...
BX1828	24.06 ± 0.08	24.75 ± 0.19	...	...	...

Table 5.3—Continued

Name	$m_{3.6\mu m}$ (mag)	$m_{4.5\mu m}$ (mag)	$m_{5.8\mu m}$ (mag)	$m_{8.0\mu m}$ (mag)	$f_{24\mu m}$ (μJy)
BX1833	22.56 ± 0.07	22.91 ± 0.10	...	...	...
BX1841	22.57 ± 0.12	22.81 ± 0.10	22.80 ± 0.26	...	...
BX1848	23.93 ± 0.18	24.32 ± 0.31	...	...	12.37 ± 3.66
BX1851	22.44 ± 0.14	22.60 ± 0.12	...	...	...
BX1856	23.49 ± 0.12	23.87 ± 0.13	23.82 ± 0.31	23.30 ± 0.28	...
BX1860	22.73 ± 0.12	22.75 ± 0.12	22.57 ± 0.22	...	29.60 ± 5.65
BX28	...	...	22.71 ± 0.09	22.45 ± 0.07	...
BX82	23.30 ± 0.13	23.55 ± 0.18	...	...	...
BX84	22.08 ± 0.10	21.98 ± 0.13	21.88 ± 0.27	22.30 ± 0.36	79.03 ± 8.93
BX150	22.34 ± 0.12	22.12 ± 0.12	21.87 ± 0.35	...	46.91 ± 7.02
BX160	21.52 ± 0.07	21.32 ± 0.07	20.98 ± 0.07	20.95 ± 0.09	142.16 ± 12.02
BX184	22.80 ± 0.07	22.95 ± 0.25	...	...	...
BX274	20.07 ± 0.07	20.58 ± 0.07	21.05 ± 0.07	21.76 ± 0.10	...
BX283	24.55 ± 0.19	24.75 ± 0.33	...	...	...
BX289	23.35 ± 0.07	23.87 ± 0.12	...	...	106.57 ± 10.79
BX305	22.03 ± 0.07	22.00 ± 0.07	21.90 ± 0.10	21.71 ± 0.10	69.40 ± 8.58
BX308	22.53 ± 0.10	22.75 ± 0.12	22.79 ± 0.24	...	...
BX313	22.65 ± 0.07	22.58 ± 0.07	22.36 ± 0.12	22.55 ± 0.16	48.78 ± 7.14
BX341	22.47 ± 0.07	22.58 ± 0.09	...	22.91 ± 0.26	...
BM1008	22.68 ± 0.07	22.60 ± 0.08	23.20 ± 0.31	22.90 ± 0.33	27.49 ± 5.81
BM1010	22.69 ± 0.07	22.88 ± 0.12	...	...	37.37 ± 6.38
BM1011	22.21 ± 0.07	22.25 ± 0.07	22.40 ± 0.10	23.06 ± 0.23	20.91 ± 5.23
BM1017	22.99 ± 0.12	22.91 ± 0.21	...	...	20.63 ± 5.26
BM1030	22.23 ± 0.11	22.34 ± 0.16	22.25 ± 0.28	...	24.53 ± 5.49
BM1048	22.10 ± 0.07	22.22 ± 0.07	22.47 ± 0.12	22.65 ± 0.18	21.68 ± 4.91
BM1053	24.02 ± 0.10	24.32 ± 0.20	...	...	15.70 ± 4.30
BM1061	23.77 ± 0.15	23.96 ± 0.20	...	...	...
BM1063	22.53 ± 0.08	22.54 ± 0.09	22.46 ± 0.34	...	36.89 ± 6.27
BM1064	22.48 ± 0.07	22.57 ± 0.08	23.00 ± 0.30	...	25.19 ± 8.15
BM1069	21.72 ± 0.07	21.67 ± 0.08	21.56 ± 0.18	22.05 ± 0.27	91.10 ± 9.75

Table 5.3—Continued

Name	$m_{3.6\mu m}$ (mag)	$m_{4.5\mu m}$ (mag)	$m_{5.8\mu m}$ (mag)	$m_{8.0\mu m}$ (mag)	$f_{24\mu m}$ (μJy)
BM1072	22.36 ± 0.07	22.69 ± 0.09	23.32 ± 0.32	...	...
BM1074	23.33 ± 0.07	23.99 ± 0.16	23.26 ± 0.24	...	72.02 ± 9.69
BM1083	21.59 ± 0.07	21.34 ± 0.07	20.73 ± 0.08	20.47 ± 0.07	112.88 ± 10.96
BM1092	22.84 ± 0.07	22.86 ± 0.07	23.03 ± 0.20	23.54 ± 0.24	...
BM1095	23.37 ± 0.08	23.67 ± 0.15	...	...	...
BM1098	22.09 ± 0.07	22.01 ± 0.07	22.45 ± 0.19	22.63 ± 0.19	30.18 ± 5.68
BM1099	23.08 ± 0.11	23.15 ± 0.17	...	...	21.09 ± 4.92
BM1119	21.60 ± 0.07	21.50 ± 0.07	21.32 ± 0.08	21.56 ± 0.23	152.61 ± 12.41
BM1121	22.46 ± 0.20	...	...	...	21.54 ± 5.35
BM1122	23.27 ± 0.10	23.30 ± 0.16	...	...	...
BM1132	22.98 ± 0.07	23.06 ± 0.07	23.08 ± 0.23	23.27 ± 0.21	...
BM1135	21.63 ± 0.07	21.57 ± 0.09	21.49 ± 0.16	21.96 ± 0.30	111.37 ± 10.70
BM1136	21.15 ± 0.07	21.11 ± 0.07	21.37 ± 0.20	21.16 ± 0.12	99.45 ± 10.16
BM1139	22.46 ± 0.14	22.61 ± 0.20	...	...	220.77 ± 14.97
BM1144	22.73 ± 0.08	22.70 ± 0.08	22.91 ± 0.29	...	...
BM1146	23.20 ± 0.11	23.55 ± 0.20	...	...	...
BM1148	23.11 ± 0.07	23.24 ± 0.11	...	23.08 ± 0.30	14.51 ± 4.14
BM1149	24.15 ± 0.25	...	...	...	...
BM1153	21.65 ± 0.07	21.43 ± 0.07	21.42 ± 0.10	21.54 ± 0.12	122.95 ± 11.20
BM1155	23.21 ± 0.07	23.28 ± 0.13	...	...	...
BM1156	22.10 ± 0.07	21.94 ± 0.07	21.18 ± 0.08	19.97 ± 0.07	324.45 ± 18.07
BM1158	21.75 ± 0.07	21.72 ± 0.07	21.96 ± 0.25	21.67 ± 0.07	64.77 ± 8.27
BM1159	21.97 ± 0.07	22.41 ± 0.07	22.79 ± 0.15	22.62 ± 0.10	22.06 ± 5.67
BM1160	22.93 ± 0.09	23.01 ± 0.12	23.70 ± 0.26	...	19.79 ± 5.13
BM1161	23.97 ± 0.36	...	...	...	...
BM1163	23.18 ± 0.10	...	22.74 ± 0.36	...	...
BM1171	23.45 ± 0.17	23.69 ± 0.23	...	...	...
BM1172	23.60 ± 0.16	23.53 ± 0.17	...	...	...
BM1174	22.70 ± 0.07	22.95 ± 0.09	23.38 ± 0.17	23.38 ± 0.30	...
BM1175	22.53 ± 0.16	22.55 ± 0.20	...	...	14.64 ± 4.56

Table 5.3—Continued

Name	$m_{3.6\mu m}$ (mag)	$m_{4.5\mu m}$ (mag)	$m_{5.8\mu m}$ (mag)	$m_{8.0\mu m}$ (mag)	$f_{24\mu m}$ (μJy)
BM1180	22.02 ± 0.12	21.95 ± 0.15	21.97 ± 0.32	...	...
BM1181	22.47 ± 0.07	22.51 ± 0.07	22.87 ± 0.17	23.31 ± 0.26	15.39 ± 3.97
BM1190	18.63 ± 0.07	18.37 ± 0.07	18.10 ± 0.07	17.79 ± 0.07	866.43 ± 29.50
BM1193	...	...	...	...	...
BM1195	21.84 ± 0.07	21.82 ± 0.07	21.99 ± 0.21	...	50.43 ± 7.35
BM1196	24.12 ± 0.22	24.22 ± 0.32	...	...	...
BM1197	22.32 ± 0.07	22.28 ± 0.07	22.77 ± 0.21	22.90 ± 0.34	18.80 ± 4.79
BM1198	22.38 ± 0.07	22.34 ± 0.09	22.41 ± 0.24	23.05 ± 0.34	39.46 ± 6.52
BM1200	22.85 ± 0.10	22.89 ± 0.16	22.99 ± 0.35	...	16.70 ± 5.56
BM1201	23.54 ± 0.09	24.00 ± 0.21	...	...	...
BM1204	22.53 ± 0.07	22.60 ± 0.10	22.96 ± 0.21	...	22.35 ± 5.17
BM1205	22.70 ± 0.07	22.54 ± 0.07	22.58 ± 0.13	22.58 ± 0.17	9.45 ± 2.18
BM1207	22.47 ± 0.08	23.63 ± 0.20	...	...	171.28 ± 13.26
BM1209	22.28 ± 0.11	22.49 ± 0.15	22.34 ± 0.29	...	15.47 ± 4.89
BM1211	23.53 ± 0.07	23.84 ± 0.15	...	...	...
BM1212	22.77 ± 0.09	22.74 ± 0.09	...	...	18.44 ± 4.75
BM1226	23.12 ± 0.07	23.15 ± 0.07	...	...	...
BM1289	24.13 ± 0.28	24.38 ± 0.35	...	...	20.23 ± 5.04
BM1293	22.51 ± 0.12	23.01 ± 0.14	...	...	18.29 ± 4.65
BM1299	20.91 ± 0.07	21.04 ± 0.07	21.10 ± 0.07	21.27 ± 0.10	...
BM1303	22.23 ± 0.08	22.03 ± 0.09	22.06 ± 0.23	22.35 ± 0.26	134.70 ± 11.81
BM1324	22.45 ± 0.07	22.66 ± 0.07	22.50 ± 0.14	...	12.72 ± 3.68
BM1326	20.38 ± 0.07	20.29 ± 0.07	20.48 ± 0.07	20.02 ± 0.07	303.20 ± 17.57
BM1334	21.97 ± 0.07	21.89 ± 0.09	22.10 ± 0.26	22.36 ± 0.30	15.31 ± 3.99
BM1335	21.15 ± 0.07	21.05 ± 0.07	21.19 ± 0.17	...	...
BM1339	21.93 ± 0.07	22.01 ± 0.10	22.37 ± 0.27	22.56 ± 0.33	38.02 ± 6.21
BM1345	21.72 ± 0.07	21.96 ± 0.07	21.89 ± 0.07	22.15 ± 0.09	...
BM1358	21.11 ± 0.07	20.97 ± 0.07	20.91 ± 0.07	21.22 ± 0.08	202.76 ± 14.41
BM1362	22.10 ± 0.07	22.07 ± 0.07	22.21 ± 0.13	22.74 ± 0.22	33.89 ± 6.18
BM1369	23.59 ± 0.12	23.83 ± 0.20	...	...	167.91 ± 14.29

Table 5.3—Continued

Name	$m_{3.6\mu m}$ (mag)	$m_{4.5\mu m}$ (mag)	$m_{5.8\mu m}$ (mag)	$m_{8.0\mu m}$ (mag)	$f_{24\mu m}$ (μJy)
BM1375	21.88 ± 0.12	22.09 ± 0.10	22.29 ± 0.23	22.23 ± 0.28	...
BM1376	23.69 ± 0.25	...	...	...	...
BM1384	21.91 ± 0.07	21.63 ± 0.07	21.27 ± 0.09	20.75 ± 0.07	63.82 ± 8.16
BM1396	21.48 ± 0.07	21.39 ± 0.07	21.54 ± 0.07	21.81 ± 0.11	69.19 ± 8.79
BM1413	22.39 ± 0.07	22.73 ± 0.10	22.62 ± 0.14	...	...
BM35	22.66 ± 0.08	22.96 ± 0.13	...	...	...
BM63	23.55 ± 0.11	23.56 ± 0.14	...	...	...
BM69	...	...	...	...	32.72 ± 5.84
BM70	23.24 ± 0.07	23.69 ± 0.19	...	...	...
BM72	22.24 ± 0.16	...	...	...	...
C2	23.35 ± 0.13	23.39 ± 0.19	...	...	...
C11	23.72 ± 0.11	23.86 ± 0.15	23.25 ± 0.24	...	...
C12	22.63 ± 0.08	22.54 ± 0.09	...	...	23.76 ± 5.39
C14	23.19 ± 0.10	23.16 ± 0.11	...	...	...
C16	22.04 ± 0.07	21.93 ± 0.09	21.68 ± 0.17	21.47 ± 0.22	88.80 ± 9.55
C17	...	...	...	...	...
C18	23.83 ± 0.15	23.92 ± 0.25	...	...	...
C20	...	...	...	...	...
C29	23.25 ± 0.07	23.36 ± 0.08	23.61 ± 0.34	23.25 ± 0.17	43.89 ± 7.13
C30	23.80 ± 0.19	23.81 ± 0.16	...	...	...
C33	23.20 ± 0.13	23.28 ± 0.28	23.22 ± 0.36	...	19.04 ± 4.48
C35	23.09 ± 0.12	23.06 ± 0.11	...	...	32.76 ± 5.96
C40	23.68 ± 0.15	23.69 ± 0.22	...	...	...
C41	23.08 ± 0.23	...	...	...	...
C42	23.56 ± 0.25	23.39 ± 0.26	...	...	...
C48	23.73 ± 0.20	23.87 ± 0.25	...	...	...
C53	24.07 ± 0.22	23.98 ± 0.21	...	...	13.77 ± 4.06
C54	24.44 ± 0.08	24.61 ± 0.18	...	...	...
S03-C5	23.11 ± 0.17	23.40 ± 0.30	...	...	29.94 ± 5.94
S03-C7	24.25 ± 0.17	24.56 ± 0.33	...	...	20.33 ± 5.11

Table 5.3—Continued

Name	$m_{3.6\mu m}$ (mag)	$m_{4.5\mu m}$ (mag)	$m_{5.8\mu m}$ (mag)	$m_{8.0\mu m}$ (mag)	$f_{24\mu m}$ (μJy)
S03-C8	23.41 ± 0.11	23.49 ± 0.25	...	...	13.33 ± 3.81
S03-C17	23.72 ± 0.26	...	...	...	28.35 ± 5.67
S03-C26	20.86 ± 0.07	21.30 ± 0.07	21.50 ± 0.10	21.61 ± 0.18	43.24 ± 6.81
S03-oC14	...	...	...	...	53.30 ± 8.56
S03-oC26	...	...	...	...	...
S03-oC29	...	...	...	...	...
S03-oC34	22.65 ± 0.07	22.42 ± 0.07	22.21 ± 0.15	21.91 ± 0.19	19.34 ± 4.99
D8	...	...	...	...	...
D14	...	...	...	...	...
D16	24.42 ± 0.10	24.79 ± 0.23	...	...	9.65 ± 2.65
D19	24.07 ± 0.21	23.94 ± 0.28	...	...	...
D20	24.43 ± 0.17	24.71 ± 0.22	...	...	13.01 ± 4.12
D23	...	...	...	...	...
D25	24.86 ± 0.23	25.13 ± 0.31	...	...	...
D26	24.07 ± 0.24	23.97 ± 0.25	...	...	18.54 ± 5.06
D28	22.36 ± 0.07	22.30 ± 0.08	22.16 ± 0.16	22.06 ± 0.14	40.12 ± 7.10
D29	24.04 ± 0.23	...	...	...	75.03 ± 9.11
D32	24.11 ± 0.16	24.17 ± 0.22	...	...	12.98 ± 4.02
D34	23.42 ± 0.10	23.65 ± 0.13	23.62 ± 0.26	...	...
D35	23.72 ± 0.11	23.82 ± 0.17	...	...	8.87 ± 2.85
D38	23.07 ± 0.18	23.01 ± 0.24	22.72 ± 0.28	22.69 ± 0.34	...
D39	24.36 ± 0.26	...	...	...	...
D41	23.86 ± 0.07	23.84 ± 0.07	...	23.92 ± 0.35	...
D45	20.93 ± 0.07	21.22 ± 0.07	21.43 ± 0.17	21.44 ± 0.18	...
D47	24.35 ± 0.33	24.21 ± 0.26	...	...	...
D55	23.27 ± 0.07	23.22 ± 0.07	23.35 ± 0.26	23.04 ± 0.26	...
S03-D3	...	...	...	...	...
S03-D6	...	...	...	...	35.73 ± 6.15
S03-oD3	23.86 ± 0.19	...	...	...	15.44 ± 4.45
S03-oD12	23.16 ± 0.15	23.10 ± 0.22	...	...	96.52 ± 10.03

Table 5.3—Continued

Name	$m_{3.6\mu m}$ (mag)	$m_{4.5\mu m}$ (mag)	$m_{5.8\mu m}$ (mag)	$m_{8.0\mu m}$ (mag)	$f_{24\mu m}$ (μJy)
MD4	23.97 ± 0.23	...	...	...	...
MD6	22.70 ± 0.07	22.57 ± 0.21	...	22.68 ± 0.32	114.58 ± 10.76
MD13	22.37 ± 0.08	22.57 ± 0.16	...	...	...
MD27	20.59 ± 0.07	20.50 ± 0.07	20.33 ± 0.07	20.76 ± 0.08	20.96 ± 4.79
MD31	22.03 ± 0.07	21.95 ± 0.11	21.70 ± 0.20	21.83 ± 0.32	13.38 ± 4.06
MD33	22.94 ± 0.10	23.03 ± 0.07	22.94 ± 0.17	23.42 ± 0.21	...
MD34	23.79 ± 0.08	23.78 ± 0.11	23.97 ± 0.30	...	97.28 ± 9.88
MD39	20.04 ± 0.07	19.98 ± 0.07	19.45 ± 0.07	18.82 ± 0.07	487.88 ± 22.21
MD43	22.25 ± 0.07	22.48 ± 0.07	22.55 ± 0.24	22.95 ± 0.31	38.64 ± 6.45
MD48	22.74 ± 0.07	22.62 ± 0.07	22.67 ± 0.15	22.46 ± 0.20	34.53 ± 6.57
MD49	23.13 ± 0.09	23.15 ± 0.14	23.13 ± 0.28	23.05 ± 0.27	15.57 ± 4.18
MD50	24.09 ± 0.15	24.04 ± 0.13	...	...	...
MD54	23.15 ± 0.17	23.03 ± 0.19	...	...	...
MD55	23.54 ± 0.11	23.52 ± 0.21	...	...	12.85 ± 3.76
MD74	21.99 ± 0.07	21.73 ± 0.07	21.34 ± 0.12	20.78 ± 0.07	123.38 ± 11.27
MD75	22.19 ± 0.07	22.63 ± 0.12	22.70 ± 0.15	22.73 ± 0.35	25.41 ± 5.76
MD78	...	...	...	...	...
MD79	22.92 ± 0.09	22.82 ± 0.10	22.62 ± 0.16	23.01 ± 0.35	23.18 ± 5.14
MD83	23.95 ± 0.21	24.26 ± 0.31	...	...	9.66 ± 3.04
S03-MD3	20.65 ± 0.07	21.13 ± 0.07	21.46 ± 0.23	22.00 ± 0.29	22.37 ± 4.97
S03-MD12	21.59 ± 0.07	21.20 ± 0.07	20.48 ± 0.07	19.85 ± 0.07	139.71 ± 12.00
S03-MD45	21.07 ± 0.07	20.91 ± 0.07	20.97 ± 0.07	21.23 ± 0.10	178.12 ± 13.52
S03-oMD19	23.31 ± 0.07	23.25 ± 0.07	23.23 ± 0.24	22.90 ± 0.20	18.47 ± 4.87
S03-oMD56	23.73 ± 0.13	24.13 ± 0.23	23.79 ± 0.26	...	...
S03-M16	23.49 ± 0.11	23.52 ± 0.15	...	...	31.96 ± 6.38
S03-M23	20.83 ± 0.07	20.88 ± 0.07	21.04 ± 0.07	21.08 ± 0.07	...
S03-M25	24.32 ± 0.33	...	...	...	...
S03-M35	22.76 ± 0.08	22.65 ± 0.09	22.35 ± 0.14	22.47 ± 0.20	23.46 ± 5.16

Table 5.4. Stellar Population Parameters

Name[a]	z[b]	$E(B-V)_\infty$	Age_∞ (Myr)	SFR_∞ ($M_\odot$ yr^{-1})	M^*_∞ (10^{10} M$_\odot$)	τ[c] (Myr)	$E(B-V)_\tau$	Age_τ (Myr)	SFR_τ ($M_\odot$ yr^{-1})	M^*_τ (10^{10} M$_\odot$)	Notes [d]
BX1035	2.236	0.24	20	234	0.466	20	0.24	15	185	0.419	
BX1040	2.468	0.09	2100	14	3.030	200	0.03	571	7	2.220	
BX1042	2.607	0.18	509	36	1.820	200	0.15	321	23	1.810	
BX1050	2.322	0.27	15	118	0.179	50	0.26	15	98	0.173	
BX1051	2.098	0.12	404	24	0.963	100	0.02	286	7	1.100	
BX1055	2.491	0.12	255	37	0.956	100	0.04	227	14	1.210	
BX1060	2.081	0.24	806	64	5.150	100	0.01	509	4	5.810	
BX1064	2.086	0.14	509	22	1.100	100	0.02	321	5	1.230	
BX1065	2.701	0.08	1434	35	5.040	100	0.00	360	10	3.570	
BX1071	1.996	0.21	161	43	0.690	10	0.14	55	2	0.600	
BX1074	1.750	0.20	1139	26	2.970	100	0.09	360	7	2.490	
BX1075	2.221	0.25	128	91	1.160	50	0.09	203	8	2.270	
BX1080	2.390	0.25	203	78	1.590	50	0.11	203	9	2.430	
BX1081	1.801	0.24	286	46	1.310	50	0.06	255	2	2.030	
BX1084	2.437	0.12	227	82	1.860	100	0.05	227	29	2.570	
BX1085	2.236	0.30	10	201	0.201	20	0.08	90	3	0.602	
BX1086	2.444	0.28	20	139	0.277	50	0.06	203	4	1.250	
BX1089	2.049	0.17	1609	33	5.360	100	0.06	404	7	4.160	
BX1100	2.079	0.14	255	68	1.720	50	0.10	114	34	1.510	

Table 5.4—Continued

Name[a]	z[b]	$E(B-V)_\infty$	Age_∞ (Myr)	SFR_∞ ($M_\odot$ yr^{-1})	M^*_∞ (10^{10} M$_\odot$)	τ[c] (Myr)	$E(B-V)_\tau$	Age_τ (Myr)	SFR_τ ($M_\odot$ yr^{-1})	M^*_τ (10^{10} M$_\odot$)	Notes [d]
BX1104	2.441	0.11	286	37	1.050	100	0.05	227	15	1.280	
BX1106	2.917	0.10	905	29	2.670	100	0.01	321	9	2.160	
BX1116	2.048	0.13	571	29	1.650	100	0.00	360	5	1.900	
BX1121	1.878	0.17	806	45	3.640	100	0.02	404	7	3.850	
BX1125	2.222	0.15	203	15	0.304	50	0.01	203	2	0.456	
BX1129	1.973	0.17	203	122	2.480	50	0.10	143	37	3.110	
BX1140	1.487	0.18	806	13	1.070	100	0.01	454	1	1.240	
BX1145	2.325	0.07	806	7	0.562	200	0.02	454	3	0.571	
BX1157	2.081	0.08	3000	22	6.720	500	0.02	1278	10	5.740	
BX1161	1.891	0.24	203	86	1.740	20	0.17	90	11	1.930	
BX1164	2.593	0.15	15	67	0.101	∞	0.15	15	67	0.101	
BX1166	1.334	0.14	1139	6	0.649	100	0.00	404	1	0.544	
BX1169	1.871	0.17	454	33	1.490	100	0.07	286	10	1.680	
BX1170	2.443	0.20	806	49	3.950	100	0.04	404	7	3.710	
BX1172	2.806	0.20	10	127	0.127	50	0.00	161	5	0.571	
BX1174	2.349	0.07	719	18	1.300	5000	0.07	719	18	1.360	
BX1185	2.205	0.26	719	39	2.820	200	0.21	404	22	2.820	
BX1186	2.079	0.22	10	52	0.052	10	0.20	10	26	0.045	
BX1192	1.996	0.18	2600	36	9.450	100	0.10	404	11	5.980	

Table 5.4—Continued

Name[a]	z[b]	$E(B-V)_\infty$	Age_∞ (Myr)	SFR_∞ ($M_\odot$ yr^{-1})	M^*_∞ (10^{10} M$_\odot$)	τ[c] (Myr)	$E(B-V)_\tau$	Age_τ (Myr)	SFR_τ ($M_\odot$ yr^{-1})	M^*_τ (10^{10} M$_\odot$)	Notes[d]
BX1197	2.593	0.06	1434	23	3.350	500	0.04	719	19	2.990	
BX1201	2.000	0.15	203	33	0.671	20	0.04	102	3	0.797	
BX1204	2.205	0.21	640	36	2.330	50	0.05	255	3	2.250	
BX1208	2.589	0.20	15	104	0.157	100	0.01	255	7	0.786	
BX1222	2.442	0.21	9	102	0.093	10	0.20	8	69	0.090	
BX1228	1.997	0.35	8	375	0.312	20	0.34	8	276	0.284	
BX1229	1.343	0.26	50	50	0.251	10	0.24	20	25	0.162	
BX1233	2.856	0.07	2200	26	5.780	1000	0.00	2100	10	7.240	
BX1238	2.261	0.14	640	25	1.590	200	0.09	404	13	1.640	
BX1240	2.282	0.14	114	44	0.507	10	0.05	50	3	0.460	
BX1244	1.012	0.28	20	50	0.100	20	0.28	15	40	0.090	
BX1245	2.093	0.01	1015	15	1.540	500	0.00	571	13	1.390	
BX1250	1.855	0.15	640	18	1.150	100	0.07	286	7	1.110	
BX1252	2.931	0.07	255	36	0.917	50	0.00	161	9	1.050	
BX1253	1.933	0.13	1139	19	2.190	200	0.05	571	7	2.240	
BX1264	2.942	0.00	2100	10	2.140	5000	0.00	2100	10	2.640	
BX1265	2.434	0.12	255	34	0.873	50	0.01	180	6	1.060	
BX1267	1.996	0.11	1900	22	4.100	5000	0.10	2500	25	8.120	IRAC
BX1269	2.275	0.24	255	127	3.250	50	0.17	143	41	3.440	

Table 5.4—Continued

Name[a]	z[b]	$E(B-V)_\infty$	Age_∞ (Myr)	SFR_∞ ($M_\odot$ yr^{-1})	M^*_∞ (10^{10} M$_\odot$)	τ[c] (Myr)	$E(B-V)_\tau$	Age_τ (Myr)	SFR_τ ($M_\odot$ yr^{-1})	M^*_τ (10^{10} M$_\odot$)	Notes [d]
BX1274	2.596	0.10	640	32	2.050	∞	0.10	640	32	2.050	
BX1277	2.268	0.09	454	25	1.110	100	0.00	286	7	1.200	
BX1281	2.410	0.13	509	14	0.694	100	0.00	360	2	0.809	
BX1283	2.427	0.10	2600	17	4.340	200	0.00	719	5	3.260	
BX1284	2.273	0.07	1139	14	1.540	100	0.00	321	5	1.150	
BX1287	1.675	0.28	9	305	0.278	10	0.00	90	0	0.921	
BX1288	2.301	0.08	509	21	1.060	100	0.00	286	7	1.110	
BX1289	2.488	0.17	404	46	1.850	50	0.06	203	7	2.000	
BX1290	2.980	0.00	905	11	1.020	∞	0.00	905	11	1.020	
BX1291	2.052	0.31	7	469	0.339	100	0.31	7	448	0.336	
BX1296	1.988	0.23	3250	56	18.300	5000	0.20	3250	43	19.900	
BX1297	2.274	0.24	2750	37	10.200	200	0.06	806	7	7.550	
BX1303	2.305	0.10	1700	11	1.800	100	0.01	360	3	1.190	
BX1305	2.234	0.15	2100	17	3.480	200	0.01	719	4	2.780	
BX1307	2.002	0.20	404	92	3.720	10	0.18	50	12	1.810	
BX1311	2.484	0.10	286	58	1.660	50	0.00	180	11	1.890	
BX1313	2.635	0.20	15	121	0.183	1000	0.20	15	120	0.183	
BX1315	1.671	0.22	571	46	2.620	100	0.17	255	22	2.560	
BX1316	2.088	0.13	3000	23	6.980	1000	0.10	1434	18	5.670	

Table 5.4—Continued

Name[a]	z[b]	$E(B-V)_\infty$	Age_∞ (Myr)	SFR_∞ ($M_\odot$ yr^{-1})	M^*_∞ (10^{10} M$_\odot$)	τ[c] (Myr)	$E(B-V)_\tau$	Age_τ (Myr)	SFR_τ ($M_\odot$ yr^{-1})	M^*_τ (10^{10} M$_\odot$)	Notes [d]
BX1317	1.789	0.18	321	46	1.480	20	0.09	102	4	1.410	K_s
BX1324	1.818	0.34	509	65	3.320	10	0.26	90	0	2.710	
BX1326	2.984	0.00	806	13	1.040	∞	0.00	806	13	1.040	
BX1327	2.209	0.07	1139	16	1.870	200	0.01	509	7	1.750	
BX1330	2.363	0.06	571	27	1.520	100	0.01	255	12	1.410	
BX1332	2.214	0.29	15	282	0.427	20	0.09	90	8	1.400	
BX1334	3.371	0.00	1800	9	1.700	500	0.00	1609	9	10.500	
BX1339	1.988	0.09	1139	13	1.450	100	0.01	321	5	1.090	
BX1343	2.268	0.13	1015	31	3.170	100	0.02	360	7	2.650	
BX1348	1.921	0.09	509	9	0.468	100	0.01	255	4	0.426	
BX1349	1.873	0.33	509	87	4.440	∞	0.33	509	87	4.440	
BX1354	2.088	0.03	321	6	0.199	100	0.00	180	4	0.189	
BX1358	2.943	0.04	641	12	0.753	100	0.00	255	6	0.660	
BX1362	1.664	0.14	1609	16	2.580	200	0.10	509	9	2.160	
BX1363	2.297	0.16	719	37	2.630	100	0.00	404	5	2.760	
BX1364	2.183	0.15	719	29	2.110	100	0.06	321	8	1.980	
BX1368	2.443	0.16	454	61	2.790	100	0.07	286	18	3.000	
BX1376	2.430	0.07	255	16	0.416	50	0.00	143	5	0.426	
BX1378	1.971	0.21	203	56	1.130	20	0.14	81	10	1.100	

Table 5.4—Continued

Name[a]	z[b]	$E(B-V)_\infty$	Age_∞ (Myr)	SFR_∞ ($M_\odot$ yr^{-1})	M^*_∞ (10^{10} M$_\odot$)	τ[c] (Myr)	$E(B-V)_\tau$	Age_τ (Myr)	SFR_τ ($M_\odot$ yr^{-1})	M^*_τ (10^{10} M$_\odot$)	Notes[d]
BX1387	2.324	0.11	640	14	0.929	200	0.07	360	9	0.897	spurious 8 μm
BX1388	2.032	0.29	3000	43	13.000	500	0.21	1139	24	10.400	
BX1391	1.906	0.22	203	50	1.010	20	0.14	90	6	1.120	
BX1397	2.133	0.15	1015	30	3.080	100	0.04	360	7	2.650	
BX1399	2.033	0.18	1800	15	2.670	200	0.14	509	9	2.050	
BX1401	2.481	0.18	1139	85	9.650	100	0.01	454	9	8.580	
BX1408	2.482	0.28	640	57	3.680	100	0.15	360	11	3.880	
BX1409	2.237	0.29	2000	34	6.740	100	0.14	454	5	4.810	K_s
BX1420	2.133	0.24	255	87	2.210	50	0.12	180	15	2.720	
BX1425	1.864	0.10	905	10	0.903	100	0.00	321	3	0.769	
BX1427	2.548	0.13	719	29	2.070	100	0.01	360	6	2.050	
BX1431	2.001	0.11	321	24	0.770	100	0.02	255	8	0.918	
BX1434	1.994	0.15	454	21	0.956	200	0.13	286	15	0.931	
BX1439	2.188	0.18	2750	34	9.270	200	0.05	719	9	6.590	K_s
BX1443	1.684	0.30	571	135	7.730	∞	0.30	571	135	7.730	
BX1446	2.320	0.12	321	32	1.040	100	0.05	255	11	1.290	
BX1451	2.245	0.21	905	41	3.740	200	0.18	404	25	3.330	
BX1458	1.864	0.28	509	31	1.570	50	0.13	227	3	1.560	
BX1460	3.134	0.00	2000	14	2.870	2000	0.00	1700	12	3.170	

Table 5.4—Continued

Name[a]	z[b]	$E(B-V)_\infty$	Age_∞ (Myr)	SFR_∞ ($M_\odot$ yr^{-1})	M^*_∞ (10^{10} $\mathrm{M}_\odot$)	τ[c] (Myr)	$E(B-V)_\tau$	Age_τ (Myr)	SFR_τ ($M_\odot$ yr^{-1})	M^*_τ (10^{10} $\mathrm{M}_\odot$)	Notes [d]
BX1461	2.107	0.15	255	20	0.514	200	0.14	203	15	0.535	
BX1479	2.377	0.10	905	22	1.950	100	0.03	321	7	1.600	
BX1480	2.545	0.21	203	80	1.630	5000	0.21	203	79	1.640	
BX1485	2.548	0.14	1139	105	11.900	∞	0.14	1139	105	11.900	
BX1495	2.247	0.13	1139	13	1.470	100	0.00	404	2	1.210	
BX1501	1.877	0.18	321	50	1.600	100	0.06	321	10	2.350	
BX1504	2.864	0.09	255	29	0.743	50	0.00	161	7	0.827	
BX1514	2.135	0.17	1900	18	3.450	200	0.06	640	6	2.870	K_s
BX1525	1.689	0.29	1609	39	6.310	200	0.24	509	23	5.350	
BX1530	2.421	0.14	360	29	1.030	500	0.14	286	26	1.010	
BX1535	2.299	0.27	15	159	0.241	20	0.09	90	4	0.797	
BX1542	1.018	0.31	15	25	0.038	200	0.31	15	24	0.038	
BX1559	2.408	0.06	719	21	1.480	∞	0.06	719	21	1.480	
BX1567	2.225	0.19	571	73	4.150	50	0.05	227	9	4.030	
BX1568	1.787	0.23	15	145	0.220	10	0.00	102	0	0.997	
BX1572	1.782	0.34	8	199	0.165	∞	0.34	8	199	0.165	
BX1574	1.808	0.26	806	41	3.270	50	0.14	227	6	2.840	
BX1588	2.221	0.25	143	207	2.960	10	0.15	64	5	3.220	
BX1605	1.974	0.01	571	13	0.723	1000	0.00	454	12	0.689	

Table 5.4—Continued

Name[a]	z[b]	$E(B-V)_\infty$	Age_∞ (Myr)	SFR_∞ ($M_\odot$ yr^{-1})	M^*_∞ (10^{10} M$_\odot$)	τ[c] (Myr)	$E(B-V)_\tau$	Age_τ (Myr)	SFR_τ ($M_\odot$ yr^{-1})	M^*_τ (10^{10} M$_\odot$)	Notes [d]
BX1616	2.205	0.04	2500	5	1.250	500	0.01	905	4	0.967	
BX1617	2.320	0.12	321	13	0.419	∞	0.12	404	13	0.516	
BX1630	2.220	0.07	456	16	0.727	100	0.01	255	7	0.771	
BX1636	2.300	0.28	255	129	3.300	10	0.24	45	20	1.770	
BX1641	1.433	0.22	10	54	0.055	50	0.22	10	48	0.053	
BX1642	2.007	0.14	360	25	0.914	∞	0.14	360	25	0.914	
BX1650	2.097	0.17	203	85	1.730	50	0.07	161	19	2.270	
BX1694	2.007	0.12	360	38	1.370	100	0.05	255	14	1.650	
BX1708	1.987	0.34	1278	78	9.940	10	0.41	30	84	1.600	
BX1817	1.860	0.37	114	109	1.240	50	0.36	72	74	1.180	
BX1820	2.457	0.34	360	191	6.870	∞	0.34	360	191	6.870	
BX1821	2.590	0.20	286	41	1.180	100	0.10	286	10	1.610	
BX1823	1.818	0.40	2750	69	18.900	200	0.26	719	20	14.300	
BX1826	2.929	0.01	2100	12	2.540	200	0.00	509	8	1.810	
BX1827	1.988	0.46	7	392	0.284	∞	0.46	7	392	0.284	
BX1848	2.648	0.07	571	12	0.700	100	0.00	321	3	0.792	
BX82	1.023	0.20	404	6	0.225	10	0.01	227	0	0.310	
BX84	2.163	0.16	1278	38	4.860	∞	0.16	1278	38	4.860	
BX150	2.277	0.16	2400	26	6.290	100	0.06	321	10	2.350	

Table 5.4—Continued

Name[a]	z[b]	$E(B-V)_\infty$	Age_∞ (Myr)	SFR_∞ ($M_\odot$ yr^{-1})	M^*_∞ (10^{10} M$_\odot$)	τ[c] (Myr)	$E(B-V)_\tau$	Age_τ (Myr)	SFR_τ ($M_\odot$ yr^{-1})	M^*_τ (10^{10} M$_\odot$)	Notes [d]
BX184	1.998	0.45	7	676	0.489	∞	0.45	7	676	0.489	
BX305	2.482	0.29	719	88	6.300	100	0.17	360	18	6.290	
BX308	2.376	0.21	719	38	2.730	100	0.03	454	3	3.040	
BX313	2.323	0.15	905	32	2.880	∞	0.15	905	32	2.880	
BX341	2.117	0.05	905	25	2.280	∞	0.05	905	25	2.280	
BM1008	1.799	0.24	15	149	0.226	200	0.24	15	142	0.223	
BM1011	1.677	0.23	161	53	0.846	20	0.14	102	4	1.230	
BM1030	1.142	0.35	35	51	0.177	10	0.33	20	22	0.138	
BM1048	1.380	0.17	255	32	0.806	10	0.13	55	2	0.570	
BM1053	1.459	0.04	640	3	0.219	200	0.02	321	2	0.197	
BM1061	2.089	0.00	3000	4	1.070	∞	0.00	3000	4	1.070	
BM1063	2.087	0.10	3000	14	4.150	200	0.01	640	6	2.740	
BM1064	1.524	0.17	255	28	0.708	10	0.04	114	0	0.971	
BM1069	2.028	0.14	3000	29	8.650	500	0.06	1434	9	7.850	
BM1072	1.143	0.27	15	74	0.112	10	0.28	10	61	0.105	
BM1092	1.479	0.26	20	66	0.131	20	0.00	180	0	0.759	
BM1095	1.447	0.07	571	7	0.387	50	0.00	203	1	0.382	
BM1098	1.671	0.22	255	51	1.290	10	0.14	72	1	1.220	
BM1122	1.990	0.16	30	57	0.172	20	0.15	20	43	0.147	

Table 5.4—Continued

Name[a]	z[b]	$E(B-V)_\infty$	Age_∞ (Myr)	SFR_∞ ($M_\odot$ yr^{-1})	M^*_∞ (10^{10} M$_\odot$)	τ[c] (Myr)	$E(B-V)_\tau$	Age_τ (Myr)	SFR_τ ($M_\odot$ yr^{-1})	M^*_τ (10^{10} M$_\odot$)	Notes [d]
BM1135	1.872	0.20	905	55	4.990	1000	0.20	640	52	4.660	
BM1139	1.919	0.07	1139	18	2.040	∞	0.07	1139	18	2.040	
BM1148	2.049	0.13	20	89	0.178	20	0.12	15	70	0.159	
BM1149	1.630	0.17	15	30	0.045	∞	0.17	15	30	0.045	
BM1153	2.444	0.12	2600	50	13.100	1000	0.04	2600	14	17.800	
BM1155	2.020	0.01	905	11	1.030	2000	0.00	806	10	1.040	
BM1159	1.016	0.12	286	19	0.533	100	0.10	180	11	0.568	
BM1160	1.364	0.23	128	20	0.255	10	0.10	90	0	0.440	
BM1161	2.045	0.00	2750	4	1.190	∞	0.00	2750	4	1.190	
BM1163	1.874	0.20	286	23	0.669	100	0.18	161	16	0.632	
BM1171	2.082	0.07	806	10	0.831	∞	0.07	806	10	0.831	
BM1172	1.864	0.08	321	13	0.423	1000	0.07	286	13	0.416	
BM1175	1.773	0.21	114	53	0.605	∞	0.21	114	53	0.605	
BM1180	1.598	0.18	806	32	2.580	100	0.10	321	10	2.320	
BM1181	1.743	0.30	7	645	0.467	∞	0.30	7	645	0.467	
BM1195	1.289	0.24	640	25	1.610	10	0.28	30	18	0.336	
BM1196	1.863	0.00	404	6	0.238	∞	0.00	404	6	0.238	
BM1197	1.566	0.20	360	30	1.090	10	0.09	114	0	1.280	
BM1198	1.780	0.30	15	203	0.307	10	0.31	10	169	0.290	

Table 5.4—Continued

Name[a]	z[b]	$E(B-V)_\infty$	Age_∞ (Myr)	SFR_∞ ($M_\odot$ yr^{-1})	M^*_∞ (10^{10} M$_\odot$)	τ[c] (Myr)	$E(B-V)_\tau$	Age_τ (Myr)	SFR_τ ($M_\odot$ yr^{-1})	M^*_τ (10^{10} M$_\odot$)	Notes [d]
BM1200	2.078	0.09	640	23	1.490	1000	0.08	571	20	1.550	
BM1201	1.001	0.04	806	2	0.200	100	0.00	286	1	0.178	
BM1204	1.489	0.12	360	21	0.742	20	0.02	128	1	0.821	
BM1205	1.711	0.04	3500	8	2.720	1000	0.03	1434	7	2.090	
BM1207	1.083	0.31	15	57	0.087	50	0.35	10	88	0.098	
BM1209	1.775	0.34	10	365	0.365	10	0.32	9	222	0.331	
BM1226	1.355	0.35	10	104	0.104	50	0.34	10	90	0.099	
BM1289	2.380	0.23	8	139	0.115	10	0.23	7	108	0.114	
BM1299	1.595	0.35	114	203	2.320	5000	0.35	114	202	2.330	
BM1303	1.721	0.30	719	34	2.470	∞	0.30	719	34	2.470	
BM1334	1.893	0.24	509	58	2.930	100	0.17	255	25	2.900	
BM1335	1.489	0.51	10	1061	1.060	50	0.51	10	914	1.010	
BM1339	1.338	0.37	10	309	0.309	10	0.12	81	0	1.030	
BM1358	1.807	0.34	1278	81	10.400	500	0.32	719	63	10.100	
BM1369	1.879	0.41	7	277	0.200	50	0.44	6	394	0.253	
BM1375	2.109	0.07	2500	23	5.720	500	0.04	905	18	4.520	
BM1396	1.743	0.33	128	143	1.830	20	0.26	81	22	2.400	
BM72	1.571	0.19	1139	14	1.580	200	0.13	454	7	1.190	
C2	2.991	0.20	454	40	1.830	1000	0.34	40	163	0.666	

Table 5.4—Continued

Name[a]	z[b]	$E(B-V)_\infty$	Age_∞ (Myr)	SFR_∞ ($M_\odot$ yr^{-1})	M^*_∞ (10^{10} M$_\odot$)	τ[c] (Myr)	$E(B-V)_\tau$	Age_τ (Myr)	SFR_τ ($M_\odot$ yr^{-1})	M^*_τ (10^{10} M$_\odot$)	Notes [d]
C11	2.990	0.31	9	326	0.297	20	0.01	114	2	0.895	
C12	2.975	0.39	10	891	0.891	10	0.12	81	1	2.520	
C14	2.973	0.46	8	779	0.648	50	0.46	8	694	0.628	
C16	2.929	0.46	9	2025	1.850	∞	0.46	9	2025	1.850	
C29	3.110	0.11	1015	26	2.690	100	0.00	360	6	2.160	
C30	3.328	0.04	454	25	1.140	200	0.00	321	15	1.160	
C33	3.130	0.03	454	36	1.650	5000	0.02	454	35	1.660	
C35	3.363	0.07	1680	28	4.660	500	0.04	806	20	3.970	
C41	3.148	0.04	2000	15	3.030	1000	0.00	2000	8	5.340	
C42	3.411	0.12	227	55	1.260	2000	0.12	227	53	1.260	
C48	3.206	0.26	15	179	0.270	50	0.02	180	6	1.050	
C53	3.103	0.30	9	249	0.227	200	0.30	9	243	0.227	
S03-C7	2.658	0.34	5	546	0.274	10	0.34	5	397	0.258	
S03-C8	2.988	0.12	255	45	1.140	50	0.00	203	5	1.460	
S03-C17	3.163	0.00	1900	11	2.140	5000	0.00	1900	11	2.470	
D14	2.979	0.04	2000	13	2.580	1000	0.04	1015	11	1.990	
D16	2.930	0.00	719	8	0.558	∞	0.00	719	8	0.558	
D23	3.125	0.06	1015	47	4.750	200	0.00	454	23	3.910	
D25	2.970	0.07	10	55	0.056	50	0.06	10	49	0.054	

Table 5.4—Continued

Name[a]	z[b]	$E(B-V)_\infty$	Age_∞ (Myr)	SFR_∞ ($M_\odot$ yr^{-1})	M^*_∞ (10^{10} M$_\odot$)	τ[c] (Myr)	$E(B-V)_\tau$	Age_τ (Myr)	SFR_τ ($M_\odot$ yr^{-1})	M^*_τ (10^{10} M$_\odot$)	Notes [d]
D26	2.975	0.03	2100	7	1.500	2000	0.01	1800	6	1.630	
D28	2.932	0.41	9	1343	1.230	50	0.10	203	16	4.620	
D29	3.451	0.04	203	34	0.697	100	0.01	143	21	0.675	
D32	2.962	0.00	1015	9	0.944	∞	0.00	1015	9	0.944	
D34	2.972	0.14	1139	19	2.190	200	0.04	571	6	2.040	
D35	3.196	0.38	6	787	0.474	10	0.37	6	522	0.432	
D38	2.940	0.23	128	102	1.300	50	0.18	102	44	1.470	
D39	2.987	0.23	10	135	0.135	∞	0.23	10	135	0.135	
D47	3.191	0.00	1278	8	1.050	∞	0.00	1278	8	1.050	
D55	3.245	0.26	9	521	0.475	∞	0.26	9	521	0.475	
S03-oD3	2.725	0.00	806	11	0.906	500	0.00	509	10	0.882	
S03-oD12	2.418	0.28	25	129	0.324	10	0.27	15	74	0.262	
MD4	2.867	0.07	905	12	1.120	500	0.06	571	10	1.060	
MD6	3.243	0.05	1900	34	6.460	200	0.00	571	15	4.910	
MD13	2.974	0.19	321	112	3.600	50	0.04	227	9	4.190	
MD33	2.932	0.34	8	706	0.587	50	0.00	227	5	2.150	
MD48	2.926	0.16	1434	37	5.280	200	0.11	509	19	4.410	
MD49	2.850	0.29	9	485	0.442	50	0.00	203	6	1.780	
MD50	3.236	0.00	905	12	1.090	100	0.00	255	7	0.874	

Table 5.4—Continued

Name[a]	z[b]	$E(B-V)_\infty$	Age_∞ (Myr)	SFR_∞ ($M_\odot$ yr^{-1})	M^*_∞ (10^{10} M$_\odot$)	τ[c] (Myr)	$E(B-V)_\tau$	Age_τ (Myr)	SFR_τ ($M_\odot$ yr^{-1})	M^*_τ (10^{10} M$_\odot$)	Notes [d]
MD54	2.939	0.12	1900	21	4.070	500	0.10	806	17	3.330	
MD55	2.956	0.20	128	60	0.761	50	0.08	161	10	1.160	
MD75	2.790	0.55	4	7037	2.800	50	0.55	4	6701	2.780	
MD83	3.213	0.00	404	18	0.717	∞	0.00	404	18	0.717	
S03-M16	2.939	0.01	2100	12	2.470	200	0.00	509	8	1.780	
S03-M25	3.106	0.00	1015	11	1.120	200	0.00	360	9	0.904	
S03-M35	3.229	0.35	10	910	0.910	10	0.34	9	558	0.830	

[a]We did not fit the stellar populations of galaxies that had no data longward of $\mathcal{R}$-band (indicated by notation "BX/BM only"), had uncertain redshifts, or are identified as AGN/QSO from their optical spectra. We also do not present SED parameters for those galaxies with optical and IRAC photometry inconsistent with a simple stellar population (these sources had large $\chi^2 > 10$ or those sources with 8 μm or 24 μm excesses.

[b]Uncertain redshifts are denoted with "?".

[c]Best-fit star formation history decay timescale in Myr. In some cases, a model with constant star formation ($\tau = \infty$) provided the best-fit.

[d]Sources with 8 μm excess (above that expected from the best-fit stellar population) are indicated. Those 8 μm excess objects with large 24 μm fluxes are also indicated. These sources are likely to be obscured AGN. Objects with large K_s-band residuals are indicated (i.e., those sources whose K_s-band measurement lies more than 3 σ away from the best-fit stellar population). MD31 is the only directly-detected X-ray source which shows no optical signatures of an AGN, has a relatively faint 24 μm flux, and has photometry that is consistent with a stellar population. The IRAC photometry for BX1267 may suffer from a deblending problem and these (IRAC) data were not used in the SED fit.

Table 5.5. Stellar Masses

Sample	$N_{\rm sed}$[a]	$\log[M^*_{\rm med}/{\rm M}_\odot]$[b]	$\log[M^*/{\rm M}_\odot]$[c]
BM	51 (3)	9.87 (10.70)	9.85 ± 0.58 (10.58 ± 0.51)
BX	157 (7)	10.20 (10.98)	10.15 ± 0.52 (10.94 ± 0.38)
LBG	46 (0)	10.05 (...)	10.03 ± 0.44 (...)
Total	254 (10)	10.10 (10.98)	10.06 ± 0.53 (10.83 ± 0.43)

[a]Number of galaxies for which we derived best-fit SED parameters (including stellar mass), regardless of whether the galaxies were imaged at $K_{\rm s}$. The parentheses indicate the number of galaxies with *measured* $K_{\rm s} < 21.82$, or $K_{\rm s}({\rm Vega}) < 20$.

[b]Median stellar mass assuming a constant star formation (CSF) history. Numbers in parentheses give the median stellar mass for those galaxies with $K_{\rm s} < 21.82$, or $K_{\rm s}({\rm Vega}) < 20$.

[c]Mean and dispersion of stellar mass distribution assuming a CSF history. Numbers in parentheses give the mean stellar mass and dispersion for those galaxies with $K_{\rm s} < 21.82$, or $K_{\rm s}({\rm Vega}) < 20$.

Table 5.6. AGN at $z > 1.4$

Name	z	X-ray?[a]	Optical?[b]	8 μm?[c]	24 μm?[d]	Notes[e]
BX1637	2.487	no	yes (AGN)	yes	yes	ACS point source
BX160	2.460	no	yes (AGN)	yes	yes	$K_s = 21.87$
BM1083	2.414	yes	yes (QSO)	yes	yes	
BM1119	1.717	yes	no	yes	yes	$K_s = 21.74$
BM1156	2.211	no[f]	yes (AGN)	yes	yes	very weak X-ray source
BM1384	2.243	yes	yes (AGN)	yes	no	$K_s = 21.69$
MD31	2.981	yes	no	no	no	ACS point source
MD39	2.583	yes	yes (QSO)	yes	yes	$K_s = 20.07$
MD74	2.635	no	no	yes	yes	
S03-oC34	3.413	yes	yes (QS0)	no	no	
S03-MD12	2.647	yes	yes (AGN)	yes	yes	

[a]Indicates if the source lies within $1\farcs5$ of an X-ray counterpart in the 2 Ms data (Alexander et al. 2003).

[b]Indicates if the source shows high ionization optical emission lines indicative of AGN/QSO.

[c]Indicates if the source has a significant 8 μm excess compared with the flux at shorter wavelengths, larger than would be expected from a single stellar population.

[d]Indicates if the source has a 24 μm flux $f_{24\mu m} > 100$ μJy.

[e]K_s magnitudes are indicated for AGN with $K_s < 21.82$, or K_s(Vega) $\lesssim 20$.

[f]BM1156 is not included in the *Chandra* 2 Ms catalogs, but further refinements to the X-ray data reduction procedure yielded a very weak detection (N. Brandt, private communication).

Chapter 6

REST-FRAME UV LUMINOSITY FUNCTION AND STAR FORMATION RATE DENSITY OF $z \sim 2$ GALAXIES*†

Naveen A. Reddy,[a] Kurt L. Adelberger,[b] Charles C. Steidel,[a] Max Pettini,[c] Alice E. Shapley, [d] & Dawn K. Erb[e]

[a]California Institute of Technology, MS 105–24, Pasadena, CA 91125

[b]McKinsey & Company, 1420 Fifth Avenue, Suite 3100, Seattle, WA 98101

[c]Institute of Astronomy, Madingley Road, Cambridge CB3 OHA, UK

[d]Department of Astrophysical Sciences, Peyton Hall-Ivy Lane, Princeton, NJ 08544

[e]Harvard-Smithsonian Center for Astrophysics, 60 Garden Street, Cambridge, MA 02138

Abstract

We have used rest-frame UV color selection, combined with spectroscopy, to evaluate the UV luminosity function (LF) and star formation rate density (SFRD) at $z \sim 2$. Our sample includes 8190 photometric candidates in 7 independent fields, and spectroscopic redshifts

*Based on data obtained at the W. M. Keck Observatory, which is operated as a scientific partnership among the California Institute of Technology, the University of California, and NASA, and was made possible by the generous financial support of the W. M. Keck Foundation.

†A version of this chapter will be submitted to *The Astrophysical Journal*.

for 830 galaxies with $z > 1$. The large spectroscopic sample allows us to very accurately quantify the foreground contamination rate and reddening distributions of galaxies in our sample. We use Monte Carlo simulations to assess the effects of photometric scatter and Lyα line perturbations to the observed BX/BM colors of galaxies. The resulting incompleteness estimates for our sample are used to reconstruct the intrinsic UV LF at $z \sim 2$, the results of which indicate little evolution in the UV LF from $z \sim 4$ to $z \sim 2$ (to $\mathcal{R} = 25.5$). Integrating the luminosity function and assuming a Salpeter IMF, we compute an SFRD (to $0.1L^*_{z=3}$) of $0.034 \pm 0.004\ M_\odot\ \mathrm{yr}^{-1}\ \mathrm{Mpc}^{-3}$ at $z = 2.2$, suggesting a modest decline in the SFRD, by a factor of 1.2, from $z \sim 4$ to $z \sim 2$.

6.1 Introduction

Constraining the star formation history and stellar mass evolution of galaxies is a central component in understanding structure formation in the Universe. Observations of the stellar mass and star formation rate density, the QSO density, and galaxy morphology at both low ($z \lesssim 1$) and high ($z \gtrsim 3$) redshifts indicate that most of the activity responsible for shaping the bulk properties of galaxies to their present form occured in the epochs between $1 \lesssim z \lesssim 3$ (e.g., Dickinson et al. 2003b; Rudnick et al. 2003; Madau et al. 1996; Lilly et al. 1996, 1995; Steidel et al. 1999; Shaver et al. 1996; Fan et al. 2001; Di Matteo et al. 2003; Conselice et al. 2004; Papovich et al. 2003; Shapley et al. 2001; Giavalisco et al. 1996). While this period in the Universe was perhaps the most active in terms of galaxy evolution and accretion activity, it was not until recently that advances in detector sensitivity and efficiency, the increased resolution and light-gathering capability afforded by larger 8 to 10 meter class telescopes, and a number of new powerful imagers and spectrographs on space-based missions such as *HST*, *Spitzer*, *GALEX*, and *Chandra*, allowed for the study of large numbers of galaxies at $z \sim 2$. These developments have prompted a spate of multi-wavelength surveys of high redshift galaxies from the far-IR/submm to IR, near-IR, optical, and UV, enabling us to examine the SEDs of star-forming galaxies over much of the 7 decades of frequency over which stars emit their light either directly or indirectly through dust processing (e.g., Steidel et al. 2003, 2004; Daddi et al. 2004b,a; Franx et al. 2003; van Dokkum et al. 2003, 2004; Abraham et al. 2004; Chapman et al. 2005; Smail 2003).

The first surveys that efficiently amassed large samples of high redshift galaxies used

the observed BX/BM colors of galaxies to identify those with a deficit of Lyman continuum flux (e.g., Steidel et al. 1995) in the $U_{\rm n}$ band (i.e., U "drop-outs") for galaxies at $z \sim 3$. Those initial results have been adapted to select galaxies at higher redshifts using the ($z > 4$; e.g., Bouwens et al. 2005, 2004; Dickinson et al. 2004; Bunker et al. 2004; Yan et al. 2003) and moderate redshifts ($1.4 \lesssim z \lesssim 3$; Adelberger et al. 2004; Steidel et al. 2004). Combining these high redshift results with those from *GALEX* (e.g., Wyder et al. 2005), we now have an unprecedented view of the rest-frame UV properties of galaxies from the epoch of reionization to the present, perhaps the only wavelength for which star-forming galaxies have been studied across more than $\sim 97\%$ of the age of the Universe. The accessibility to rest-frame UV wavelengths over almost the entire age of the Universe makes rest-frame UV luminosity functions (LFs) useful tools in assessing the cosmic star formation history in a consistent manner.

For the past several years, our group has taken advantage of the unrivaled near-UV sensitivity of the blue channel of the Low Resolution Imaging Spectrograph (LRIS-B) on the Keck I telescope to conduct a large survey to rest-frame UV color-select and spectroscopically followup galaxies at redshifts $1.4 \lesssim z \lesssim 3.0$ in seven uncorrelated fields. The color selection criteria are described in Adelberger et al. (2004); Steidel et al. (2004). Initial results from the survey, including analyses of the star formation rates, stellar populations, stellar and dynamical masses, gas-phase metallicities, morphologies, outflow properties, and clustering are presented in many papers by our group (e.g., Shapley et al. 2005; Adelberger et al. 2005a,b; Erb et al. 2006a,c,b; Reddy et al. 2006b, 2005; Reddy & Steidel 2004; Steidel et al. 2005). In this paper we focus on estimating the rest-frame UV LF of optically-selected galaxies at $z \sim 2$. The detailed calculations of the incompleteness corrections presented here, combined with extensive multi-wavelength data in several fields of the $z \sim 2$ survey (particularly $K_{\rm s}$ and *Spitzer*/IRAC data), can be used to estimate the rest-frame optical LFs and stellar mass functions at $z \sim 2$; the results of these additional analyses will be presented elsewhere. As discussed elsewhere (e.g., Adelberger et al. 2004; Steidel et al. 2004; Reddy et al. 2006c), rest-frame UV selection is arguably the most efficient method of culling and spectroscopically confirming large samples of high redshift galaxies. With a careful accounting of extinction, photometric imprecision, and systematic effects caused by observational limitations, rest-frame UV selected samples can be used to estimate the

cosmological star formation history (e.g., Steidel et al. 1999; Adelberger & Steidel 2000; Bouwens et al. 2004, 2005, 2006; Bunker et al. 2004, 2006).

There are two primary methods by which one can attempt to construct "complete" luminosity functions that make a reasonable account of all star formation at a given epoch. The first method is to observe galaxies over as wide a range in wavelengths as possible in order to establish a census of all galaxies that dominate the star formation rate density. For example, the union of rest-frame UV (Adelberger et al. 2004; Steidel et al. 2004), rest-frame optical (Franx et al. 2003; Daddi et al. 2004b), and submillimeter-selected samples (e.g., Smail et al. 1997; Hughes et al. 1998; Barger et al. 1998; Chapman et al. 2005) should account for optically bright galaxies with little to moderate dust extinction as well as the population of optically faint and heavily reddened galaxies. One can then examine the intersection between these various samples and, taking into account overlap, compute the total star formation rate density (Reddy et al. 2005). Unfortunately, this technique poses several challenging problems, not the least of which is the practicality of obtaining (and having access to) multi-wavelength data in a large number of uncorrelated fields, disparate data quality and photometric depth between optical and near-IR images, and the inefficiency of spectroscopically identifying galaxies in near-IR selected samples to properly account for the sampled volumes.

The second approach, and one that we adopt in this paper, is to estimate sample completeness using Monte Carlo simulations. This method involves simulating many realizations of the intrinsic distribution of galaxy properties at high redshift, subjecting these realizations to the same photometric methods and selection criteria as applied to real data, and adjusting the simulated realizations until convergence between the expected and observed distribution of galaxy properties is achieved. The method thus corrects for a large fraction of galaxies that might be "missing" from the sample, just as long as some of them are spectroscopically observed. The obvious disadvantage of the method is that some (optically faint) galaxies will never be scattered into our selection window and hence we cannot account for such galaxies in our analysis. We note, later on in this paper, that a relatively large fraction of even the most dust-obscured galaxies at high redshift are still optically bright enough for spectroscopy (e.g., Chapman et al. 2005) and/or satisfy our optical color criteria. It is therefore likely that, at least by number, the vast majority of galaxies failing

our selection criteria are optically faint because they have little star formation, not because they are heavily dust obscured (we discuss the effect of extinction corrections as a function of bolometric luminosity in § 6.5.4). Nevertheless, applying this method to joint photometric and spectroscopic samples of high redshift galaxies allows one to assess the systematic effects of photometric scattering and the intrinsic variation in colors due to line emission and absorption with unprecedented accuracy. The primary goal of this paper is to apply this Monte Carlo approach of assessing sample completeness to our large photometric and spectroscopic sample of rest-frame UV-selected galaxies at redshifts $z \sim 2$.

The foray of observations into the epoch around $z \sim 2$ has occurred relatively recently, and with it have come various determinations of the UV LFs at these epochs (Gabasch et al. 2004; Le Fèvre et al. 2005). Unfortunately, such studies are often limited either because (1) they are magnitude limited (resulting in inefficient selection of galaxies at the redshifts of interest and even fewer galaxies with secure spectroscopic redshifts and poorly determined contamination fraction), (2) they generally rely on photometric redshifts that are highly uncertain at $z \sim 2$ (e.g., Shapley et al. 2005; Reddy et al. 2006b), and/or (3) they are estimated over a relatively small number of fields such that cosmic variance may be an issue. While magnitude limited surveys allow one to easily quantify the selection function with little thought, as we show below, Monte Carlo simulations combined with accurate spectroscopy can be used to quantify even the relatively complicated redshift selection functions and biases of color-selected samples of high redshift galaxies. This "simulation" approach allows one to assess a number of systematics (e.g., photometric imprecision, perturbation of colors due to line strengths, effects of seeing, etc.) and their potential effect on the derived LF; these systematic effects have been left untreated in previous calculations, of the LFs at $z \sim 2-3$ (Gabasch et al. 2004; Le Fèvre et al. 2005), but are nonetheless found to be important in accurately computing the LF (e.g., Adelberger & Steidel 2000; Bouwens et al. 2004, 2005, 2006). With this paper we present the first completeness-corrected spectroscopic estimate of the UV LF and star formation rate density (SFRD) at $z \sim 2$, computed across the seven independent fields of our survey.

The outline of this paper is as follows. In § 6.2, we describe the fields of our survey and the color criteria used to selected candidate galaxies at $z \sim 2$. We then proceed with a description of the spectroscopic followup and quantify the fraction of contaminants, includ-

ing low redshift ($z < 1$) star forming galaxies and low and high redshift AGN and QSOs, within the sample. We conclude § 6.2 by demonstrating that the redshift distribution for the spectroscopic sample is not significantly biased when compared with the redshift distribution of all photometric candidates at $z \sim 2$. In § 6.3, we detail the Monte Carlo method used to assess both photometric bias and error, the effect of Lyα line perturbations on the observed BX/BM colors of galaxies, and the approximate effective volumes of the survey. We also describe a more robust method than the $V_{\rm eff}$ method for determining the luminosity function. Using this refined method, we quantify the BX selection function (§ 6.3.5) and proceed with discussing the best-fit reddening distribution (§ 6.4) and luminosity function (§ 6.5). We use multi-wavelength data to place our extinction corrections to the observed UV luminosity function on a secure footing, then proceed in § 6.6 to discuss our value of the total star formation rate density at $z \sim 2$ and the comparison with similarly-selected samples at $z \sim 3 - 4$. A flat ΛCDM cosmology is assumed with $H_0 = 70$ km s^{-1} Mpc^{-1}, $\Omega_\Lambda = 0.7$, and $\Omega_{\rm m} = 0.3$.

6.2 Sample Selection and Observations

6.2.1 Fields

Our $z \sim 2$ survey is primarily being conducted in fields chosen for having $V \leq 17.5$ mag QSOs with redshifts $2.5 \lesssim z \lesssim 2.8$, ideally placed to study the correlation between $z \sim 2$ galaxies and HI and high-metallicity (e.g., CIV) absorbing systems in the IGM (see Adelberger et al. 2005b). We have extended our survey to include the GOODS-North field (encompassing the original HDF-North field) and the Extended Groth Strip (EGS) field to take advantage of the multi-wavelength data amassed for these fields. Field observations were conducted under similar conditions as the $z \sim 3$ fields of Steidel et al. (2003), to a 3σ depth of $\mathcal{R}_{\rm AB} \sim 27.5$. The 7 fields of the $z \sim 3$ survey are summarized in Table 6.1 (instruments used and dates of observation are shown in Table 1 of Steidel et al. 2004).

One of the unique advantages of our analysis is that we use seven uncorrelated fields in order to compute the LF, negating the need for uncertain normalization corrections to account for clustering and cosmic variance. For example, we find evidence for significant large-scale structure within several fields of the $z \sim 2$ survey, generally characterized by

overdensities in redshift space above what would be expected given our redshift selection function. By averaging results over seven fields well distributed throughout the sky, we can estimate the LF insensitive to variations in large-scale structure, and furthermore estimate the magnitude that cosmic variance has on the obtained results.

6.2.2 BX Color Selection

Even with *a priori* knowledge of the intrinsic properties of all $z \sim 2$ galaxies, constructing a practical set of selection criteria using a limited set of filters to select all galaxies with $1.9 \lesssim z \lesssim 2.8$ and reject all others is intractable. As a result, we are forced to design criteria that mitigate the competing interests of culling as many galaxies at the targeted redshift range while rejecting those that are not (e.g., Adelberger et al. 2004). High redshift galaxy surveys will, as a consquence, have rather complex selection functions. The approach described in § 6.3 allows one to quantify such selection functions with relative ease.

The criteria used to select galaxies with redshifts $1.9 \lesssim z \lesssim 2.8$ based on their rest-frame UV colors were designed to select objects with intrinsic properties similar to those of $z \sim 3$ Lyman break galaxies, but observed at $z \sim 2$. The colors at $z \sim 2$ were estimated from spectral synthesis analysis of 70 LBGs with broadband $U_{\rm n}G\mathcal{R}JK_{\rm s}$ photometry and spectroscopic redshifts (Adelberger et al. 2004; Steidel et al. 2004). Initial spectroscopy of $z \sim 2$ candidates led to a refinement of the criteria used to select galaxies at redshifts $1.9 \lesssim z \lesssim 2.8$ to their present form:

$$\begin{aligned} G - \mathcal{R} &\geq -0.2 \\ U_n - G &\geq G - \mathcal{R} + 0.2 \\ G - \mathcal{R} &\leq 0.2(U_n - G) + 0.4 \\ U_n - G &\leq G - \mathcal{R} + 1.0, \end{aligned} \tag{6.1}$$

termed as "BX" selection (Adelberger et al. 2004; Steidel et al. 2004), with fluxes in units of AB magnitudes (Oke & Gunn 1983). Additionally, we exclude all sources with $\mathcal{R} < 19$ that are saturated in our images. The above criteria yielded 8190 candidates in the seven fields, with an average surface density of ~ 5 arcmin^{-2}, uncorrected for interloper contamination (see § 6.2.4). Since a variety of different instruments and filter sets were used and fields

were observed with slightly varying conditions, this can lead to systematic differences in the observed colors of galaxies from one field to another (this has been dealt with in Steidel et al. 2003 where systematics in colors are largely removed). We have incorporated some of these effects (e.g., seeing, airmass of the observation, CCD response, and filter shape) in computing the expected colors of galaxies with known intrinsic properties, but we cannot possibly model all field-to-field variations in photometry and whichever biases remain (e.g., errors in the zero-points used) are discussed in § 6.3.3.

6.2.3 Spectroscopic Followup

We took advantage of the unique UV sensitive capabilities of the blue channel of the Low Resolution Imaging Spectrograph (LRIS-B) to obtain spectroscopy of $z \sim 2$ candidates in the line-rich region between rest-frame 1100 and 2000 Å. The instrument description, spectroscopic setup, and data reduction are described in Steidel et al. (2003) and Steidel et al. (2004).

Candidates were placed on slitmasks according to a simple prioritization scheme. Objects with $\mathcal{R} = 23.5 - 24.5$ and those within $1'$ of QSOs were generally assigned high priorities. Objects with fainter magnitudes, where absorption line spectroscopy is more difficult, or brigher magnitudes, where the contamination fraction is larger, were assigned lower priorities. In some cases, objects were placed on masks based on other criteria (e.g., near-IR $J-K$ color; K magnitude; association with X-ray, submillimeter, or MIPS source; etc.). For optimal efficiency, lower priority sources were added to slitmasks if a higher priority object was unavailable. Redshifts were determined primarily from some combination of the Lyα line and UV resonance lines such as SiII, OI, CII, FeII, AlII, and AlIII. Redshifts obtained using either the Lyα line or interstellar absorption lines are almost always redshifted and blueshifted, respectively, with respect to near-IR nebular emission lines (e.g., NII and Hα) by several hundred kilometers per second. While these systematic offsets are likely to arise in the presence of outflowing gas (Adelberger et al. 2003, 2005b), they are much smaller than the typical bin size used to compute the reddening and luminosity distributions and so will not appreciably affect our results.

Of the 1302 BX candidates targeted for spectroscopy, 830 have redshift $z > 1$, with a mean redshift $\langle z \rangle = 2.2 \pm 0.3$. The remaining are either interlopers (§ 6.2.4) or objects for

which we were unable to obtain redshifts (§ 6.2.5). The histogram of the 830 redshifts is shown in Figure 6.1. A preliminary version of this figure based on 749 redshifts is presented in Steidel et al. (2004), along with sample spectra of a few optically-bright BX galaxies.

6.2.4 Interloper Contribution and AGN

The region of color space defined by BX selection (e.g., Figure 6.2) is also expected to include galaxies outside of the targeted redshift range, including star-forming galaxies at $z \lesssim 0.2$ and stars (see Figure 10 of Adelberger et al. 2004). Spectroscopy shows that there is indeed a subset of BX candidates that is composed of interlopers–candidates with redshifts $z < 1$–with a much higher contamination rate among candidates with $\mathcal{R} < 23.5$ (Table 6.2 in this paper and Table 2 of Steidel et al. 2004 for a preliminary version). One can impose a rough magnitude cutoff to consider only those candidates with $\mathcal{R} \geq 23.5$, but this would preclude the analysis of the bright end of the BX distribution. Other options to reduce the contamination fraction include using the $\mathcal{R} - K$ color where the associated bands no longer bracket strong spectral breaks for low redshift sources. For example, the BzK criteria of Daddi et al. (2004b) can be used to reduce the foreground contamination fraction.

The interloper fractions are apt to decrease as the survey progresses and we become more adept at excluding them from masks based on other multi-wavelength data, such as their $\mathcal{R} - K$ colors. However, until now, we have not used any of the techniques discussed above to actively discriminate against placing possible interlopers on slitmasks; doing so would complicate our ability to apply the observed contamination fractions to determine the interloper rate among all BX sources. Therefore, the fractions in column (4) of Table 6.2 are assumed to represent the overall fraction of interlopers as a function of $\mathcal{R}$ for the photometric sample.

The BX criteria also include a small number of broad-lined QSOs and broad and narrow line ($\sigma < 2000$ km s^{-1}) AGN whose UV colors are similar to those of high redshift star-forming galaxies, but that show prominant (and in some cases broad) emission lines such as Lyα, CIV, and NV. The detection rate of such sources is $\sim 2.8\%$ (similar to the rate found among UV-selected $z \sim 3$ galaxies; Steidel et al. 2002), and all except one of the sources with $19.0 < \mathcal{R} < 22.0$ and $z > 1$ are QSOs. These spectroscopically confirmed AGN and QSOs have a negligible effect on the luminosity function for $\mathcal{R} > 22$.

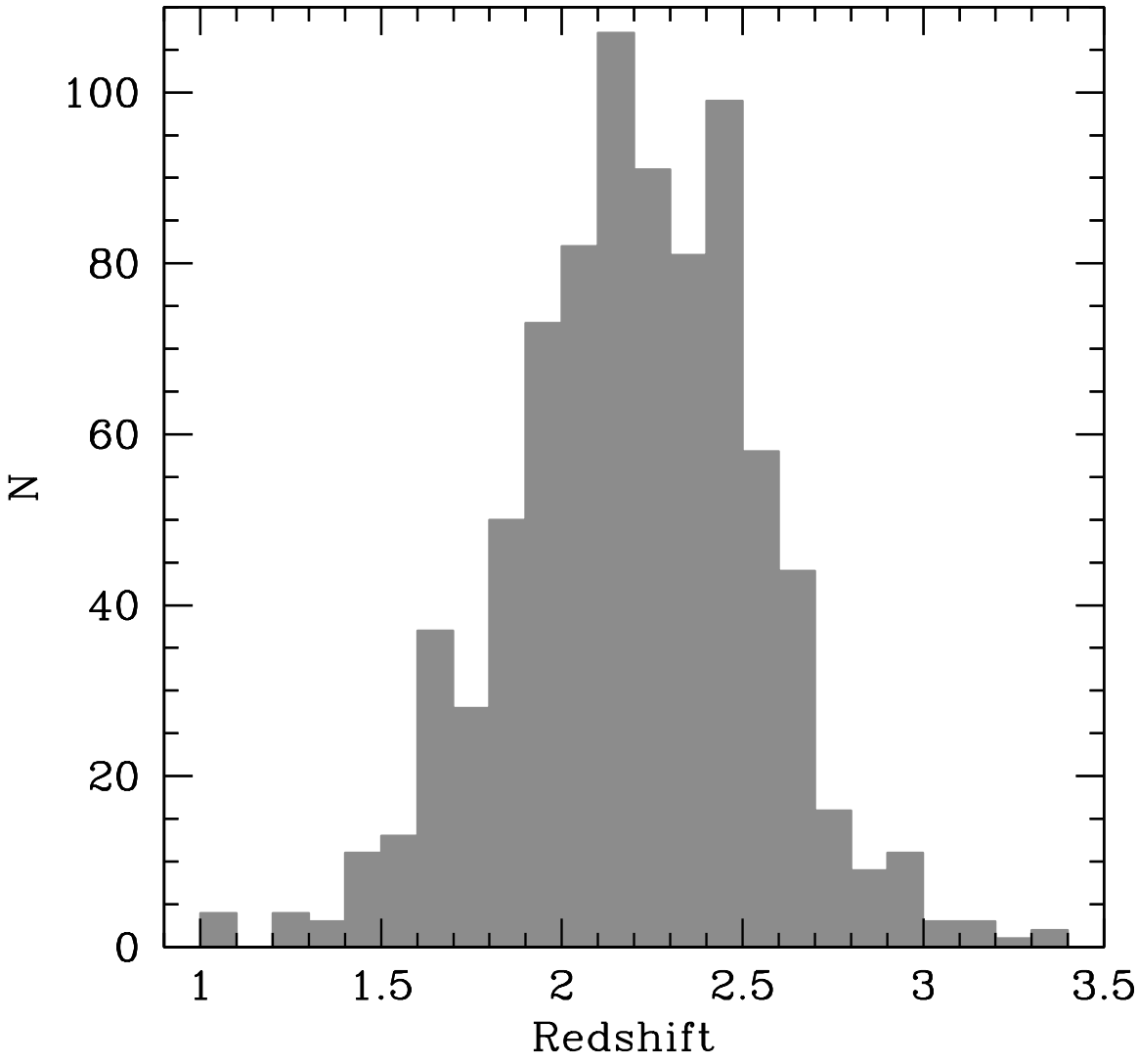

Figure 6.1 Redshift distribution for 830 spectroscopically confirmed BX galaxies with $z > 1$. A preliminary version of this figure based on 749 redshifts is Figure 2 of Steidel et al. (2004).

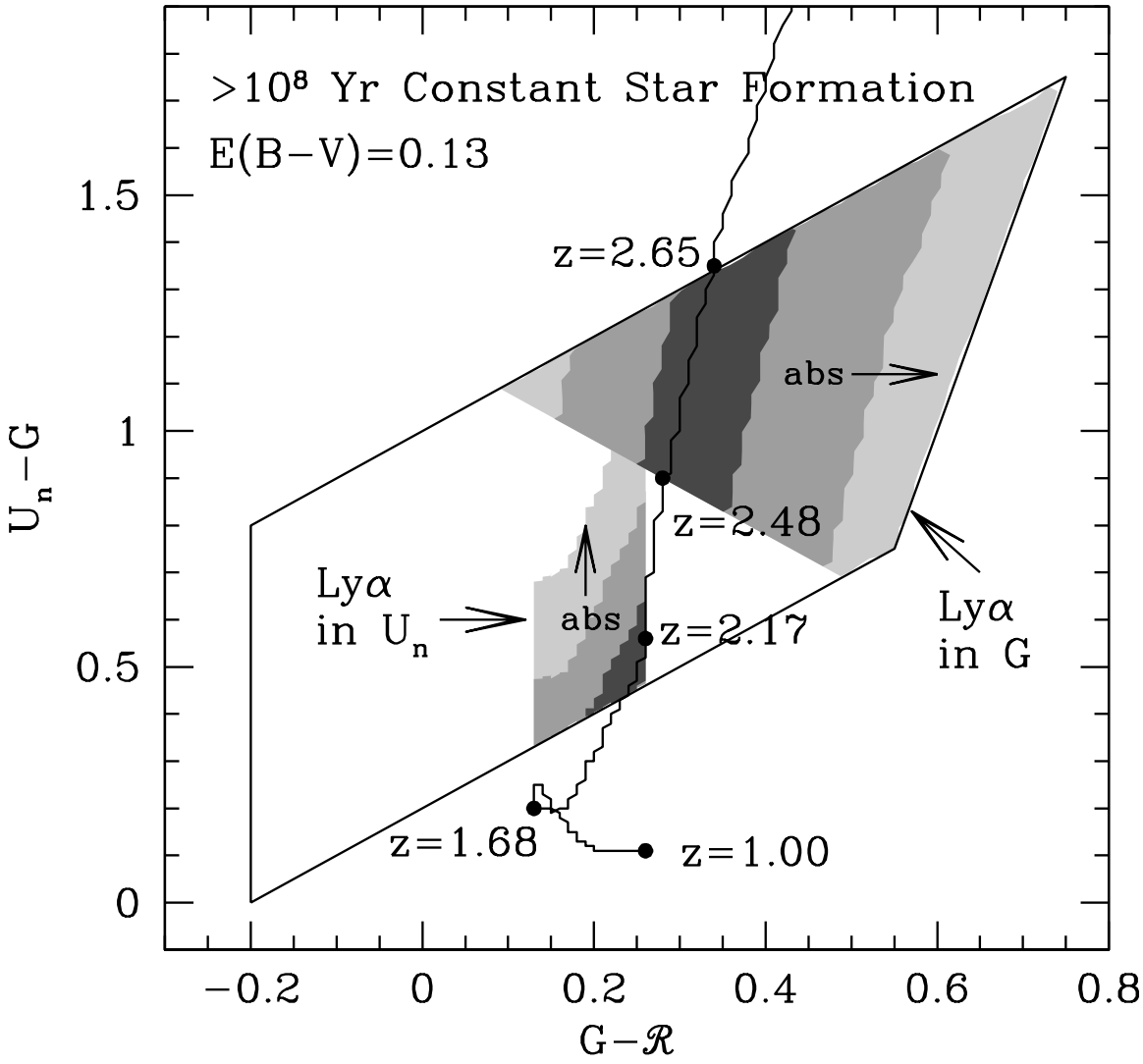

Figure 6.2 Perturbation of BX/BM colors from Lyα absorption and emission. The trapezoid is the BX selection window defined by Equation 6.1. The BX/BM colors of a template galaxy with constant star formation for > 100 Myr (after which the UV colors are essentially constant) and $E(B-V) = 0.125$ (the mean for the $z \sim 2$ sample) assuming a Calzetti et al. (2000) extinction law is shown by the solid curve, proceeding from redshift $z = 1$ to 3. The lower and upper shaded regions correspond to redshift ranges where the Lyα line falls in the $U_{\rm n}$ and G-bands, respectively. In the absence of photometric errors, galaxies with redshifts $1.68 \lesssim z \lesssim 2.17$ and $2.48 \lesssim z \lesssim 2.93$ will fall in the dark gray regions with a probability of 64% based on the $W_{\rm Ly\alpha}$ distribution in Figure 6.4. The medium and light gray regions correspond to scattering probabilities of 30% and 6%, respectively. Arrows labelled "abs" indicate the direction of increasing Lyα absorption.

6.2.5 Spectroscopic Completeness

Much of the analysis presented here is focused on assessing the photometric and spectroscopic completeness of our sample. The photometric completeness (i.e., the fraction of galaxies at $z \sim 2$ that satisfy BX color selection) is discussed in § 6.3. Here we focus on the extent to which the redshift distribution of the spectroscopic sample reflects that of the photometric sample as a whole. The redshift selection function for the spectroscopic sample of BX galaxies is very likely to reflect the overall redshift selection function of BX galaxies. First, the success of measuring redshifts is primarily a function of the weather conditions (e.g., cirrus, seeing) at the time of observation, with a 90% success rate in the best conditions. Repeat observations of objects for which we were unable to secure a redshift initially indicate that the redshift distribution of spectroscopic failures is similar to that of spectroscopic successes. Second, Figure 6.3 demonstrates that optical apparent magnitude is independent of redshift, keeping in mind that the $\mathcal{R} = 25.5$ limit is applied to the photometric (and hence also spectroscopic) sample. This is important because if the apparent magnitude showed a systematic variation with redshift, we might expect the redshift distribution of spectroscopically identified candidates to differ from candidates in general given that our mask prioritization scheme gives more weight to candidates with magnitudes in the range $23.5 \lesssim \mathcal{R} \lesssim 24.5$ (§ 6.2.3). Finally, the success of measuring a redshift is independent of the presence of Lyα emission or absorption for all but the faintest galaxies in our sample ($\mathcal{R} \sim 25.5$), implying that the observed $W_{\mathrm{Ly}\alpha}$ distribution is representative of the photometric sample (see § 6.3.2 for further discussion). Given these results, we proceed under the assumption that spectroscopic selection does not significantly bias the underlying redshift distribution of the photometric sample.

6.3 Incompleteness Corrections

A primary aim of this analysis is to connect the observed properties of BX galaxies to the underlying population of *all* $z \sim 2$ galaxies. To this end, we have constructed a plausible population of $z \sim 2$ galaxies with a range of redshifts, luminosities, and reddening, and determined the fraction of these galaxies that would satisfy the BX criteria. Inverting these fractions and applying them to the observed counts allows one to reconstruct the underlying

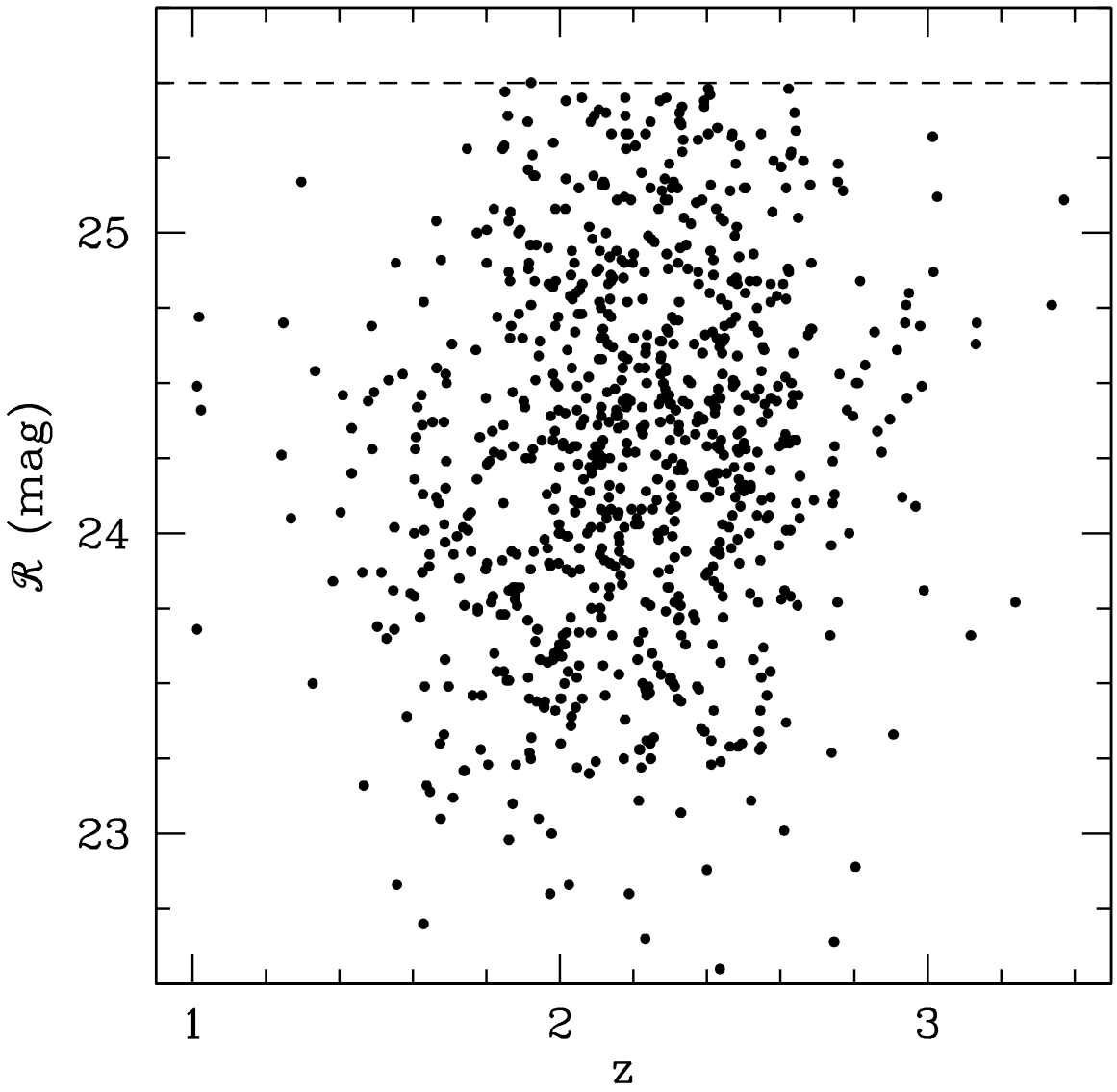

Figure 6.3 Apparent magnitude versus redshift for spectroscopically confirmed BX objects in the redshift range $1.0 < z < 4.0$. The dashed horizonatal line indicates the self-imposed $\mathcal{R} = 25.5$ limit to the photometric (and hence spectroscopic) samples.

distribution of $z \sim 2$ galaxies. We note that we can only correct the incompleteness for those galaxies which are scattered into our sample, as discussed in § 6.4, and not for those which we do not observe. In this section we discuss in detail the procedure used to reconstruct the intrinsic population of $z \sim 2$ galaxies.

6.3.1 Monte Carlo Simulations

We employed a Monte Carlo approach to both determine the transformation between the intrinsic properties of a galaxy (e.g., its luminosity, reddening, and redshift) and its observed BX/BM colors and quantify the effects of photometric errors in their measured BX/BM colors, similar to the method used in Shapley et al. (2001), Adelberger & Steidel (2000), and Steidel et al. (1999). Template galaxies with intrinsic sizes of $0\farcs05$ to $0\farcs8$ and exponential light profiles were convolved with the average PSF (typically $1''$) of the imaging data. Variations in the light profile used (e.g., exponential, de Vaucouleur) have a negligible effect on the simulation results; the intrinsic size of the light emitting region is almost always smaller than the seeing disk.

The expected BX/BM colors of a galaxy with a particular redshift and reddening are computed by assuming a Bruzual & Charlot (1996) template galaxy with constant star formation for 1 Gyr and a Calzetti et al. (2000) extinction law. The BX selection criteria were designed to select $z \sim 2$ galaxies with a range of SEDs similar to those found for LBGs at higher redshifts (Adelberger et al. 2004). Spectral synthesis modelling and external multi-wavelength information indicates that most UV-selected $z \sim 2$ galaxies can be described by long duration (> 100 Myr) starbursts and the constant star formation model described above should reproduce this behavior to the extent required by the simulations (e.g., Shapley et al. 2005). In particular, the BX/BM colors of $z \sim 2$ galaxies are essentially constant after 10^8 years of star formation, once the mix of O and B stars stabilizes.[1] The Calzetti et al. (2000) reddening law reproduces the *average* expected star formation rates of $z \sim 2$ galaxies based on extinction-free stacked X-ray and radio estimates (e.g., Reddy & Steidel 2004) and further reproduces the average dust obscuration of galaxies with bolometric luminosities in

[1] We note that there is considerable leeway in the best-fit star formation histories for the optical/IR SEDs of UV-selected $z \sim 2$ galaxies, but external constraints point to burst timescales of $\tau > 100$ Myr (Shapley et al. 2005).

the range $10^{11} \lesssim L_{\rm bol} \lesssim 10^{12.2}$ where the bulk of our sample lies (Reddy et al. 2006b). The use of a constant star forming model and the Calzetti reddening law should therefore adequately quantify the SEDs of most $z \sim 2$ galaxies. An advantage of spectroscopic followup of photometrically selected BX galaxies is that we can also constrain the effects of IGM opacity and Lyα absorption/emission (§ 6.3.2), both of which are redshift dependent. All of these perturbing effects will result in a wide range of spectral shapes and should account for any galaxies at $z \sim 2$ that are not exactly described by a Calzetti et al. (2000) attenuated constant star forming SED. We subsequently use the quantity "$E(B-V)$" to parameterize the rest-frame UV spectral shapes of $z \sim 2$ galaxies.

A large distribution of galaxy colors were then computed assuming a particular luminosity function (LF) and the observed $E(B-V)$ distribution for spectroscopically confirmed $z \sim 2$ sources. Small variations in the assumed LF do little to change the results, and are meant only to sufficiently populate redshift space and BX/BM color space with a realistic distribution of objects. The results are also insensitive to small variations in the assumed $E(B-V)$ distribution as long as the range of $E(B-V)$ chosen reflects that expected for $z \sim 2$ galaxies. A by-product of the luminosity function analysis is that we also compute the best-fit underlying $E(B-V)$ distribution. The validity of the assumed LF and $E(B-V)$ distributions can be tested by comparing with the inferred LF and $E(B-V)$ distributions. Significant differences between the assumed and inferred distributions imply that the initial assumptions for the LF and $E(B-V)$ distribution were different from their true values. The colors were corrected for opacity due to the intergalactic medium (IGM) assuming a Madau (1995) model, and corrected for filter and CCD responses and airmasses appropriate for the seven $z \sim 2$ fields. The end product is a transformation between the true properties of a galaxy (e.g., its redshift, $E(B-V)$, and luminosity) and its expected BX/BM colors.

These expected BX/BM colors are randomly assigned to simulated galaxies that are then added to the images in increments of 200 galaxies at a time. This ensures that the image including all added (simulated) galaxies has confusion statistics similar to the observed image, since this will effect the photometric uncertainties and systematics due to blending. We then attempt to recover these simulated galaxies using the same software used to recover the real data, and record whether a simulated galaxy is detected and what its observed magnitude and colors are. We repeated this procedure until approximately 2×10^6 simulated

galaxies were added to the $U_{\rm n}$, G, and $\mathcal{R}$ images of each of the seven fields.

6.3.2 Lyα Equivalent Width Distribution

The presence of Lyman alpha absorption and/or emission can perturb the observed BX/BM colors of $z \sim 2$ galaxies by up to 0.75 mag depending on the redshift and intrinsic Lyα equivalent width (EW). To estimate the scattering of colors due to Lyα, we measured the Lyα EW ($W_{\rm Ly\alpha}$) for 482 spectroscopically confirmed objects in the seven fields and the resulting distribution is shown in Figure 6.4a. The tails of the $W_{\rm Ly\alpha}$ distribution of Figure 6.4a are asymmetric. The excess at $W_{\rm Ly\alpha} > 50$ Å stems from the fact that Case B recombination predicts $W_{\rm Ly\alpha} = 150$ Å when there is no attenuation of Lyα. The lack of any excess at $W_{\rm Ly\alpha} < -50$ Å simply reflects an upper bound on the HI column density of about $\sim 10^{21}$ cm^{-2}, and for densities higher than this, $W_{\rm Ly\alpha}$ changes by a negligible amount. The scattering probability associated with this $W_{\rm Ly\alpha}$ distribution is shown in Figure 6.2. This figure demonstrates how galaxies that are and are not targeted by the BX criteria can be shifted in and out of the BX selection window.

On the other hand, $z \sim 2$ galaxies might preferentially be seen in absorption if absorbed galaxies at these redshifts are more likely to be scattered into the BX selection window than emission line galaxies (or, conversely, emission line galaxies are more likely to be scattered out of the BX selection window than absorption line galaxies). For example, Figure 6.2 indicates that galaxies with redshifts $1.68 \lesssim z \lesssim 2.17$ may have a greater probability for being selected if Lyα is seen in absorption. We can test this by examining the $W_{\rm Ly\alpha}$ distribution as a function of redshift, also shown in panels (b)-(d) of Figure 6.4. The distributions are absorption dominated in all cases, though the effect is most pronounced for galaxies with redshifts $z > 2.48$ (where Lyα falls in the G-band) as shown in Figure 6.4d. The fact that galaxies with redshifts $2.17 < z \leq 2.48$ show similar $W_{\rm Ly\alpha}$ profile (Figure 6.4c) as those at higher and lower redshifts where the BX/BM colors may be perturbed by the presence of the Lyα line suggests that $z \sim 2$ galaxies are absorption dominated irrespective of the chosen selection criteria.

These results suggest that the observed $W_{\rm Ly\alpha}$ profile accurately traces the underlying $W_{\rm Ly\alpha}$ distribution for photometrically selected BX galaxies. If galaxy morphology were the primary factor in shaping the observed profile then, since our sample is selected inde-

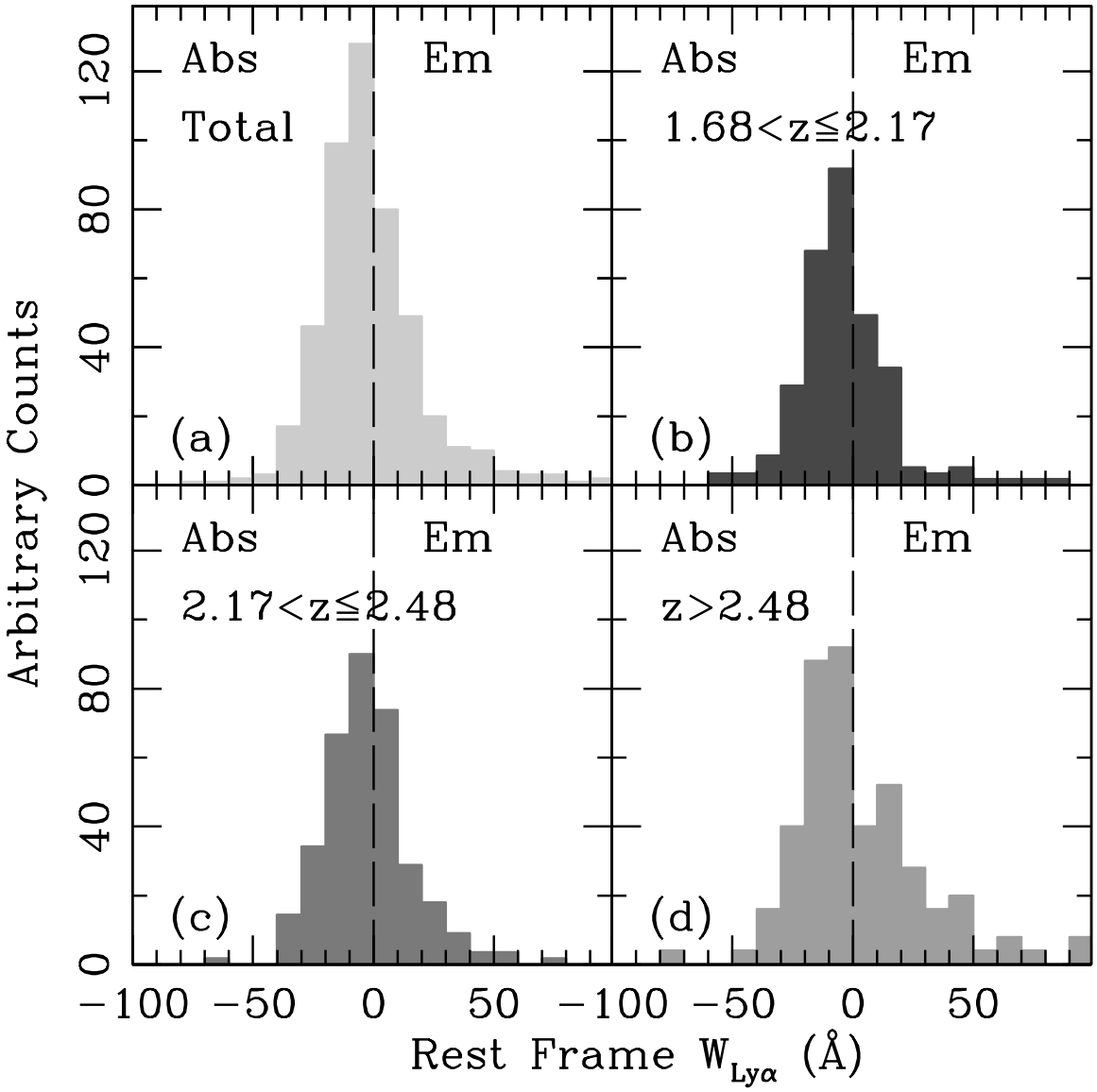

Figure 6.4 (a) Rest frame Lyα equivalent width ($W_{\mathrm{Ly}\alpha}$) distribution for 482 spectroscopically observed $z \sim 2$ galaxies. Panels (b), (c), and (d) show the $W_{\mathrm{Ly}\alpha}$ distribution for subsets in redshift. The distributions are absorption dominated in all cases.

pendent of morphology, it is reasonable to assume that the superset of simulated galaxies discussed above has a similar $W_{\mathrm{Ly}\alpha}$ distribution. The Lyα line is certainly also affected by conditions in the reionization regions around massive stars like temperature, dust content, and metallicity, but our BX criteria select independently of these quantities as well (the primary selection factor is the presence of current star formation). Systematics due to inherent differences in the physical conditions of HI ionization regions and galaxy morphology are therefore likely outweighed by the systematics associated with our observations (e.g., the ability to measure Lyα absorption in galaxies with weak continua). For the purposes of our simulations, we make the reasonable approximation that the observed $W_{\mathrm{Ly}\alpha}$ distribution can be applied to our simulated galaxies to obtain the average perturbation of the BX/BM colors.

6.3.3 Photometric Uncertainties

We have used the results of the Monte Carlo simulations (§ 6.3.1) to estimate the photometric errors and determine optimal bin sizes for subsequent analysis (§ 6.3.4). For each simulated galaxy that is detected, we have recorded the true and measured BX/BM colors. As the uncertainties may vary depending on magnitude or color, we have binned the detected galaxies in magnitude and color for each field and have only considered galaxies that would be detected as candidates since these are the only objects that are relevant to our analysis. We used bin sizes of 0.5 mag in $\mathcal{R}$ and 0.2 mag in $U_{\mathrm{n}} - G$ and $G - \mathcal{R}$ color to determine the uncertainties in the recovered magnitudes and colors of objects in each field. Systematic bias in the $G - \mathcal{R}$ color was estimated by computing the quantity $\Delta[G - \mathcal{R}] = (G - \mathcal{R})_{\mathrm{meas}} - (G - \mathcal{R})_{\mathrm{true}}$, which was typically $\lesssim 0.04$ mag, and a random uncertainty estimated to be $\sigma(\Delta[G - \mathcal{R}]) \sim 0.09$ mag. The typical random uncertainties in $U_{\mathrm{n}} - G$ and $\mathcal{R}$ are ~ 0.15 mag and ~ 0.13 mag, respectively. These quantities were determined using the same method as presented in Shapley et al. (2005), Steidel et al. (2003), and Shapley et al. (2001). The uncertainties were generally larger for objects faint in $\mathcal{R}$ (Steidel et al. 2003). The field-to-field results were consistent with each other (i.e., the typical biases and uncertainties from field-to-field were within 0.1 mag of each other). The photometric errors are slightly smaller in size to the bin sizes (0.2 mag) used to make a rough estimate of the reddening and luminosity distribution. A more refined method dis-

cussed in the next section will correct for any systematic scattering of objects into adjacent bins due to photometric error and/or Lyα perturbations to the colors.

6.3.4 Quantifying the Selection Function

6.3.4.1 Effective Volume ($V_{\rm eff}$) Method

The fraction of galaxies with a given set of binned properties that satisfy the BX criteria can be directly computed from the results of the Monte Carlo simulations. These binned properties might be the optical luminosity ($\mathcal{L}$), redshift (z), and reddening ($E(B-V)$) of a galaxy. Under the assumption that these properties are independent of each other, and if we let the indices i, j, and k run over the range of values of $\mathcal{L}$, z, and $E(B-V)$, then the true number of galaxies in the ijkth bin can be approximated as

$$n_{ijk}^{true} \simeq n_{ijk}^{obs}/\bar{p}_{ijk} \tag{6.2}$$

where $\bar{p}_{ijk}$ are the mean probabilities that a galaxy in the ijkth bin is selected by the BX criteria (Adelberger 2002). These probabilities $\bar{p}_{ijk}$ are simply

$$\bar{p}_{ijk} = \frac{1}{n_{ijk}} \sum^{n} p_{ijkn} \tag{6.3}$$

where p_{ijkn} is the probability that the nth simulated galaxy in the ijkth bin will be selected as a BX object, and n_{ijk} is the total number of simulated galaxies in the ijkth bin. The values p_{ijkn} take into account the probability that the colors of the nth simulated galaxy will be perturbed by the $W_{\rm Ly\alpha}$ distribution of Figure 6.4 and still be selected as a BX object. They also fold in the probability that a non-candidate simulated galaxy will fall in the BX selection window. Dividing by n_{ijk} normalizes the mean probabilities $\bar{p}_{ijk}$ and accounts for both the fraction of galaxies whose photometric errors scatter them out of the BX selection window and galaxies which are not detected in the simulations. If the true comoving volume corresponding to the jth bin in redshift is V_j, then the effective volume associated with the jth bin in z is

$$V_j^{\rm eff} \equiv V_j \sum^{ik} \bar{p}_{ijk} = V_j \times \xi_j, \tag{6.4}$$

where we have defined ξ_j to be the "completeness coefficients":

$$\xi_j \equiv \sum^{ik} \bar{p}_{ijk}. \tag{6.5}$$

The photometric properties of each field are unique due to differences in the observing conditions, and this will affect the computed ξ_j. We have therefore determined the completeness coefficients for each field and averaged them together to obtain mean completeness coefficients, $\bar{\xi}_j$.

6.3.4.2 Transitional Probability Function

While the procedure just described can be used to make an initial guess as to the shape of the reddening and luminosity distributions, it can lead to spurious results, particularly for objects whose true colors are such that they lie outside of or close to the edges of the BX selection window. Equation 6.2 is approximately true only if the average measured properties of a galaxy are the same as the true (simulated) properties, and this will certainly not be the case for galaxies that are preferentially scattered into the BX window due to photometric errors or the presence of Lyα absorption/emission (e.g., Adelberger 2002). The approach described above will also not take into account photometric bias and the preferential scattering of objects from one bin to another if the bin sizes are comparable to (or smaller than) the photometric errors (Adelberger 2002).

One alternative approach is to determine the $\bar{p}_{ijk}$ relevant for the measured (not true) properties of a galaxy, where the indices i, j, and k run over the measured properties of galaxies. This requires knowing the relative contributions of each true bin to a particular bin in measured properties and is a rather complicated problem. An easier approach is to solve the problem "backwards" and is one suggested by Adelberger (2002) that takes advantage of the known probabilities that a galaxy with particular true properties $\mathcal{L}Ez_{\rm true}$ will have measured properties $\mathcal{L}Ez_{\rm meas}$, as determined from the Monte Carlo simulations. These "transitional" probabilites ($\bar{p}_{i'j'k'\rightarrow ijk}$, where $i'j'k'$ run over the true properties and ijk run over the observed properties) can be applied to our initial guesses of the $E(B-V)$ and luminosity distributions from the "$V_{\rm eff}$" method described above to obtain the expected number of objects in each bin of measured properties. The expected and observed redshift,

$E(B-V)$, and color distributions are compared, the initial guesses are tweaked, and the procedure is repeated until convergence is reached when the expected counts reproduce the observed distribution of objects. A formal solution relevant for the $z \sim 3$ analysis of Adelberger & Steidel (2000) is presented in Adelberger (2002). We took advantage of both the $U_{\rm n} - G$ and $G - \mathcal{R}$ colors in our analysis of the $z \sim 2$ sample to provide more stringent constraints on the $E(B-V)$ distribution, something that was not possible at $z \sim 3$ where most galaxies only had limits in $U_{\rm n}$ either due to severe blanketing by the Lyα forest or the supression of continuum flux shortward of the Lyman limit.

We first applied this iterative method on the spectroscopic sample to determine the best-fit $E(B-V)$ distribution. Once the refined reddening distribution was in hand, we held it fixed to compute the luminosity function using the entire photometric sample. The code used to find the maximum likelihood distributions is complicated, so we independently assessed our results by creating a large number of random realizations of the $E(B-V)$ and luminosity distributions. Galaxies were simulated according to each of these distributions, the transitional probabilities were applied to these simulated populations, and the expected distributions were compared with the observed distributions. We took the best-fit $E(B-V)$ and luminosity distributions to be those that gave the minimum χ^2 between the expected and observed distributions. The iteratative and Monte Carlo approach both gave consistent results. Uncertainties were estimated from the Monte Carlo realizations of the $E(B-V)$ and luminosity distributions.

6.3.5 BX Selection Function

The derived transitional probability function can be visualized in Figure 6.5 where we show the relative probability distribution for galaxies between $1.0 < z < 3.0$ to be selected by the BX criteria. This distribution reflects both photometric error and Lyα perturbation of the expected BX/BM colors. One noticeable feature of Figure 6.5 is the divergent behavior of the selection function for low ($z < 1.9$) and high ($z > 2.8$) redshift galaxies, where higher redshift galaxies have redder $U_{\rm n} - G$ colors. This can be understood, in part, by examining Figure 6.2. If $z \sim 2$ galaxies can be reasonably described by the SED and reddening assumed above then we would expect that galaxies with $z > 2.8$ would only be scattered into the BX window if there were large changes in their colors, either due to

photometric errors or Lyα perturbation. First, we find no evidence that photometric errors increase for galaxies at higher redshifts. Second, galaxies at $z \sim 3$ that are selected by the LBG criteria are preferentially emission-line objects and it is more likely that their colors would be perturbed *away* from the BX selection window rather than towards it. Third, the $(1+z)$ dependence of the observed $W_{\mathrm{Ly}\alpha}$ will result in a larger color change for higher redshift galaxies such that the scattering probability distribution covers a larger area in color space, making it less likely for a particular source to fall within the BX selection window. Finally, the $U_{\mathrm{n}} - G$ color changes more rapidly for higher redshift galaxies where Lyα forest absorption begins to increasingly affect the U_{n}-band. All of these effects could explain the relatively small number of $z > 2.8$ galaxies singled out with the BX criteria. The advantage of BX/BM selection is that the dropoff in BX efficiency for $z > 2.8$ can be compensated for by adopting the $z \sim 3$ LBG criteria, whose selection function begins to rise for $z > 2.8$ and which use exactly the same filter set, negating the need for additional observations (Steidel et al. 2003).

Unlike the $z > 2.8$ galaxies discussed above, $z < 1.9$ galaxies are crowded into a narrower region of color space as is evident from Figure 6.2. Small variations in colors as a result of photometric errors or Lyα absorption can shift a large number of $z < 1.9$ galaxies into the BX selection window. This effect can be viewed in Figure 6.5, where there is a high relative probability for galaxies with blue $U_{\mathrm{n}} - G$ colors (the "BM" galaxies; e.g., Figure 10 of Adelberger et al. 2004) to satisfy BX selection, partly due to the effect of Lyα absorption in these systems (cf., Figure 6.4b). The highest density region in this figure (between the two white curves of Figure 6.5) occurs in the same color space expected to be occupied by galaxies at redshifts where the Lyα line does not affect the BX/BM colors ($2.17 < z \leq 2.48$). Figure 6.5 also demonstrates the fallacy of the assumption in Equation 6.2, where the true and observed BX/BM colors may be significantly and, more importantly, systematically different for galaxies lying in particular regions of color space.

The effects of IGM opacity, Lyα absorption/emission, and photometric error (§ 6.3.1, 6.3.2, 6.3.3) imply that simple boxcar approximations to the selection function (even in photometric surveys) are unrealistic, irrespective of the wavelengths used to select galaxies. The advantage of our combined Monte Carlo, photometric, and spectroscopic approach is that even complicated selection functions can be quantified relatively easily and thus be

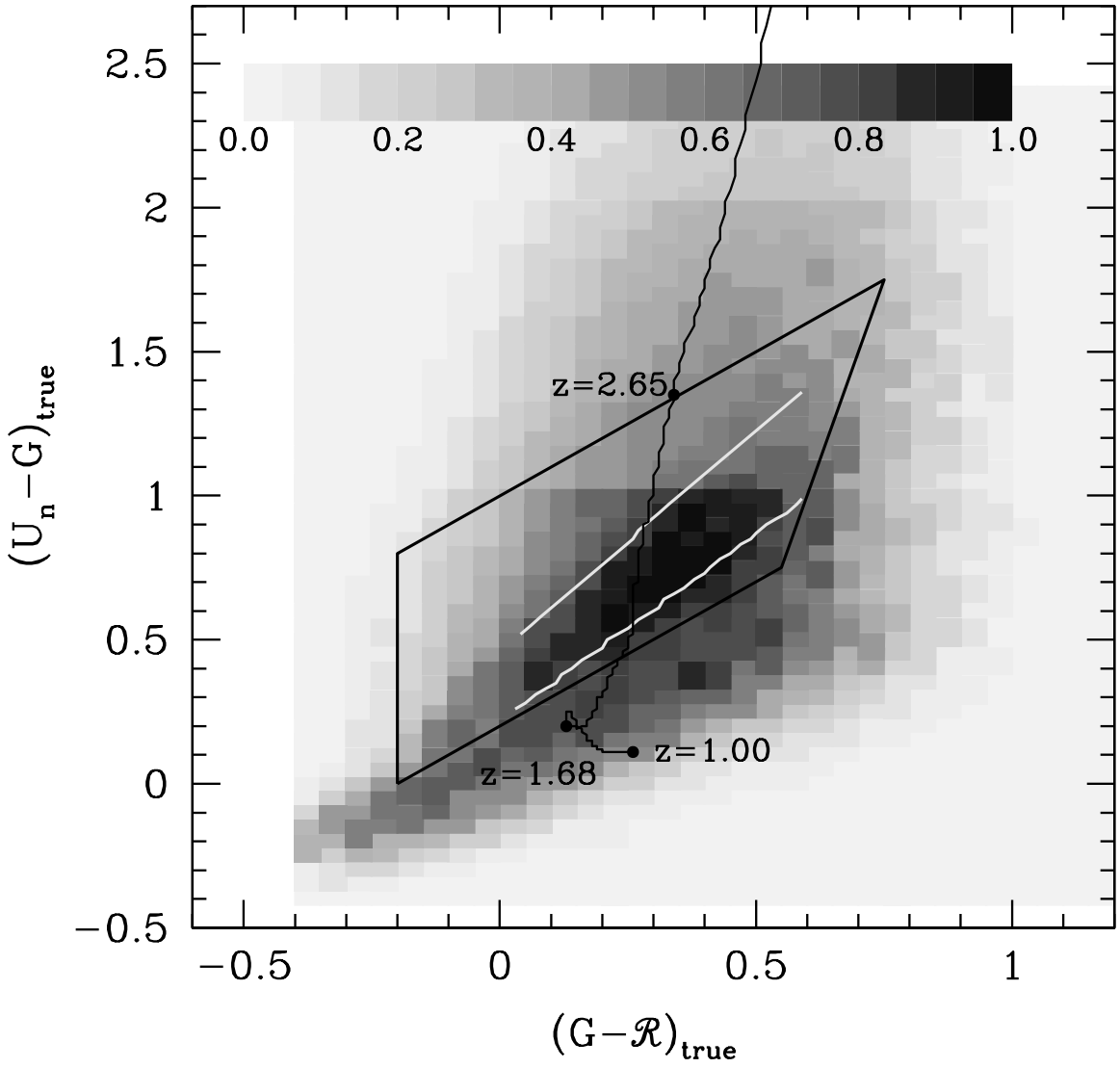

Figure 6.5 Relative probability distribution for galaxies with intrinsic colors $(U_{\rm n} - G)_{\rm expected}$ and $(G - \mathcal{R})_{\rm expected}$ to be detected and selected as BX objects. The distribution is non-zero exterior to the BX window (trapezoid) as a result of photometric error and Lyα line perturbations of the colors. Galaxies with expected (or intrinsic) $U_{\rm n} - G$ colors bluer than required to satisfy BX criteria are particularly prone to selection as discussed in § 6.3.5. The region between the white curves denotes the swath of color space where galaxies with redshifts $2.17 < z \leq 2.48$ are expected to lie. These galaxies' colors are unaffected by Lyα line perturbations.

corrected for in the final analysis.

6.4 Reddening Distribution

The iterative approach discussed in § 6.3.4 yields the expected redshift distribution given an assumed $E(B-V)$ and luminosity distribution. The shape of the redshift distribution is insensitive to changes in the shape of the luminosity function, and is primarily determined by the shape of the $E(B-V)$ distribution, or distribution in spectral shapes of galaxies. Figure 6.6 shows that the expected redshift distribution (black curve) given our best-fit reddening and luminosity distributions reproduces the observed redshift distribution (histogram). This suggests that the field-to-field photometric biases (e.g., offsets in zero-points) essentially average out and do not appreciably affect the inferred distributions.

The inferred best-fit $E(B-V)$ distribution for $z \sim 2$ galaxies is shown in Figure 6.7 as a black curve, along with the observed distribution uncorrected for completeness, photometric errors, and Lyα perturbations, indicated by the shaded histograph. Qualitatively, the inferred and observed distributions are similar. We expect a general tendency for galaxies to be "pushed" towards lower values of $E(B-V)$ than their observed values, in particular because the BX/BM colors are generally overestimated—and thus $E(B-V)$—in our photometry (§ 6.3.3), but also because correcting the BX/BM colors for Lyα absorption will shift the distribution towards lower $E(B-V)$ values. There is only marginal evidence from Figure 6.7 that the distribution is shifted towards lower values, and in fact an opposite trend occurs for the reddest galaxies. Quantitatively there is a significant deviation in the number of inferred objects with $E(B-V) > 0.4$, though the difference is still consistent with the observed number. We believe that this excess of red galaxies is real. First, as discussed above, correcting for all known photometric and Lyα biases should shift the $E(B-V)$ distribution towards lower values and could not account for the excess of red galaxies. Second, from our Monte Carlo realizations of the $E(B-V)$ distribution, only those distributions with such an excess are able to successfully reproduce the observed redshift distribution. Observationally, we see evidence for quite a few red galaxies at $z \sim 2$.

There are several reasons to suggest that the shape of the $E(B-V)$ distribution is primarily a result of a variation in the dust contents of $z \sim 2$ galaxies. First, we argued in § 6.2.5 that the redshift distribution of spectroscopic BX galaxies was likely to be similar to

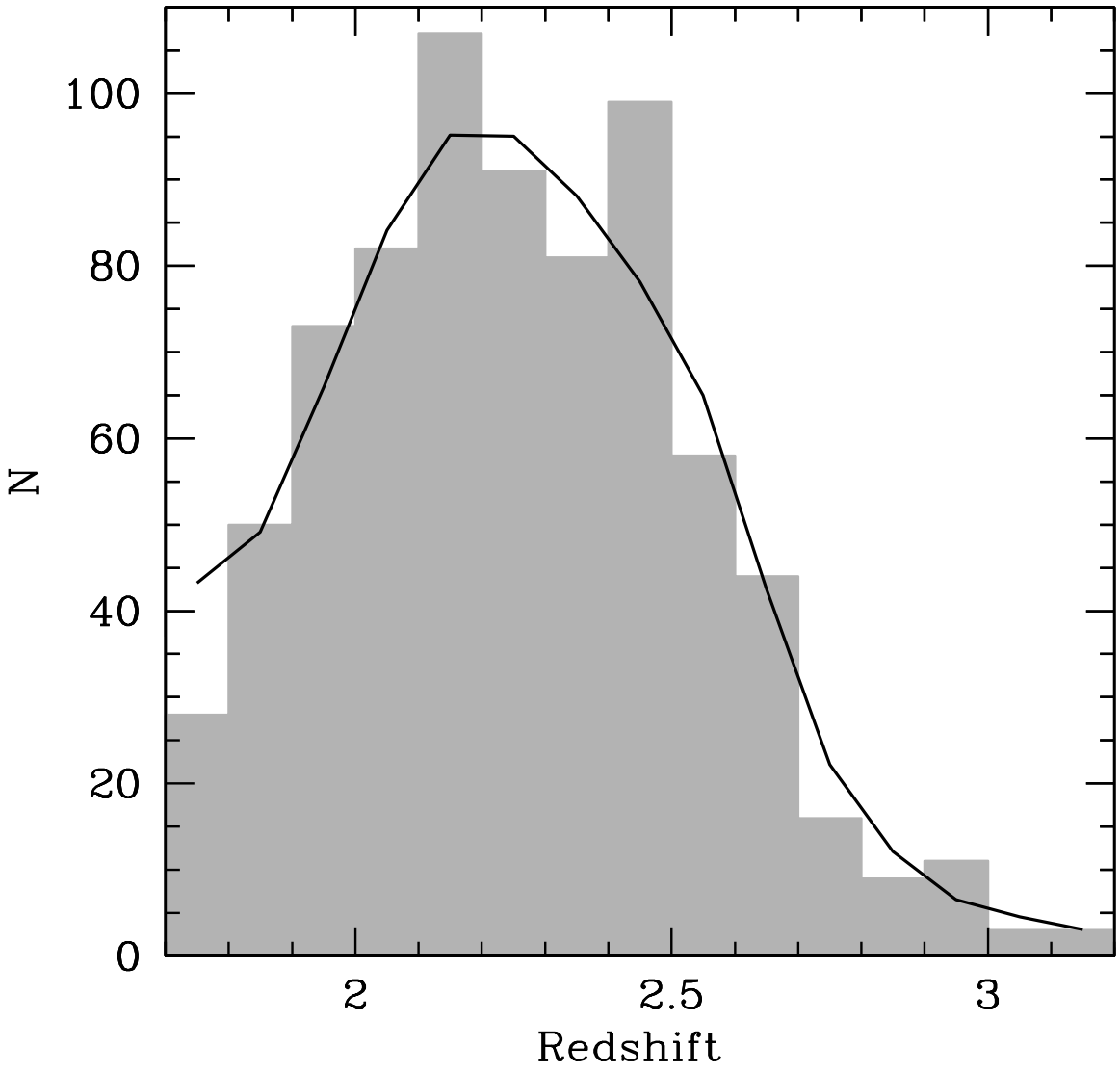

Figure 6.6 Expected redshift distribution (black curve) given our best-fit reddening and luminosity distributions (Figures 6.7 and 6.9), compared with the observed redshift distribution of BX galaxies (shaded histogram).

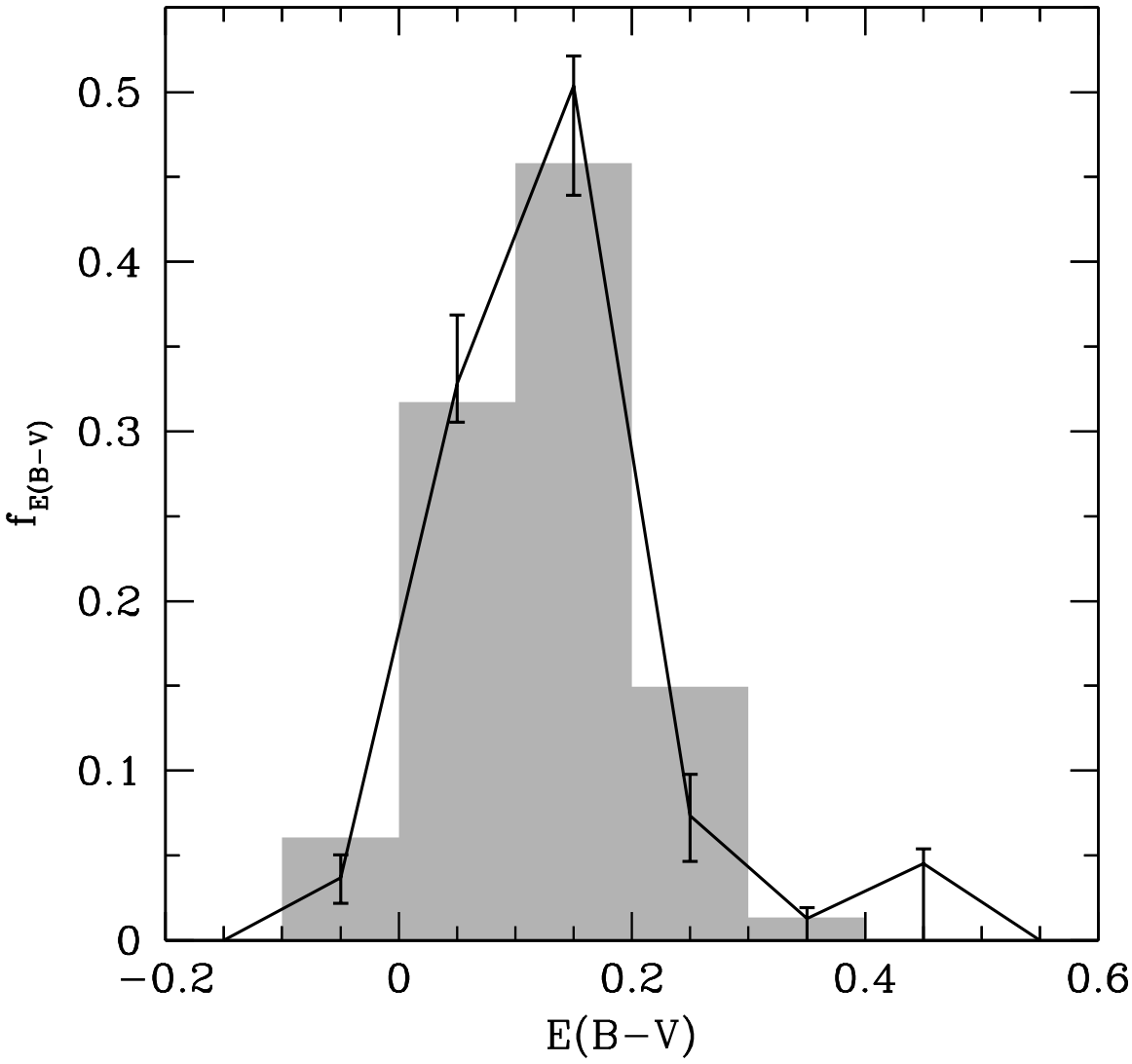

Figure 6.7 Best-fit $E(B-V)$ distribution of $z \sim 2$ BX galaxies (black curve), corrected for completeness and the effects of Lyα emission/absorption. Error bars are estimated from the Monte Carlo simulations. Also shown is the observed distribution uncorrected for the effects discussed above (shaded histogram). The best-fit distribution has $\langle E(B-V) \rangle = 0.13 \pm 0.09$, implying a mean bolometric attenuation factor of 4.

that of the photometric sample. We therefore expect that the average IGM opacity correction to the BX/BM colors is similar between the spectroscopic and photometric samples. Second, we have already taken into account the effect of Lyα on the observed colors. Third, the stochastic nature of photometric errors makes it highly unlikely that such errors would correlate with $E(B-V)$ for the range of $E(B-V)$ considered here.[2] The only remaining explanation is that the $E(B-V)$ distribution is predominantly shaped by the different amounts of reddening by dust (e.g., Pettini et al. 1998; Calzetti et al. 2000). Perhaps the most compelling evidence for this is the observed correlation between bolometric star formation rates and extinction: galaxies with higher dust-corrected star formation rates (computed based on their inferred $E(B-V)$ and that reproduce extinction-free longer wavelength estimates) have a higher attenuation factor on average (Reddy & Steidel 2004) and in individual galaxies (Reddy et al. 2006b). Such a trend could only be explained by the correlation between $E(B-V)$ and attenuation factor. The mean attenuation factor of 4 estimated from the $E(B-V)$ distribution is similar to that found by Reddy & Steidel (2004) and Reddy et al. (2006b) based on stacked X-ray/radio and rest-frame 7.7 μm estimates, respectively. The above discussion is relevant for most galaxies at $z \sim 2$ with moderate extinction. The $E(B-V)$ for relatively dust-free (or very young) galaxies is probably dominated by variation in the SEDs of high redshift galaxies, and so $E(B-V)$ is not a direct indicator of reddening for these galaxies (which is why we measure a non-negligible number density of galaxies with $E(B-V) < 0$).

It is worthwhile to point out here that the relevance of the $E(B-V)$ distribution derived here extends only insofar as the applicability of our initial assumptions in creating a plausible distribution of $z \sim 2$ galaxies. In particular, the fraction of red galaxies is likely underestimated: we know that there are populations of very red actively star forming galaxies that do not follow the standard Calzetti et al. (2000) and Meurer et al. (1999) attenuation laws. We remind the reader that we cannot account for objects that have a zero probability of being scattered into our sample. Furthermore, there are red passively evolving galaxies that are missed in UV-selected surveys due to an insignificant amount of current star formation. These galaxies would have such red UV colors that they would either

[2]The situation might be different for very red galaxies that only have photometric limits in the shorter wavelength band, but the relative number of such objects is small and should not appreciably affect our results.

satisfy the $z \sim 3$ LBG criteria (Steidel et al. 2003 and Steidel et al. 2004) or have optical magnitudes $\mathcal{R} > 25.5$ and would therefore be missed from our survey (Adelberger & Steidel 2000). Such types of galaxies are not reflected in our simulations and hence will not be corrected for by applying the derived completeness coefficients, but such passively-evolving galaxies will contribute negligibly to the total star formation rate density.

The validity of extending the best-fit luminosity function to arbitrarily faint magnitudes depends strongly on the shape of the $E(B-V)$ distribution for faint ($\mathcal{R} > 25.5$) galaxies, for which we have no information. Although purely photometric surveys of high redshift galaxies achieve greater depths (as they are not limited to relatively bright magnitudes where ground-based spectroscopy is feasible), the lack of spectroscopic information makes it difficult to accurately constrain the $E(B-V)$ distribution for such objects due to Lyα/IGM opacity perturbations to the observed colors. One alternative is to search for a trend in the shape of the $E(B-V)$ distribution over a range of luminosities where we do have spectroscopic information. Any trend that exists may then extend to faint objects. We have plotted the inferred $E(B-V)$ distribution for $z \sim 2$ galaxies as a function of magnitude in Figure 6.8 and find no significant trend with magnitude. We also find no correlation between reddening and redshift and for all redshift bins considered, we find an excess of galaxies with $E(B-V) > 0.4$. This strongly suggests that the excess is not some artifact introduced by our completeness corrections (since, effectively, the BX/BM colors of a galaxy will be identified with a pair in redshift-$E(B-V)$ space), but is an underlying feature of $z \sim 2$ galaxies. Therefore, we assume that the $E(B-V)$ distribution is constant for the range of redshifts and optical magnitudes considered here (see § 6.5.4) for further discussion.

In general, as pointed out above, $E(B-V)$ as a reddening indicator becomes a meaningless quantity for the most dust-obscured galaxies where the standard extinction laws no longer apply and where the optical emission scales with SFR only in those regions of a galaxy where the attenuation factor is less than ~ 10. In addition to these dusty galaxies, relatively dust-free galaxies with no measurable current star formation are also expected to be faint in the rest-frame UV, and in these cases, $E(B-V)$ likely reflects intrinsic changes in the SEDs rather than the actual dust contents. We reconsider in § 6.5.4 those galaxies where $E(B-V)$ may not be an accurate proxy for the dust obscuration, but, as we show later, this does not change our finding that the average obscuration factor of $z \sim 2$ galaxies

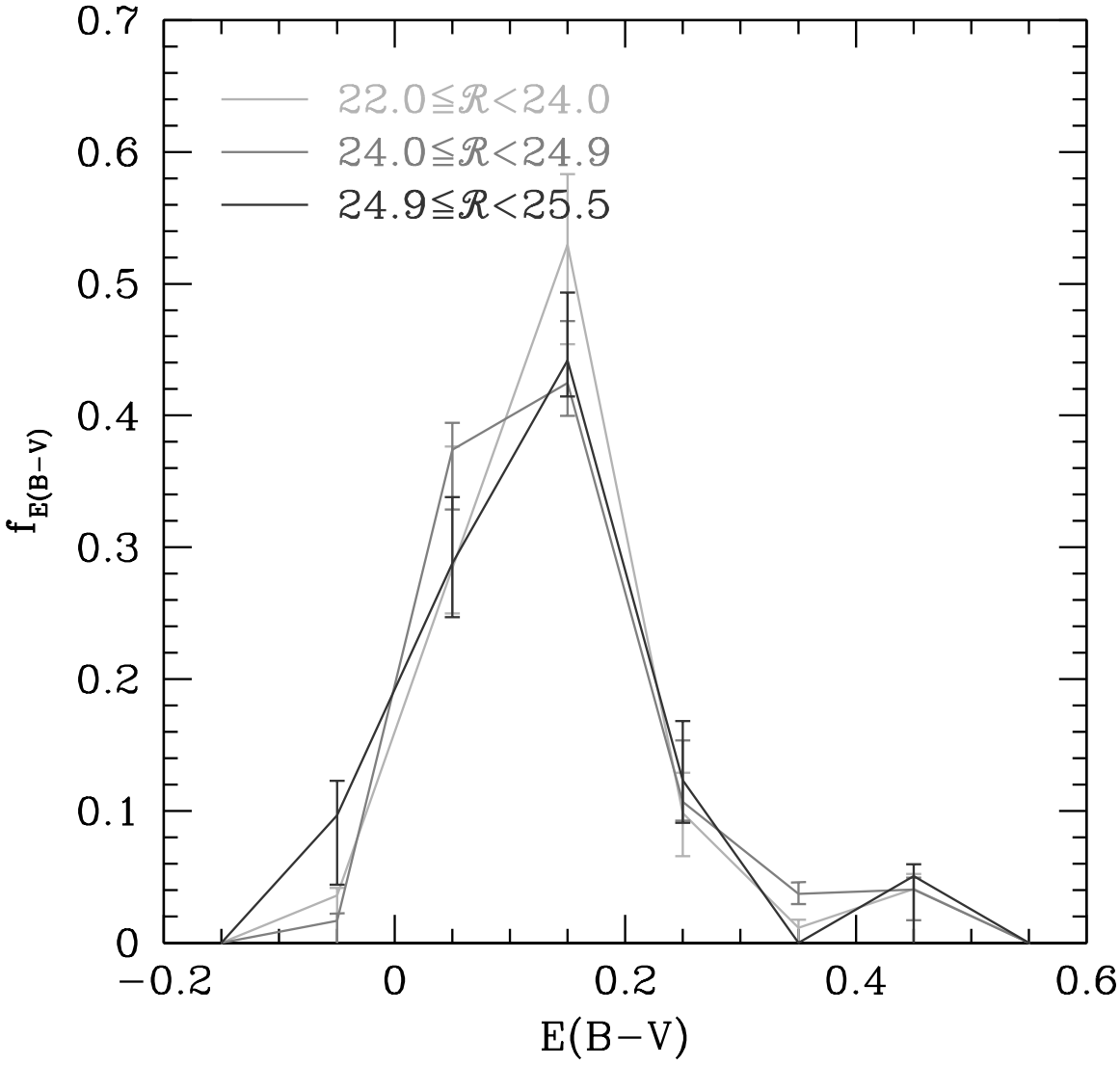

Figure 6.8 Inferred $E(B-V)$ distribution for three $\mathcal{R}$ magnitude bins. All three are generally similar within the error bars and we note that galaxies with a range of optical magnitude contribute to the excess of galaxies with $E(B-V) > 0.4$.

does not significantly change as a function of apparent magnitude, at least to $\mathcal{R} = 25.5$.

6.5 UV Luminosity Function

6.5.1 Preferred LF

The maximum-likelihood rest-frame 1500 Å luminosity function for $z \sim 2$ galaxies is shown in Figure 6.9. This LF was computed by using the entire photometric sample and holding the best-fit $E(B-V)$ distribution (as determined from the spectroscopic sample; Figure 6.7) fixed. The extension of the spectroscopically determined $E(B-V)$ distribution to the photometric sample is a reasonable approximation given the discussion of § 6.2.5 and § 6.4. By nature of the method used to compute the LF, the LF includes corrections for the systematic effects of photometric bias and Lyα perturbations. The error in the luminosity function reflects both Poisson counting statistics and field-to-field variations. We used the apparent magnitude at G-band to compute the LF at $z \sim 2$ in order to more closely correspond to the rest-frame wavelength, 1500 Å, of the $z \sim 3$ and $z \sim 4$ UV LFs from Steidel et al. (1999) and Adelberger & Steidel (2000), which are also shown in Figure 6.9 for comparison. Absolute magnitudes were computed using the standard relation

$$M_{1500} = m_{\rm G} - 5\log(d_{\rm L}/10\,{\rm pc}) + 2.5\log(1+z), \tag{6.6}$$

where M_{1500} is the absolute magnitude at rest-frame 1500 Å and $m_{\rm G}$ is the observed G-band magnitude. We have made the reasonable assumption that the K-correction is approximately zero for the average rest-UV SED of BX-selected galaxies after a star formation age of 100 Myr. By this point, the mix of O and B stars in the galaxy has stabilized and, for a Salpeter (1955) IMF, the SED is essentially flat across the observed BX/BM bands. The best-fit Schechter (1976) function and parameters for the $z \sim 2$ LF are also indicated. The uncertainties on the faint-end slope α, characteristic luminosity M^*, and characteristic number density ϕ^* are estimated by simulating many realizations of the LF as allowed by the errors, fitting a Schechter function to these realizations, and then determining the dispersion in measured values for α, M^*, and ϕ^* for these realizations.

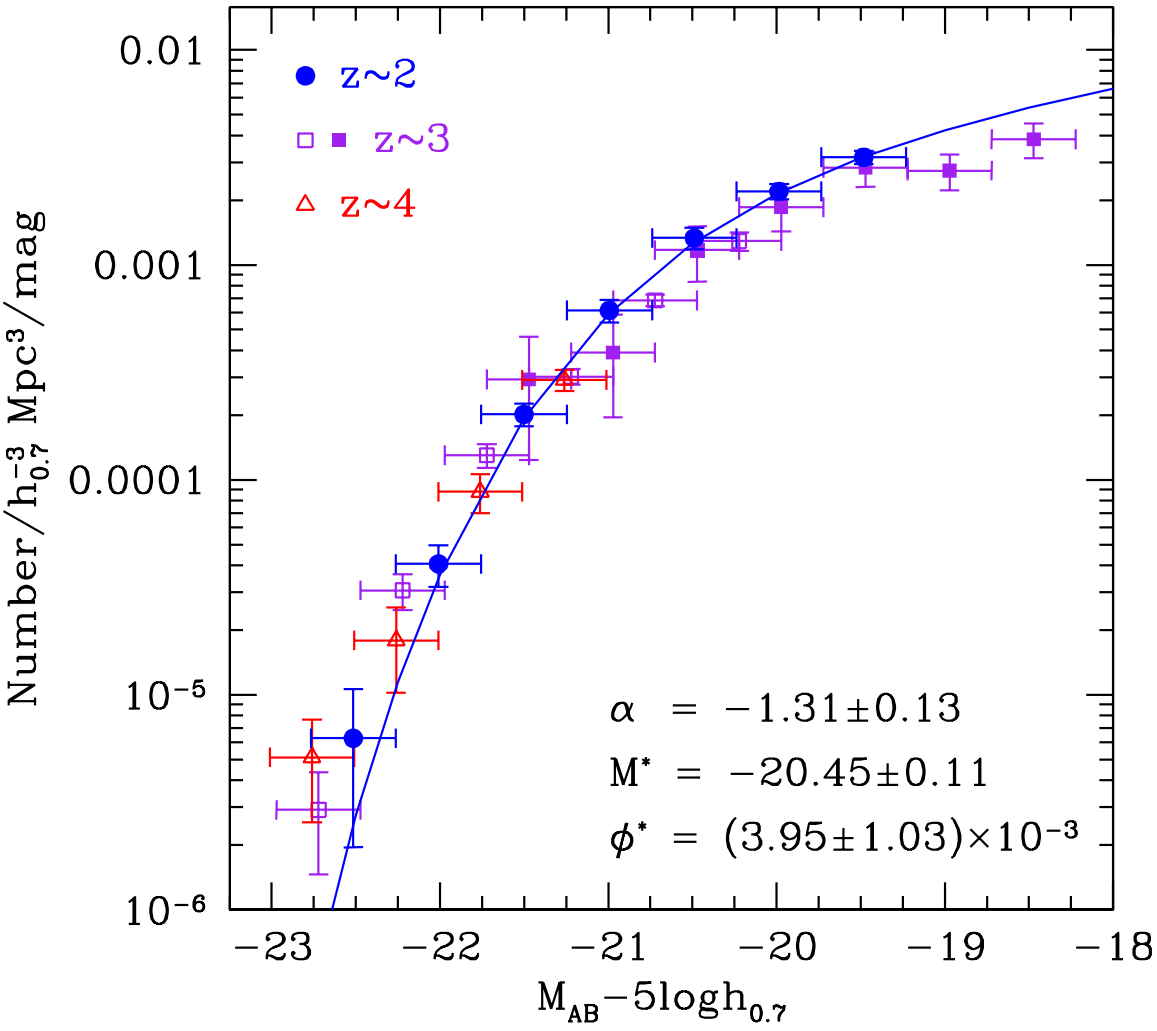

Figure 6.9 Rest-frame UV luminosity function at $z \sim 2$ (solid circles) compared with those of Steidel et al. (1999) and Adelberger & Steidel (2000) at $z \sim 3$ (squares) and $z \sim 4$ (triangles). All data have been recast with $h = 0.7$, $\Omega_\lambda = 0.7$, and $\Omega_{\rm m} = 0.3$. To match the rest-frame wavelength, the observed $G-$, $\mathcal{R}-$, and I-band fluxes were used to compute the luminosity function at $z \sim 2$, $z \sim 3$, and $z \sim 4$, respectively. The ground-based and HST data at $z \sim 3$ are indicated by empty and filled squares, respectively. The best-fit Schechter (1976) function for the $z \sim 2$ LF is indicated by the solid curve. No shift in normalization was used to make this plot.

6.5.2 Faint-End Slope, α

The faint-end slope (α) for $z \sim 2$ galaxies is somewhat shallower than that found for similarly selected galaxies (but including *HST* data at the faint-end) at $z \sim 3$ ($\alpha \sim -1.6$; Steidel et al. 1999; Adelberger & Steidel 2000), although the difference is not particularly significant given the covariance between α and M^* (Figure 6.10) and the fact that the spectroscopic samples considered here only probe about a magnitude below M^*. For example, forcing a steeper faint-end slope results in a brighter best-fit M^*. To illustrate this degeneracy further, Figure 6.11 shows our preferred fit to the $z \sim 2$ UV LF along with the fit if we assume the $z \sim 3$ best-fit LF (with $\alpha = -1.6$) shifted to $z \sim 2$. Despite the numerical differences in the best-fit parameters, the UV LFs at $z \sim 2$, $z \sim 3$, and $z \sim 4$ are in excellent agreement within the uncertainties for $-23 < M^* < -19$.

The spectroscopic sample allows us to accurately constrain the LF, taking into account sample completeness, interloper fraction, and line perturbations, for galaxies with $\mathcal{R} < 25.5$. It is below this limit that we consider our LF to be most robust, and Figure 6.9 indicates little evolution between $z \sim 2 - 4$ for $\mathcal{R} < 25.5$. The results for galaxies fainter than $\mathcal{R} = 25.5$ are less certain given that our determination of the $z \sim 2$ faint-end slope is based on galaxies that extend only ~ 2.5 times fainter than M^* for the $z \sim 2$ sample. The Steidel et al. (1999) analysis of the $z \sim 3$ LF included U-dropout galaxies in HDF-N where the redshift distribution was modeled using the color criteria of Dickinson (1998) and assuming the range of intrinsic spectral shapes of LBGs found by Adelberger & Steidel (2000). Based on the combined Keck spectroscopic and HDF-N U-dropout samples, Steidel et al. (1999) found a steep faint-end slope $\alpha = -1.60 \pm 0.13$. Subsequent studies based on fewer fields, but that go deeper, indicate a shallower slope around $\alpha \sim -1.4$ (Sawicki & Thompson 2005). However, in the absence of spectroscopic constraints on the selection function, these deeper studies must rely on uncertain assumptions regarding the reddening and redshift distribution of these fainter sources that may ultimately lead to systematic problems in accurately determining the faint-end slope. Nonetheless, deep photometric surveys have allowed us to probe a regime of the LF that was previously unexplored (Sawicki & Thompson 2005). For the remaining analysis, we will assume $\alpha = -1.6$ derived by Steidel et al. (1999) for the $z \sim 3$ LBG UV LF.

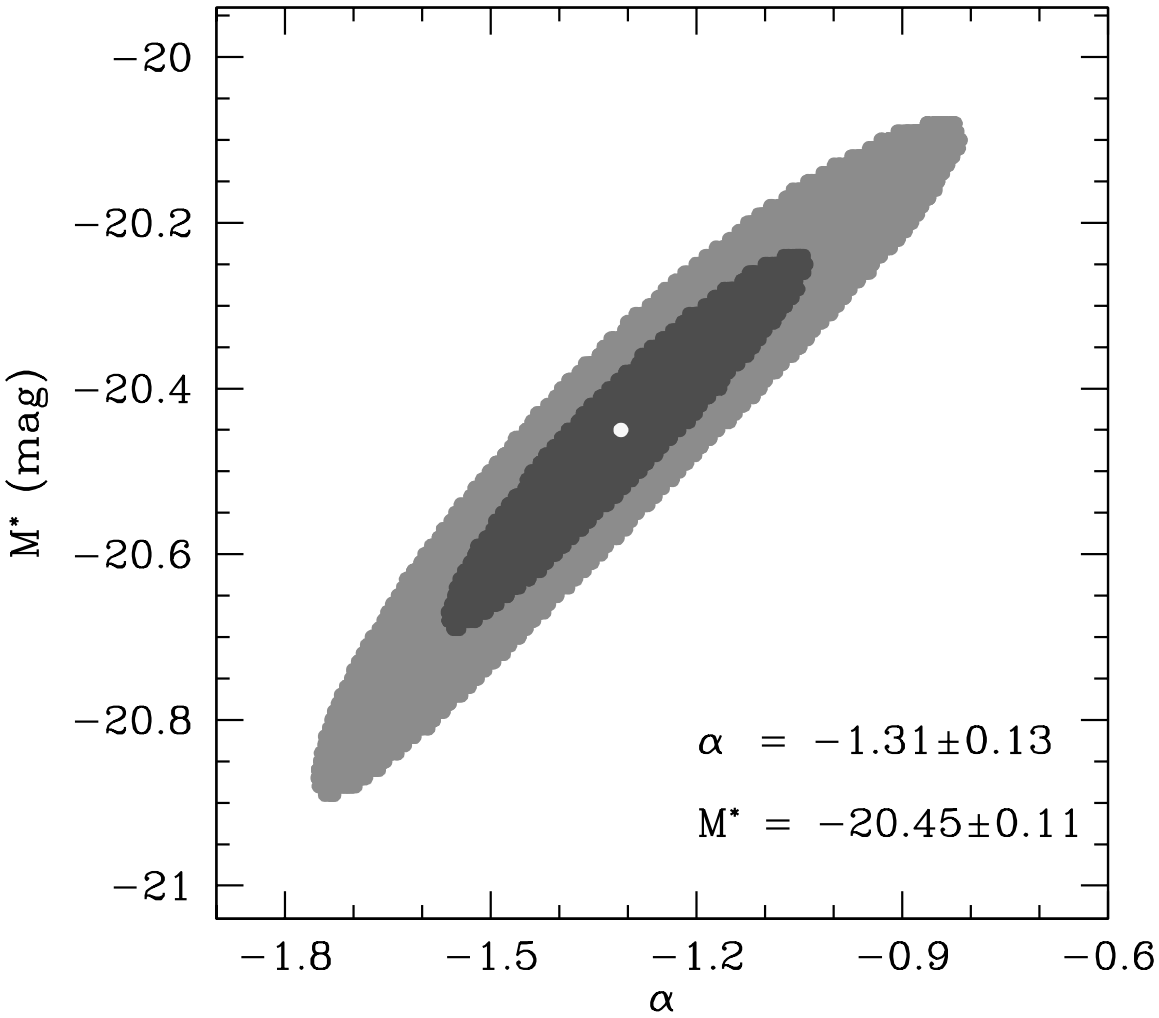

Figure 6.10 Covariance between best-fit faint-end slope (α) and M^*. The dark and light regions correspond to 68% and 95% confidence intervals, respectively, and the white point indicates our best-fit values. This plot was contructed by holding α and M^* fixed for each point and minimizing χ^2 with respect to ϕ^*.

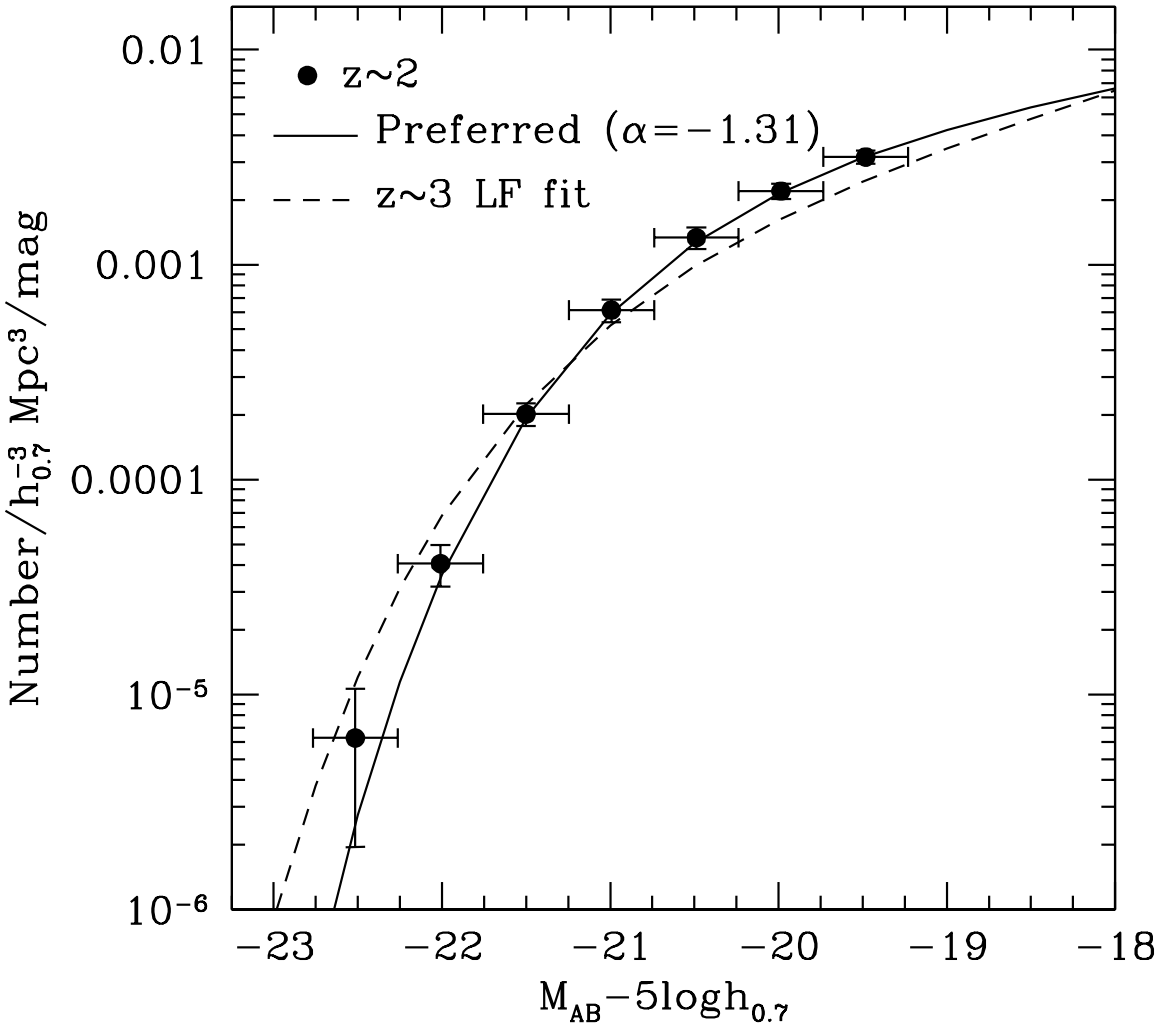

Figure 6.11 Illustration of the degeneracy between fitted Schechter (1976) parameters to the LF. Our preferred fit (solid curve) and the $z \sim 3$ fit (dashed curve) found by Adelberger & Steidel (2000), shifted to $z \sim 2$, are shown on top of the points at $z \sim 2$.

6.5.3 Field-to-Field Variations

Access to multiple uncorrelated fields allows us to judge the effects of large scale structure on the derived LF. The dispersion in normalization between the luminosity functions derived in individual fields is a strong function of $\mathcal{R}$, as shown in Figure 6.12. The fractional dispersion in normalization is much larger at the bright end for $\mathcal{R} < 22.5$ and decreases significantly for galaxies with fainter magnitudes. This trend is likely due to statistical fluctuations at the bright end due to the smaller number of sources and/or the fact that the clustering correlation function is a strong function of magnitude. We further note that at least four of the seven fields show significant redshift-space overdensities (e.g., HS1700 field; Steidel et al. 2005). The effect of such overdensities on the derived LF will of course depend on the redshift of the overdensities with respect to the BX selection function. An overdensity at $z = 2.8$ is unlikely to affect the derived LF to the same extent as an overdensity at $z = 2.3$ (placing it in the middle of the BX selection function). One option when working in single fields is to use the available spectroscopy and known selection function to model the effects of such overdensities on the derived LFs, or use Monte Carlo simulations to estimate uncertainties in the normalization of the derived LF (Bouwens et al. 2006). Because our analysis is done is seven uncorrelated fields spread throughout the sky, we assume that the average LF is representative of $z \sim 2$ galaxies. Any remaining uncertainty in normalization of the average LF is added in quadrature with Poisson counting error to determine the total error bars shown in Figure 6.9. We remind the reader that the *systematic* effects of photometric bias and Lyα perturbations are already reflected in the derived LF.

6.5.4 Bolometric Measures of the Luminosity Function

After accounting for the various systematic and random effects discussed above, we must finally correct the LF for the attenuation of UV emission by dust. Before the advent of panchromatic galaxy surveys, it was common to simply apply an average correction for extinction, typically a factor of $4 - 5$ (Steidel et al. 1999). Subsequently, extensive multi-wavelength data have placed our extinction corrections on a much more solid footing. For instance, initial X-ray and radio stacking analyses (e.g., Nandra et al. 2002; Reddy & Steidel 2004) indicated that high redshift UV-selected populations with $\mathcal{R} < 25.5$ have average obscuration factors ($L_{\rm IR}/L_{\rm UV}$) around $4 - 5$ (supporting the average correction

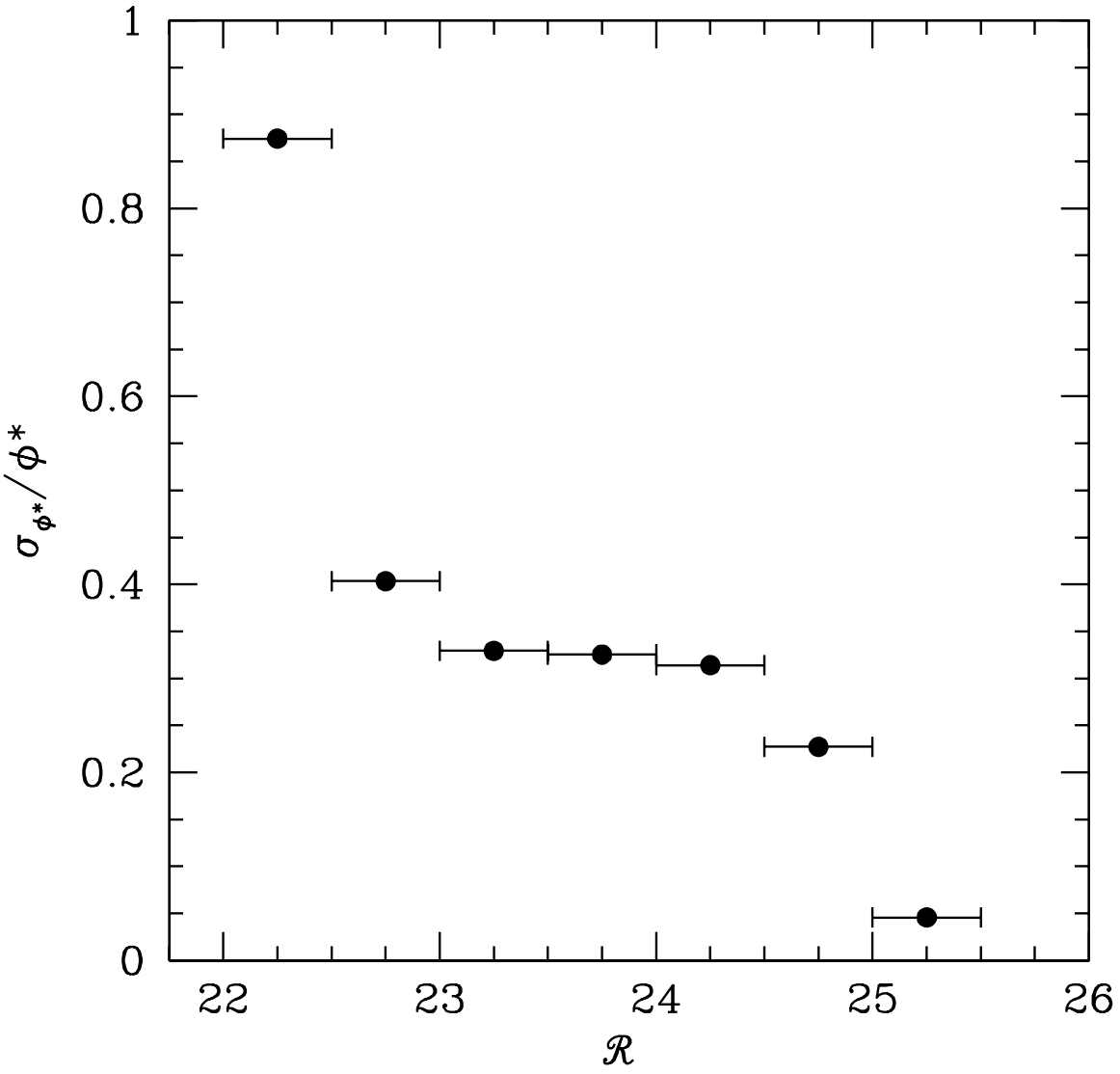

Figure 6.12 Fractional dispersion in normalization of the UV LF as a function of apparent magnitude.

advocated by Steidel et al. (1999)). Further progress was made by taking advantage of the unique sensitivity of the *Spitzer* MIPS instrument, allowing us to directly detect for the first time the dust emission from M^* galaxies at $z \gtrsim 1.5$ (Reddy et al. 2006b). The Reddy et al. (2006b) analysis confirmed the *average* trends established by previous X-ray stacking studies, and further demonstrated that moderate luminosity galaxies ($10^{11} \lesssim L_{\rm bol} \lesssim 10^{12.3}$) at $z \sim 2$ follow the Meurer et al. (1999) attenuation law found for local UV-selected starburst galaxies. The importance of this analysis for the present study is that we can directly relate the $E(B-V)$ distribution of most $z \sim 2$ galaxies (§ 6.4) with the their distribution in obscuration, $L_{\rm IR}/L_{\rm UV}$.

Of course, in order to accurately constrain the average extinction correction, we must consider the dust obscuration factors of galaxies that do not follow the Meurer et al. (1999) and Calzetti et al. (2000) laws. We must also consider the possibility that the average extinction correction changes with apparent magnitude. In § 6.4 and Figure 6.8, the simulations demonstrate that the $E(B-V)$ distribution is relatively constant as a function of apparent magnitude. To consider the possible effects of galaxies where $E(B-V)$ does not correlate with obscuration, we relied on our intepretation of the *Spitzer* MIPS data for a sample of BX-selected galaxies in the GOODS-N field; these data give us an independent probe of the dust emission in $z \sim 2$ galaxies. Figure 6.13 shows the dust-obscuration factors, parameterized as $L_{\rm bol}$, where $L_{\rm bol} \equiv L_{\rm IR} + L_{\rm UV}$, as a function of observed optical magnitude, from the MIPS analysis of Reddy et al. (2006b). The red points indicate BX/BM-selected objects, most of which are BX galaxies, detected at 24 μm, and the large pentagon and crosses denote the average stack and distribution in $\mathcal{R}$ magnitude, respectively, for galaxies undetected at 24 μm. While there is some evidence that the *dispersion* in attenuation factor increases towards fainter magnitudes, as would be expected if optically faint galaxies have contributions from both heavily dust-obscured objects as well as those with intrinsically low star formation rates, the results of Figure 6.13 suggest that the *average* extinction correction is approximately constant over the range in $\mathcal{R}$ magnitude considered here.[3] The results confirm the trends noted by Adelberger & Steidel (2000), who used local templates to deduce that the observed UV luminosities of galaxies at redshifts $z = 0$, $z \sim 1$, and $z \sim 3$,

[3]We note that Reddy et al. (2006b) excluded objects from their analysis which were directly detected in the *Chandra* 2 Ms data in the GOODS-N field (Alexander et al. 2003) of which almost all are AGN.

are insensitive to dust obscuration, $L_{\rm bol}/L_{\rm UV}$ (e.g., Figure 17 of Adelberger & Steidel 2000). We have confirmed this trend explicitly at redshifts $1.5 \lesssim z \lesssim 2.6$.

The MIPS analysis of Reddy et al. (2006b) indicates that 65% of BX/BM-selected galaxies are detected to $f_{24\mu{\rm m}} = 8$ μJy (3 σ). Therefore, weighting the mean obscuration factor of 24 μm detected and undetected galaxies by 0.65 and 0.35, respectively, we deduce a mean extinction ($L_{\rm bol}/L_{\rm UV}$) of BX-selected galaxies of ≈ 4.5 to $\mathcal{R} = 25.5$. The average is in excellent agreement with the values obtained from stacked X-ray and radio estimates (e.g., Nandra et al. 2002; Reddy & Steidel 2004) and in accordance with the value advocated by Steidel et al. (1999) for UV-selected samples, at least for $z \lesssim 3 - 4$, to $\mathcal{R} = 25.5$.[4] We will assume the average extinction correction of ≈ 4.5 when correcting the observed UV luminosities to total bolometric luminosities.

6.6 Discussion

6.6.1 Evolution in the Luminosity Function

The most obvious result of Figure 6.9 is that the rest-frame UV LF shows little evolution from $z \sim 3$ to $z \sim 2$ to within the errors over all magnitudes $\mathcal{R} < 25.5$; the number density of galaxies in bins of absolute magnitude appears to be constant over the ~ 800 Myr timespan between $z = 3$ and $z = 2.2$. As our method of constraining the reddening and luminosity distributions take into account a number of systematic effects (e.g., contamination fraction particularly at the bright end of the LF, photometric bias and errors, Lyα line perturbations to the observed colors) that were not considered in previous analyses (Gabasch et al. 2004; Le Fèvre et al. 2005) or only partially considered (Sawicki & Thompson 2005; Steidel et al. 1999; Adelberger & Steidel 2000), we regard our UV LF as the most robust determination at $z \sim 2$ to $\mathcal{R} = 25.5$.

We remind the reader that the luminosity function is calculated by first constraining the intrinsic reddening distribution, and systematic differences in the reddening distributions at $z \sim 2$ and $z \sim 3$ may underly any differences we expect to see in the luminosity function. Figure 6.14 compares our inferred $z \sim 2$ reddening distribution (solid line) with those

[4]There is some indication that rest-UV-selected samples at even higher redshifts $z \gtrsim 5 - 6$ have lower average attenuation factors than at $z \sim 3$, in keeping with the scenario that higher redshift sources have lower extinction (Bouwens et al. 2006).

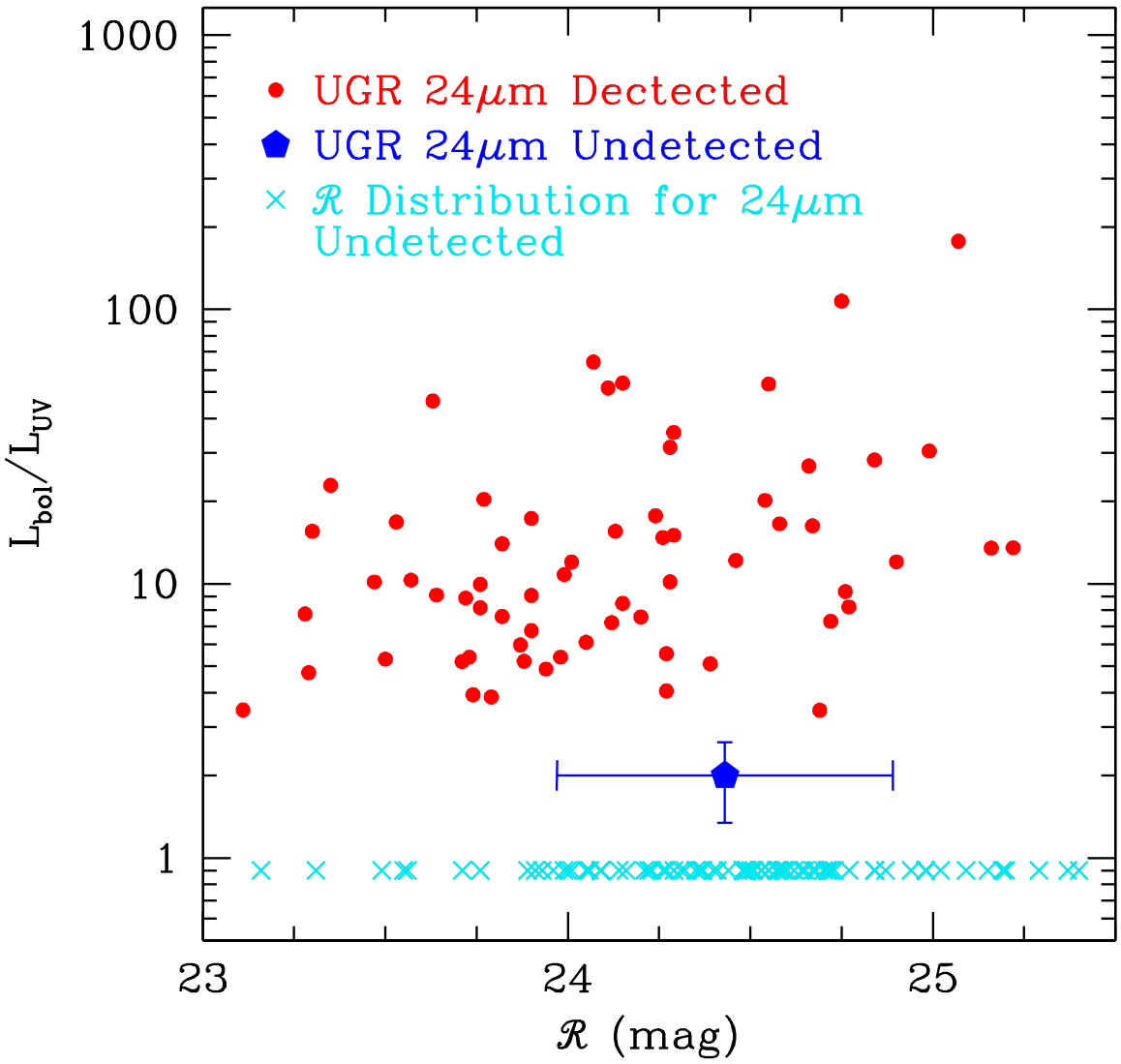

Figure 6.13 Distribution of attenuation factors, parameterized as $L_{\rm bol}/L_{\rm UV}$, as inferred from *Spitzer* MIPS data, as a function of apparent optical magnitude $\mathcal{R}$ for BX/BM-selected galaxies with redshifts $1.5 \lesssim z \lesssim 2.6$. Also indicated is the stacked average for 48 galaxies undetected at 24 μm (large pentagon) and the distribution in $\mathcal{R}$ magnitude for a larger sample of 73 galaxies undetected at 24 μm.

computed at $z \sim 3$ after treating photometric errors and completeness (dotted line) and Lyα perturbations to the $G - \mathcal{R}$ colors (dashed line). As noted earlier, we believe the small difference in the number of red sources, $E(B-V) > 0.3$, between the $z \sim 2$ and $z \sim 3$ distributions to be real, but qualitatively the distributions are quite similar over a large range of $E(B-V)$, and neither show significant differences as a function of optical magnitude to $\mathcal{R} = 25.5$ (e.g., see also Adelberger 2002). These results demonstrate that the differences in reddening distributions at $z \sim 2$ and $z \sim 3$ are not conspiring to make their LFs appear equal.

Note that this lack of evolution in the LF does not specifically address how a galaxy of a particular luminosity will evolve. For example, the lack of evolution at the bright end ($M_{1600} < -22$) of the luminosity function does not imply that there is a stagnant population of UV-bright galaxies that is unevolving. Rather, if galaxies follow an exponentially declining star formation history, then UV-bright galaxies at $z \sim 3$ are very likely to become fainter in the UV by $z \sim 2$ (but not necessarily absent from the $z \sim 2$ sample). A precipitously declining star formation history may imply that some UV-bright galaxies at $z \sim 3$ will be too faint to be included in UV-selected samples at $z \sim 2$. In any case, it is clear that if there is indeed a lack of evolution at the bright-end of the luminosity function, then whichever UV-bright galaxies fall out of UV-selected samples by $z \sim 2$ must be made up in number by younger galaxies, those that are merging and just "turning on", and/or those that are caught in an active phase of star formation at $z \sim 2$. The net effect is that the number density of galaxies with ($M_{1600} < -22$) remains essentially constant. Formally, and keeping in mind the degeneracy between α and M^*, we find that M^* fades by 0.53 ± 0.26 mag from $z \sim 3$ to $z \sim 2$.

Similar to our inferences regarding the bright end of the LF, we also find little evolution in the number density of moderate luminosity galaxies (around M^*) between $z \sim 3$ and $z \sim 2$, within the errors, regardless of the evolutionary tracks of individual galaxies between these epochs. Again, a number of effects may come into play. $M^*_{z=3}$ galaxies at $z \sim 3$ may either fade above $M^*_{z=2}$ as $z \sim 2$ while at the same time $> M^*_{z=3}$ galaxies at $z \sim 3$ may merge to form $M^*_{z=2}$ or brighter than $M^*_{z=2}$ galaxies at $z \sim 2$. The lack of evolution across the entire magnitude range considered here indicates that these competing effects essentially cancel each other out such that the number of galaxies at any given luminosity

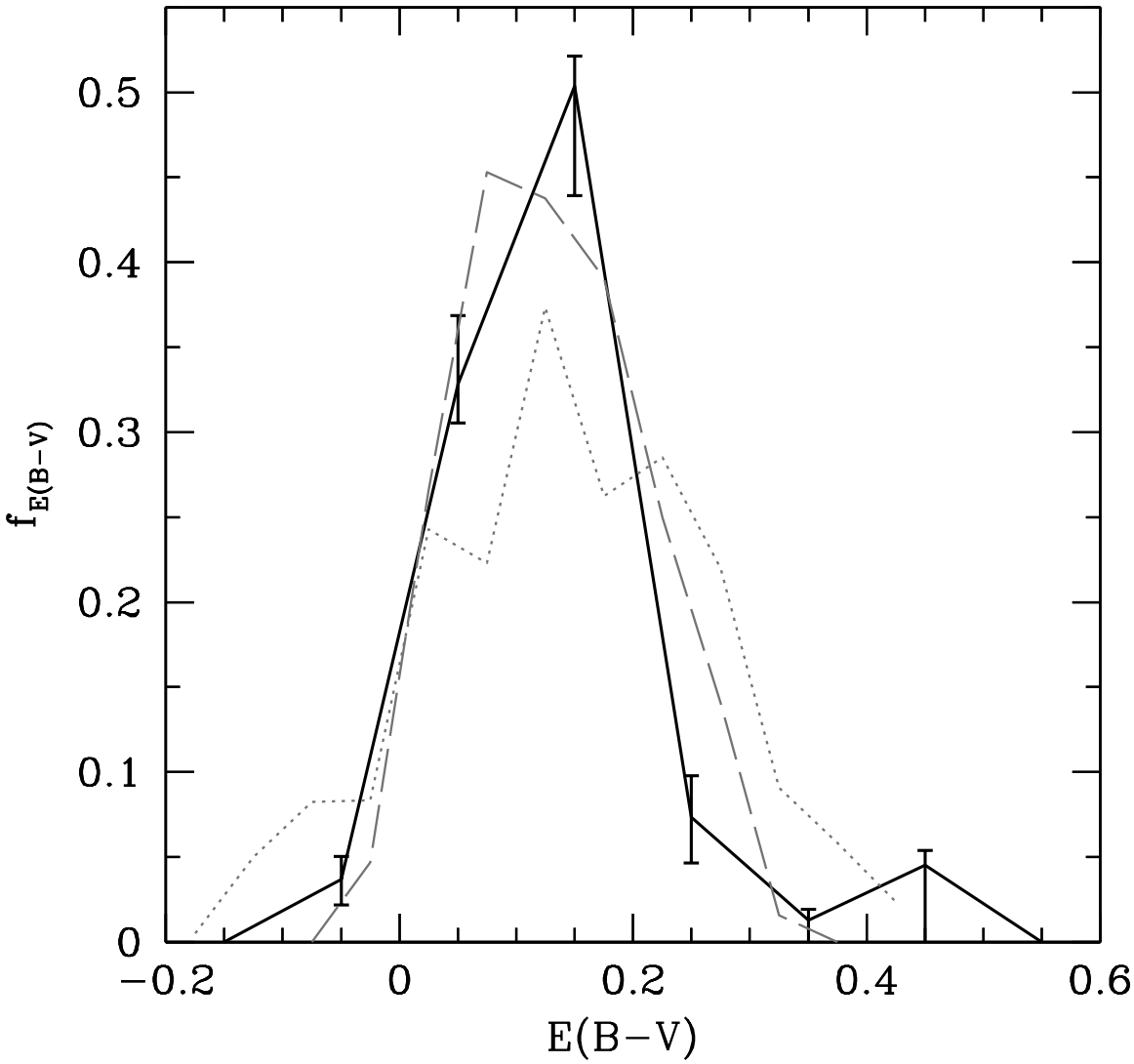

Figure 6.14 Comparison of the $z \sim 2$ $E(B-V)$ distribution (solid black curve) and those at $z \sim 3$: the dotted and dashed lines are from Figure 12 of Adelberger & Steidel (2000) and represent the inferred distribution after correcting only for photometric errors and completeness and the inferred distribution after correcting only for Lyα perturbations to the $G - \mathcal{R}$ colors, respectively.

remains essentially constant. We briefly note that an analysis of *photometric* candidates (selected in exactly the same way) to $\mathcal{R} = 27$ by Sawicki & Thompson (2005) indicates a steepening of the faint-end slope with cosmic time from $z \sim 4$ to $z \sim 3$ and no evolution at the bright end. On the other hand, Ouchi et al. 2004 find evolution at the bright end and no change at the faint end. We do not discuss these results any further, but note that deep spectroscopy, combined with multi-wavelength stacking analyses, should help constrain the redshift distribution and dust properties of optically-selected but faint ($\mathcal{R} > 25.5$) galaxies. The robust result from our analysis is that the UV luminosity function of galaxies brighter than $M_{\rm AB} \approx -19$ is essentially identical between redshifts $z \sim 2 - 3$. Furthermore, the bright end of the UV LF at $z \sim 4$ ($M_{\rm AB} \lesssim -21$) is identical to the $z \sim 2 - 3$ UV LFs over the same range of intrinsic luminosities.

We note that while the LFs at $z \sim 2$, $z \sim 3$, and $z \sim 4$ are consistent with each other within the errors, we do find small systematic effects. First, there may be an evolution at the bright end such that the number density of luminous ($M < -22.5$) galaxies decreases from $z \sim 4 - 3$ to $z \sim 2$ (as can be seen more clearly in Figure 6.11). Quantifying this possible evolution is difficult since the number statistics at the bright end are poor (i.e., Poisson errors dominate) and the Schechter function may not provide a good fit for these brighter sources. In the latter case, a double power-law may be more appropriate. Second, the number density of moderate luminosity galaxies ($-21 \lesssim M \lesssim -19$) is systematically larger than what is observed at $z \sim 3$ for the same range of intrinsic luminosity (Figure 6.11). As we show below, it is the moderate luminosity sources which contribute most signficantly to the UV luminosity density.

6.6.2 Evolution in the Luminosity Density

In order to compute the comoving luminosity density, we first converted our UV LF from AB magnitudes to luminosity using the relationship

$$L_\nu = \frac{4\pi d_{\rm L}^2}{(1+z)} 10^{-0.4(48.60+m_{\rm AB})}, \tag{6.7}$$

where $d_{\rm L}$ is the luminosity distance corresponding to redshift z, and we have assumed the average redshift for the BX sample of $\langle z \rangle = 2.2 \pm 0.3$. This conversion indicates $L_\nu^* =$

$(6.58 \pm 0.92) \times 10^{28}$ ergs s^{-1} Hz^{-1}, corresponding to an *unobscured* star formation rate of $\approx 9\ M_{\odot}$ yr^{-1} assuming the Madau et al. (1998) conversion for a Salpeter (1955) IMF between 0.1 and 100 M$_{\odot}$ (Kennicutt 1998a). Assuming a mean dust-obscuration factor of $\langle L_{\rm bol}/L_{\rm UV}\rangle \approx 4.5$ implies that L^* galaxies at $z \sim 2$ have a total mean SFR of $\approx 41\ M_{\odot}$ yr^{-1}. This value of the bolometric SFR corresponds to a galaxy with total infrared luminosity of $\approx 2.4 \times 10^{11}$ L$_{\odot}$ using the calibration of Kennicutt (1998a), and is roughly equal to the mean inferred infrared luminosity of $\simeq 2 \times 10^{11}$ L$_{\odot}$ (Reddy et al. 2006b) for $\mathcal{R} < 25.5$ BX/BM-selected galaxies with redshifts $1.5 \lesssim z \lesssim 2.6$. In other words, BX selection allows one to cull a large sample of galaxies whose luminosities are representative of the typical luminosity of $z \sim 2$ galaxies.

To facilitate comparison with previous work, we compute the UV luminosity density by integrating the LFs at various redshifts down to $0.1L^*_{z=3}$, where $L^*_{z=3} \approx 1.10 \times 10^{29}$ ergs s^{-1} Hz^{-1}. Figure 3.20 shows a compilation of a few estimates of the SFRD, assuming a Salpter IMF in converting UV luminosity density to SFRD, where all points have been recast using the same cosmology. Our value of the SFRD at $z \sim 2.2$ is $0.034 \pm 0.004\ M_{\odot}$ yr^{-1} Mpc^{-3} uncorrected for extinction and $0.153 \pm 0.018\ M_{\odot}$ yr^{-1} Mpc^{-3} after applying a factor of 4.5 extinction correction, as discussed above. The value of $0.034\ M_{\odot}$ yr^{-1} Mpc^{-3} we obtain at $z \sim 2$ is slightly larger (by a factor of ~ 1.2) than the value at $z \sim 3$ when integrating to $0.1L^*_{z=3}$. The reason for this modest increase in SFRD between $z \sim 3$ and $z \sim 2$ is the excess of moderate luminosity galaxies observed at $z \sim 2$, as noted above. Our results indicate a peak in the SFRD at $z \sim 2.2$, followed by a slow decline for $z \gtrsim 4$. If the average extinction correction changes as function of redshift, the decline at epochs earlier than $z \sim 4$ may be more precipitous than shown in Figure 3.20. In particular, Bouwens et al. (2006) find evidence that the average extinction factor appropriate for *I*-dropout galaxies at $z \sim 6$ may be a factor of 3 times lower than at $z \sim 3$ (based on the average rest-frame UV colors of the two populations), suggesting that the SFRD may evolve more rapidly between $z = 6$ and $z = 3$. What is clear is that some process must have been involved in turning around the "upsizing" in SFRD from $z = 6$ to $z = 2$, and possible explanations for the observed evolution include feedback from supernovae and/or AGN (e.g., Hopkins et al. 2005; Scannapieco et al. 2005).

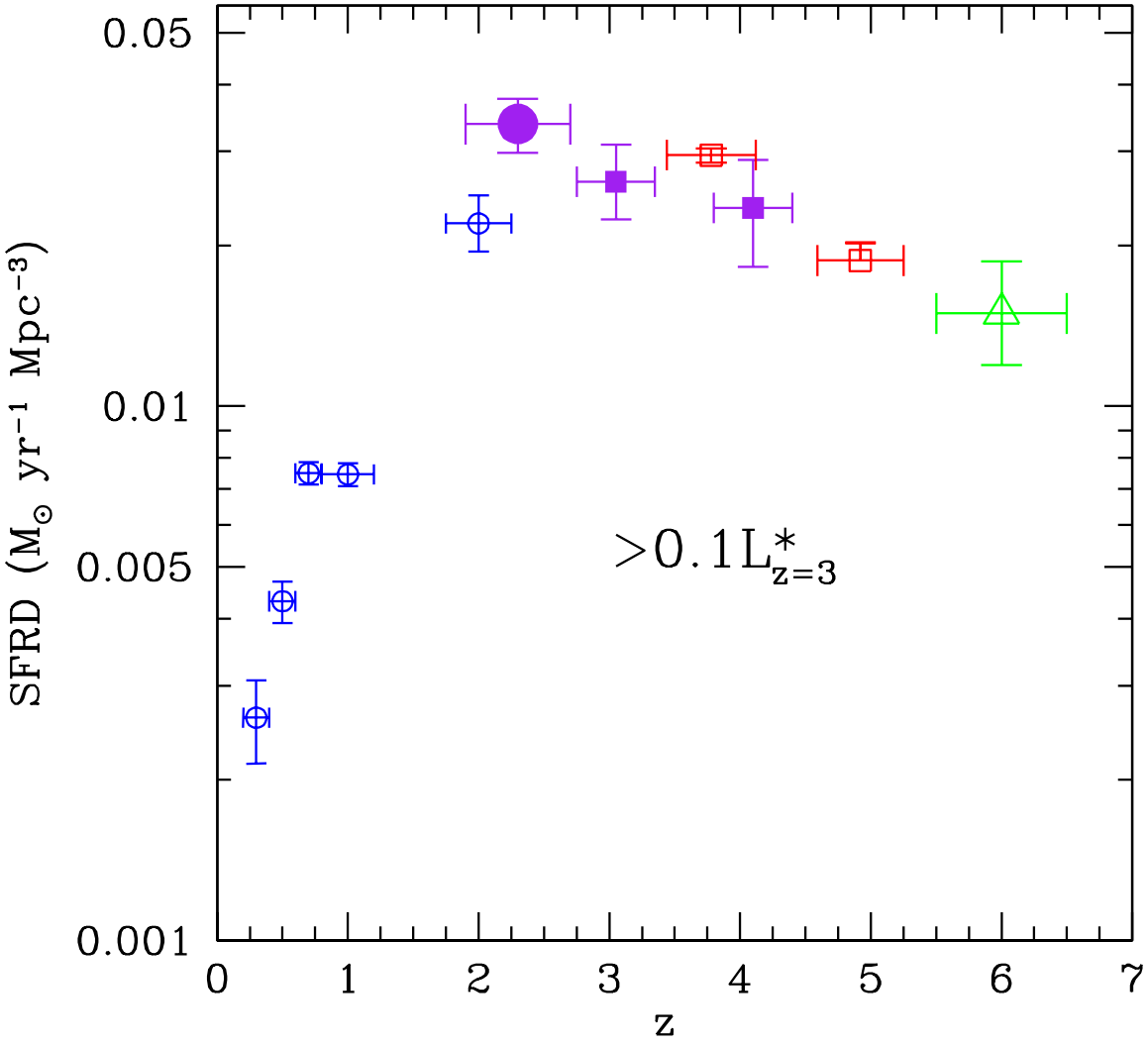

Figure 6.15 Cosmic star formation history integrated to $0.1L^*_{z=3}$, uncorrected for extinction and assuming a Salpeter IMF, derived from various UV-selected samples. The result from this work is shown by the large filled circle. For comparison, we show points from Schiminovich et al. (2005) (blue open squares), Steidel et al. (1999) (filled squares), Giavalisco et al. (2004a) (red open squares), and Bouwens et al. (2006) (triangle).

6.7 Conclusions

We have used rest-frame UV color selection, combined with spectroscopy, to evaluate the UV luminosity function (LF) and star formation rate density (SFRD) at $z \sim 2$. Our sample includes 8190 photometric candidates in seven independent fields, and spectroscopic redshifts for 830 galaxies with $z > 1$. The large spectroscopic sample allows us to very accurately quantify the foreground contamination rate and reddening distributions of galaxies in our sample. We use Monte Carlo simulations to assess the effects of photometric scatter and Lyα line perturbations to the observed BX/BM colors of galaxies. The resulting incompleteness estimates for our sample are used to reconstruct the intrinsic UV LF at $z \sim 2$, the results of which indicate little evolution in the UV LF from $z \sim 4$ to $z \sim 2$ (to $\mathcal{R} = 25.5$). Integrating the luminosity function and assuming a Salpeter IMF, we compute an SFRD (to $0.1L^*_{z=3}$) of 0.034 ± 0.004 $M_\odot$ yr^{-1} Mpc^{-3} at $z = 2.2$ (uncorrected for extinction), suggesting a modest decline in the SFRD of a factor of 1.2 assuming a constant extinction correction from $z \sim 4$ to $z \sim 2$.

We thank the staff of the Keck Observatory for their help in obtaining the data presented here. The work presented here has been supported by grant AST 03-07263 from the National Science Foundation and by the David and Lucile Packard Foundation.

Table 6.1. Survey Fields

Field Name	α[a] (J2000.0)	δ[b] (J2000.0)	Field Size (arcmin^2)	$N_{\rm cand}$[c]	$N_{z>1}$[d]
GOODS-N	12 36 51	+62 13 14	154	909	158
Q1307	13 07 45	+29 12 51	259	1763	68
Westphal	14 17 43	+52 28 49	227	612	59
Q1623	16 25 45	+26 47 23	290	1347	247
Q1700	17 01 01	+64 11 58	232	1472	79
Q2343	23 46 05	+12 49 12	216	1018	172
Q2346	23 48 23	+00 27 15	280	1069	47

[a]Right ascension in hours, minutes, and seconds

[b]Declination in degrees, arcminutes, and arcseconds

[c]Number of BX candidates

[d]Number of spectroscopically confirmed BX candidates with $z > 1$

Table 6.2. Interloper Contribution

$\mathcal{R}$	$N_{z\geq 0}$[a]	$N_{0\leq z<1}$[b]	Interloper Fraction
$19.0 - 22.0$	53	45	0.85
$22.0 - 22.5$	18	16	0.89
$22.5 - 23.0$	34	23	0.68
$23.0 - 23.5$	113	35	0.31
$23.5 - 24.0$	195	30	0.15
$24.0 - 24.5$	280	14	0.05
$24.5 - 25.0$	198	9	0.05
$25.0 - 25.5$	112	2	0.02

[a]Number of sources with redshifts

[b]Number of sources with $z < 1$

Chapter 7

Epilogue

We have made significant progress in understanding the overlap between samples selected at $z \sim 2$, the extinction properties of galaxies in these samples, and the mutual contribution of these galaxies to the total star formation rate density (SFRD) at $z \sim 2$. We have also demonstrated how Monte Carlo simulations can be used to quantify the systematic effects that plague color-selected samples of high redshift galaxies, and how the corrections they yield can be used to reconstruct galaxy populations at high redshifts. Despite these advancements, there are a number of issues that remain unresolved but are critical toward our understanding of the star formation history and buildup of stellar mass in the universe.

First, our knowledge of the properties of optically faint galaxies with $\mathcal{R} > 25.5$ is still relatively sparse, even though they may contribute significantly to the total SFRD depending on the faint-end slope of the observed UV luminosity function of the population. While we know from observations that such galaxies are either very dust-obscured or are faint simply because they have intrinsically low star formation rates, following up such objects with optical spectroscopy is difficult due to their faintness. In some cases, spectroscopy of very dusty galaxies can be aided by spectroscopically targeting their radio counterparts (Chapman et al. 2005), but this often comes at the price of a much more complicated redshift selection function. Ideally, we would like to be able to quantify the redshift distribution of $\mathcal{R} > 25.5$ galaxies selected in exactly the same way as $\mathcal{R} < 25.5$ galaxies where the redshift selection function is already known very precisely. Progress on this front will likely come slowly as larger than 10 m telescopes come online, allowing for optical spectroscopy of large numbers of $\mathcal{R} \sim 26.5 - 27.5$ galaxies in short integration times. In the meantime, we can rely on improvements such as the atmospheric dispersion corrector (ADC), slated

for installation on Keck I in Fall 2006, to allow us to integrate in a single field for extended periods of time without causing slit losses due to atmospheric dispersion.

Another ingredient required to assess the bolometric contribution of $\mathcal{R} > 25.5$ galaxies to the SFRD is their average extinction correction, i.e., the correction required to recover a bolometric luminosity from an observed UV luminosity. When assessing the total SFRD, it is common to integrate the luminosity function well past the point to which we have quantified the average extinction of galaxies, and an important question is whether the extinction correction we derive for galaxies with $\mathcal{R} < 25.5$ can be applied to galaxies with $\mathcal{R} > 25.5$. This uncertainty may dominate the systematic error in any determination of the SFRD if in fact $\mathcal{R} > 25.5$ galaxies contribute significantly to the SFRD. The average extinction factor may be higher if the SFRD contributed by $\mathcal{R} < 25.5$ objects is dominated by dust-obscured galaxies, or it may be lower if the SFRD is dominated by more numerous galaxies with intrinsically low star formation rates. Multi-wavelength stacking analyses, including stacking the rest-frame UV spectra of spectroscopically confirmed galaxies with $\mathcal{R} > 25.5$, will help address the average extinction properties and stellar populations of these optically faint galaxies.

Finally, we noted in Chapter 6 that evolution in the luminosity function (or lack thereof) does not specifically address how a galaxy of a particular luminosity will evolve. For example, while having a large number of fields certainly helps to average out cosmic variance that would otherwise influence effective volume estimates, it is clear that galaxies evolve differently depending on their large-scale environment. We have identified cluster-scale overdensities in several of our $z \sim 2$ survey fields, and detailed spectral synthesis modeling of galaxies in one of these fields indicates that galaxies within overdensities are on average twice as old and have stellar masses twice as large as galaxies in the surrounding "low-density" environment (we note that even the optically bright galaxies in "low-density" environments will likely end up in rich clusters by $z = 0$; Steidel et al. 2005). These differences in age and stellar mass are expected if the sites of earliest galaxy formation occurred in the progenitors of today's rich clusters where galaxy-scale matter fluctuations crossed the threshold for collapse significantly earlier than in lower density regions.

The mechanisms that act to supress star formation in virialized clusters (e.g., harassment, tidal stripping) are not expected to be present in non-virialized proto-clusters at high

redshift. Yet, we already find significant differences in the stellar populations of galaxies as a function of environment at $z = 2.3$, well before these star formation suppression mechanisms are established. We might expect the older and more massive proto-cluster galaxies to have exhausted their gas supply more quickly, and to have settled to a quiescent stage of star formation earlier, than field galaxies at similar redshifts. However, a different scenario is suggested by the observed increase in frequency of IR luminous starbursts in clusters as a function of redshift (Duc et al. 2004), in addition to clustering results which indicate that submillimeter galaxies at $z \sim 2-2.5$ typically reside in overdense regions (Blain et al. 2004). These high redshift results suggest that the low velocity dispersion and high volume density of (gas-rich) massive galaxies in overdensities make proto-clusters ideal environments for merger-induced star formation activity.

One of our future goals is to extend the use of MIPS data as a star formation rate indicator for $z \sim 2$ galaxies (e.g., Chapter 4) to examine the bolometric star formation rates, and combined with stellar mass estimates, the specific star formation rates, of galaxies as a function of large-scale environment. These analyses should convincingly tell us if unvirialized proto-clusters are conducive to star formation and/or undergo a different star formation history than high redshift galaxies in lower density regions. Ultimately, our combined analyses of the census of galaxies at high redshift, their contribution to the star formation rate density, and tracking the evolution of individual galaxies as a function of large scale environment will help to further our understanding of the star formation and stellar mass history of the Universe.

Bibliography

Abraham, R. G., Glazebrook, K., McCarthy, P. J., Crampton, D., Murowinski, R., Jørgensen, I., Roth, K., Hook, I. M., Savaglio, S., Chen, H., Marzke, R. O., & Carlberg, R. G. 2004, AJ, 127, 2455

Adelberger, K. L. 2002, PhD thesis, California Institute of Technology

Adelberger, K. L., Erb, D. K., Steidel, C. C., Reddy, N. A., Pettini, M., & Shapley, A. E. 2005a, ApJ, 620, L75

Adelberger, K. L., Shapley, A. E., Steidel, C. C., Pettini, M., Erb, D. K., & Reddy, N. A. 2005b, ApJ, 629, 636

Adelberger, K. L. & Steidel, C. C. 2000, ApJ, 544, 218

Adelberger, K. L., Steidel, C. C., Shapley, A. E., Hunt, M. P., Erb, D. K., Reddy, N. A., & Pettini, M. 2004, ApJ, 607, 226

Adelberger, K. L., Steidel, C. C., Shapley, A. E., & Pettini, M. 2003, ApJ, 584, 45

Alexander, D. M., Bauer, F. E., Brandt, W. N., Schneider, D. P., Hornschemeier, A. E., Vignali, C., Barger, A. J., Broos, P. S., Cowie, L. L., Garmire, G. P., Townsley, L. K., Bautz, M. W., Chartas, G., & Sargent, W. L. W. 2003, AJ, 126, 539

Alexander, D. M., Bauer, F. E., Chapman, S. C., Smail, I., Blain, A. W., Brandt, W. N., & Ivison, R. J. 2005, ApJ, 632, 736

Almaini, O., Lawrence, A., & Boyle, B. J. 1999, MNRAS, 305, L59

Alonso-Herrero, A., Takagi, T., Baker, A. J., Rieke, G. H., Rieke, M. J., Imanishi, M., & Scoville, N. Z. 2004, ApJ, 612, 222

Armus, L., Charmandaris, V., Spoon, H. W. W., Houck, J. R., Soifer, B. T., Brandl, B. R., Appleton, P. N., Teplitz, H. I., Higdon, S. J. U., Weedman, D. W., Devost, D., Morris, P. W., Uchida, K. I., van Cleve, J., Barry, D. J., Sloan, G. C., Grillmair, C. J., Burgdorf, M. J., Fajardo-Acosta, S. B., Ingalls, J. G., Higdon, J., Hao, L., Bernard-Salas, J., Herter, T., Troeltzsch, J., Unruh, B., & Winghart, M. 2004, ApJS, 154, 178

Baker, A. J., Lutz, D., Genzel, R., Tacconi, L. J., & Lehnert, M. D. 2001, A&A, 372, L37

Barger, A. J., Cowie, L. L., Capak, P., Alexander, D. M., Bauer, F. E., Fernandez, E., Brandt, W. N., Garmire, G. P., & Hornschemeier, A. E. 2003, AJ, 126, 632

Barger, A. J., Cowie, L. L., & Richards, E. A. 2000, AJ, 119, 2092

Barger, A. J., Cowie, L. L., Sanders, D. B., Fulton, E., Taniguchi, Y., Sato, Y., Kawara, K., & Okuda, H. 1998, Nature, 394, 248

Bell, E. F. 2002, ApJ, 577, 150

—. 2003, ApJ, 586, 794

Bell, E. F., Papovich, C., Wolf, C., Le Floc'h, E., Caldwell, J. A. R., Barden, M., Egami, E., McIntosh, D. H., Meisenheimer, K., Pérez-González, P. G., Rieke, G. H., Rieke, M. J., Rigby, J. R., & Rix, H.-W. 2005, ApJ, 625, 23

Benítez, N. 2000, ApJ, 536, 571

Blain, A. W., Chapman, S. C., Smail, I., & Ivison, R. 2004, ApJ, 611, 725

Blain, A. W., Kneib, J.-P., Ivison, R. J., & Smail, I. 1999, ApJ, 512, L87

Bolzonella, M., Miralles, J.-M., & Pelló, R. 2000, A&A, 363, 476

Borys, C., Chapman, S., Halpern, M., & Scott, D. 2003, MNRAS, 344, 385

Boselli, A., Lequeux, J., Sauvage, M., Boulade, O., Boulanger, F., Cesarsky, D., Dupraz, C., Madden, S., Viallefond, F., & Vigroux, L. 1998, A&A, 335, 53

Bouwens, R. J., Illingworth, G. D., Blakeslee, J. P., & Franx, M. 2006, ArXiv Astrophysics e-prints

Bouwens, R. J., Illingworth, G. D., Thompson, R. I., & Franx, M. 2005, ApJ, 624, L5

Bouwens, R. J., Thompson, R. I., Illingworth, G. D., Franx, M., van Dokkum, P. G., Fan, X., Dickinson, M. E., Eisenstein, D. J., & Rieke, M. J. 2004, ApJ, 616, L79

Brandt, W. N., Hornschemeier, A. E., Schneider, D. P., Alexander, D. M., Bauer, F. E., Garmire, G. P., & Vignali, C. 2001, ApJ, 558, L5

Brusa, M., Comastri, A., Daddi, E., Cimatti, A., Mignoli, M., & Pozzetti, L. 2002, ApJ, 581, L89

Bruzual, G. & Charlot, S. 1996, private communication (BC96 manual)

—. 2003, MNRAS, 344, 1000

Bunker, A., Stanway, E., Ellis, R., McMahon, R., Eyles, L., & Lacy, M. 2006, New Astronomy Review, 50, 94

Bunker, A. J., Stanway, E. R., Ellis, R. S., & McMahon, R. G. 2004, MNRAS, 355, 374

Burgarella, D., Perez-Gonzalez, P., Buat, V., Takeuchi, T. T., Lauger, S., Rieke, G., & Ilbert, O. 2005, ArXiv Astrophysics e-prints

Calzetti, D., Armus, L., Bohlin, R. C., Kinney, . A. L., Koornneef, J., & Storchi-Bergmann, T. 2000, ApJ, 533, 682

Calzetti, D. & Heckman, T. M. 1999, ApJ, 519, 27

Capak, P., Cowie, L. L., Hu, E. M., Barger, A. J., Dickinson, M., Fernandez, E., Giavalisco, M., Komiyama, Y., Kretchmer, C., McNally, C., Miyazaki, S., Okamura, S., & Stern, D. 2004, AJ, 127, 180

Chabrier, G. 2003, PASP, 115, 763

Chapman, S. C., Blain, A. W., Ivison, R. J., & Smail, I. R. 2003, Nature, 422, 695

Chapman, S. C., Blain, A. W., Smail, I., & Ivison, R. J. 2005, ApJ, 622, 772

Charmandaris, V., Mirabel, I. F., Tran, D., Laurent, O., Cesarsky, C. J., Gallais, P., Sauvage, M., & Vigroux, L. 1997, in Extragalactic Astronomy in the Infrared, 283–+

Cimatti, A., Daddi, E., Renzini, A., Cassata, P., Vanzella, E., Pozzetti, L., Cristiani, S., Fontana, A., Rodighiero, G., Mignoli, M., & Zamorani, G. 2004, Nature, 430, 184

Cimatti, A., Mignoli, M., Daddi, E., Pozzetti, L., Fontana, A., Saracco, P., Poli, F., Renzini, A., Zamorani, G., Broadhurst, T., Cristiani, S., D'Odorico, S., Giallongo, E., Gilmozzi, R., & Menci, N. 2002a, A&A, 392, 395

Cimatti, A., Pozzetti, L., Mignoli, M., Daddi, E., Menci, N., Poli, F., Fontana, A., Renzini, A., Zamorani, G., Broadhurst, T., Cristiani, S., D'Odorico, S., Giallongo, E., & Gilmozzi, R. 2002b, A&A, 391, L1

Cohen, J. G. 2001, AJ, 121, 2895

Cohen, J. G., Cowie, L. L., Hogg, D. W., Songaila, A., Blandford, R., Hu, E. M., & Shopbell, P. 1996, ApJ, 471, L5+

Cohen, J. G., Hogg, D. W., Blandford, R., Cowie, L. L., Hu, E., Songaila, A., Shopbell, P., & Richberg, K. 2000, ApJ, 538, 29

Comastri, A. & Fiore, F. 2004, A&SS, 294, 63

Condon, J. J. 1992, ARAA, 30, 575

Condon, J. J., Anderson, M. L., & Helou, G. 1991, ApJ, 376, 95

Conselice, C. J., Grogin, N. A., Jogee, S., Lucas, R. A., Dahlen, T., de Mello, D., Gardner, J. P., Mobasher, B., & Ravindranath, S. 2004, ApJ, 600, L139

Cowie, L. L., Barger, A. J., Hu, E. M., Capak, P., & Songaila, A. 2004, AJ, 127, 3137

Cowie, L. L., Songaila, A., Hu, E. M., & Cohen, J. G. 1996, AJ, 112, 839

Daddi, E., Cimatti, A., Renzini, A., Fontana, A., Mignoli, M., Pozzetti, L., Tozzi, P., & Zamorani, G. 2004a, ApJ, 617, 746

Daddi, E., Cimatti, A., Renzini, A., Vernet, J. ., Conselice, C., Pozzetti, L., Mignoli, M., Tozzi, P. an d Broadhurst, T., di Serego Alighieri, S., Fontana, A., Nonino, M., Rosati, P., & Zamorani, G. 2004b, ApJ, 600, L127

Daddi, E., Dickinson, M., Chary, R., Pope, A., Morrison, G., Alexander, D. M., Bauer, F. E., Brandt, W. N., Giavalisco, M., Ferguson, H., Lee, K.-S., Lehmer, B. D., Papovich, C., & Renzini, A. 2005a, astro-ph/0507504

Daddi, E., Renzini, A., Pirzkal, N., Cimatti, A., Malhotra, S., Stiavelli, M., Xu, C., Pasquali, A., Rhoads, J., Brusa, M., Di Serego Alighieri, S., Ferguson, H., Koekemoer, A., Moustakas, L., Panagia, N., & Windhorst, R. 2005b, astro-ph/0503102

Dale, D. A., Helou, G., Contursi, A., Silbermann, N. A., & Kolhatkar, S. 2001, ApJ, 549, 215

Dale, D. A., Silbermann, N. A., Helou, G., Valjavec, E., Malhotra, S., Beichman, C. A., Brauher, J., Contursi, A., Dinerstein, H. L., Hollenbach, D. J., Hunter, D. A., Kolhatkar, S., Lo, K.-Y., Lord, S. D., Lu, N. Y., Rubin, R. H., Stacey, G. J., Thronson, H. A., Werner, M. W., & Corwin, H. G. 2000, AJ, 120, 583

Dawson, S., Stern, D., Bunker, A. J., Spinrad, H., & Dey, A. 2001, AJ, 122, 598

Desert, F.-X., Boulanger, F., & Puget, J. L. 1990, A&A, 237, 215

Di Matteo, T., Croft, R. A. C., Springel, V., & Hernquist, L. 2003, ApJ, 593, 56

Dickinson, M. 1998, in The Hubble Deep Field, ed. M. Livio, S. M. Fall, & P. Madau, 219–+

Dickinson, M., Giavalisco, M., & The Goods Team. 2003a, in The Mass of Galaxies at Low and High Redshift, 324–+

Dickinson, M., Papovich, C., Ferguson, H. C., & Budavári, T. 2003b, ApJ, 587, 25

Dickinson, M., Stern, D., Giavalisco, M., Ferguson, H. C., Tsvetanov, Z., Chornock, R., Cristiani, S., Dawson, S., Dey, A., Filippenko, A. V., Moustakas, L. A., Nonino, M., Papovich, C., Ravindranath, S., Riess, A., Rosati, P., Spinrad, H., & Vanzella, E. 2004, ApJ, 600, L99

Diplas, A. & Savage, B. D. 1994, ApJS, 93, 211

Duc, P.-A., Fadda, D., Poggianti, B., Elbaz, D., Biviano, A., Flores, H., Moorwood, A., Franceschini, A., & Cesarsky, C. 2004, in IAU Colloq. 195: Outskirts of Galaxy Clusters: Intense Life in the Suburbs, 347–351

Elbaz, D., Cesarsky, C. J., Chanial, P., Aussel, H., Franceschini, A., Fadda, D., & Chary, R. R. 2002, A&A, 384, 848

Engelbracht, C. W., Gordon, K. D., Rieke, G. H., Werner, M. W., Dale, D. A., & Latter, W. B. 2005, ApJ, 628, L29

Erb, D. K., Shapley, A. E., Pettini, M., Steidel, C. C., Reddy, N. A., & Adelberger, K. L. 2006a, ArXiv Astrophysics e-prints

Erb, D. K., Shapley, A. E., Steidel, C. C., Pettini, M., Adelberger, K. L., Hunt, M. P., Moorwood, A. F. M., & Cuby, J.-G. 2003, ApJ, 591, 101

Erb, D. K., Steidel, C. C., Shapley, A. E., Pettini, M., Reddy, N. A., & Adelberger, K. L. 2006b, ArXiv Astrophysics e-prints

—. 2006c, ArXiv Astrophysics e-prints

Förster Schreiber, N. M., Roussel, H., Sauvage, M., & Charmandaris, V. 2004a, A&A, 419, 501

Förster Schreiber, N. M., Sauvage, M., Charmandaris, V., Laurent, O., Gallais, P., Mirabel, I. F., & Vigroux, L. 2003, A&A, 399, 833

Förster Schreiber, N. M., van Dokkum, P. G., Franx, M., Labbé, I., Rudnick, G., Daddi, E., Illingworth, G. D., Kriek, M., Moorwood, A. F. M., Rix, H.-W., Röttgering, H., Trujillo, I., van der Werf, P., van Starkenburg, L., & Wuyts, S. 2004b, ApJ, 616, 40

Fabian, A. C. & Iwasawa, K. 1999, MNRAS, 303, L34

Fadda, D., Flores, H., Hasinger, G., Franceschini, A., Altieri, B., Cesarsky, C. J., Elbaz, D., & Ferrando, P. 2002, A&A, 383, 838

Fadda, D. e. a. 2006, submitted

Fan, X., Strauss, M. A., Schneider, D. P., Gunn, J. E., Lupton, R. H., Becker, R. H., Davis, M., Newman, J. A., Richards, G. T., White, R. L., Anderson, J. E., Annis, J., Bahcall, N. A., Brunner, R. J., Csabai, I., Hennessy, G. S., Hindsley, R. B., Fukugita, M., Kunszt, P. Z., Ivezić, Ž., Knapp, G. R., McKay, T. A., Munn, J. A., Pier, J. R., Szalay, A. S., & York, D. G. 2001, AJ, 121, 54

Feigelson, E. D., Broos, P., Gaffney, J. A., Garmire, G., Hillenbrand, L. A., Pravdo, S. H., Townsley, L., & Tsuboi, Y. 2002, ApJ, 574, 258

Flores, H., Hammer, F., Thuan, T. X., Césarsky, C., Desert, F. X., Omont, A., Lilly, S. J., Eales, S., Crampton, D., & Le Fèvre, O. 1999, ApJ, 517, 148

Forster Schreiber, N. M., Genzel, R., Lehnert, M. D., Bouche, N., Verma, A., Erb, D. K., Shapley, A. E., Steidel, C. C., Davies, R., Lutz, D., Nesvadba, N., Tacconi, L. J., Eisenhauer, F., Abuter, R., Gilbert, A., Gillessen, S., & Sternberg, A. 2006, ArXiv Astrophysics e-prints

Franx, M., Labbé, I., Rudnick, G., van Dokkum , P. G., Daddi, E., Förster Schreiber, N. M., Moorwood, A., Rix, H., Röttgering, H., van de Wel, A., van der Werf, P., & van Starkenburg, L. 2003, ApJ, 587, L79

Frayer, D. T., Chapman, S. C., Yan, L., Armus, L., Helou, G., Fadda, D., Morganti, R., Garrett, M. A., Appleton, P., Choi, P., Fang, F., Heinrichsen, I., Im, M., Lacy, M., Marleau, F., Masci, F. J., Shupe, D. L., Soifer, B. T., Squires, G. K., Storrie-Lombardi, L. J., Surace, J. A., Teplitz, H. I., & Wilson, G. 2004, ApJS, 154, 137

Gabasch, A., Salvato, M., Saglia, R. P., Bender, R., Hopp, U., Seitz, S., Feulner, G., Pannella, M., Drory, N., Schirmer, M., & Erben, T. 2004, ApJ, 616, L83

Gallego, J., Zamorano, J., Aragon-Salamanca, A., & Rego, M. 1995, ApJ, 455, L1+

Genzel, R. & Cesarsky, C. J. 2000, ARAA, 38, 761

Giavalisco, M., Dickinson, M., Ferguson, H. C., Ravindranath, S., Kretchmer, C., Moustakas, L. A., Madau, P., Fall, S. M., Gardner, J. P., Livio, M., Papovich, C., Renzini, A., Spinrad, H., Stern, D., & Riess, A. 2004a, ApJ, 600, L103

Giavalisco, M., Ferguson, H. C., Koekemoer, A. M., Dickinson, M., Alexander, D. M., Bauer, F. E., Bergeron, J., Biagetti, C., Brandt, W. N., Casertano, S., Cesarsky, C., Chatzichristou, E., Conselice, C., Cristiani, S., Da Costa, L., Dahlen, T., de Mello, D., Eisenhardt, P., Erben, T., Fall, S. M., Fassnacht, C., Fosbury, R., Fruchter, A., Gardner, J. P., Grogin, N., Hook, R. N., Hornschemeier, A. E., Idzi, R., Jogee, S., Kretchmer, C., Laidler, V., Lee, K. S., Livio, M., Lucas, R., Madau, P., Mobasher, B., Moustakas,

L. A., Nonino, M., Padovani, P., Papovich, C., Park, Y., Ravindranath, S., Renzini, A., Richardson, M., Riess, A., Rosati, P., Schirmer, M., Schreier, E., Somerville, R. S., Spinrad, H., Stern, D., Stiavelli, M., Strolger, L., Urry, C. M., Vandame, B., Williams, R., & Wolf, C. 2004b, ApJ, 600, L93

Giavalisco, M., Koratkar, A., & Calzetti, D. 1996, ApJ, 466, 831

Gilli, R. 2004, Advances in Space Research, 34, 2470

Glazebrook, K., Abraham, R. G., McCarthy, P. J., Savaglio, S., Chen, H., Crampton, D., Murowinski, R., Jørgensen, I., Roth, K., Hook, I., Marzke, R. O., & Carlberg, R. G. 2004, Nature, 430, 181

Goldader, J. D., Meurer, G., Heckman, T. M., Seibert, M., Sanders, D. B., Calzetti, D., & Steidel, C. C. 2002, ApJ, 568, 651

Grimm, H.-J., Gilfanov, M., & Sunyaev, R. 2002, A&A, 391, 923

Gunn, J. E. & Stryker, L. L. 1983, ApJS, 52, 121

Haas, M., Klaas, U., Müller, S. A. H., Chini, R., & Coulson, I. 2001, A&A, 367, L9

Hansen, M. & Peng Oh, S. 2005, astro-ph/0507586

Helou, G., Khan, I. R., Malek, L., & Boehmer, L. 1988, ApJS, 68, 151

Helou, G., Lu, N. Y., Werner, M. W., Malhotra, S., & Silbermann, N. 2000, ApJ, 532, L21

Helou, G., Malhotra, S., Hollenbach, D. J., Dale, D. A., & Contursi, A. 2001, ApJ, 548, L73

Hogg, D. W., Tremonti, C. A., Blanton, M. R., Finkbeiner, D. P., Padmanabhan, N., Quintero, A. D., Schlegel, D. J., & Wherry, N. 2005, ApJ, 624, 162

Hopkins, P. F., Hernquist, L., Cox, T. J., Di Matteo, T., Martini, P., Robertson, B., & Springel, V. 2005, ApJ, 630, 705

Hornschemeier, A. E., Brandt, W. N., Garmire, G. P., Schneider, D. P., Barger, A. J., Broos, P. S., Cowie, L. L., Townsley, L. K., Bautz, M. W., Burrows, D. N., Chartas, G.,

Feigelson, E. D., Griffiths, R. E., Lumb, D., Nousek, J. A., Ramsey, L. W., & Sargent, W. L. W. 2001, ApJ, 554, 742

Houck, J. R., Soifer, B. T., Weedman, D., Higdon, S. J. U., Higdon, J. L., Herter, T., Brown, M. J. I., Dey, A., Jannuzi, B. T., Le Floc'h, E., Rieke, M., Armus, L., Charmandaris, V., Brandl, B. R., & Teplitz, H. I. 2005, ApJ, 622, L105

Hughes, D. H., Serjeant, S., Dunlop, J., Rowan-Robinson, M., Blain, A., Mann, R. G., Ivison, R., Peacock, J., Efstathiou, A., Gear, W., Oliver, S., Lawrence, A., Longair, M., Goldschmidt, P., & Jenness, T. 1998, Nature, 394, 241

Hunt, M. P., Steidel, C. C., Adelberger, K. L., & Shapley, A. E. 2004, ApJ, 605, 625

Kauffmann, G., Heckman, T. M., Tremonti, C., Brinchmann, J., Charlot, S., White, S. D. M., Ridgway, S. E., Brinkmann, J., Fukugita, M., Hall, P. B., Ivezić, Ž., Richards, G. T., & Schneider, D. P. 2003, MNRAS, 346, 1055

Kennicutt, R. C. 1998a, ARAA, 36, 189

—. 1998b, ApJ, 498, 541

Kim, D.-W., Fabbiano, G., & Trinchieri, G. 1992, ApJ, 393, 134

Kong, X., Charlot, S., Brinchmann, J., & Fall, S. M. 2004, MNRAS, 349, 769

Labbé, I., Huang, J., Franx, M., Rudnick, G., Barmby, P., Daddi, E., van Dokkum, P. G., Fazio, G. G., Förster Schreiber, N. M., Moorwood, A. F. M., Rix, H.-W., Röttgering, H., Trujillo, I., & van der Werf, P. 2005, astro-ph/0504219

Laird, E., Nandra, K., Adelberger, K. L., Steidel, C. C., & Reddy, N. A. 2005, astro-ph/0501411

Le Fèvre, O., Paltani, S., Arnouts, S., Charlot, S., Foucaud, S., Ilbert, O., McCracken, H. J., Zamorani, G., Bottini, D., Garilli, B., Le Brun, V., Maccagni, D., Picat, J. P., Scaramella, R., Scodeggio, M., Tresse, L., Vettolani, G., Zanichelli, A., Adami, C., Bardelli, S., Bolzonella, M., Cappi, A., Ciliegi, P., Contini, T., Franzetti, P., Gavignaud, I., Guzzo, L., Iovino, A., Marano, B., Marinoni, C., Mazure, A., Meneux, B., Merighi, R., Pellò, R., Pollo, A., Pozzetti, L., Radovich, M., Zucca, E., Arnaboldi, M., Bondi, M., Bongiorno,

A., Busarello, G., Gregorini, L., Lamareille, F., Mathez, G., Mellier, Y., Merluzzi, P., Ripepi, V., & Rizzo, D. 2005, Nature, 437, 519

Lehmer, B. D., Brandt, W. N., Alexander, D. M., Bauer, F. E., Conselice, C. J., Dickinson, M. E., Giavalisco, M., Grogin, N. A., Koekemoer, A. M., Lee, K.-S., Moustakas, L. A., & Schneider, D. P. 2005, AJ, 129, 1

Lilly, S. J., Le Fevre, O., Hammer, F., & Crampton, D. 1996, ApJ, 460, L1+

Lilly, S. J., Tresse, L., Hammer, F., Crampton, D., & Le Fevre, O. 1995, ApJ, 455, 108

Lowenthal, J. D., Koo, D. C., Guzman, R., Gallego, J., Phillips, A. C., Faber, S. M., Vogt, N. P., Illingworth, G. D., & Gronwall, C. 1997, ApJ, 481, 673

Madau, P. 1995, ApJ, 441, 18

Madau, P., Ferguson, H. C., Dickinson, M. E., Giavalisco, M., Steidel, C. C., & Fruchter, A. 1996, MNRAS, 283, 1388

Madau, P., Pozzetti, L., & Dickinson, M. 1998, ApJ, 498, 106

Makovoz, D. & Marleau, F. R. 2005, astro-ph/0507007

Meurer, G. R., Heckman, T. M., & Calzetti, D. 1999, ApJ, 521, 64

Nandra, K., Mushotzky, R. F., Arnaud, K., Steidel, C. C., Adelberger, K. L., Gardner, J. P., Teplitz, H. I., & Windhorst, R. A. 2002, ApJ, 576, 625

Normand, P., Rouan, D., Lacombe, F., & Tiphene, D. 1995, A&A, 297, 311

Oke, J. B., Cohen, J. G., Carr, M., Cromer, J., Dingizian, A., Harris, F. H., Labrecque, S., Lucinio, R., Schaal, W., Epps, H., & Miller, J. 1995, PASP, 107, 375

Oke, J. B. & Gunn, J. E. 1983, ApJ, 266, 713

Ouchi, M., Shimasaku, K., Okamura, S., Furusawa, H., Kashikawa, N., Ota, K., Doi, M., Hamabe, M., Kimura, M., Komiyama, Y., Miyazaki, M., Miyazaki, S., Nakata, F., Sekiguchi, M., Yagi, M., & Yasuda, N. 2004, ApJ, 611, 660

Papovich, C., Dickinson, M., & Ferguson, H. C. 2001, ApJ, 559, 620

Papovich, C., Giavalisco, M., Dickinson, M., Conselice, C. J., & Ferguson, H. C. 2003, ApJ, 598, 827

Papovich, C., Moustakas, L. A., Dickinson, M., Le Floc'h, E., Rieke, G. H., Daddi, E., Alexander, D. M., Bauer, F., Brandt, W. N., Dahlen, T., Egami, E., Eisenhardt, P., Elbaz, D., Ferguson, H. C., Giavalisco, M., Lucas, R. A., Mobasher, B., Pérez-González, P. G., Stutz, A., Rieke, M. J., & Yan, H. 2006, ApJ, 640, 92

Persic, M., Rephaeli, Y., Braito, V., Cappi, M., Della Ceca, R., Franceschini, A., & Gruber, D. E. 2004, A&A, 419, 849

Pettini, M., Kellogg, M., Steidel, C. C., Dickins on, M., Adelberger, K. L., & Giavalisco, M. 1998, ApJ, 508, 539

Pettini, M., Shapley, A. E., Steidel, C. C., Cuby, J.-G., Dickinson, M., Moorwood, A. F. M., Adelberger, K. L., & Giavalisco, M. 2001, ApJ, 554, 981

Phillips, A. C., Guzman, R., Gallego, J., Koo, D. C., Lowenthal, J. D., Vogt, N. P., Faber, S. M., & Illingworth, G. D. 1997, ApJ, 489, 543

Pope, A., Borys, C., Scott, D., Conselice, C., Dickinson, M., & Mobasher, B. 2005, MNRAS, 358, 149

Pozzi, F., Gruppioni, C., Oliver, S., Matute, I., La Franca, F., Lari, C., Zamorani, G., Serjeant, S., Franceschini, A., & Rowan-Robinson, M. 2004, ApJ, 609, 122

Puget, J. L. & Leger, A. 1989, ARAA, 27, 161

Ranalli, P., Comastri, A., & Setti, G. 2003, A&A, 399, 39

Reddy, N. A., Adelberger, K. L., Steidel, C. C., Shapley, A. E., Pettini, M., & Erb, D. K. 2006a, in preparation

Reddy, N. A., Erb, D. K., Steidel, C. C., Shapley, A., Adelberger, K. L., & Pettini, M. 2005, ApJ, 633, 748

Reddy, N. A. & Steidel, C. C. 2004, ApJ, 603, L13

Reddy, N. A., Steidel, C. C., Fadda, D., Yan, L., Pettini, M., Shapley, A. E., Erb, D. K., & Adelberger, K. L. 2006b, ArXiv Astrophysics e-prints

—. 2006c, ArXiv Astrophysics e-prints

Richards, E. A. 2000, ApJ, 533, 611

Rix, S. A., Pettini, M., Leitherer, C., Bresolin, F., Kudritzki, R.-P., & Steidel, C. C. 2004, ApJ, 615, 98

Roussel, H., Sauvage, M., Vigroux, L., & Bosma, A. 2001, A&A, 372, 427

Rowan-Robinson, M., Lari, C., Perez-Fournon, I., Gonzalez-Solares, E. A., La Franca, F., Vaccari, M., Oliver, S., Gruppioni, C., Ciliegi, P., Héraudeau, P., Serjeant, S., Efstathiou, A., Babbedge, T., Matute, I., Pozzi, F., Franceschini, A., Vaisanen, P., Afonso-Luis, A., Alexander, D. M., Almaini, O., Baker, A. C., Basilakos, S., Barden, M., del Burgo, C., Bellas-Velidis, I., Cabrera-Guerra, F., Carballo, R., Cesarsky, C. J., Clements, D. L., Crockett, H., Danese, L., Dapergolas, A., Drolias, B., Eaton, N., Egami, E., Elbaz, D., Fadda, D., Fox, M., Genzel, R., Goldschmidt, P., Gonzalez-Serrano, J. I., Graham, M., Granato, G. L., Hatziminaoglou, E., Herbstmeier, U., Joshi, M., Kontizas, E., Kontizas, M., Kotilainen, J. K., Kunze, D., Lawrence, A., Lemke, D., Linden-Vørnle, M. J. D., Mann, R. G., Márquez, I., Masegosa, J., McMahon, R. G., Miley, G., Missoulis, V., Mobasher, B., Morel, T., Nørgaard-Nielsen, H., Omont, A., Papadopoulos, P., Puget, J.-L., Rigopoulou, D., Rocca-Volmerange, B., Sedgwick, N., Silva, L., Sumner, T., Surace, C., Vila-Vilaro, B., van der Werf, P., Verma, A., Vigroux, L., Villar-Martin, M., Willott, C. J., Carramiñana, A., & Mujica, R. 2004, MNRAS, 351, 1290

Rubin, K. H. R., van Dokkum, P. G., Coppi, P., Johnson, O., Förster Schreiber, N. M., Franx, M., & van der Werf, P. 2004, ApJ, 613, L5

Rudnick, G., Rix, H., Franx, M., Labbé, I. ., Blanton, M., Daddi, E., Förster Schreiber, N. M., Moorwood, A., Röttgering, H., Trujillo, I., van de Wel, A., van der Werf, P., van Dokkum, P. G., & van Starkenburg, L. 2003, ApJ, 599, 847

Salpeter, E. E. 1955, ApJ, 121, 161

Sanders, D. B. & Mirabel, I. F. 1996, ARAA, 34, 749

Sawicki, M. & Thompson, D. 2005, ArXiv Astrophysics e-prints

Scannapieco, E., Silk, J., & Bouwens, R. 2005, ApJ, 635, L13

Schechter, P. 1976, ApJ, 203, 297

Schiminovich, D., Arnouts, S., Milliard, B., & GALEX Science Team. 2003, American Astronomical Society Meeting Abstracts, 203,

Schiminovich, D., Ilbert, O., Arnouts, S., Milliard, B., Tresse, L., Le Fèvre, O., Treyer, M., Wyder, T. K., Budavári, T., Zucca, E., Zamorani, G., Martin, D. C., Adami, C., Arnaboldi, M., Bardelli, S., Barlow, T., Bianchi, L., Bolzonella, M., Bottini, D., Byun, Y.-I., Cappi, A., Contini, T., Charlot, S., Donas, J., Forster, K., Foucaud, S., Franzetti, P., Friedman, P. G., Garilli, B., Gavignaud, I., Guzzo, L., Heckman, T. M., Hoopes, C., Iovino, A., Jelinsky, P., Le Brun, V., Lee, Y.-W., Maccagni, D., Madore, B. F., Malina, R., Marano, B., Marinoni, C., McCracken, H. J., Mazure, A., Meneux, B., Morrissey, P., Neff, S., Paltani, S., Pellò, R., Picat, J. P., Pollo, A., Pozzetti, L., Radovich, M., Rich, R. M., Scaramella, R., Scodeggio, M., Seibert, M., Siegmund, O., Small, T., Szalay, A. S., Vettolani, G., Welsh, B., Xu, C. K., & Zanichelli, A. 2005, ApJ, 619, L47

Schmidt, M., Schneider, D. P., & Gunn, J. E. 1995, AJ, 110, 68

Seibert, M., Heckman, T. M., & Meurer, G. R. 2002, AJ, 124, 46

Shapley, A. E., Erb, D. K., Pettini, M., Steidel, C. C., & Adelberger, K. L. 2004, ApJ, 612, 108

Shapley, A. E., Steidel, C. C., Adelberger, K. L., Dickinson, M., Giavalisco, M., & Pettini, M. 2001, ApJ, 562, 95

Shapley, A. E., Steidel, C. C., Erb, D. K., Reddy, N. A., Adelberger, K. L., Pettini, M., Barmby, P., & Huang, J. 2005, ApJ, 626, 698

Shapley, A. E., Steidel, C. C., Pettini, M., & Adelberger, K. L. 2003, ApJ, 588, 65

Shaver, P. A., Wall, J. V., Kellermann, K. I., Jackson, C. A., & Hawkins, M. R. S. 1996, Nature, 384, 439

Smail, I. 2003, in IAU Symposium

Smail, I., Ivison, R. J., & Blain, A. W. 1997, ApJ, 490, L5+

Smail, I., Ivison, R. J., Blain, A. W., & Kneib, J.-P. 2002, MNRAS, 331, 495

Soifer, B. T., Sanders, D. B., Madore, B. F., Neugebauer, G., Danielson, G. E., Elias, J. H., Lonsdale, C. J., & Rice, W. L. 1987, ApJ, 320, 238

Stark, A. A., Gammie, C. F., Wilson, R. W., Bally, J., Linke, R. A., Heiles, C., & Hurwitz, M. 1992, ApJS, 79, 77

Steidel, C. C., Adelberger, K. L., Giavalisco, M., Dickinson, M., & Pettini, M. 1999, ApJ, 519, 1

Steidel, C. C., Adelberger, K. L., Shapley, A. E., Erb, D. K., Reddy, N. A., & Pettini, M. 2005, ApJ, 626, 44

Steidel, C. C., Adelberger, K. L., Shapley, A. E., Pettini, M., Dickinson, M., & Giavalisco, M. 2003, ApJ, 592, 728

Steidel, C. C., Giavalisco, M., Dickinson, M., & Adelberger, K. L. 1996, AJ, 112, 352

Steidel, C. C. & Hamilton, D. 1993, AJ, 105, 2017

Steidel, C. C., Hunt, M. P., Shapley, A. E., Adelberger, K. L., Pettini, M., Dickinson, M., & Giavalisco, M. 2002, ApJ, 576, 653

Steidel, C. C., Pettini, M., & Hamilton, D. 1995, AJ, 110, 2519

Steidel, C. C., Shapley, A. E., Pettini, M., Adelberger, K. L., Erb, D. K., Reddy, N. A., & Hunt, M. P. 2004, ApJ, 604, 534

Strickland, D. K., Heckman, T. M., Colbert, E. J. M., Hoopes, C. G., & Weaver, K. A. 2004, ApJ, 606, 829

Sturm, E., Lutz, D., Tran, D., Feuchtgruber, H., Genzel, R., Kunze, D., Moorwood, A. F. M., & Thornley, M. D. 2000, A&A, 358, 481

Swinbank, A. M., Smail, I., Chapman, S. C., Blain, A. W., Ivison, R. J., & Keel, W. C. 2004, ApJ, 617, 64

Tielens, A. G. G. M., Hony, S., van Kerckhoven, C., & Peeters, E. 1999, in ESA SP-427: The Universe as Seen by ISO, 579–+

van Dokkum, P. G., Förster Schreiber, N. M., Franx, M., Daddi, E., Illingworth, G. D., Labbé, . I., Moorwood, A., Rix, H., Röttgering, H., Rudnick, G. ., van der Wel, A., van der Werf, P., & van Starkenburg, L. 2003, ApJ, 587, L83

van Dokkum, P. G., Franx, M., Förster Schreiber, . N. M., Illingworth, G. D., Daddi, E., Knudsen, K. K., Labbé, I., Moorwood, A., Rix, H., Röttgering H., Rudnick, G., Trujillo, I., van der Werf, P., van der Wel, A., van Starkenburg, L., & Wuyts, S. 2004, ApJ, 611, 703

van Dokkum, P. G., Quadri, R., Marchesini, D., Rudnick, G., Franx, M., Gawiser, E., Herrera, D., Wuyts, S., Lira, P., Labbé, I., Maza, J., Illingworth, G. D., Förster Schreiber, N. M., Kriek, M., Rix, H.-W., Taylor, E. N., Toft, S., Webb, T., & Yi, S. K. 2006, ApJ, 638, L59

Vanzella, E., Cristiani, S., Dickinson, M., Kuntschner, H., Moustakas, L. A., Nonino, M., Rosati, P., Stern, D., Cesarsky, C., Ettori, S., Ferguson, H. C., Fosbury, R. A. E., Giavalisco, M., Haase, J., Renzini, A., Rettura, A., Serra, P., & The Goods Team. 2005, A&A, 434, 53

Wang, W.-H., Cowie, L. L., & Barger, A. J. 2004, ApJ, 613, 655

Webb, T. M. A., Lilly, S. J., Clements, D. L., Eales, S., Yun, M., Brodwin, M., Dunne, L., & Gear, W. K. 2003, ApJ, 597, 680

Weedman, D., Charmandaris, V., & Zezas, A. 2004, ApJ, 600, 106

Williams, R. E., Baum, S., Bergeron, L. E., Bernstein, N., Blacker, B. S., Boyle, B. J., Brown, T. M., Carollo, C. M., Casertano, S., Covarrubias, R., de Mello, D. F., Dickinson, M. E., Espey, B. R., Ferguson, H. C., Fruchter, A., Gardner, J. P., Gonnella, A., Hayes, J., Hewett, P. C., Heyer, I., Hook, R., Irwin, M., Jones, D., Kaiser, M. E., Levay, Z., Lubenow, A., Lucas, R. A., Mack, J., MacKenty, J. W., Madau, P., Makidon, R. B.,

Martin, C. L., Mazzuca, L., Mutchler, M., Norris, R. P., Perriello, B., Phillips, M. M., Postman, M., Royle, P., Sahu, K., Savaglio, S., Sherwin, A., Smith, T. E., Stiavelli, M., Suntzeff, N. B., Teplitz, H. I., van der Marel, R. P., Walker, A. R., Weymann, R. J., Wiggs, M. S., Williger, G. M., Wilson, J., Zacharias, N., & Zurek, D. R. 2000, AJ, 120, 2735

Williams, R. E., Blacker, B., Dickinson, M., Dixon, W. V. D., Ferguson, H. C., Fruchter, A. S., Giavalisco, M., Gilliland, R. L., Heyer, I., Katsanis, R., Levay, Z., Lucas, R. A., McElroy, D. B., Petro, L., Postman, M., Adorf, H.-M., & Hook, R. 1996, AJ, 112, 1335

Wilson, J. C., Eikenberry, S. S., Henderson, C. P., Hayward, T. L., Carson, J. C., Pirger, B., Barry, D. J., Brandl, B. R., Houck, J. R., Fitzgerald, G. J., & Stolberg, T. M. 2003, in Instrument Design and Performance for Optical/Infrared Ground-based Telescopes. Edited by Iye, Masanori; Moorwood, Alan F. M. Proceedings of the SPIE, Volume 4841, pp. 451-458 (2003)., 451–458

Wirth, G. D., Willmer, C. N. A., Amico, P., Chaffee, F. H., Goodrich, R. W., Kwok, S., Lyke, J. E., Mader, J. A., Tran, H. D., Barger, A. J., Cowie, L. L., Capak, P., Coil, A. L., Cooper, M. C., Conrad, A., Davis, M., Faber, S. M., Hu, E. M., Koo, D. C., Le Mignant, D., Newman, J. A., & Songaila, A. 2004, AJ, 127, 3121

Wyder, T. K., Treyer, M. A., Milliard, B., Schiminovich, D., Arnouts, S., Budavári, T., Barlow, T. A., Bianchi, L., Byun, Y.-I., Donas, J., Forster, K., Friedman, P. G., Heckman, T. M., Jelinsky, P. N., Lee, Y.-W., Madore, B. F., Malina, R. F., Martin, D. C., Morrissey, P., Neff, S. G., Rich, R. M., Siegmund, O. H. W., Small, T., Szalay, A. S., & Welsh, B. Y. 2005, ApJ, 619, L15

Yan, H., Dickinson, M., Eisenhardt, P. R. M., Ferguson, H. C., Grogin, N. A., Paolillo, M., Chary, R., Casertano, S., Stern, D., Reach, W. T., Moustakas, L. A., & Fall, S. M. 2004, ApJ, 616, 63

Yan, H., Windhorst, R. A., & Cohen, S. H. 2003, ApJ, 585, L93

Yan, L., Chary, R., Armus, L., Teplitz, H., Helou, G., Frayer, D., Fadda, D., Surace, J., & Choi, P. 2005, ApJ, 628, 604

Yun, M. S., Reddy, N. A., & Condon, J. J. 2001, ApJ, 554, 803